Structure and Reactivity of Iron Single Crystal Surfaces

by Sharon Booyens

in partial fulfilment of the requirements for the degree

Doctor of Philosophy in Chemistry

Cardiff, December 2010

ProQuest LLC
789 East Eisenhower Parkway
P.O. Box 1346
Ann Arbor, MI 48106-1346

Declaration

This work has not previously been accepted in substance for any degree and is not concurrently submitted in candidature for any degree.

This thesis is being submitted in partial fulfilment of the requirements for the degree of PhD.

This thesis is the result of my own independent work/investigation, except where otherwise stated. Other sources are acknowledged in explicit references.

I hereby give consent for my thesis, if accepted, to be available for photocopying and for inter-library loan, and for the title and abstract to be made available to outside organisations.

Name Sharon Booyens

Signature 

Date 17 December 2010

Dedicated To My Husband, Eugene

Abstract

DFT calculations show that CO in the shallow hollow site of Fe(111) is the most stable adsorption configuration, in agreement with previous reports. However, CO diffusion is facile and dissociation from the newly optimised di-bridge state occurs with the lowest barrier; the state has a tilting angle of 57° with regards to the surface normal. In general pathways possessing transition states in which O is bridged (instead of terminally bonded) is more favourable. The lowest activation energy barrier for CO dissociation was calculated to be ~1 eV (RPBE). ¼ ML of additional C was shown to stabilize the CO molecule if close interaction is avoided, but C has a destabilizing effect on the dissociated species, since it frequently blocks the most favourable site for O adsorption, which forces both atoms into less favourable configurations. In the presence of C the lowest energy pathway starts with CO in the deep hollow site and ends with C in a quasi fourfold position (QFF) and O in a QFFμ^3 site (the di bridge state is not stable on the C/Fe surface); E_a = 0.63 eV. In this pathway the atoms are highly coordinated at each stage and only have to move a short distance to reach the end states. The reaction energies of all CO dissociation pathways on C/Fe(111) are endothermic and significantly higher compared to the clean surface mainly due to the unfavourable end states, which should make CO dissociation on this surface rather improbable.

In practice Fe single crystals are difficult to clean and small amounts of contaminants can lead to reconstruction of the surface, as observed with STM and LEED. Oxidation of Fe(111) leads to a mixture of oxides, with FeO being the dominant species (as judged by the XPS peak position). Dosing the clean surface with O_2 leads to simple LEED patterns, but a mixture of surface adatoms can lead to complicated patterns consisting of more than one overlayer structure. Dosing Fe(110) with C_2H_4 at 473 K results in the formation of C surface species as well as islands which are tentatively attributed to graphene.

Sticking probability measurements with a molecular beam reactor show that the initial sticking probability of C_2H_4 on Fe(111) decreases with temperature from 0.35 at 373 K to 0.13 at 873 K. Steady state sticking commences above 573 K and only steady state sticking is observed above 723 K. Between 373 and 673 K the carbon deposits resulting from C_2H_4 dosing decreases O_2 sticking compared to the clean surface (~0.24 on C/Fe(111) *vs.* ~0.30 on the clean surface), since the surface now accommodates both species. Above this

temperature O_2 sticking increases significantly compared to the clean surface as it reacts with surface C to form CO gas: 0.06 *vs.* 0.34 at 773 K. CO production continues to increase with increasing surface temperature even though the XPS C 1s signal decreases above 673 K (apparently due to C diffusing into the subsurface region). This implies O on the surface provides a driving force for C in the subsurface / bulk to segregate to the surface. However, a large portion of the C resides in the bulk and can therefore not be cleaned off in this way.

Acknowledgements

There are many people whose help and support have been invaluable to me during my time at Cardiff and I would like to take this opportunity to thank them.

First of all I would like to thank my employer, *Sasol Technology*, for giving me the opportunity to further my studies, but also to broaden my horizons and worldview. The experience has made me a better scientist and person. My colleagues at *SASOL*, notably Dr. Tracy Bromfield, my group leader at the time, whose initiative, encouragement and efficacy enabled me to pursue the degree. Dr. Bruce Anderson for his continued interest, effort and input into my work. Mr. Philip Gibson, my departmental manager, for his support and understanding when things did not go to plan.

Prof. Mike Bowker, my supervisor, for welcoming me into his group and helping me to see the project through. Dr. Dave Willock, my co-supervisor and one of the best teachers I've met, for his guidance in the computational chemistry.

Dr. Phil Davies, my mentor, who frequently took on my problems as his own, and who was always nearby to give guidance and advice; your energy and enthusiasm is an inspiration to me. Dr. Dyfan Edwards, most of all for the great amount of energy he has exerted in trouble shooting and problem solving! Dr. Dave Morgan, who knows something of everything and is always willing to share his knowledge, know-how and practical help.

Thanks to the fellow students in the *Surface Science & Catalysis* group for their friendship, kindness and assistance with (among other things) setting up for bake out of "the Beast"! Alun Davies and the rest of the support staff, whose creativity and craftsmanship have brought us through crises multiple times.

Eugene, my husband, for sacrificing to share this unforgettable adventure with me; with whom I can share the joys and disappointments of my work and whose unconditional support and empathy is a great source of strength to me. Our family, for their boundless love, passionate desire for our well-being/happiness and for tolerating the time we spent away from them.

Index

P.T.O.

List of Abbreviations

a.c.	Alternating Current
AES	Auger Electron Spectroscopy
ASF	Anderson-Schulz-Flory (plot/model/distribution)
AFM	Atomic Force Microscopy
bcc	Body Centered Cubic
CTL	Coal-to-Liquids
d.c.	Direct Current
DFT	Density Functional Theory
ESD	Energy Dispersive X-ray Spectroscopy
fcc	Face Centered Cubic
FT	The Fischer-Tropsch Reaction
FTS	Fischer-Tropsch Synthesis
GGA	Generalized Gradient Approximation
GTL	Gas-to-Liquids
hcp	Hexagonal Closed Packed
HF	Hatree-Fock Calculation Method
hsp	Higher Order Saddle Point
HREELS	High Resolution Electron Energy Loss Spectroscopy
IMFP	Inelastic Mean Free Path
KS	Kohn-Sham DFT equations

P.T.O.

LDA	Local Density Approximation
LEED	Low Energy Electron Diffraction
MS	Mass Spectroscopy (/Spectrometer)
PBE	Perdew-Burke-Ernzerhof functional
PDOS	Projected Density of States
PES	Potential Energy Surface
PW91	Perdew-Wang 91 functional
RFA	Retarding Field Analyzer
RPBE	Revised Perdew-Burke-Ernzerhof functional
SAM	Scanning Auger Microscopy
SEM	Scanning Electron Microscopy
SPM	Scanning Probe Microscopy
STM	Scanning Tunneling Spectroscopy
TPD	Temperature Programmed Desorption
UHV	Ultra High Vacuum
TS	Transition State
VASP	Vienna Ab-initio Simulation Package
WGS	Water Gas Shift Reaction
XPS	X-Ray Photoelectron Spectroscopy
ZPE	Zero Point Energy

CHAPTER 1

Surface Science & Heterogeneous Catalysis

1.1. Introduction

Perhaps the greatest reason to study chemical reactions on surfaces is to gain a better understanding of heterogeneous catalysis. Heterogeneous catalysis forms the basis of the chemical industry; more than 90% of the chemical manufacturing processes in use worldwide utilize catalysts in some way: much of the food we eat, the medicines we take, many fabrics in our clothes, construction materials in our buildings, fuels that transport us by road, sea or air are produced by heterogeneously catalysed reactions.[1]

Surface science plays an increasingly significant role in the process of gaining greater understanding in heterogeneous catalysis. Through surface science studies of single crystals, complex real catalytic systems that are influenced by multiple variables, can be reduced to well-defined models; and the governing principles of the real system can potentially be systematically uncovered.

The aim of this chapter is to give an overview of some fundamental principles of surface science and heterogeneous catalysis and to illustrate the importance and relevance of surface science studies in the understanding of heterogeneous catalytic processes.

1.2. Heterogeneous Catalysis

The term *catalysis* was first coined by Baron J.J. Berzelius[2] in 1835 to describe the property of a substance that facilitates a chemical reaction without being consumed in it. A catalyst functions by providing an alternative pathway with lower activation energy than that of the original, as illustrated in Figure 1.1. The equilibrium composition of reactants and products is determined solely by thermodynamics, but catalysts can greatly affect the rate of a reaction.

Catalysts are classified as *homogeneous* if they are present in the same phase as the reactants (usually liquid) and *heterogeneous* if they are present in a different phase (usually solid, with reactants being gases or liquids).[3] This particular characteristic is also an important advantage of heterogeneous catalysis – in that the catalyst can usually be separated from the product stream with relative ease. In addition, heterogeneous catalysts are typically more tolerant of extreme operating conditions than their homogeneous analogues.

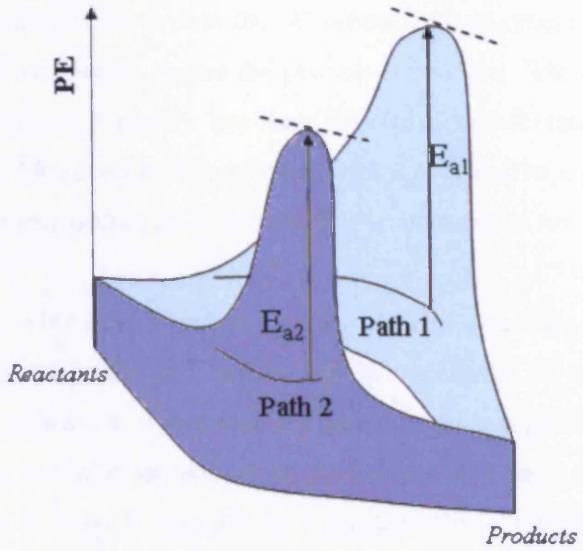

Figure 1.1 – Diagram illustrating the function of a catalyst: An alternative pathway (path 2) with lower activation energy than the original (path 1) is provided to increase the rate of the reaction.

There is no single, all-embracing theory of heterogeneous catalysis as for relativity or electromagnetism; but there is, however, a body of principles which serves as an interpretive and predictive framework for coping with heterogeneous processes.[4] Some important fundamental principles will be discussed in the subsequent sections.

1.3. Reactions at Surfaces

1.3.1. Gas Adsorption[5]

Heterogeneous catalysts are typically solids and require the chemisorptive adsorption of at least one of the (gas) reactants in the reaction for activation (and therefore catalysis) to proceed.

Adsorption is the bond formation between a molecule (the adsorbate) and a surface (the adsorbent). *Associative adsorption* happens when a molecule adsorbs on a surface from the gas phase and remains fully intact; while *dissociative adsorption* involves the breaking of the original gas phase bond.

Adsorption can be divided into two broad categories depending on the magnitude of their adsorption enthalpies: physisorption and chemisorption. *Physisorption* is essentially the

balancing of weak attractive forces with the repulsive force associated with close contact. Electron density is redistributed within the adsorbate and adsorbent separately (no formal chemical bond is formed), which makes the process reversible. The enthalpy of adsorption (ΔH_{ad}^{0}) for physisorption is typically less than 35 kJ/mol and therefore in the order of the heat of condensation. Adsorption is non-specific (not confined to a particular surface site) which allows for the formation of multi-layers of adsorbate on the surface.

Chemisorption on the other hand involves the formation of a strong chemical bond (ionic or covalent) between the adsorbate and surface (*i.e.* the exchange of electrons). The heat of adsorption can be significantly higher than for physisorption, typically $35 < -\Delta H_{ad}^{0} < 1000$ kJ/mol, but this value is highly dependent on the surface coverage, adsorbent substrate and surface face since each bond is specific to a surface site (a particular atom or group of atoms).

Although these distinctions can be made, a roughly continuous spectrum of interaction strengths exists when going from physisorption to chemisorption.

1.3.2. Adsorption Isotherms[5-7]

The *fractional coverage*, θ, of an adsorbate on a surface is defined as:

$$\theta = \frac{Number\ of\ surface\ sites\ occupied\ by\ adsorbate}{Total\ number\ of\ substrate\ adsorbate\ sites} = \frac{N_{occupied}}{N_{total}} \qquad [1.1]$$

N_{total} is often numerically equivalent to the total number of surface atoms of the substrate. If $\theta = 1$, the coverage is said to be one monolayer (1 ML).

An *adsorption isotherm* is the relation between the fractional coverage, θ, on the surface and the gas pressure in the chamber, P, that is in equilibrium with the surface at constant temperature.[3] At sufficiently low gas pressures all adsorption isotherms are linear:

$$P = constant \times \theta \qquad [1.2]$$

One of the most basic isotherms was developed by (and named after) Irving Langmuir and describes an ideal chemisorption systems based on the following assumptions:[8,9]

1. Adsorption occurs on specific sites and all adsorption sites are equivalent.
2. A dynamic equilibrium exists between the gas and the adsorbed layer at constant temperature.
3. An adsorption site can be occupied by only one molecule of adsorbate (*i.e.* once all the sites are occupied, adsorption ceases; a maximum of one monolayer can be deposited).
4. Once adsorbed, molecules are localized (cannot migrate to adjacent sites) and the enthalpy of adsorption per site remains constant irrespective of the coverage.

The Langmuir equation can be derived for the associative adsorption of a gas phase molecule (*M*) in dynamic equilibrium with the surface (*S* represents one surface site):

$$M_{(g)} + S \underset{k_d}{\overset{k_a}{\rightleftharpoons}} M\text{-}S \qquad [1.3]$$

k_a and k_d are the rate constants for adsorption and desorption respectively. The rate constant k_a is related to S_0, the sticking probability of the gas on the clean surface and Z, the Knudsen collision factor. So that the

$$Rate\ of\ adsorption = S_0 Z P (1-\theta) = k_a P (1-\theta) \qquad [1.4]$$

With P the gas pressure and $(1-\theta)$ the fractional monolayer coverage of sites on the surface not occupied by adsorbate molecules. Similarly, the

$$Rate\ of\ desorption = k_d \theta \qquad [1.5]$$

Showing that the rate of desorption is not directly dependent on the gas pressure. At equilibrium, the rate of adsorption and desorption are equal:

$$k_a P (1-\theta) = k_d \theta \qquad [1.6]$$

Upon rearrangement the *Langmuir adsorption isotherm* for associative adsorption is obtained:

$$\theta = \frac{N_{occupied}}{N_{total}} = \frac{KP}{1+KP} \qquad \left(K = \frac{k_a}{k_d}\right) \qquad [1.7]$$

At low pressure

$$P \xrightarrow{\lim} 0, \quad \left(\frac{KP}{1+KP}\right) = 0 \quad \text{and} \quad \theta = \frac{KP}{1+small\ nr} = KP \qquad [1.8]$$

At high pressure

$$P \xrightarrow{\lim} \infty, \quad \left(\frac{KP}{1+KP}\right) = 1 \text{ and } \theta = 1 \qquad [1.9]$$

This signifies that all the adsorption sites are filled and a complete monolayer is formed. The equilibrium constant, K, represents the affinity of a particular molecule for the surface. Large values of K imply a strong bond is formed between the adsorbate and substrate, whereas for small values of K the opposite is true.

The Langmuir isotherm can be used to calculate the number of adsorption sites on the surface of a substrate and ultimately the surface area. By rearranging equation 1.7 we get

$$\frac{P}{N_{occupied}} = \frac{1}{N_{total}K} + P\left(\frac{1}{N_{total}}\right) \qquad [1.10]$$

Since *equation 1.10* is a linear relationship, and a plot of $\frac{P}{N_{occupied}}$ *vs.* P gives a straight line with gradient $\frac{1}{N_{total}}$ and intercept $\frac{1}{N_{total}K}$ (N can also be replaced by the volume or mass of the gas). By knowing N_{total}, the surface area of the substrate can be calculated with the relationship

$$SA = N_{total} \times A_m \qquad [1.11]$$

With SA being the surface area, N the total number of adsorption sites and A_m the area of one molecule. Since the reaction rate is directly related to the surface area, catalytic activity

must always be normalized to the surface area when determining (and comparing) intrinsic activities of different catalysts.

To overcome the restrictions of the Langmuir isotherm, various other models have been developed; the Brunauer, Emmett and Teller (BET) isotherm being one of the most commonly used to determine the surface area of a catalyst. This isotherm describes multilayer formation by physisorption, in a layer by layer fashion. Other isotherms include the Freundlich isotherm, which accounts for the heat of adsorption being coverage dependent; and the Temkin isotherm for energetically non-equivalent sites.

1.3.3. Kinetics of Surface Adsorption

Figure 1.2 illustrates the possible pathways of a molecule that is approaching a surface. One dimensional diagrams like this spring from the work of Lennard and Jones in the 1930's, developed to further understanding of H_2 adsorption on metal surfaces. The diagram represents non-activated adsorption, since no energy barrier is encountered by the molecule in the process of approaching the surface.

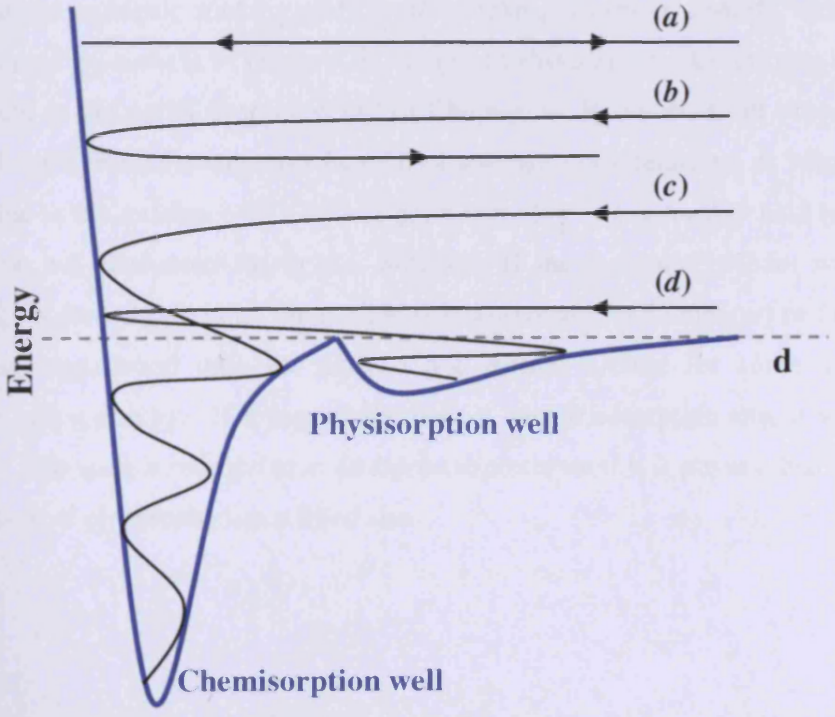

Figure 1.2 – Possible pathways of a molecule interacting with a surface *a*) elastic scattering; *b*) inelastic scattering; *c*) sticking (chemisorption); *d*) trapping (physisorption).[10]

The particle must lose enough energy to stick to the surface; therefore, an elastically scattered particle, which by definition doesn't lose energy (and similarly an inelastically scattered particle) always leaves the surface to returns to the gas phase. Trajectory *a* and *b* in Figure 1.2 represents elastic and inelastic scattering respectively.[8]
Trajectory *c* represents the sticking event. Sticking refers to the transfer of a molecule into a bound adsorbed state on the surface. The diagram shows that when the molecule approaches the surface, it is scattered off the repulsive wall; however, in the process it loses sufficient energy for the total energy to drop below zero of the potential energy curve. Then more energy is lost and the molecule can drop to the bottom of the chemisorption well.

For this Langmuir type behaviour (dictating the direct adsorption from the gas phase into a chemisorbed state) the probability of a gas molecule being accommodated on the surface, the *sticking probability,* is defined as:

$$S = S_0(1-\theta) \qquad [1.12]$$

$$\text{with } S = \frac{\text{rate of adsorption of molecules on the surface}}{\text{rate of collision of molecules with the surface (Z)}} \qquad \text{and } S = S_0 \text{ at } \theta = 0$$

Equation 1.12 implies that more vacant sites on the surface result in an increase in the probability of the molecule sticking and that the sticking decreases linearly with coverage; this is represented by *curve a* in Figure 1.3. Langmuir dissociative adsorption is represented by *curve b* and is discussed in more detail in Chapter 5. However, from experiment it is known that *S* can exceed the value predicted by Langmuir considerations, as with *curve c* in Figure 1.3, due to the existence of a mobile precursor state (*i.e.* a weakly held intermediate state) which is not accounted for in this isotherm. If the molecule collides with a filled adsorption site it can rebound into the gas phase (as predicted by Langmuir) or form a weak van der Waals-type bond with the surface and diffuse around for some time, whilst continuously losing energy. If it eventually finds a vacant adsorption site, it will become chemisorbed. The state is referred to as an *intrinsic* precursor if it is physisorbed on a vacant site and *extrinsic* if physisorbed on a filled site.

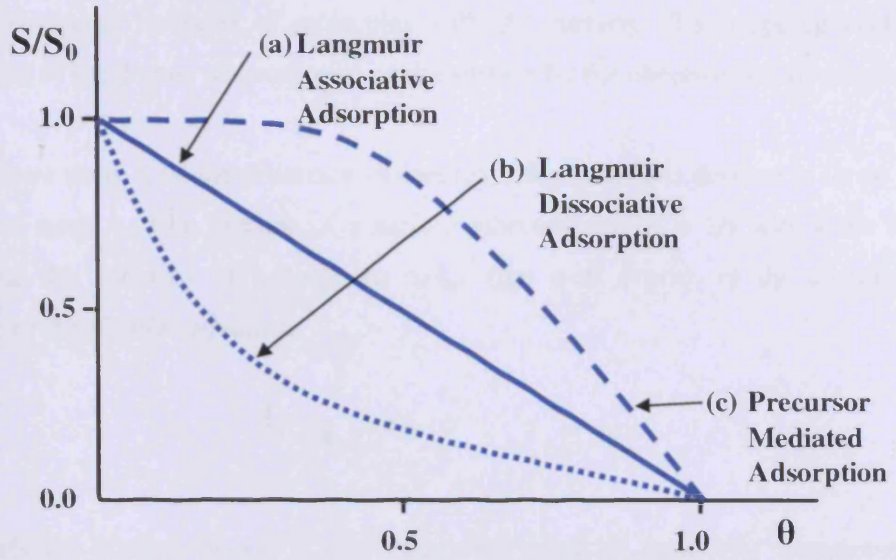

Figure 1.3 – The variation of sticking probability with surface coverage for Langmuir associative / dissociative, or precursor adsorption.[6]

To distinguish this process from sticking, a new definition is required: *trapping* is the process in which a molecule is transferred from the gas phase into a temporarily bound state at the surface; illustrated in by trajectory *d* in Figure 1.2. Polarization effects cause a dipolar interaction with the surface which leads to an attraction and lowering of the potential energy of the system. At closer approach electronic repulsion causes the potential energy to increase again and so the molecule is trapped into this "potential well" (or physisorption well) for some time. To enter the chemisorption well from here a barrier must be overcome. The mechanism that accounts for the possibility of precursor-mediated adsorption is described by

$$A_{gas} \underset{k_d}{\overset{k_t}{\rightleftharpoons}} A_{physisorbed} \xrightarrow{k_c} A_{chemisorbed} \qquad [1.13]$$

With k_t the rate constant for trapping the molecule into the physisorbed state; k_d the rate constant for desorption; and k_c the rate constant for chemisorption from the precursor state. The probability of a molecule being adsorbed into a precursor state is defined in terms of the *trapping coefficient*, α (also called the condensation coefficient):

$$\alpha = \frac{k_t}{Z} \qquad [1.14]$$

With Z the rate of collision of molecules with the surface. The trapping coefficient is independent of the degree of occupation of the surface by the chemisorbed overlayer.

The *residence time*, τ, of the precursor molecule on the surface is defined in terms of a pre-exponential term, τ_0, (the lifetime of a surface vibration and $\tau_0 = 1/\nu$ with ν the frequency factor) and the enthalpy of adsorption, ΔH_{ad}^{0} (the well depth), of the adsorption state according to the *Frenkel equation*:

$$\tau = \tau_0 e^{-\Delta H_{AD}^{0} / RT} \qquad [1.15]$$

If a vibrational lifetime of $\sim 10^{-13}$ s is assumed (typical of molecular vibrations) and the adsorption enthalpy of a gas molecule on the surface is known, the residence time at different temperatures can be calculated with equation 1.15. The longer the molecule resides at the surface, the more probable the process of energy exchange (thermalization) with the surface. Also, in general a deeper potential energy well will result in longer residence time. The relationship between trapping and sticking is expressed as

$$S_0 = \frac{\alpha}{1 + k_d / k_a} \qquad [1.16]$$

The interaction of a molecule with the surface can also be explained in terms of the *thermal accommodation coefficient*, γ, (defined in equation 1.17), which is dependent on the initial gas temperature and therefore the initial kinetic energy of the gas molecule. The thermal accommodation coefficient is defined as the rate at which molecules colliding with a surface can lose their energy and become adsorbed.

$$\gamma = \frac{T_f - T_i}{T_s - T_i} \qquad [1.17]$$

With T_i the initial temperature of the gas phase molecule; T_f the final temperature of the gas phase molecule after collision with the surface and T_s the temperature of the surface. If $T_i = T_f$, no exchange of energy occurred between the molecule and the surface, $\gamma = 0$ and the molecule is elastically scattered. If $T_f = T_s$, thermalization of the gas with the surface has taken place, $\gamma = 1$ and the adsorbate molecule is completely accommodated on the surface.

For scenarios where the initial kinetic energy of the molecule in gas phase ($E_i = \frac{3}{2}kT_i$) is less than the depth of the physisorption well, $E_{precursor}$, the molecule will gradually lose energy and become accommodated. When E_i is similar to $E_{precursor}$, the energy exchange is less efficient and γ decreases; at $E_i = E_{precursor}$ γ passes through a minimum; and as E_i exceeds $E_{precursor}$, γ increases up to the classical limit, whereby at very high gas temperatures ($T \rightarrow \infty$) the energy transfer is again calculated in terms of a simple inelastic collision between two particles - the adsorbate and the surface atom:

$$\gamma(\infty) = \frac{2.4\mu}{(1+\mu)^2}; \quad \mu = \frac{mass\ of\ adsorbate\ atom}{mass\ of\ surface\ atom} \qquad [1.18]$$

Energy transfer at these high temperature conditions is most efficient when the adsorbate and surface atoms are of similar mass ($\mu = 1$).

Figure 1.4 shows a one-dimensional plot of potential energy *vs.* reaction coordinate for the reaction

$$H_{2(g)} \rightarrow H_{2(precursor)} \rightarrow 2H_{ads} \qquad [1.19]$$

Curve *a* displays the interaction of the individual H atoms with the surface and *curve b* the interaction of the H_2 molecule. Adsorption into the precursor state (*curve b*) is a non-activated process, since there is no activation barrier and $\Delta H_{phys,\,H2} = -\Delta H_{des,\,H2}$. However, for the molecule to enter into the chemisorbed atomic state, it must overcome the activation barrier, E^a_{diss}, which is formed at the crossing of the curves. If E^a_{diss} (dissociation via surface adsorption) is compared to the much larger gas phase dissociation energy D(H-H), however, it is clear that dissociation will be facilitated by the surface with respect to the gas phase.

It is important to note that the heat of adsorption for the molecule, $\Delta H^0_{ads,H_2}$ (and for the individual atoms, $\Delta H^0_{ads,H}$) is highly dependent on the surface coverage, so the depth of each potential energy well and the activation energy barrier of adsorption are also coverage dependent.

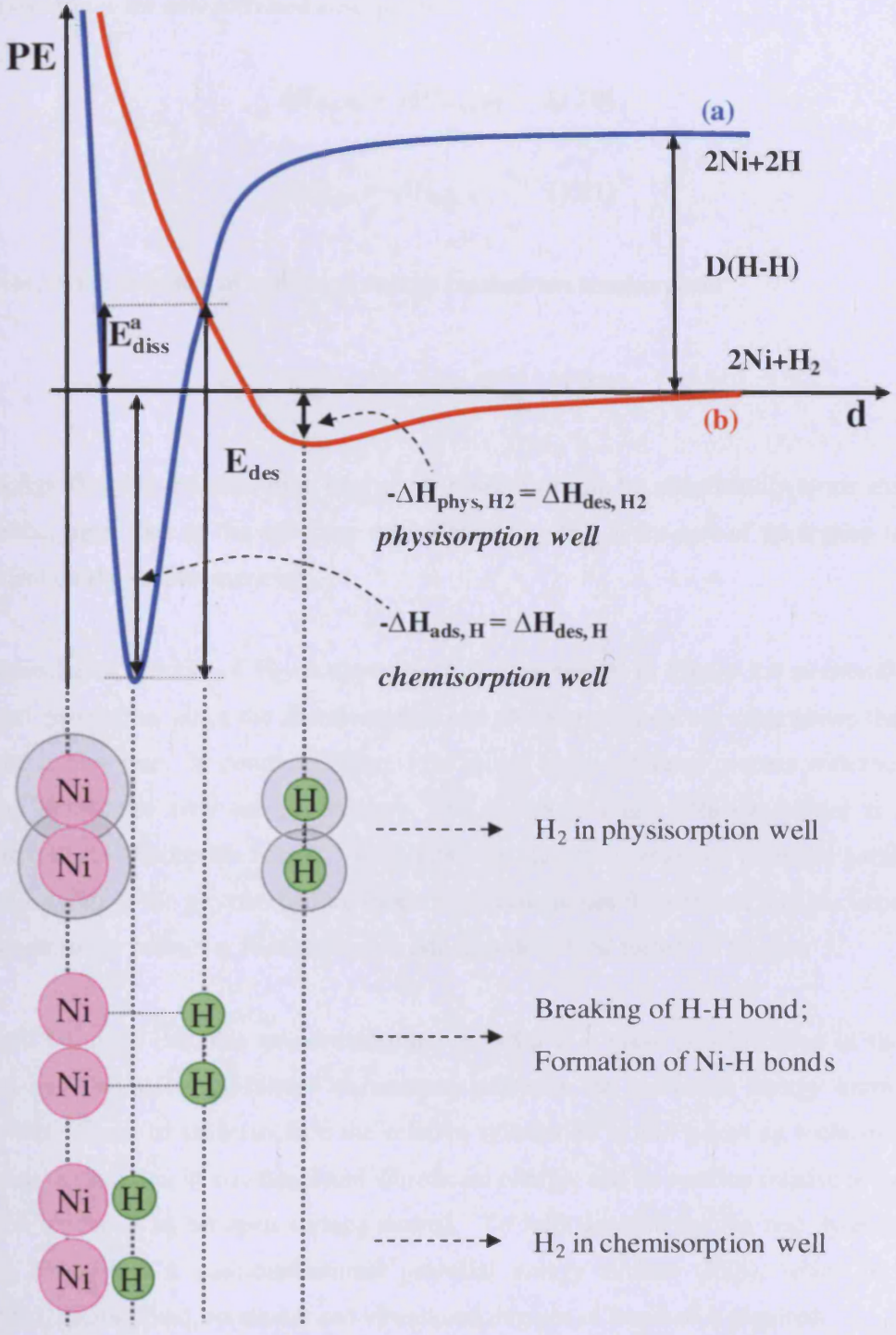

Figure 1.4 – One dimensional potential energy diagram of H_2 adsorption on Ni. Curve *a* represents dissociation and *b* associative adsorption

The graph also shows that desorption is an activated process, since the adsorbates must climb out of the potential energy wells in order to desorb. Therefore, from Figure 1.4, in terms of thermodynamics for non-activated adsorption:

$$\Delta H_{des,H2} = -\Delta H_{phys,\,H2} \qquad [1.20]$$

$$\Delta H_{des,H} = -\Delta H_{ads,\,H} \qquad [1.21]$$

However, in the presence of activation energy barriers to chemisorption

$$E^a_{des} + \Delta H_{ads,\,H} = E^a_{diss} \qquad [1.22]$$

Which signifies that the activation energy for desorption can be significantly larger than for adsorption, again due to the coverage dependence of $\Delta H_{ads,H}$; the rate of desorption is also dependent on the surface coverage.

The dissociation process of H_2 on the surface as represented in Figure 1.4 is classified as activated adsorption, since the chemisorption and physisorption curves cross above the zero potential energy line. In contrast, Figure 1.5*a* shows a non-activated process with the lines crossing below the zero energy. Figure 1.5*b* shows that the diffusion barrier is small compared to the desorption barrier. This relatively shallow corrugated potential parallel to the surface allows the physisorbed molecule to diffuse across the surface; this has important consequences for precursor mediated adsorption, as discussed further in Chapter 5.

It should be noted that this one-dimensional diagram is a gross simplification of the real process and that many additional parameters influence the activation energy barrier for adsorption. Some of these include the relative orientation of the incoming molecule with respect to the surface; its rotational and vibrational energy; and its position relative to surface sites (on top of or in between surface atoms). To fully account for the real dynamics of surface adsorption, a multidimensional potential energy surface (PES), which includes positional, translational, rotational and vibrational degrees of freedom is required.

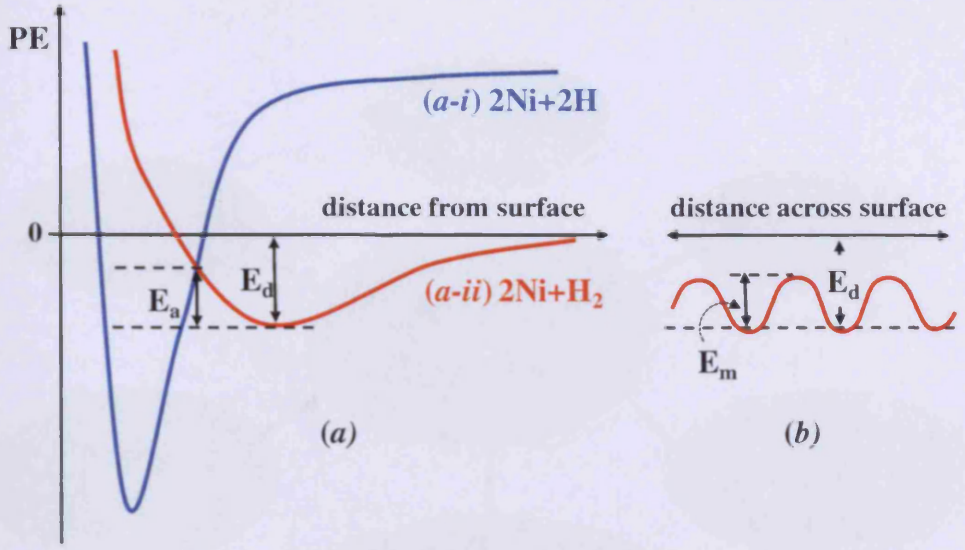

Figure 1.5 – Crossed potential energy curves for *a-i*) chemisorption and *a-ii*) physisorption with dissociation as a function of *a*) distance from the surface and *b*) across the surface.

1.4. Surface Science

1.4.1. Introduction

The interfaces between phases have been of intense interest to scientists for hundreds of years, but the term surface science only came into existence in the 1960's. Since then the field has expanded explosively; driven by the development of ultrahigh vacuum environments and the techniques for preparing macroscopic single crystal surfaces. Surface science finds application in many everyday processes, some of which are shown in Figure 1.6. According to Friend,[11] arguably the most important and fruitful application of surface science is heterogeneous catalysis: "Perhaps one of the greatest triumphs of modern surface science is that rates of catalytic reactions on supported, transition metal particles can often be reproduced on very well-defined single crystal surfaces. The ability to reliably interrogate catalytic chemistry on single crystals allows for methodical exploration of the influence of atomic structure on catalytic activity."

Another important area of study is corrosion of materials, because of its impact on systems (like cars, pipelines, central heating) and human health (allergies, toxic metals, etc.). Semiconductor fabrication has also benefitted greatly from surface science studies. These materials find widespread application in the computer, automotive, medical and security industry to name but a few.

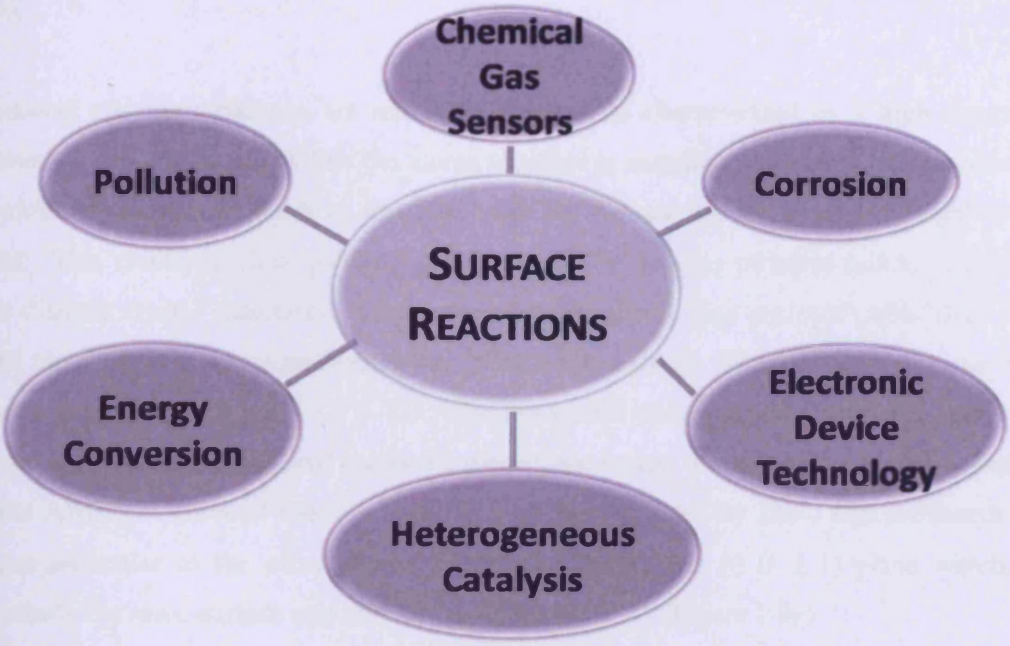

Figure 1.6 – Applications and research areas related to surface science.

1.4.2. Single Crystals

The term *single crystal* refers to a solid in which the crystal lattice of the entire sample is continuous and unbroken to the edges with no grain boundaries. Grain boundaries can have significant effects on the physical and electrical properties of a material and eliminating them allows scientists to study the systems in their simplest forms. The opposite of a single crystal sample is an amorphous structure in which very limited short range order exist. In between the two extremes are polycrystalline phases, which are made up of a number of smaller single crystals known as crystallites.[12]

Metal single crystals can be prepared using a number of methods: In the seeding method a rod of the single crystal is drawn slowly from a metal melt.[8] Vapour deposition is usually employed to manufacture semi-conductors single crystals. Once prepared, the crystal is cut via spark erosion or grinding. X-ray back-scattering is employed to align diffracted x-ray beams associated with the desired plane in order to maintain the correct cut throughout the preparation procedure.

Single crystals can be cut along specific orientations to reveal a particular surface with a high degree of order and simplicity. These surfaces offer a limited number of sites on which molecules can bind. This relative simplicity allows us to evaluate how the molecule adsorbs

on and interacts with the surface, and it is this simplicity on which this field of science is based.

In general metallic structures are relatively simple and characterized by a high degree of symmetry. The forces which link the atoms together in metallic crystals are non-directional, meaning that each atom tends to surround itself by the maximum amount of neighbouring atoms. This results in close packing, similar to that of spheres of equal radius, and yields three distinct crystal structures: body centered cubic (bcc); face centered cubic (fcc) (also called close packed cubic) and hexagonal close packed (hcp). The unit cells of these three systems are shown in Figure 1.7 – 1.9. The hexagonal close packed structure is non-cubic and the close packed hexagonal layers are placed one on top of the other in a repeat stacking pattern ABAB... Three of the four axes (*w, x, y*) are separated by 120°, with the fourth axis (*z*) perpendicular to the other three. Figure 1.7 shows the (0 0 0 1) plane which has essentially the same surface structure as the dense fcc(111) (Figure 1.9*c*).

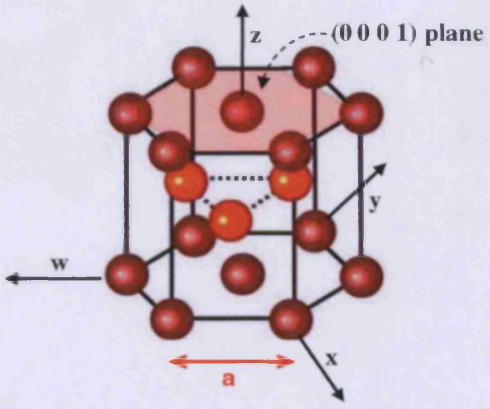

Figure 1.7 – Unit cell of a hcp crystal showing the (0 0 0 1) plane

1.4.3. Miller Indices

The different planes of a surface are assigned according to the *Miller index*. The index consists of three integers (*x, y, z*) for materials adopting bulk cubic structures and four integers (*w, x, y, z*) for hexagonal close packed structures. Indices consisting of only zeros and ones are referred to as low index planes. The low Miller index planes of bcc and fcc crystals are shown in Figure 1.8 & 1.9 respectively. Mutually perpendicular axes *x*, *y* and *z* define a simple cubic lattice with lattice constant '*a*'; the crystallographic plane to be labelled is indicated by the shaded area.

(111) plane of a bcc crystal

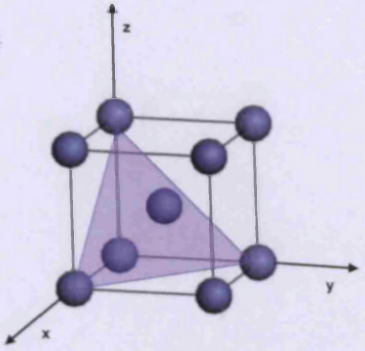

(a-i)

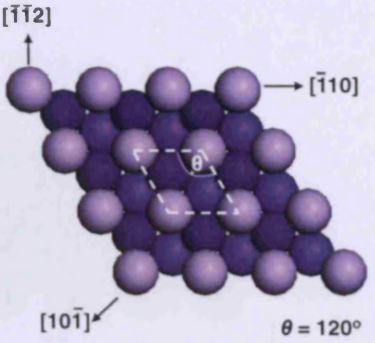

(a-ii)

(100) plane of a bcc crystal

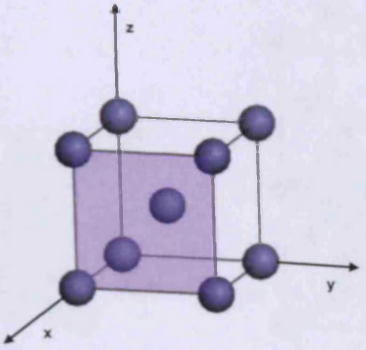

(b-i)

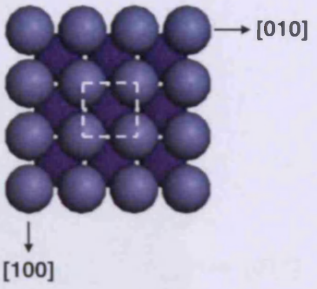

(b-ii)

(110) plane of a bcc crystal

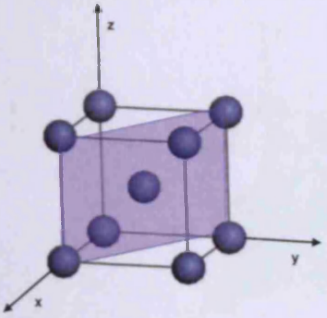

(c-i)

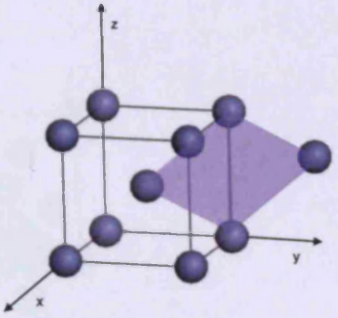

(c-ii)

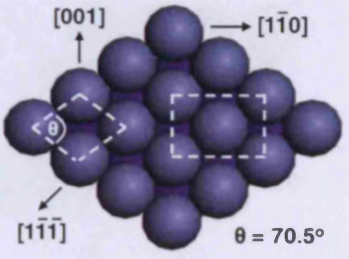

(c-iii)

Figure 1.8 – Low Miller index surfaces of bcc crystals; arranged from least to most dense. *a)* The (111) plane; *b)* the (100) plane, primitive unit cell shown in *b-ii*; and *(c)* the (110) plane; primitive unit cell is shown in *c-ii*.

(110) plane of a fcc crystal

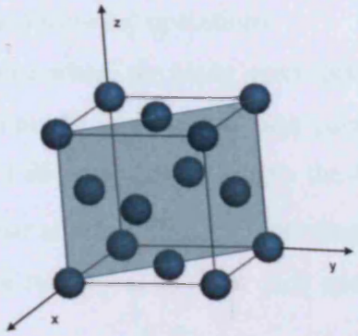

(a-i)

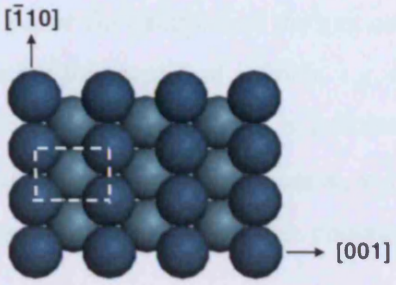

(a-ii)

(100) plane of a fcc crystal

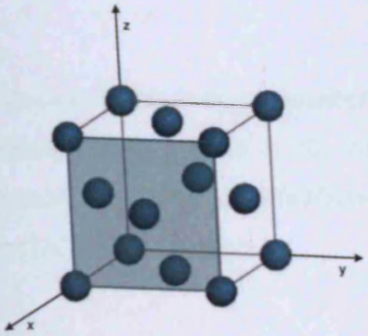

(b-i)

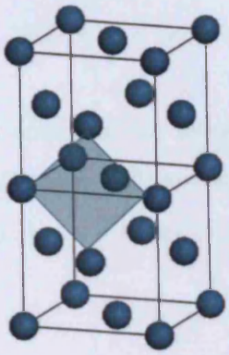

(b-ii)

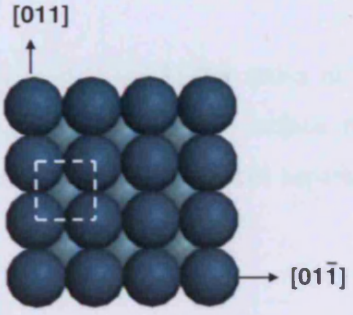

(b-iii)

(111) plane of a fcc crystal

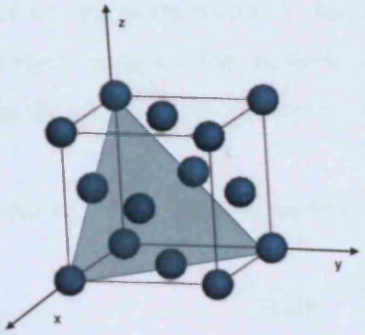

(c-i)

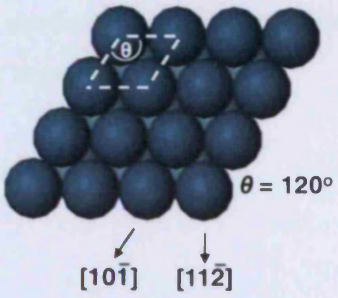

(c-ii)

Figure 1.9 – Low Miller index surfaces of fcc crystals arranged from least to most dense. *a)* The (110) plane; *b)* the (100) plane, primitive unit cell shown in *b-ii;* and *c)* the (111) plane.

With the help of Figure 1.8 & 1.9 the Miller index of each surface can be determined by performing the following operations:

(i) Determine where the plane intercepts the x-, y- and z-axes (in multiples of the unit cell dimension *a*). If the plane runs parallel to the axis the intercept is at infinity, *e.g.* in Figure 1.8*b* the plane intercepts the cube at 1, ∞, ∞. A negative intercept is indicated with a bar above the index (neglecting the minus sign), so that ∞, ∞, -1 becomes $\infty, \infty, \bar{1}$.

(ii) Take the reciprocal value of each intercept; if fractions result, multiply by the common denominator, *e.g.* $\frac{1}{3}, \frac{2}{3}, 1$ becomes 1, 2, 3.

High Miller index planes can be described in terms of the three low index planes by using microfacet notation

$$n(x, y, z) \times (u, v, w)$$

where n is the average number of atoms in the terrace, (x, y, z) is the Miller index of the terrace and (u, v, w) is the Miller index of the step; *e.g.* a fcc(11, 1, 1) surface may alternatively be labelled 6(100)×(111), *i.e.* a series of six atom wide (100) terraces separated by (100) × (111) steps.

1.4.4. Real Single Crystals

When a surface is cut, bonds must be broken and the surface atoms no longer have their full complement of coordination partners. Because of this, the surface atoms find themselves in higher energy states compared to the bulk atoms. Table 1.1 shows the coordination numbers of the atoms in the bulk and top surface layers of bcc and fcc crystals.

Table 1.1 – Coordination numbers of surface atoms in fcc and bcc planes.

	fcc	bbc
Bulk	12	8
(111)	9	4
(100)	8	5
(110)	7	6

To compensate for the loss in coordination, and lower the energy of the surface atoms, the surface undergoes *relaxation*. The more severe the coordination loss, *i.e.* the more open and more energetic the surface, the more pronounced the surface relaxation. The surface energy for bcc metals decreases in the order (111) > (100) > (110); and for fcc metals (110) > (100) > (111). *Surface relaxation* is the oscillatory change in the interplanar spacing Δd, as graphically shown in Figure 1.10.

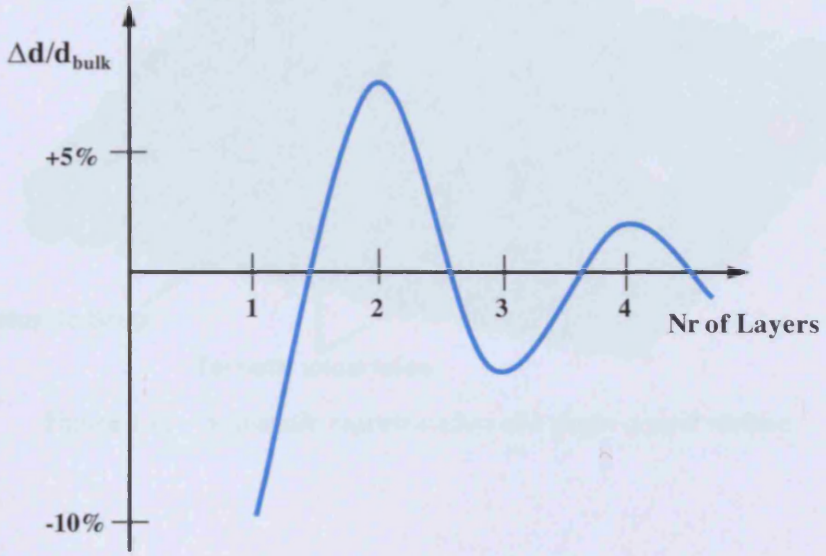

Figure 1.10 – Oscillatory change in interlayer spacing of a single crystal due to surface relaxation.[6]

It can be explained as follows. To increase coordination (and lower the energy) the first layer contracts towards the second layer, causing over-coordination in the second layer. To counter the increased coordination in the second layer the third layer expands to move away from the second layer. This pattern continues deeper into the bulk of the crystal until the oscillation is completely damped. This region for which $|\Delta d| > 0$ is called the *selvedge* to distinguish it from the bulk and will vary in thickness according to the density of the surface under consideration. If the surface energy is sufficiently large, not only surface relaxation, but also surface reconstruction will occur.

Apart from surface relaxation and reconstruction, atomic scale defects also lead to deviations in the perfect atomic arrangements. Ideally, single crystals consist only of flat planes (terraces), but in addition real systems have steps (also called ledges) that may have kinks (a step on a step) and point defects such as atomic vacancies or surface adatoms. The defects

lead to a change in the local arrangement and electronic properties of the surface atoms around it, *i.e.* the formation of different surface sites. Figure 1.11 is the so called terrace-step-kink model which illustrates the different surface sites.

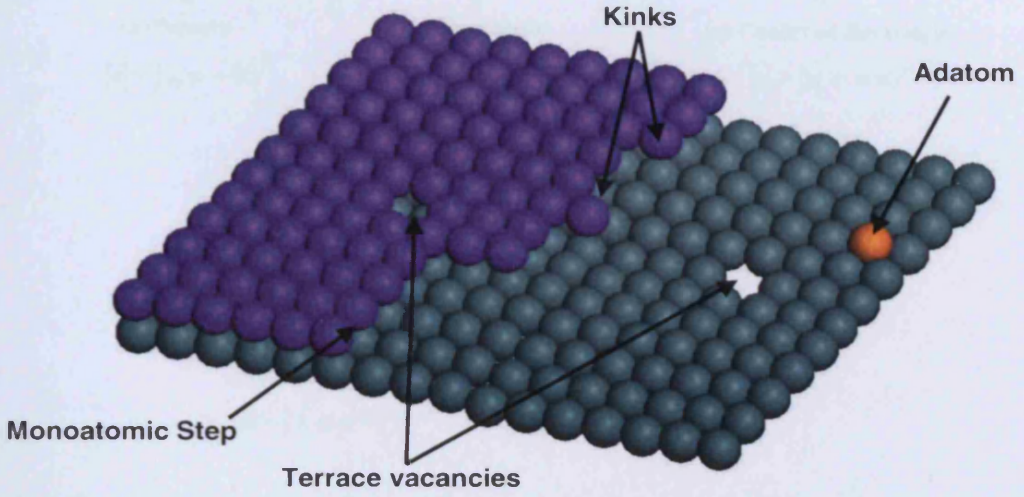

Figure 1.11 – Schematic representation of a single crystal surface.

1.5. Naming Overlayer Structures

The unit cells of all three dimensional structures (crystals) can be characterized by one of 14 Bravais lattices. The unit cell of a crystal surface, where periodicy is lost in one dimension, can only consist of one of five Bravais lattices (shown in Figure 1.12). These are hexagonal (with a sixfold rotational axis); square (with a fourfold rotational axis), centered or primitive rectangle (with mirror symmetry) and oblique (which lacks all of these symmetries). Combining these five bravais nets with the ten different possible point groups leads to 17 two-dimensional space groups. Thus there are only 17 symmetrically different types of surface structures (space groups) possible, although there are an infinite number of possible surface structures. No centered square Bravais net exists as a symmetrically distinct mesh from the primitive square, but the notation is still widely used.

The basis vectors $\boldsymbol{a}$ and $\boldsymbol{b}$ shown in Figure 1.12 describe the unit cell in real space. These vectors define the smallest parallelogram from which the structure of the surface can be constructed by simple translations. The reciprocal space representation of the real space lattice is described by the basis vectors $\boldsymbol{a}^*$ and $\boldsymbol{b}^*$. Overlayer structures can be defined in Wood's notation or matrix notation as discussed below.

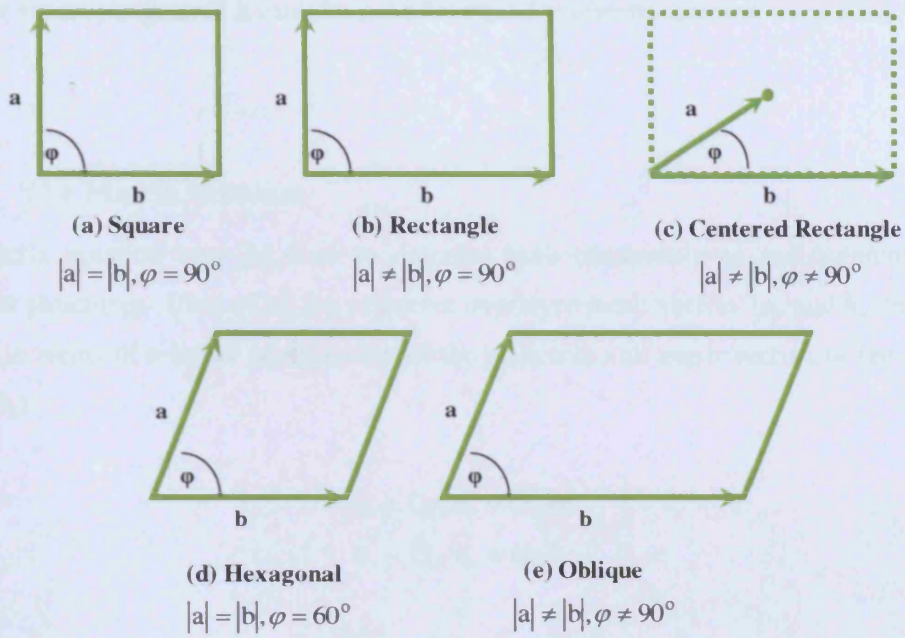

Figure 1.12 – The five Bravais lattices in two dimensions arranged in order of decreasing symmetry. *a*) Square, *b*) Rectangle, *c*) Centered Rectangle, *d*) Hexagonal and *e*) Oblique

1.5.1. Wood's Notation

Wood's notation defines the ratio of the lengths of the surface and substrate meshes and also the angle through which one mesh must be rotated to align the two pairs of primitive translation vectors; or more fully:

$$M(hkl)\left(\frac{|\mathbf{a}_o|}{|\mathbf{a}_s|} \times \frac{|\mathbf{b}_o|}{|\mathbf{b}_s|}\right) - \mathrm{R}\theta° - \mathrm{A}$$

Where M is the chemical symbol of the substrate; $h\ k\ l$ is the Miller index of the surface plane; $|\boldsymbol{a}_s|$ and $|\boldsymbol{b}_s|$ is the magnitude of the substrate net vectors; $|\boldsymbol{a}_o|$ and $|\boldsymbol{b}_o|$ is the magnitude of the overlayer net vectors; θ is the angle between the substrate and overlayer meshes (omitted if zero); and A is the chemical symbol of the surface species. A 0.5 ML sulphur phase on Fe(100) could be described as Fe(100)($\sqrt{2} \times \sqrt{2}$)R45° – S – (0.5ML). Two additional examples are shown in Figure 1.13. Wood notation only suited if the angles of the surface and substrate unit meshes matches (called commensurate structures), *i.e.* if the

overlayer and substrate meshes have the same Bravais net or where one is rectangular and the other square; in general it can't be used for mixed symmetry meshes.

1.5.2. The Matrix Notation

This matrix notation may be used to describe both commensurate and incommensurate overlayer structures. First of all the primitive overlayer mesh vectors (a_o and b_o) need to be defined in terms of a linear combination of the primitive unit mesh vectors of the substrate (a_s and b_s):

$$\mathbf{a}_o = G_{11}\,\mathbf{a}_s + G_{12}\mathbf{b}_s$$
$$\mathbf{b}_o = G_{21}\,\mathbf{a}_s + G_{22}\mathbf{b}_s$$

Where G_{ij} are the four coefficients which form the matrix G:

$$G = \begin{pmatrix} G_{11} & G_{12} \\ G_{21} & G_{22} \end{pmatrix}$$

Signifying that the substrate and overlayer are related by

$$\begin{pmatrix} \mathbf{a}_o \\ \mathbf{b}_o \end{pmatrix} = G \begin{pmatrix} \mathbf{a}_s \\ \mathbf{b}_s \end{pmatrix}$$

The area of the substrate unit mesh is given by $|\mathbf{a} \times \mathbf{b}|$, and *det G* (the determinant of G, calculated by $G_{11}\,G_{22} - G_{12}\,G_{21}$) is the ratio of the areas of the two meshes, which provides a convenient method for classifying the surface structure:

(i) If *det G* is integral and all the matrix components are integral, the two meshes are simply related with the adsorbate mesh having the same translational symmetry as the whole surface.

(ii) If *det G* is a rational fraction (or *det G* is integral and some matrix components are rational), the two meshes are rationally related, frequently called a coincidence lattice (net). The structure is still commensurate, but the true surface mesh is larger than either the substrate or adsorbate mesh. The size of the mesh is dictated by the distances over which the two meshes come into coincidence at regular intervals.

(iii) If *det G* is irrational the two meshes are incommensurate and no true surface mesh exists. This situation is found in cases where the adsorbate-adsorbate bonding is much stronger than the adsorbate-substrate bonding or if the adsorbed species are too large to coincide with the substrate structure.

Figure 1.13 shows examples of overlayer structures with their Wood and matrix notations. The overlayer structure in Figure 1.13*a* can also be referred to as a centered(2×2) structure (abbreviated as c(2×2)). To distinguish centred structures from primitive structures, the prefix *p* is sometimes added to the latter, *ex.* *p*(2×2).

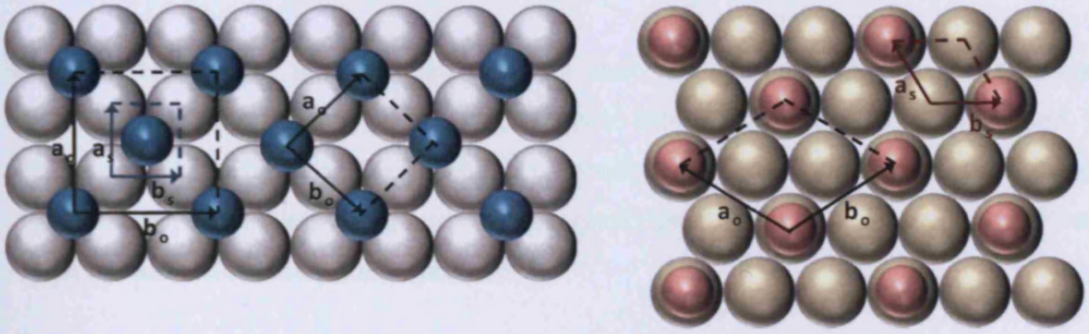

$c(2\times 2)$ or $(\sqrt{2}\times\sqrt{2})R45^{\circ}$ $\begin{bmatrix} 1 & 1 \\ -1 & 1 \end{bmatrix}$ $(\sqrt{3}\times\sqrt{3})R30^{\circ}$ $\begin{bmatrix} 2 & 1 \\ -1 & 1 \end{bmatrix}$

(a) **(b)**

Figure 1.13 – Overlayer structures named according to Wood's and the matrix notations. *a)* Centered and primitive unit cell of the c(2×2) overlayer on a surface with square symmetry. *b)* Primitive unit cell of the $(\sqrt{3}\times\sqrt{3})R30^{\circ}$ overlayer on a surface with hexagonal symmetry.

1.6. Fischer-Tropsch Catalysis

1.6.1. Introduction

The Fischer-Tropsch (FT) reaction can be summarized as the conversion of synthesis gas, (carbon monoxide and hydrogen gas) to hydrocarbons, which can be in the form of gases, liquids and solids. The general reaction scheme is shown in equation 1.23.[13]

$$nCO + (2n+1)H_2 \rightarrow C_nH_{2n+2} + nH_2O \qquad [1.23]$$

The FT Gas-to-Liquids (GTL) process has recently received renewed attention, not least because it can be used to produce valuable hydrocarbons from "stranded" natural gas, *i.e.* gas from sources that are far from major cities and impractical to exploit with conventional gas pipelines and LNG technology (liquid hydrocarbons are much easier to transport than natural gas).[14] Examples of operating GTL plants are the *Sasol* plant in Doha, Qatar and the *Shell* plant in Bintulu, Malaysia. An alternative FT technology is the CTL (Coal-to-Liquids) process which is particularly useful for countries with rich coal resources (and usually a lack of oil reserves). This application provides an alternative to crude oil which is running out and becoming more expensive. CTL provides further advantages of producing diesel with very low sulphur content* and being able to use low quality feedstock such as waste coal from mining leftovers or waste biomass from paper and pulp manufacturing processes.[15]

Sasol converts syngas to more than 200 fuel and chemical products including gasoline, diesel, candle waxes, hard waxes, hydrocarbon lubricants, methane, phenol (used in pharmaceuticals, disinfectants and plastics), cresol (used as a disinfectant), tar and pitch (used in dyes and cosmetics), ammonia, detergents etc., which are exported from South Africa to more than 70 countries worldwide.

As early as 1954, Frohning cited in a review that approximately 4000 publications and a similar amount of patents on FTS was already available in literature. A comprehensive bibliography of FTS literature – journals, conference articles, books, government reports and patents can be found in the FT Archive at www.fischer-tropsch.org.

1.6.2. History

CO hydrogenation that produces methane over Ni, Fe and Co catalysts was discovered by Sabatier and Senderens in 1902.[14] In 1923 Fischer and Tropsch reported the *Synthol process* – the production of liquid hydrocarbons rich in oxygenates, by using an alkalized Fe catalyst. Subsequently, a precipitated Co catalyst (100 Co : 5 ThO_2 : 8 MgO : 200 kieselguhr) was developed as the "standard" catalyst at atmospheric pressure. The medium pressure process (10 – 15 bar) was developed in 1936 by Fischer and Pichler. Collectively the process of converting CO and H_2 to liquid hydrocarbons over a transition metal catalyst has become

* Sulphur present in fuel leads to an increase in particulate matter and sulphur dioxide in the atmosphere, which have negative consequences for public health and the environment.

known as the *Fischer-Tropsch Synthesis Reaction*. The first FT plants began operation in Germany in 1938 to circumvent their problem of being cut off from crude oil supplies; but the plants closed down after the 2nd World War. In 1955 *Sasol* started *Sasol I* in Sasolburg, South Africa; followed by *Sasol II* and *Sasol III* in Sucunda, South Africa in 1980 and 1982 respectively.[13] The *Mossgas* plant (now called *PetroSA*) started up in Mossel Bay, South Africa in 1992 and converts natural gas over an Fe catalyst. *Shell* commissioned a plant in Bintulu, Malaysia in 1993 operating on the *Shell Middle Distillate Synthesis* process (which is essentially enhanced FTS).

1.6.3. Chemistry and Product Distribution

The rich chemistry of the FT reaction has attracted interest for many years, especially because longer chain hydrocarbons are the predominant products despite the fact that thermodynamics dictates mainly methane production. Irrespective of the operating conditions, the FT product slate takes on some unique characteristics: It always contains olefins, paraffins and oxygenates (alcohols, aldehydes, acids and ketones); products in all categories are predominantly linear; the paraffin-to-olefin ratio is lower than thermodynamically predicted; olefins are predominantly terminal (α-olefins) and theoretically only methane can be produced with 100% selectivity.[16]

The detailed product distribution of the reaction (and ideal chain growth probability, α) is influenced by the gas composition (feed and product component partial pressures), operating conditions and catalyst formulations. Further complications arise from chemical / physical changes that catalysts undergo during the reaction. Since FTS is a polymerization reaction, it consists of the following basic steps:[17]

(i) Reactant adsorption on the catalyst surface
(ii) Chain initiation
(iii) Chain growth
(iv) Chain termination
(v) Product desorption from the catalytic surface

FTS is kinetically controlled by the stepwise chain growth of CH_2 groups on the catalytic surface. Product selectivities are determined by the balance between chain propagation *vs.* chain termination. The polymerization rates, and therefore the kinetics, are independent of

the products formed. The probabilities of chain growth and chain termination are independent of chain length; therefore selectivities of various hydrocarbons can be predicted based on simple statistical distributions calculated from chain growth probability and carbon number. A widely used chain growth kinetics model is the *Anderson-Schulz-Flory* (ASF) model:[18-20]

$$W_n = n(1-\alpha)^2\alpha^{n-1} \qquad [1.24]$$

W_n is the weight percentage of a product containing n carbon atoms and α is the chain growth probability. Equation 1.24 is graphically displayed in Figure 1.14 for several products of interest.

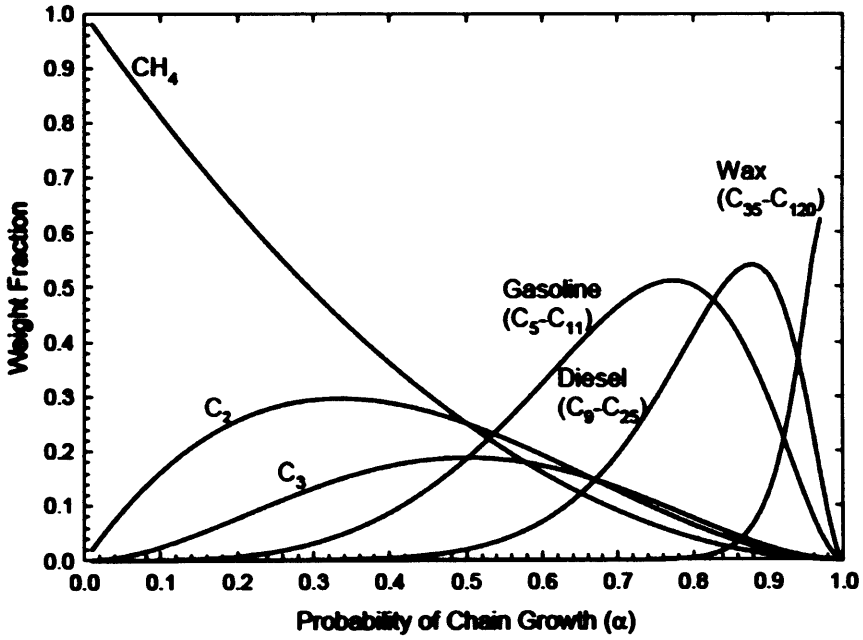

Figure 1.14 – The Anderson-Schulz-Flory plot showing the typical product distribution of the Fischer-Tropsch synthesis reaction.[18-20]

The most important reactions taking place in the reactor are summarised below.

Alkane formation, which is exothermic by 165 kJ/mol of CO:

$$nCO + (2n+1)H_2 \rightarrow C_nH_{2n+2} + nH_2O \qquad [1.25]$$

Alkene and alcohol formation:

$$nCO + 2n\,H_2 \rightarrow C_nH_{2n} + nH_2O \qquad [1.26]$$

$$nCO + 2nH_2 \rightarrow C_nH_{2n+1}OH + n\text{-}1\ H_2O \qquad [1.27]$$

Especially for Fe catalysts, other competing reactions also occur:
The water gas shift reaction (WGS)

$$CO + H_2O \rightarrow H_2 + CO_2 \qquad [1.28]$$

and the Boudouard reaction

$$2\ CO \rightarrow C_{ads} + CO_2 \qquad [1.29]$$

1.6.4. Fischer-Tropsch Catalysts[13]

Group VIII transition metals are generally regarded as good CO hydrogenation catalysts, but due to practical reasons only two metals are currently used commercially: iron and cobalt.[17] Ruthenium is highly active and selective towards heavier products at low temperatures, but the metal is very pricy. Nickel is very active, but produces predominantly methane. Most metals retain their metallic state in the process, with the exception of Fe, which undergo phase transformations to oxides and carbides. Control of these phase transformations can be important in maintaining catalytic activity and preventing breakdown of the catalyst particles.

Commercial FT catalysts can be divided into three broad categories:[13] fused iron catalysts, precipitated iron catalysts and supported cobalt catalysts. Iron catalysts have been developed for use at low (473 – 513 K) or high temperature (573 – 623 K). Co is used only at low temperatures, because increased temperature leads to excessive methane production. The choice of metal and the particular catalyst depends on the available feedstock and desired end product. Each of these catalysts has scope for further improvement, often associated with changes in the catalyst that take place under synthesis conditions. An understanding of these changes is important in the enhancement of the catalytic performance. Other improvements relate to increasing catalyst activity, selectivity towards desired products and inhibiting the formation of undesirable products, especially methane.

The Fused Fe Catalyst

The fused Fe catalyst is used in the production of liquid fuels, since products are comparatively olefinic and short chained (typically C5 – C12). Catalytic activity and selectivity are enhanced by the addition of alkali promoters and in addition structural promoters are added to increase the surface area of the final catalyst. These promoters are added into a molten bath of magnetite which is then cooled to form a solid, and crushed into a fine powder. In the reactor the magnetite powder is first reduced in hydrogen to convert it to the metallic state and then exposed to syngas for FT synthesis.

In the reactor the core of the larger particles tends to revert to magnetite while the remainder of the catalyst consists of different iron carbides. Free carbon tends to accumulate at promoter rich grain boundaries and causes the catalyst particles to swell and break over time. To re-establish the optimum average particle size and promoter concentration, periodic partial unloading and reloading of fresh catalyst is done online.

The Precipitated Fe Catalyst

Precipitated Fe catalysts are suitable for use at low temperatures in slurry phase reactors. These reactors contain liquid hydrocarbons which effectively reduces the methane selectivity to fractions as low as 3% of the carbon in the overall product yield. This requires operation at lower temperatures than those used for the fused catalyst; and higher catalytic surface area compensates for the resulting decrease in reaction rates. The higher surface areas of these catalysts inevitably lead to weaker particles, therefore the addition of structural promoters and procedures to improve catalyst strength are important issues during catalyst preparation. In contrast to the fused catalyst where iron oxide is used as a raw material, more costly iron metal is used for the precipitated catalyst. The metal is dissolved into an aqueous acidic solution (typically nitric acid) and the desired quantities of promoters are added. Again alkali promotion is important and in addition Cu is added to serve as a reduction enhancer for the subsequent reduction/conditioning step. A typical Fe catalyst is made up according to the following ratio: 100 Fe / 13 Al_2O_3 / 10 Cu / 5 K.

The catalyst is precipitated by adding a basic solution (sodium carbonate or ammonia) after which the precipitate is filtered, washed, dried and formed into the shape required for use in the FT reactor. Extrusion techniques are used to prepare pellets for fixed bed reactors and spray driers can be used to produce catalyst powder.

The Supported Co Catalyst

Cobalt catalysts consist of cobalt (and promoter) particles deposited on a pre-shaped oxide supports. Typical supports comprise of one or more materials such as silica, alumina, titanium or zinc oxide. For slurry bed reactors, supports are typically prepared with a spray drier to obtain the desired particle sizes. A subsequent classification step refines the size distribution. Preparations for fixed bed reactors are typically done with extrusion techniques. Heat treatment improves the mechanical strength of the support. Pore size control is important to regulate the amount of Co that is placed on the support and the catalyst performance. Cobalt is impregnated onto the support together with promoter metals such as lanthanum, platinum, palladium, rhenium and ruthenium which enhance the reduction step that provides cobalt metal on the catalyst surface. Unlike for the Fe catalysts, Co catalysts in slurry reactors can be regenerated by exposing the spent catalyst (oxidized under synthesis conditions or fouled by heavy hydrocarbons) to H_2 at elevated temperatures. Another contrast to Fe catalysts is that the product slate is predominantly paraffinic. Compared to the LTFT Fe catalyst the CH_4 selectivity is higher; nevertheless the best Co catalysts still have a carbon selectivity to CH_4 of ± 5%. Oxygenate selectivity in the aqueous phase is generally lower than for Fe catalysts. An important benefit of Co catalysts for natural gas conversion is its inactivity towards the water gas shift (WGS) reaction, which means that carbon dioxide formation is negligible.

1.6.5. Proposed Mechanisms of Fischer-Tropsch Catalysis

The vastly complex product spectrum of the FT reaction alludes to the complex chemistry occurring on the catalytic surface. The original *carbide mechanism* entailed the formation of the metal carbide followed by its hydrogenation to produce various products,[21] however later it was thought that this mechanism was inconsistent with thermodynamic data for the formation of hydrocarbons by hydrogenation of the carbide at temperatures used for the synthesis reaction.[22]

In the late 1980's, however, surface science studies of Maitlis showed that CO can adsorb on Rh to produce a carbon covered surface with little oxygen.[23] It was concluded that CO chemisorbs and dissociates to C_{ads} and O_{ads} followed by the fast hydrogenation of the adsorbed O to produce water, while hydrogenation of C to form CH_2 is much slower. The carbide theory was again considered more seriously, but with the requirement that carbide formation is limited to the surface or near surface region. More elaborate versions of this

mechanism have been proposed and are shown in Scheme 1.1 and 1.2 (taken from ref. 24, a review by Davis). Dry considers the steps involving the hydrogenation of surface C to be rate-limiting and the other reactions to be at equilibrium.

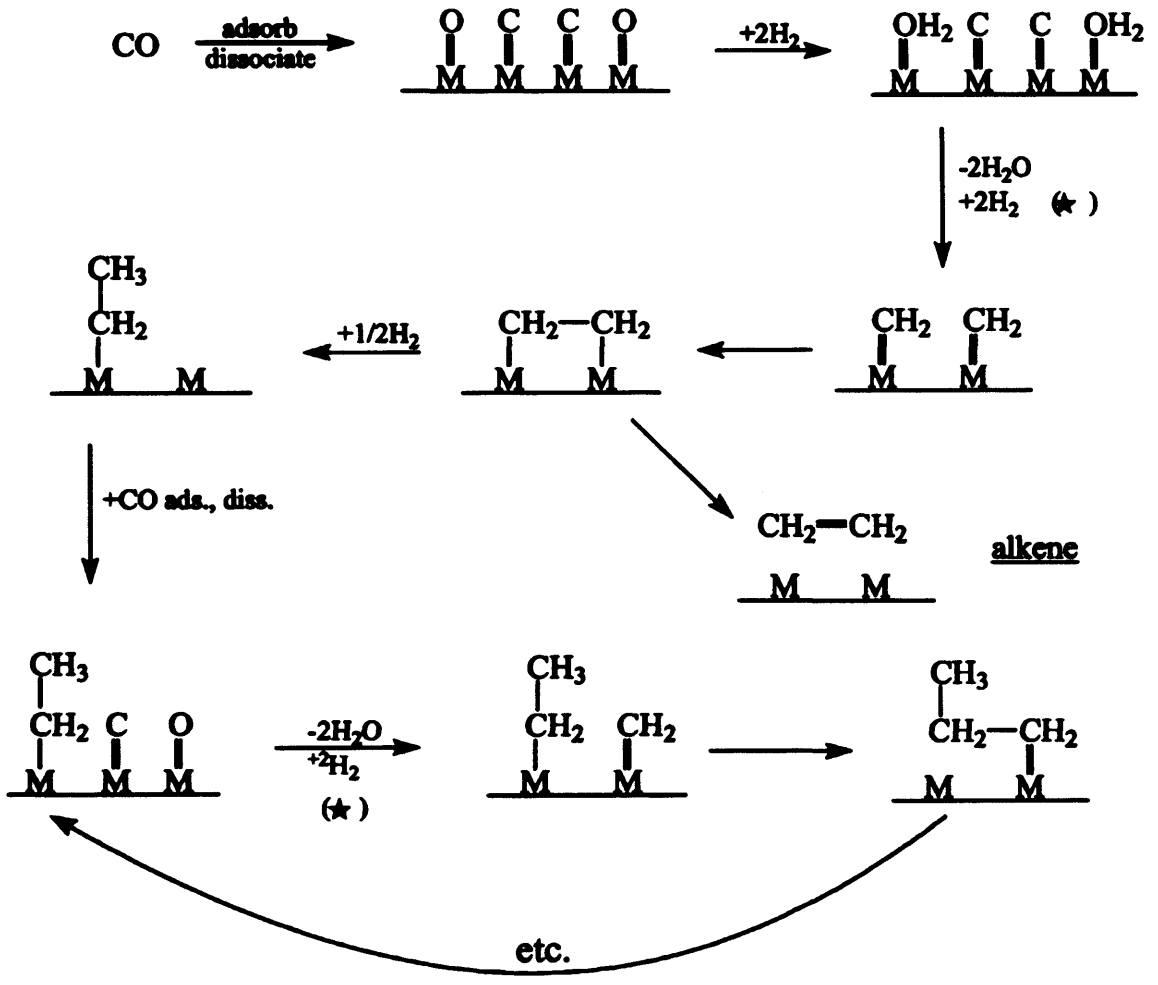

Scheme 1.1 – The Carbide Mechanism as modified by Dry; scheme taken from ref. 24.

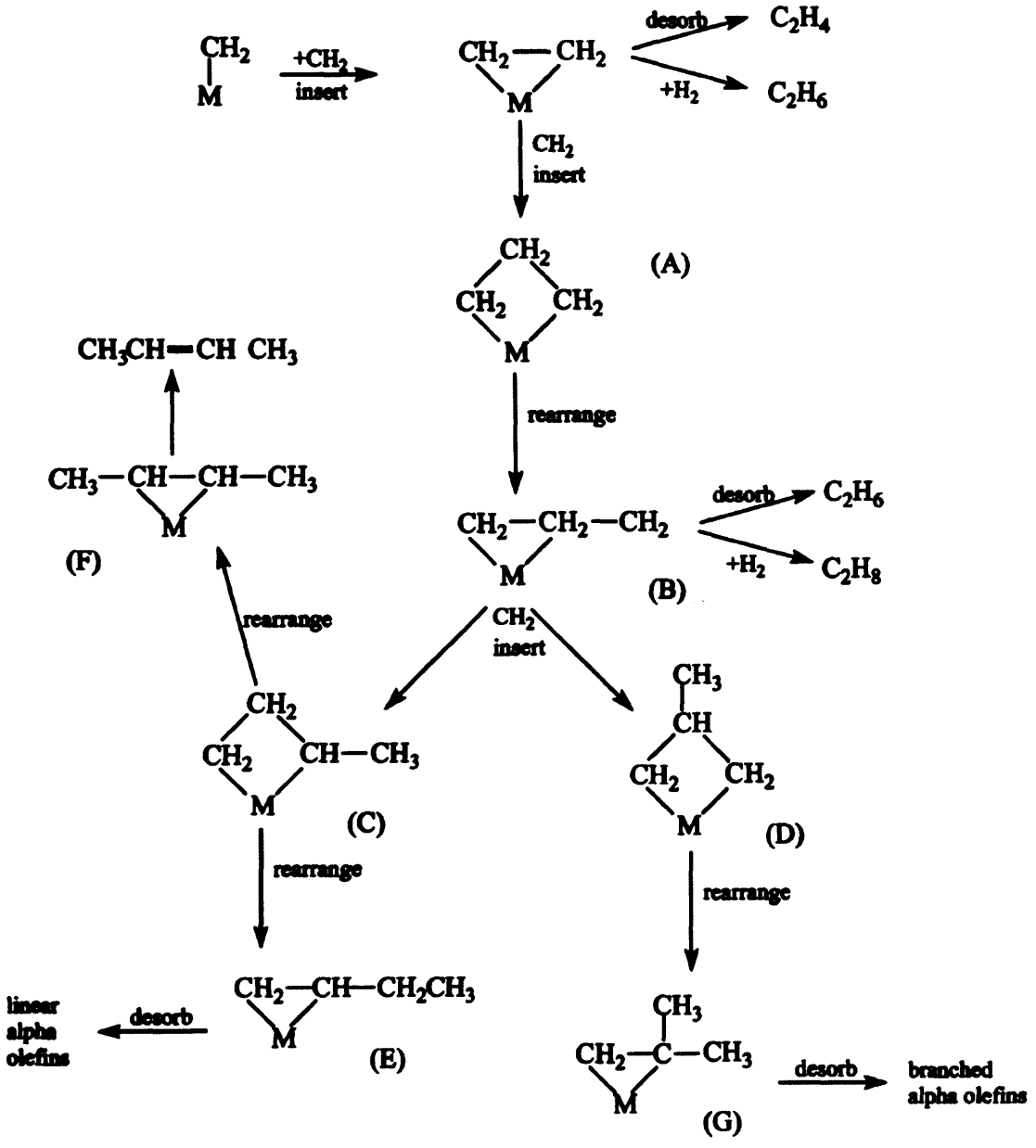

Scheme 1.2 – A later version of the Carbide (Carbene) mechanism.[24]

In the 1950's the *enol (oxygenate) mechanism* gained widespread acceptance.[25] This mechanism involves the chemisorption of CO which then reacts with adsorbed hydrogen to form M=CHOH species on the surface (see Scheme 1.3). The structure grows by condensation and water elimination using adjacent groups.

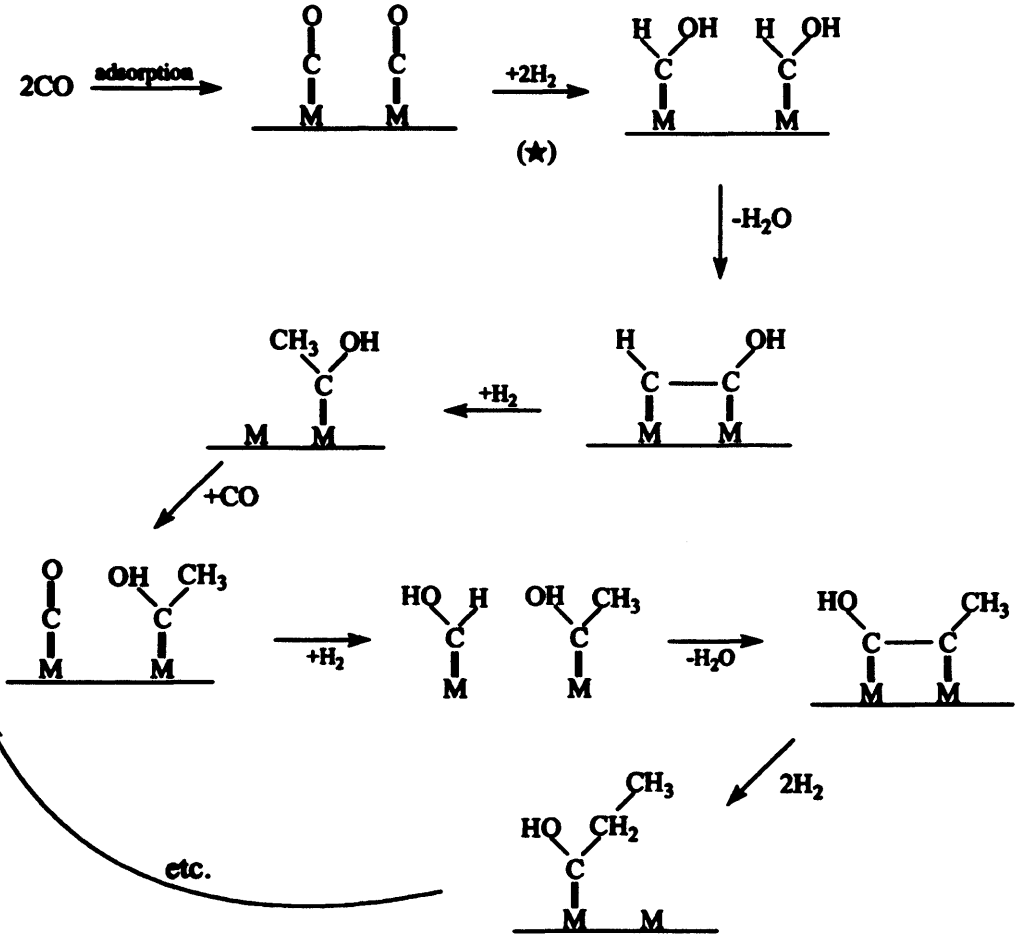

Scheme 1.3 – The enol mechanism for Fischer-Tropsch Synthesis.[24]

Initial ^{14}C-tracer experiments at atmospheric pressure and later medium pressure work provided strong support for the enol mechanism (see ref. 24).

Another proposal that received attention was the *insertion mechanism*, which involves the insertion of CO into a metal-methyl or metal-methylene carbon bond, which is then hydrogenated to produce an alcohol or alkene. The mechanism is shown in Scheme 1.4.[26] Hydrogenation of the COH_2^* surface species together with water elimination is assumed to be the rate controlling step.

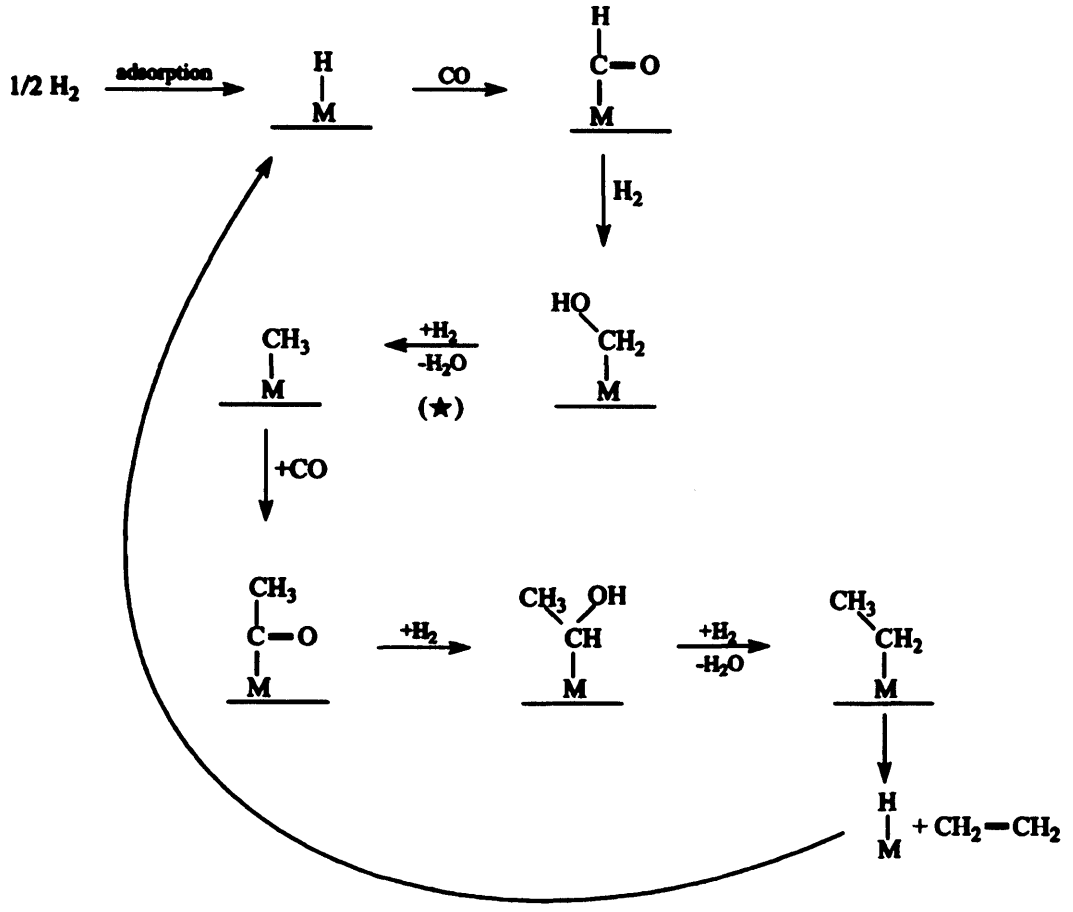

Scheme 1.4 – The insertion mechanism.[24]

Work by Davis *et. al.*[24] suggested that the FT mechanisms on Fe and Co are different. They concluded that carbide is the more active form of the Fe catalyst and that an oxygenate intermediate is involved in the (low temperature) reaction catalysed by Fe. Tracer studies on Co were in agreement with mechanisms involving the carbene intermediate and both CO_2 and alcohols were said to be able to act as insert gases.[27] Tracer studies on a Rh catalyst showed that $^{13}C_2H_4$ added to syngas acts as a chain initiator.

1.7. Outline of the Thesis

The main aim of this thesis is to study the adsorption of small molecules, relevant to the Fischer-Tropsch reaction (CO, C_2H_4 and also O_2), on Fe single crystal surfaces. The effect that these adsorbates have on the composition, structure and/or reactivity of the surfaces is discussed. Similarly the effect of bulk contaminants is also explored, since these are likely to be a part of the real catalytic system. Results from both experiment and density functional theory (DFT) calculations are included and two iron single crystals were utilized in the study, namely Fe(111) and Fe(110). The former is the main focus, while some comparative results of the latter are also included.

The introduction that was presented in this chapter has hopefully provided sufficient background knowledge to lay the foundation for the remaining chapters. *Chapter 2* firstly explains the UHV system and its importance in surface science studies. Background theory and information of the techniques and equipment that were used are then discussed. *Chapter 3* is a report of DFT calculations to examine the adsorption, diffusion and dissociation of CO on Fe(111) and also the influence that atomic carbon has on these processes. In *Chapter 4* the experimental cleaning process and difficulties associated with Fe are discussed. The structure of Fe(111) and Fe(110) are explored with Low Energy Electron Diffraction (LEED), Scanning Tunnelling Microscopy (STM), Auger Electron Spectroscopy (AES) and X-ray Photoelectron Spectroscopy (XPS) and the influence of bulk contaminants or adsorbed oxygen / ethene are demonstrated. In *Chapter 5* the adsorption of ethene on Fe(111) and the reactivity of the resulting surface species are investigated with a molecular beam reactor and XPS. *Chapter 6* summarizes the most important results and conclusions of the study and presents an outlook of potential future work.

1.8. References

1. J. M. Thomas and W. J. Thomas, *Principles and Practice of Heterogeneous Catalysis, Wiley-VCH, 3rd Ed.*, 2005.
2. J. J. Berzelius, *New Phil. J.*, 1836, **23**, 223.
3. P. W. Atkins, *Concepts in Physical Chemistry, W.H. Freeman,* , 1995.
4. M. E. Davis and R. J. Davis, *Fundamentals in Chemical Reaction Engineering, McGraw-Hill Higher Education, New York, NY*, 2003.
5. E. M. McCash, *Surface Chemistry*, Oxford Univesity Press, 2001.
6. G. Attard and C. Barnes, *Surfaces*, Oxford Univesity Press, 1998.
7. M. Bowker, *The Basis and Applications of Heterogeneous Catalysis*, Oxford Unitersity Press Inc., Oxford, 1998.
8. E. M. McCash, *Surface Chemistry, Oxford University Press*, 2001.
9. *http://www.answers.com/topic/langmuir-adsorption-isotherm*.
10. K. W. Kolasinski, *Surface Science: Foundations of Catalysis and Nanoscience, Wiley & Sons, Ltd*, 2002.
11. C. M. Friend, *Scientic American*, 1993, **268**, 74.
12. *http://www.answers.com/topic/single-crystal*.
13. A. Steynberg and M. Dry, *Fischer-Tropsch Technology*, 2004, **Elsevier Science**.
14. P. L. Spath and D. C. Dayton, *Preliminary Screening - Technical and Economic Assessment of Synthesis Gas to Fuels and Chemicals with Emphasis on the Potential for Biomass-Derived Syngas*, 2003, **National Renewable Energy Laboratory, Colorado, US**.
15. *http://www.answers.com/topic/fischer-tropsch-process#Use*.
16. M. M. G. Senden, S. T. Sie, M. F. M. Post and J. Ansorge, *Engineering aspects of the conversion of natural gas into middle distillates.*, 1992.
17. *http://knol.google.com/k/the-fischer-tropsch-ft-process*.
18. G. V. Schulz, *Z. Physik. Chem.*, 1936, **B32**, 27.
19. P. J. Flory, *J. Am. Chem. Soc.*, 1936, **58**, 1877.
20. R. B. Anderson, *J. Cat.*, 1978, **55**, 114.
21. F. Fischer and H. Tropsch, *Brennstoff-Chemie*, 1926, **7**.
22. J. T. Kummer, T. W. DeWitt and P. H. Emmett, *J. Am. Chem. Soc.*, 1948, **70**, 3632-3643.
23. P. M. Maitlis, *Pure Appl. Chem.*, 1989, **61**, 1747.
24. B. H. Davis, *Fuel Process. Technol.*, 2001, **71**, 157-166.
25. O. Evans and A. Nash, *Nature*, 1954, **118**, 1926.
26. I. Wender, S. Friedman, W. A. Steiner and R. B. Anderson, *Chemical Industry*, 1958, 1694.
27. B. H. Davis, *Catal. Today*, 2009, **141**, 25.

CHAPTER 2

Experimental

P.T.O

2.1. Introduction

The understanding of a surface and its reactivity requires the knowledge of its structure, chemical composition, electronic properties and vibrational properties. Over 50 surface sensitive techniques have been developed, but no single technique can provide all of this information, and therefore complementary surface sensitive probes are often combined in studies to create a fuller picture. Probing a surface spectroscopically requires a stimulus that leads to a measured response. The *Propst*-diagram in Figure 2.1 summarises the stimulus/response combinations that can be used in surface science spectroscopic techniques.[1]

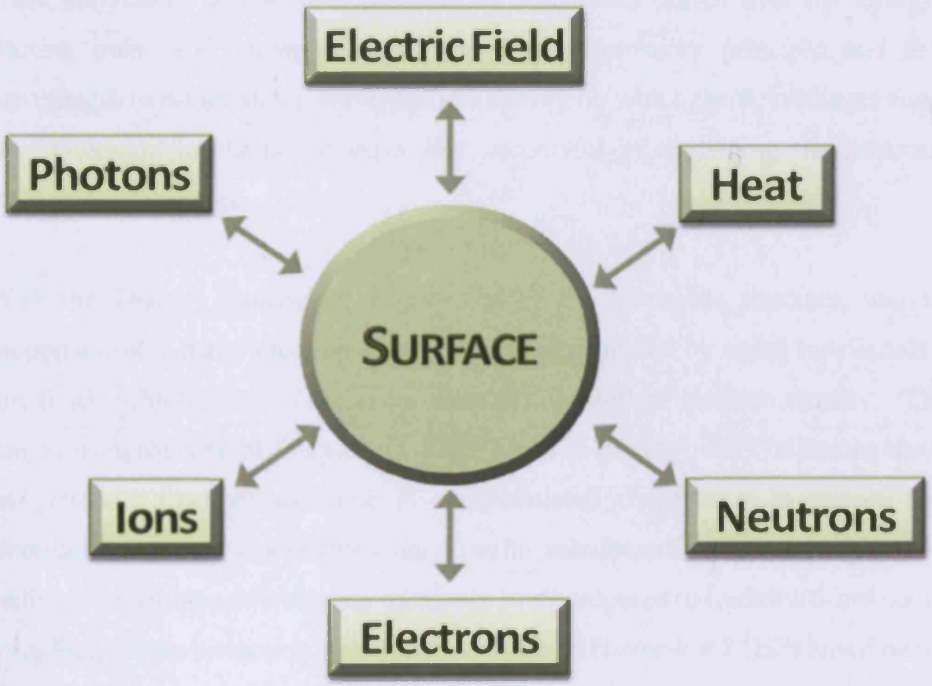

Figure 2.1 – The *Propst diagram* which summarises the possible stimuli and responses that can be used in surface science techniques.[1]

In addition to experimental techniques, first principles calculations have become increasingly relevant thanks to improved algorithms and increased computing power. The aim of this chapter is to give background on the surface science techniques and equipment that were used in the experimental part of the study and *Density Functional Theory*, which was employed in the theoretical part of the study.

2.2. Density Functional Theory[2]

2.2.1. Introduction

Computational quantum chemistry involves the development and application of theoretical algorithms and software based on quantum mechanics to predict properties of molecules from first principles. The development of Erwin Schrödinger's equation in 1926 was the springboard needed to model the interactions of complex compounds. Today, computational quantum chemists can model hundreds or thousands of electrons to predict the behaviour of interacting elements and compounds. The development can be applied to materials science, biology, engineering, molecular electronics and many other fields.

Wave mechanics is the form of q*uantum mechanics* which uses the energy quantum as starting point and incorporates Heisenberg's uncertainty principle and the de Broglie wavelength to establish the wave-particle duality on which the Schrödinger equation is based on. Quantum mechanics is especially successful in explaining the behaviour of atoms, molecules and nuclei.

With the *Density Functional Theory* (DFT) the electronic structure, and from that the properties, of a many-electron system can be determined by using functionals (functions of functions) which in this case is the spatially dependent electron density. The name DFT comes from this use of functionals of the electron density. DFT is among the most popular and versatile methods available in computational chemistry. In general results of DFT electronic structure calculations agree quite satisfactorily with experimental data and in addition computational costs are relatively low compared to traditional methods based on the complicated many-electron wavefunction, such as Hatree-Fock (HF) based methods.

2.2.2. Theoretical Basis

DFT is theoretically grounded in two Hohenberg-Kohn theorems.[3] The first demonstrates that the ground state properties of a many-electron system are uniquely determined by an electron density that depends on only three spatial coordinates. It lays the groundwork for reducing the many-body problem of N electrons with $3N$ spatial coordinates to 3 spatial coordinates, through the use of functional of the electron density. The second theorem

defines an energy functional for the system and proves that the correct ground state electron density minimizes the energy functional.

DFT calculations involve solving the *Kohn-Sham* (KS) *equations*,[4] which are the Schrödinger equations for non-interacting particles (in this case electrons) that generate the same density as any given system of interacting particles. This is significant because it reduces a complicated many-body problem of interacting electrons in a static external potential to a manageable problem of non-interacting electrons moving in an effective potential. The effective potential includes the external potential and the effects of Coulomb interactions between the electrons, *e.g.* the *exchange and correlation interactions*. The exchange interaction is represented by a potential involving exchange of space, spin coordinates or both between the particles involved. It can be visualized physically as the exchange of particles.

Correlation energy is defined as the energy difference of a correlated method relative to the HF energy, which is employed to account for the Coulomb correlation that the single-determinant does not include. Some correlation is already accounted for in the exchange term to describe the correlation between electrons with parallel spin to prevent them from being found at the same point in space. Coulomb correlation, on the other hand, describes the correlation between the spatial positions of electrons with opposite spin due to their Coulomb repulsion. Another part of the correlation is related to the overall symmetry or total spin of the system.

2.2.3. Approximations

Modelling the exchange and correlation interactions is one of the biggest challenges within KS DFT. To overcome this, approximations are applied. The simplest is the *local-density approximation* (LDA),[5] which is based on the exact exchange energy for a uniform electron gas; the exchange-correlation energy is written as

$$E_{xc}^{LDA}[n] = \int \varepsilon_{xc}(n) n(\vec{r}) d^3 r \qquad [2.1]$$

Where $\varepsilon_{xc}(n)$ the exchange-correlation energy density and $n(\vec{r})$ is the particle density. The *generalized gradient approximations* (GGA)[6] are more widely applicable. These are still

local, but also take into account the gradient of the density at the same coordinate; the exchange-correlation energy equation is

$$E_{xc}^{GGA}[n_{\downarrow}n_{\uparrow}]=\int\varepsilon_{xc}\left(n_{\uparrow},n_{\downarrow},\vec{\nabla}n_{\uparrow},\vec{\nabla}n_{\downarrow}\right)n(\vec{r})d^{3}r \quad [2.2]$$

Where $n_{\uparrow}$ and $n_{\downarrow}$ are the electron spin densities and $\vec{\nabla}n_{\uparrow}$ and $\vec{\nabla}n_{\downarrow}$ are the gradient in the spin densities. Using GGA, very good results for molecular geometries and ground state energies have been achieved. In practice the KS theory is applied in different ways depending on the system under consideration. For solid state calculations, plane wave basis sets are employed. When molecular adsorption is considered, sophisticated functionals are required and a variety of exchange-correlation functionals have been developed for chemical applications. Among the most widely used are the Perdew-Wang 1991 (PW91)[7] and the more recent Perdew-Burke-Ernerhof (PBE)[8] and Revised PBE (RPBE)[9] functionals, which were employed in the DFT study reported here. The PBE functional is known to yield reliable geometries,[10] while RPBE has been shown to improve the chemisorption energetics of atoms and molecules on transition-metal surfaces. In the original work O, CO and NO were adsorbed on Ni, Rh, and Pd surfaces and RPBE was shown to reduce overbinding by a factor of two compared to the PW91 and PBE functionals.

2.3. Ultra High Vacuum Conditions[11]

2.3.1. The Need for Ultra High Vacuum Conditions

To commence the discussion on surface science techniques, the need and practical principles of ultra high vacuum (UHV) conditions will be discussed. The rate of surface contamination is mainly dependent on the rate of bombardment with gas molecules, the sticking probability of the gas and the temperature of the environment; and can be calculated from consideration of the kinetic theory of gases: At 10^{-6} mbar the surface would be covered with 1ML of CO molecules in 3.5 s; whereas at ~10^{-10} mbar it would take 9.7 hours.* It is thus of extreme importance to keep the background pressure as low as possible. Table 2.1 is a classification of the degree of vacuum in a system according to its pressure.

* Assuming a sticking probability of 1, room temperature, and a surface density of ~10^{15} cm^{-2}.

Table 2.1 – Classification of vacuum conditions with the associated mean free path of electrons in the environment and the approximate time that it will take to form a monolayer coverage on the sample surface (assuming a sticking probability of 1).

Degree of Vacuum	Pressure (mbar)	Gas Density (molecules/m^3)	MFP (m)	Time to form 1 ML (s)
Atmospheric	~1000	2×10^{25}	7×10^{-8}	10^{-9}
Low	~1	3×10^{22}	5×10^{-5}	10^{-6}
Medium	~10^{-3}	2×10^{19}	5×10^{-2}	10^{-3}
High	~10^{-6}	3×10^{16}	50	1
Ultra High	<10^{-10}	3×10^{12}	5×10^{5}	10^{4}

The main reasons that surface science experiments require low vacuum conditions are summarised below, in order of least to most stringent:

1. The mean free path for probe and detected particles (ions, atoms, electrons) in the vacuum should be sufficiently large to travel to and from the surface without interaction with residual gas phase molecules. This requires pressures better than 10^{-4} mbar. The lifetime of channeltron and multiplier detectors are also substantially reduced at operating pressures above 10^{-6} mbar.
2. Many spectroscopic techniques are also capable of detecting molecules in the gas phase, so it is important that the number of species present on the surface should be substantially more than that in the gas phase immediately above the surface. To achieve a surface/gas phase discrimination of better than 10:1 when analysing 1% of a monolayer, the gas phase concentration should be less than 10^{12} molecules/cm^3, which converts to a partial pressure less than 10^{-4} mbar.
3. The most stringent vacuum requirement for surface science experiments, however, is to ensure that the experiments are done on a reproducibly *clean surface*. The background pressure must be such that contaminant build up on the surface is slower than the time required for the experiment. The pressure required depends on the nature of the surface, but for more reactive surfaces UHV conditions (<10^{-9} mbar) are essential. At these low pressures the mean free path of gas molecules are approximately 40 km, meaning that they will collide with chamber walls many times over before colliding with each other.

2.3.2. Achieving UHV Conditions

There are several requirements for obtaining UHV conditions, some of which are listed below:

- Chambers should be constructed out of low-outgassing materials, such as glass and certain stainless steels; the surface area inside the chamber should be minimized.
- Multiple Vacuum Pumps with high pumping speeds should be used.
- All traces of hydrocarbons should be avoided, including skin oils in fingerprints, *i.e.* gloves should be used when handling equipment.
- Before use, the system should be baked while the vacuum pumps are running to remove water and other atmospheric gases adsorbed on chamber walls.

Hydrogen diffusing out of the grain boundaries in the stainless steel is the most common background gas in a well-designed, well-baked UHV system. A typical UHV system employs a series of different pumps, since no single pump can operate throughout the whole range from atmospheric pressure to UHV.

Figure 2.2 – Turbomolecular Pump

Rotary pumps are positive-displacement pumps that consist of vanes mounted on a rotor that rotate inside a cavity; pressures as low as 10^{-3} mbar can be attained. The pumps are used to back turbomolecular pumps, *i.e.* to reduce pressures from atmospheric level to medium vacuum in order to ensure efficient use of the turbomolecular pump.

A *turbomolecular pump* (shown in Figure 2.2) is specifically designed to obtain and maintain high vacuum. The pump has a mechanical mechanism, working on the principle that gas molecules can be given momentum in a desired direction by repeated collision with a moving solid surface. Pressures as low as 10^{-10} mbar can be obtained.

Ion pumps, in contrast are non-mechanical. These pumps ionise chemically active gases and employ a strong electric field to accelerate them into a solid electrode where they react with

the chemically active surface and are removed from the atmosphere. Pressures as low as 10^{-11} mbar can be obtained in ideal circumstances, but noble gases are not effectively pumped, since they are not chemically active.

Titanium sublimation pumps (TSP) consist of titanium filaments through which a high currents are passed periodically. The current causes the filament to reach the sublimation temperature of titanium, which coats the surrounding chamber walls with a thin film of clean titanium. Since titanium is very reactive, components of the residual gas which collide with the walls will react and form a stable, solid product, causing a reduction in the chamber pressure.

2.3.3. Measuring High Vacuum

Pirani gauges are useful to measure pressures in the range of 10^{-3} to 10 mbar and are therefore used to measure the pressure in gas lines connected to the vacuum system. The gauge consists of a metal wire open to the pressure being measured. The wire is heated by the current flowing through it and cooled by the gas surrounding it. If the gas pressure is reduced, the cooling effect will decrease, causing the temperature in the wire to increase. The resistance of the wire is a function of its temperature, so by measuring the voltage across the wire and the current flowing through it, the resistance (and gas pressure) can be determined.

Thermionic gauges are the most sensitive for very low pressures (10^{-3} – 10^{-10} mbar). Electrons are produced by a filament through thermo-ionic emission, which collide with gas atoms and generate positive ions. The ions are attracted by a biased electrode called the collector. The current in the collector is proportional to the rate of ionization, which is a function of the pressure in the system.

The discussion of the elementary surface science concepts in sections 2.4 to 2.6 follow the explaination in the book of Attard & Barnes closely.[1]

2.4. Sample Cleaning

Two fundamental problems in studying solid surfaces are preparing a clean surface and keeping it clean for the duration of the experiment. One of the most common methods of

cleaning sample surfaces is *sputtering*, which involves the bombardment of the surface with high energy argon ions (100 – 3000 eV) which in the process physically removes atoms from the top few surface layers. Lighter elements are sputtered preferentially, due to favourable exchange of momentum with the argon ions (argon is also light compared to heavier metal atoms of the sample); this means that sputtering will purge the surface of a typical (higher mass) metal sample, *eg.* Pd or Co, from (lighter) surface contaminants, *eg.* O & S. Upon hitting the surface, the argon ions transfer energy to the surface atoms causing the adsorbate-metal bonds to break and the atoms to desorb from the surface. Sputtering causes severe damage to the surface, which is why it is always followed by annealing (heating) of the sample to high temperatures, typically close to the melting point of the substrate. Annealing restores the original flat surface geometry (by supplying surface atoms with enough energy to diffuse into the most favourable positions) and also causes any embedded argon ions to desorb into the vacuum. Importantly heating also causes segregation of bulk contaminants to occur due to the driving force that originates from the difference in concentration in the bulk and the now clean surface. To clean the bulk of the sample, multiple sputtering and annealing cycles should therefore be employed.

2.5. Surface Sensitivity

In order to exclusively determine the properties of the surface of a substrate (in contrast to that of the bulk) the techniques used should be both sufficiently *sensitive* and *selective*. Sensitivity is needed to detect the small amount of atoms that make up the substrate surface: the number of surface atoms of Fe(110) is ~ 1.73×10^{15} atoms/cm^2 (for Fe(111) the value is ~7.04×10^{14} atoms/cm^2), which corresponds to ~2.9×10^{-9} mol/cm^2. For sensitivity of 1% of a monolayer (needed to define surface cleanliness) a detection limit of ~10^{-12} M is required. This value is well below the limit of many analytical techniques.

Selectivity is required to ensure that the analytical signal is not swamped with bulk signal (*i.e.* only the surface atoms should be analyzed), since the surface to bulk atom ratio is typically in the order of $1:10^7$ – $1:10^8$. To achieve surface sensitivity many techniques employ the special properties of low energy electrons (see section 2.6). XPS is not completely surface sensitive, but most of the signal does originate from the top few atomic

layers and a small percentage comes from much deeper into the solid. In contrast ion scattering spectroscopy (ISS)† is completely surface sensitive.

2.6. The Interaction of Electrons with Matter

If a mono-energetic beam of primary electrons is incident on a crystal surface, the energy distribution of the emitted electrons generally takes on the form shown in Figure 2.3.

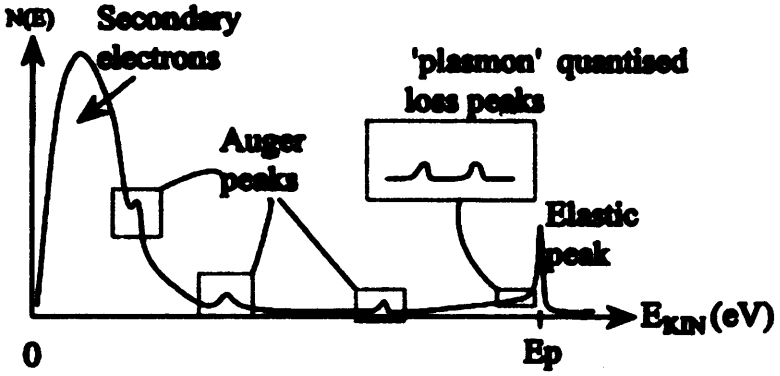

Figure 2.3 – Energy loss features of an electron beam incident on a surface.[12]

The electrons are commonly classified into three groups: *elastically scattered* (retaining the original kinetic energy), *inelastically scattered* (losing some energy by being deflected slightly and randomly) and *secondary electrons* (excited from the surface substrate itself). The peak at the incident primary energy value is due to the elastically scattered electrons; these are detected in diffraction experiments, *e.g.* LEED. This peak tends to include those electrons that have been phonon scattered, since most instruments, with the exception of vibrational energy loss analysers, cannot detect the small energy difference. Inelastically scattered electrons have lost energy in at least one inelastic scattering event. Those electrons which have suffered several such scatterings or lost energy in continuum excitations contribute to the featureless section of the spectrum extending from very low energies to the elastic peak. A few types of loss events are distinguished, as described below.

Plasmon losses occur when the photoelectron which is passing through the solid induces collective oscillations (called plasmons) within the conduction band of free electrons and as

† ISS is also referred to as Low Energy Ion Scattering (LEIS).

a result suffers an energy loss (a plasmon loss) of ~10 – 30eV. Plasmons have a fixed frequency depending on the solid, and bulk plasmons can be distinguished from surface plasmons because they are lower in energy.

Electron-hole pair excitations (inter-band transitions) consist of the promotion of an electron from a filled to an empty electron state. Since valence levels in a solid form a continuous band of energy, a continuous energy loss range of 0 – 10eV is possible. *Ionisation losses* arise from ionisation of a core level of an atomic species in the surface region; 10 – 1000eV losses are possible.

Vibrational energy losses may be brought about by exciting the quantized vibrations in the solid lattice (phonon excitations) or a discrete vibrational mode of an adsorbate molecule; these losses are small and typically 0.01 – 0.5eV. Most true secondary electrons are situated in the very intense peak lying at very low energies (typically < 50 eV) having arisen from the cascade process of energy loss of high energy primaries. However, there is no way of distinguishing between true secondaries and inelastically scattered electrons.

In contrast, small peaks can arise on the background due to electron emission associated with the decay of a discrete excited state in the surface region (created by the primary electrons); the dominant process for this is Auger electron emission (see section 2.9). The raised background on the low kinetic energy side of the Auger peaks in the *N(E)-E* spectrum results from Auger electrons that have lost energy. The overall positive slope in the expansion of high kinetic energy Auger peaks arises from scattered primary electrons. The background is continuous, because the energy loss processes are random and multiple.

In the case of an incident *electron beam*, all electrons that are finally detected must have undergone an elastic reflection in the backward direction, an elastic and inelastic collision or originate from a secondary process. Therefore the signal-to-background ratio for discrete losses and secondary processes are generally poor. If an incident *photon beam* is used as a source of excitation instead, all the same inelastic and secondary processes will result, but because no direction reversal or elastic scattering is required, the signal-to-background ratio is significantly improved.

2.6.1. Surface Sensitivity of Electrons

The inelastic mean free path (IMFP), λ, of an electron is defined as the distance that an electron beam can travel before its intensity decays to 1/e (0.368) of its original value; *i.e.* it is a measure of the average distance that an electron can travel without losing energy. A small value of λ indicates a high probability of energy loss (which translates into a small travelling distance before being absorbed), signifying that electrons with a small IMFP are highly surface sensitive. The IMFP of an electron is only weakly dependent on the material it travels through (decreasing slightly with increasing atomic number of the substrate), but highly dependent on its initial kinetic energy. Figure 2.4 shows the universal curve of electrons travelling through metals; similar curves have been developed for other types of materials. The curve represents the experimentally determined relation between the IMFP and the kinetic energy of the electron.

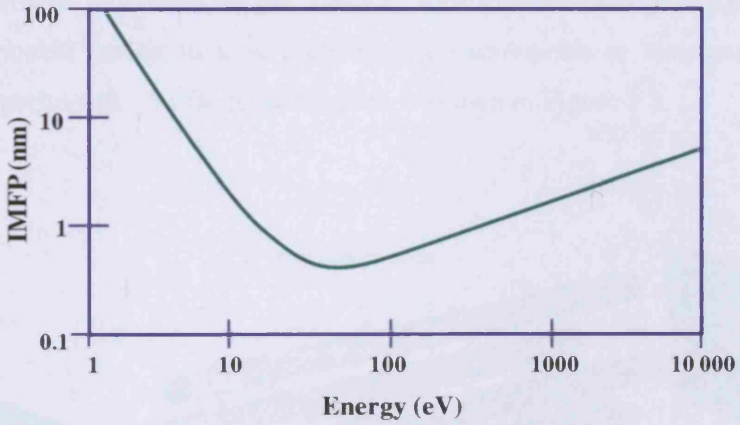

Figure 2.4 – Universal curve for metals.

Figure 2.4 shows that the greatest surface sensitivity is achieved in the kinetic energy region of 50 – 100 eV. The empirical mathematical expression of the graph is shown in equation 2.3.[13]

$$\lambda = \frac{538\,a}{E_{kin}^2} + 0.41\,a^{3/2}E_{kin}^{1/2} \qquad [2.3]$$

E_{kin} is the kinetic energy of the electrons and a the mean atomic diameter of the element. From Figure 2.4 and equation 2.1 one can deduce that for kinetic energies higher than 50 eV the IMFP is proportional to the square root of the kinetic energy (and therefore the electron velocity). This is rationalized by realizing that the faster the electron travels, the less time it takes to travel through a given thickness of the solid and the less chance it has of losing

energy. 30 eV is the critical kinetic energy value needed for the primary energy loss mechanism, plasmon excitation, which accounts for the rapid increase of the IMFP at lower kinetic energy values.

Another means of enhancing surface sensitivity of an electron beam is by changing its incidence angle to grazing (small) angles in order to increase the path length in the solid (and thus increase the chances of energy loss).

2.7. Mass Spectrometry[14]

A quadrupole mass spectrometer is used to determine the background gas composition in the chamber with the aim of checking gas purity or following the change in partial pressure of a specific component during sticking probability measurements or temperature programmed desorption experiments. A schematic diagram is shown in Figure 2.5.

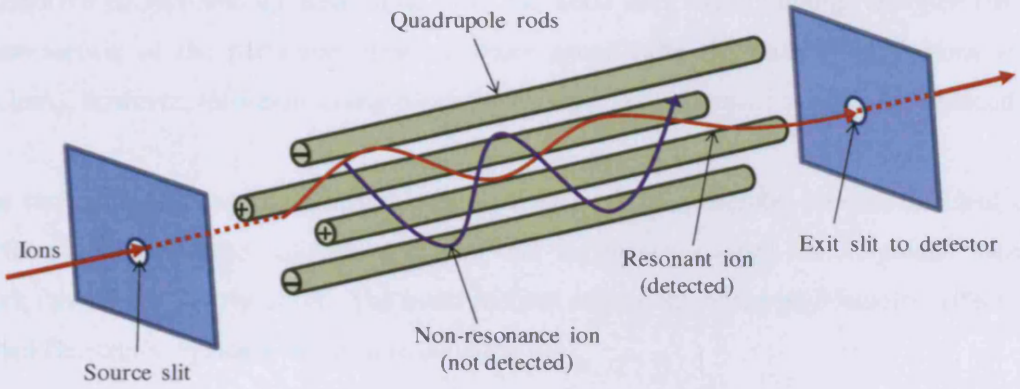

Figure 2.5 – Schematic diagram of a quadrupole mass spectrometer.[14]

The quadrupole consists of four parallel metal rods. Each opposing rod pair is connected together electrically and a radio frequency voltage is applied between the two pairs of rods. A direct current voltage is superimposed on the radio frequency voltage. Ions travel down the quadrupole between the rods. Only ions of a specific mass-to-charge ratio (m/z) will reach the detector for a given voltage ratio. The other ions will have unstable trajectories and will collide with the rods. This permits the selection of an ion with particular m/z or allows the operator to scan for a range of m/z-values by continuously varying the applied voltage.

2.8. X-Ray Photoelectron Spectroscopy (XPS)[15]

2.8.1. Basic Principles

X-ray photoelectron spectroscopy (XPS) is a quantitative technique used to determine the composition, concentration, and chemical state of elements in a material. XPS spectra are obtained by irradiating material with a beam of x-rays while simultaneously measuring the amount and kinetic energy of electrons escaping from the top 1 – 5 nm of the material. All elements heavier than lithium (Z = 3) can be detected. Line profiling (measuring the uniformity of the elemental composition across the surface) and depth profile (measuring the elemental composition as function of distance into the bulk) is possible.

The incoming radiation causes photoemission from both core and valence levels of the surface atoms, but it is the core level electrons[‡] that are of interest in XPS, while valence electrons are of significance in Ultraviolet Photoelectron Spectroscopy (UPS). Chemical identification is possible because the core level electrons deep inside the atoms are mostly insensitive to surrounding influences from the solid and retain binding energies that are characteristic of the particular element (more specifically the number of protons in the nucleus), however, information regarding the chemical environment can also be deduced.

The technique is based on Einstein's photoelectric effect, whereby photons incident on a surface induce electron emission provided that the photon energy ($h\nu$) is greater than the work function, φ,[§] of the solid. The mathematical expression of the photoelectric effect, also called Einstein's equation, is given in equation 2.4.

$$E_K = h\nu - (E_B + \phi) \qquad [2.4]$$

[‡] Core levels are the filled inner quantum shells, not involved in chemical bonding; whereas valence levels consist of partially filled outer quantum shells with more weakly bound electrons which participate in bonding.

[§] The work function, φ, is the minimum amount of energy required to free an electron in the highest occupied energy state (the Fermi level) of the solid to the vacuum. Vacuum is a state where the electron has no interaction with other particles (zero potential energy) and is at rest (zero kinetic energy); the vacuum state is therefore defined as the zero energy level.

E_K and E_B are the kinetic and binding energies of the core electron; $h\nu$ is the incident photon energy and φ is the work function of the substrate. φ (and therefore the relative vacuum level) is a function of both the elemental composition of the sample as well as the facet of the surface. Equation 2.4 is used to estimate the kinetic energy of the emitted photoelectrons on the principle of energy conservation.

Although the real kinetic energy of the electron leaving the sample depends on the work function of the sample itself (φ_s), the measured kinetic energy only depends on the work function of the analyser (φ_a, typically 4.2 – 4.8 eV) to which the sample is electrically connected. The relative energies of the photo-emission process and that measured by the analyser are shown in Figure 2.6. Also shown is the Auger process (explained in section 2.9) which occurs as a result of the core electron removal. Symbols have the same meaning as in equation 2.4 and R refers to the amount that the electron's kinetic energy was retarded by to match the pass energy.

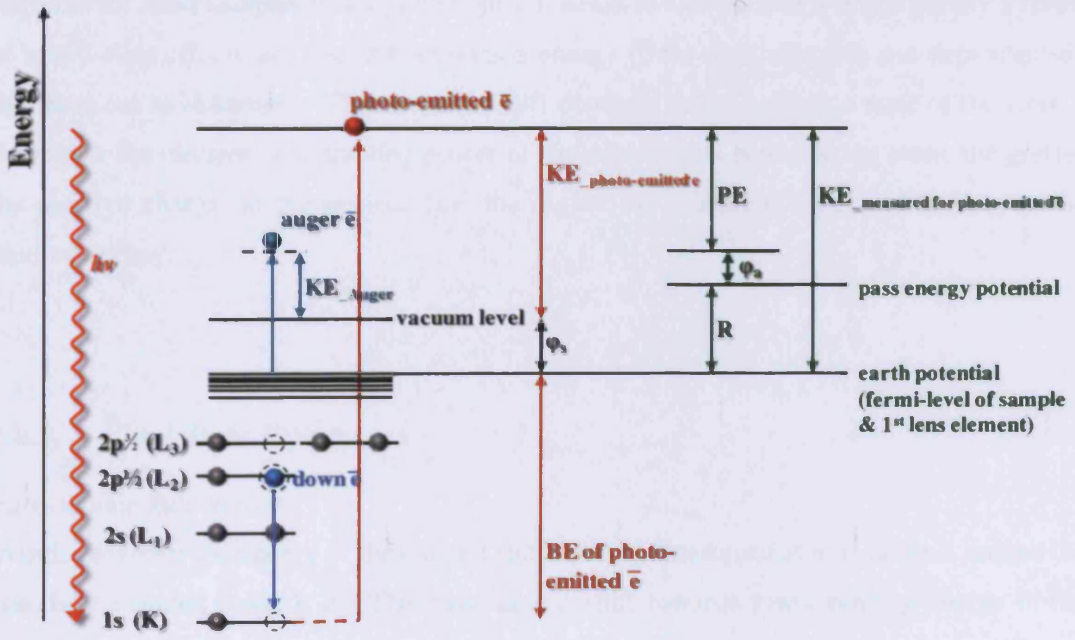

Figure 2.6 – Energy diagram for photo- and Auger electron emission. The Auger process is shown in blue (left); photo-emission is shown in red (middle); and photo-emission as measured by the XPS analyser is shown in green (right).[16]

The binding energy of the emitted electron is equal to the energy difference between the initial state of the atom (with n electrons) and the final state (with $n-1$ electrons). If it is assumed that the energy and spatial distribution of the electrons remaining after photo-emission is exactly the same as in the initial state; the binding energy (E_B) can be equated to the negative orbital energy of the emitted electron, ε:

$$E_B = -\varepsilon \qquad [2.5]$$

This approximation is called *Koopman's theorem*. In reality, however, the binding energy is influenced by both initial and final state effects.

2.8.2. Initial State Effects

Initial state effects are caused by chemical bonding, which influences the electronic configuration in and around the atom. The energy shift caused by this is called a *chemical shift* and for most samples it is a good approximation to assume that it is completely a result of initial-state effects and that the relaxation energy (final-state effect) is not dependent on the chemical environment. The chemical shift depends on the oxidation state of the atom – the higher the electron withdrawing power of the substituents bound to the atom, the greater the positive charge on the nucleus (*i.e.* the higher the oxidation state) and the higher the binding energy.

2.8.3. Final State Effects

Intra-atomic Relaxations

In order to lower the energy of the excited final state, the occupied atomic orbitals around the core hole contract towards it. This can cause a shift towards lower binding energy in the spectrum.

Extra-Atomic Relaxations

Most atomic relaxations result from rearrangement of outer-shell electrons. In metals electrons are free to move between atoms to screen the hole created by photo-ionization, which can result in binding energy shifts of ~5 – 10 eV. In insulators this is not the case and the extra-atomic relaxation is less pronounced.

Spin-Orbit Coupling

Electrons orbiting the nucleus have an orbital angular momentum, l, and a spin angular momentum, s. Before ionisation, the electrons exist in pairs with opposing spin, resulting in a zero net magnetic moment. Upon photo-ionisation, however, the atom is left with an unpaired electron, causing its spin angular momentum to interact with its orbital angular momentum. Depending on the spin of the remaining electron, it will either reinforce or oppose the angular momentum. This causes two distinct states to be formed, and thus two values for the total angular momentum, j (where $j = l \pm s$), with the opposing state at higher energy than the parallel state. These two different final states will result in a splitting of the primary photo-electron peak into two peaks with different intensities. The ratio of their intensities is related to the total angular momentum according to

$$Intensity = 2j + 1 \qquad [2.6]$$

For the Copper 2p peak with $l = 1$ and $s = ½$ the intensity ratio would be 2:1.

Other final state effects, including multiplet splitting, shake-up events and vibrational fine structure result in satellite features in the XPS spectrum.

Multiplet Splitting

Multiplet splitting results from the coupling between the unpaired core electron with an unpaired valence electron. Two states can result from this interaction: one in which the spin vectors are aligned in parallel and in the other anti-parallel. In the photo-electron spectrum this phenomenon is observed as two peaks separated by the exchange interaction energy, ΔE.

Shake-up and Shake-off Processes

In a shake-up event, the outgoing photo-electron excites a valence electron to a previously unoccupied state; causing the photo-electron to give up some of its kinetic energy. This is recognized as a discrete satellite peak at higher binding energy of the parent peak in the photo-emission spectrum.

In a shake-off process, energy from the escaping photo-electron is passed on to the valence electron, ejecting it and leaving vacancies in the core and valence levels; resulting in a

doubly ionised state. Unlike a shake-up process, the energy involved in the shake-off process is not discrete and thus not observed as a feature in the photoelectron spectrum.

2.8.4. Equipment Components[17]

X-Ray source [18]

The X-ray gun used for the purposes of this study is a twin anode *DAS 400 X-Ray Source*, allowing either Mg Kα (1253.6 eV) or Al Kα (1486.6 eV) to be selected. Electrons are extracted from a heated filament to bombard the selected anode surface which is at high positive potential. The focus ring and angled nose cone ensures that the right area is hit by the electrons. The anode is water cooled to prevent the Mg or Al surface from evaporating.

Analyser Assembly [17]

The XPS analyser assembly consists of a hemispherical electrostatic analyser, a multi-element universal lens and seven Channeltron electron multipliers as shown in Figure 2.7.

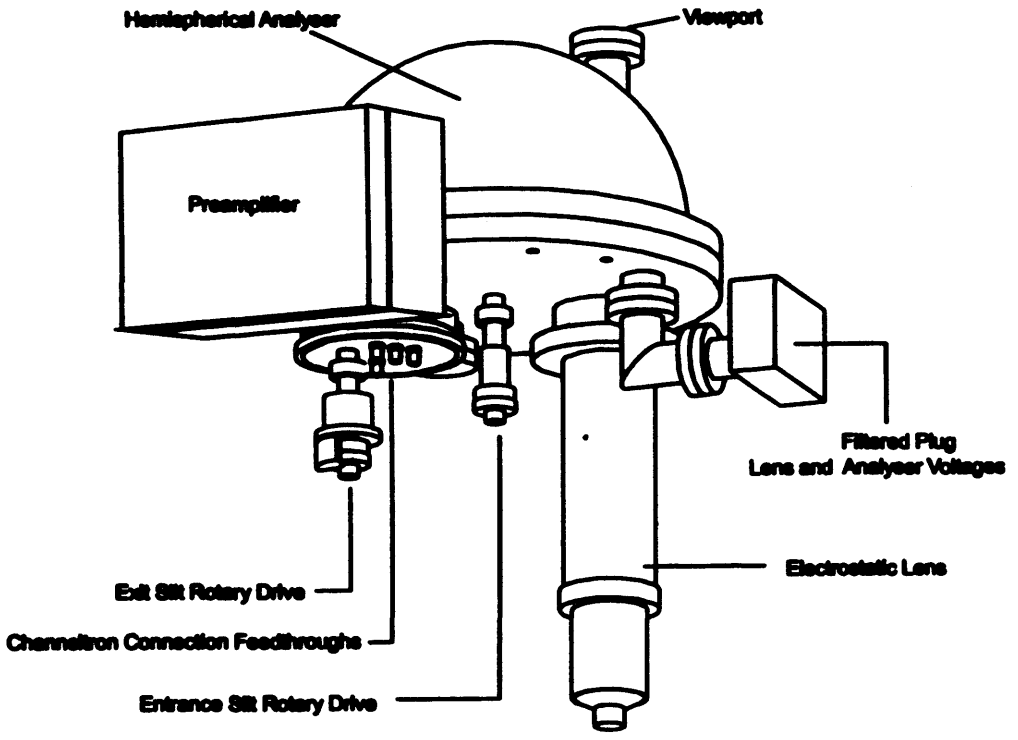

Figure 2.7 – Major components of the XPS analyser (cables not shown).[17]

Electrostatic input lens

The input lens consists of a double lens. The first adjustable lens defines the analysis area (spot size) and angular acceptance of electrons which pass through the hemispherical analyser. The second lens retards or accelerates the electrons to match the pass energy of the analyser and focuses the electrons on the entrance of the analyser entrance aperture by means of a series of cylindrical electrodes held at different potentials.

Hemispherical Analyser

The electron energy distribution (across a range of kinetic energy values) is measured with the use of an electrostatic energy analyser (illustrated in Figure 2.8) which consists of two electrically isolated concentric hemispheres with a potential difference between them. The electrostatic field separates electrons by allowing only electrons of a chosen kinetic energy (the *pass energy*) through to the detector in a continuous flow. Electrons with kinetic energies less than the chosen pass energy are attracted by the inner positive hemisphere and neutralized, while higher energy electrons hit the outer hemisphere and are also lost. The resolution of a spectrum can be improved significantly by reducing the pass energy; however, this is always accompanied by a loss in intensity.

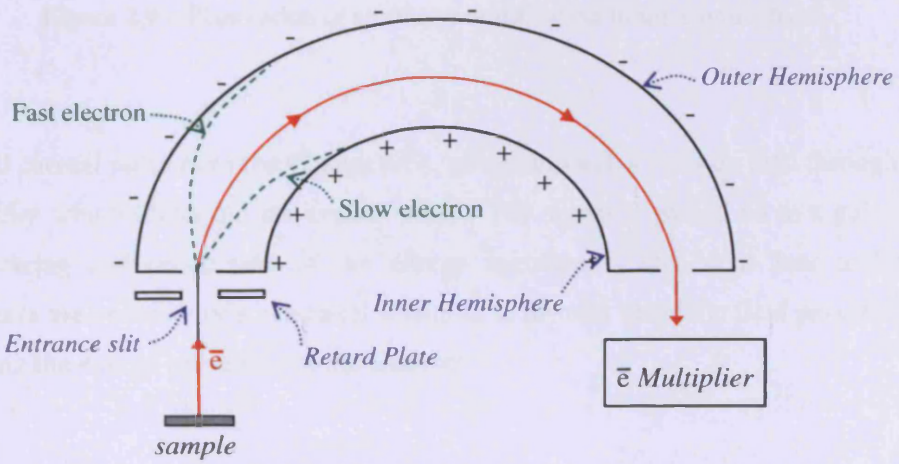

Figure 2.8 – Electrostatic energy analyser for XPS analysis.[17]

The Channeltron Detector

Seven channel electron multipliers (channeltrons) are placed across the exit plane of the analyser and have the function of amplifying the current of a single electron/ion by a factor of ~10^8 (see Figure 2.9). Electrons/ions which arrive at the input of the Channeltron detector generate secondary electrons which are then accelerated down the Channeltron by a positive voltage bias (2 – 3kV at the output). These electrons strike the Channeltron wall and progressively produce additional electrons down the channeltron up to the output, where 10^7 – 10^8 electrons arrive. The statistical nature of the multiplication process results in a Gaussian distribution of pulse heights at the output from the channeltron.

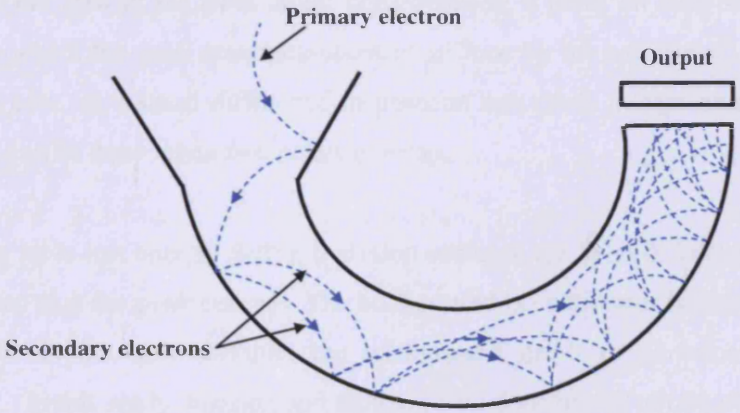

Figure 2.9 – Illustration of electron amplification in the Channeltron.[17]

The small current pulse exits the Channeltron, passes through a vacuum feed through into the *preamplifier* which filters out the system noise. The signal is passed on to a pulse counter for processing and production of the energy spectrum. The input lens and analyser hemispheres are covered by a mu-metal shielding to prevent magnetic field penetration from influencing the energy resolution of the analyser.

2.8.5. Quantitative Analysis

Although the incoming x-rays can penetrate the bulk of the solid as deep as 10^3 nm, the outgoing signal originates only from the surface region less than 5 nm deep, due to the inelastic scattering of the emitted electrons (see section 2.6.1).

Peak Measurement and Background Removal

The relative intensities of XPS peaks can be related to the concentration of species in the selvedge. The measured peak area is also dependent on the following variables:

- The photo-emission cross section (the probability of photo-emission occurring from the particular core level).
- The IMFP of the photo-emitted electron.
- The instrumental response (efficiency of the spectrometer for detection of electrons as a function of kinetic energy).

To determine the area of the peak under consideration, a point on each side of the peak is selected after which the peak area measurement is done by the software.[19] Points should be selected with care, as a small difference in position can cause a large change in peak area. Curve-fitting can be done when two peaks overlap.

Electrons that have lost energy during emission increase the level of background at binding energies higher than the peak energy. The background is continuous because the energy loss processes are random and multiple; the background needs to be removed before peak measurement. In this study, background removal was done in one of two ways depending on the peaks being measured: For adsorbate peaks linear background subtraction can be done, since there are very few inelastically scattered electrons. This involves drawing a straight line from either side of the peak. The second method is non-linear Shirley subtraction, whereby the background is assumed to arise solely by the scattering of lower kinetic energy electrons and is therefore proportional to the integrated photo-electron intensity at lower kinetic energy. This method was used for bulk metal peak area measurement.

Equation 2.7, developed by Carley and Roberts,[20] was used to determine the concentration of the surface species. The equation was developed by modifying the original equation of Madey[21] to include the photo-ionisation cross section and account for the probability that an electron is photo-emitted from a particular atomic orbital of a specific element. This value is dependent on the size and shape of the orbital and the ionising photon energy and was obtained from data tabulated by Schofield.[22]

$$\sigma_a = \frac{A_a}{A_s} \times \frac{KE_a}{KE_s} \times \frac{\mu'_s}{\mu'_a} \times \frac{N\lambda_s\rho_s}{M_s} \cos\phi \qquad [2.7]$$

σ_a = surface concentration of the adsorbate

A = Peak areas of adsorbate and surface material respectively

KE = Photoelectron Kinetic Energy of adsorbate and surface material respectively

N = Avogadro's constant

λ_s = Inelastic mean free path of the surface substrate

ρ_s = Density of the surface substrate

M_s = Molecular mass of surface substrate

μ = photo-ionic cross section of the adsorbate and substrate respectively

φ = angle at which photo-electrons are collected with respect to the sample normal

The photo-ionic cross section (μ') of Fe or C is calculated with equation 2.8 to account for the angle between the source and analyser. By including the angular distribution asymmetry parameter, β, the influence of the specific Hatree-Slater wave function is accounted for; values are tabulated for each sub-shell, *i.e.* s, p, d etc.

$$\mu' = \mu(1-\beta/2((3\cos^2\theta-1)/2)) \qquad [2.8]$$

θ = Angle between the source and analyser

μ = Photo-ionic cross section at an source-analyser angle of 90°, values are tabulated for each element

β = Angular distribution asymmetry parameter

The coverage of C on Fe(111), for example, is calculated as follows:

For Carbon:

$A_C = 43.6$

$KE_{C\,1s}$ = Al Source Energy – $BE_{C\,1s}$ = 1486.6 – 283 = 1201.6 eV

$\mu_{C\,1s\,1/2} = 1$

$\beta_C = 2$

i.e. $\mu_{1s\,1/2}' = (1 - 2/2((3\cos^2 45 - 1)/2)) = 1 - (0.25) = 0.75$

For Iron:

$A_{Fe} = 23035$

$KE_{Fe\ 2p}$ = Al Source Energy – $(BE_{Fe\ 2p\ 3/2} + BE_{Fe\ 2p1/2})/2 = 1486.6 - (706.7 + 719.7)/2 = 773.4$ eV

$\mu_{Fe\ 2p} = \mu(2p_{3/2} + 2p_{1/2}) = 10.82 + 5.60 = 16.42$

$\beta_{Fe} = 1.45$

$\therefore\ \mu_{Fe\ 2p}' = 16.42(1 - (1.45/2)(0.25)) = 13.44$

$N_A = 6.023\times10^{23}$ atoms/mole

$M_{Fe} = 55.85$ g/mole

$\lambda_{Fe} = 1.27\times10^{-9}$ m (Ref NIST 1.34)

$\rho_{Fe} = 7.87\times10^{6}$ g/m^3

$\varphi = 0°$ (analyser points directly at the sample)

$\theta = 45°$

The coverage of C on Fe is

$$\sigma_C = \frac{43.6}{23035} \times \frac{1201.6eV}{773.4eV} \times \frac{13.44}{0.75} \times \frac{(6.023\times10^{23}\ atoms/mole)(1.27\times10^{-9}\ m)(7.87\times10^{6}\ g/m^3)}{55.85\ g/mole} \cos 0°$$

$$\sigma_C = \frac{43.6}{23035} \times 2.99\times10^{21}\ atoms/m^2$$

$$\sigma_C = 5.68\times10^{18}\ atoms/m^2 \text{ (or } 5.68\times10^{14}\ atoms/cm^2\text{)}$$

The top layer of Fe(111) consists of 7.04×10^{14} atoms/cm^2, so the carbon concentration with respect to the Fe(111) surface will be ~0.80 ML. If the sample is Fe(110), the relative C-concentration will be 5.68×10^{14} / 1.73×10^{15} = 0.32 ML.

2.9. Auger Electron Spectroscopy (AES) [1, 23, 24]

2.9.1. General

The Auger effect, named after Pierre Auger who discovered it in 1925,[25] is the process by which emission of an electron from an atom causes the emission of a second electron, as was shown in Figure 2.6. The technique is a popular choice for chemical analysis, none the least

because it can easily be incorporated into the same apparatus used for LEED (see Figure 2.15 and section 2.10.1). Auger transitions are also observed during XPS measurements and can provide complementary information. Whereas XPS assumes a one-electron process, the Auger process involves at least three electrons.

When an incident electron (typically in the energy range 2 – 5 keV) causes photo-emission of a core electron, an electron vacancy is created in the deep core level, leaving the atom in an excited state.** The vacancy may be filled by a "down electron" which is initially at a higher energy state (a higher core level or the valence level) with a release of energy equal to the difference in energy between the core hole and down electron. This energy may be released in the form of an emitted photon in the process of *fluorescence*, or it can be transferred to a third electron, the Auger electron, which is then emitted from the atom.

2.9.2. Auger Emission *vs.* Fluorescence

X-ray emission is governed by selection rules for dipole radiation, *i.e.* the quantum number of the orbital angular momentum must change by ±1. The emission of characteristic x-rays from a sample is the basis of the technique Energy Dispersive X-ray Spectroscopy (EDS) which is often added to Scanning Electron Microscopy (SEM) and Scanning Auger Microscopy (SAM) to aid chemical identification.

The Auger process on the other hand, does not strictly depend on selection rules and is governed by electrostatic forces produced by the interaction of a hole in an incomplete shell with its surrounding electron clouds. The sum of the Auger and fluorescence yield is unity (see Figure 2.10).

** Auger transitions can also be excited by photons or ions.

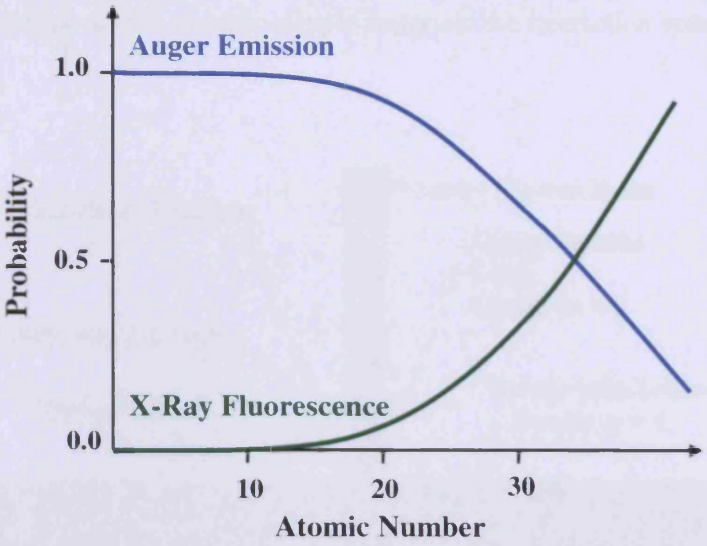

Figure 2.10 – Comparison of Auger yield *vs.* fluorescence yield as a function of atomic number.

The probability that one or the other relaxation mechanism will occur depends on the atomic number of the emitting element. Auger emission will dominate for lighter elements where electrons are less tightly bound to the nucleus, while the radiative transitions will be favoured for heavier elements, where the ionization probability for core electrons is significantly reduced. For K-level transitions of elements lighter than potassium ($Z < 15$) Auger effects will prevail; and the same is true for L- and M-level transitions with an approximate higher end cut off at tin ($Z < 50$). The low Auger electron yield for heavier elements causes the measuring of their Auger peaks to become difficult; conversely, AES is very sensitive to lighter elements. In XPS excited ions decay predominantly by Auger electron emission, since x-ray fluorescence is a minor process in this energy range (up to ~1500 eV).

2.9.3. Surface Sensitivity of AES

The energy of Auger electrons is typically 50 – 1500 eV, which translates to an IMFP of ~0.5 – 5 nm; making AES a highly surface sensitive technique. Figure 2.11 shows the interaction volumes of the different electrons with the surface. The size and shape of the primary excitation volume is a function of the energy of the primary electron beam and the sample material. The teardrop shape shown in the figure is typical of incident electrons with high energy and sample material with a low atomic number; for a low energy primary

electron beam and high atomic number sample materials the interaction volume will take on a spherical shape.

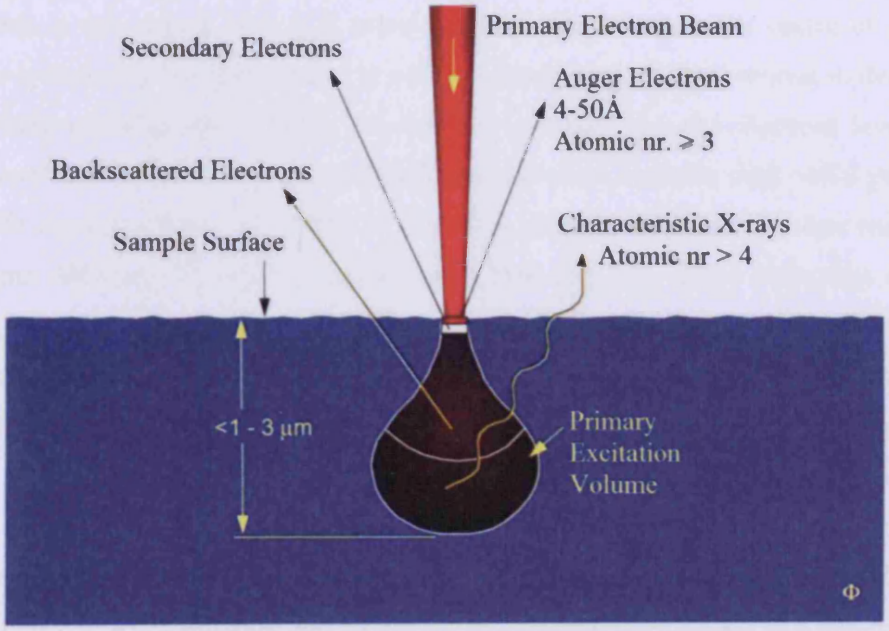

Figure 2.11 – The interaction between the incident electron beam and sample, showing the analysis volumes for Auger, secondary and backscattered electrons respectively.[24]

2.9.4. Experimental Considerations

A typical Auger spectrometer consists of an UHV system, an electron gun, scanning electronics for imaging, an energy analyser, and a computer for data storage and processing.

Any type of radiation (*e.g.* electrons, x-rays or ions) able to ionize the inner shells of atoms can be used to excite Auger electrons. The most convenient means, also used in this study, is an electron beam. Some advantages of using an electron beam is that the energy of the primary electrons does not need to be homogeneous, so no filtering is necessary; and that the beam can be focussed to very small diameters. The size of the sampling spot is determined by the emission current and beam energy. For a primary electron beam current of 100 μA and an energy of 3 kV a spot area of 1 mm^2 can be obtained. For beam currents of 10 kV the sampling area can be reduced to 0.1 μm^2.

Retarding Field Analyser (RFA)[23]

The design of LEED optics (shown in Figure 2.15) is also well suited for use as a RFA in AES, which is one reason why it is popular. The sample sits at the centre of a set of concentric spherical sector grids and as in a LEED experiment, the grid nearest to the sample is set at earth potential (the same as the sample) to ensure that the electrons leaving the sample travel in a field free space to the grids and therefore maintain their radial geometry. In a LEED experiment the next grids are set at a potential slightly less than that of the electron gun filament, as to act as a high pass filter and only allow elastically scattered electrons. In an AES experiment, however, the retarding grids are set at somewhat lower potential to allow all electrons having an energy greater than the energy corresponding to this potential to reach the fluorescence screen, which is now simply used as a current collector.

The electron current arriving at the collector is calculated as follows: If the electron energy distribution is $N(E)$, the retarding potential is set at V_0 (which corresponds to a minimum pass energy of $E_o = eV_0$) and the energy of the primary beam is E_p, the current is $\int_{E_0}^{E_P} N(E)dE$. If this current, which is a function of E_o, can be differentiated, the resulting signal is the desired energy distribution $N(E)$. This is achieved by modulating the retarding voltage, V. The difference between two currents arriving at the collector, one with retarding voltage V_o and the other with retarding voltage $V_o+\Delta V$ is $\int_{E_0}^{E_0+\Delta E} N(E)dE$. If $\Delta E = e\Delta V$ is small, the current is approximately equal to $N(E_0)\Delta E$, *i.e.* proportional to the required energy distribution. This type of modulation leads to a trade-off between signal and resolution; the resolution, ΔE, deteriorates linearly with ΔV, while the signal, $N(E)\Delta E$ increases by the same fraction. The conclusion only breaks down at high resolution (that is small ΔV) when the intrinsic limitations due to non-sphericity of the grids and field penetration between them limit the resolution to typically ~ 1eV (much better resolution is possible if the optics are designed specifically for this purpose).

The difficulty in the use of a high pass filter for a band pass application is the poor signal-to-background characteristic. The noise in the signal $N(E_0)\Delta E$ is given by $\sqrt{2\int_{E_0}^{E_P} N(E)dE}$, while a true band pass detector has a much smaller noise figure of $\sqrt{N(E)\Delta E}$. If E_0 is close to E_p these do not differ greatly and the signal-to-noise is good, but with E_o much less than E_p

the situation deteriorates significantly. Usually, the retarding potential, E_0, is modulated sinusoidally, *i.e.* the voltage $V_0 + \Delta V \sin \omega t$ is applied. It is easy to show by a Taylor series expansion that the current arriving at the collector can be expressed as a sum of harmonics, *i.e.* the d.c. term plus terms in $\sin \omega t$, $\sin 2\omega t$, etc. The d.c. current is $\int_{E_0}^{E_P} N(E)dE$ and the amplitude of the first harmonic (the term in $\sin \omega t$) is

$$A_1 = \Delta E\, N(E_0) + \frac{\Delta E^3}{8} N''(E_0) + \frac{\Delta E^5}{192} N''''(E_0) + \ldots \quad [2.9]$$

The second harmonic (sin 2ωt) has an amplitude

$$A_2 = \frac{\Delta E^2}{4} N'(E_0) + \frac{\Delta E^4}{48} N'''(E_0) + \frac{\Delta E^6}{1536} N'''''(E_0) + \ldots \quad [2.10]$$

With the primes indicating the order of derivative with respect to E. This sinusoidal modulation can be done by using a phase sensitive detector to detect the current, with frequency ω, at the collector. The current is proportional to $\Delta E\ N(E_0)$ to a first order. Provided that ΔE is kept to only a few eV, the higher-order terms can safely be neglected. It is common practice in AES to measure the amplitude in the second harmonic $\sin 2\omega t$ by using a phase sensitive detector which is referenced by a frequency doubled version of the grid modulation signal; the amplitude of this component is, to first order, proportional to the differential of the energy distribution, $N'(E)$. This is done because the structure of interest in $N(E)$ is often only a small signal on a large background. Differentiating removes the constant background and allows increased amplification (see Figure 2.12). A broad peak in particular is more readily seen in the differentiated spectrum because it is changed into a double peak, with each feature being narrower.

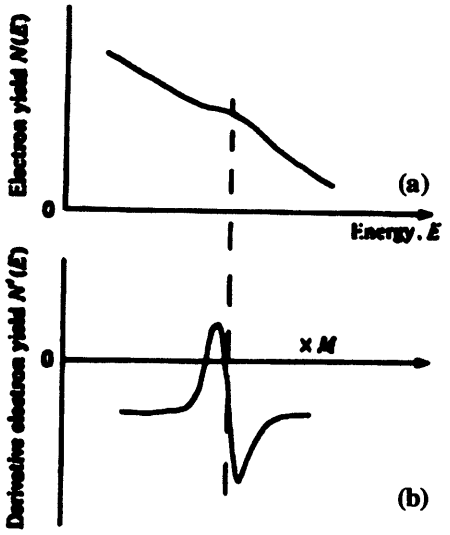

Figure 2.12 – Comparison between the normal current collection mode, $N(E)$, and the derivative mode $N'(E)$ in AES. A weak peak on a large background in normal mode is converted into a more visible double peak in derivative mode; $N'(E)$ is amplified by a large factor M.[31]

Other disadvantages of using a RFA are the significant heating effects as well as the fact that adsorbed layers may undergo electron beam stimulated desorption and dissociation. These effects are minimized by using a cylindrical mirror analyser (CMA). Signal to Noise ratios are also considerably better with a CMA.

2.9.5. Qualitative Analysis

Like in XPS, all atoms except hydrogen and helium can be detected with AES. Lithium is the lower limit for detection since the Auger process requires at least three electrons. A smooth flat surface improves the quality of the spectrum, but is not essential.

Auger peaks are assigned by three letters (adapted from X-ray notation) which specify the levels from which the core hole electron, down electron and Auger electron originate respectively. The example in Figure 2.6 would be labelled $K_1L_1L_3$, or simply KLL. If the down- and Auger-electron have originated from the valence band, the assignment KVV can be used. In general, the primary excitation shell shifts upward with atomic number: K for lithium, L for sodium, M for potassium, N for ytterbium. Heavier elements, with more energy levels, will have a greater number of possible Auger transitions. Transition probabilities determine whether certain transitions are observed as well as their relative intensities.

By convention the energy of a peak is defined as the minimum in the high energy wing of the differentiated peak. The energy of an Auger transition is difficult to calculate exactly since many electron effects and final-state energies need to be considered. However, small energy differences between final-state multiplets can be neglected for low resolution applications and elements can usually be identified with relative ease.

Kinetic Energy Measurement

The kinetic energy, E_k with which the Auger electron is emitted from the atom can, by first approximation, be determined by the equation

$$E_k = E_K - E_L - E_{L2,3} - \varphi \qquad [2.11]$$

Where E_X, $x = K; L; L_{2,3}$ is the energy of the respective electronic orbitals and φ is the work function of the analyser which is included when the electron energy is measured. As for XPS, more exact calculations of the Auger electron energies should also account for the Coulomb repulsion between the two holes in the final state, and the relaxation energies:[26]

$$E_k = E_K - E_L - E_{L2,3} - H - R_{in} - R_{ex} \qquad [2.12]$$

Where H is the interaction energy between the two holes in the final state; and R_{in} and R_{ex} are the intra-atomic and extra-atomic relaxation energies respectively which account for the contraction of the electron orbitals in the presence of the core hole. The kinetic energy of an Auger electron is unique to the emitting atom and independent of the energy of the incident radiation, which is why it can be used for chemical analysis.

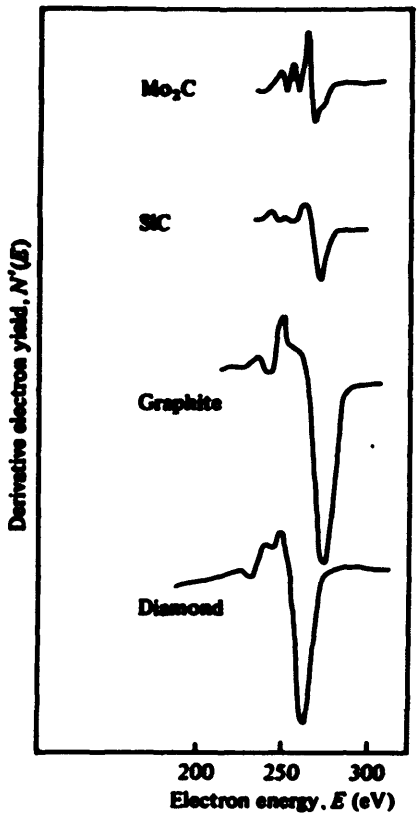

Figure 2.13 – Peak shape changes of the KLL energy transition of C in different chemical environments.[31]

Chemical Shifts and Peak Shape Changes

Energy shifts and line shapes in AES is much more complex than the one-electron core level process involved in XPS. All the complexities of true chemical shifts, inter-atomic and intra-atomic relaxation effects present in XPS also occur in AES, but the latter is further complicated by hole-hole interactions in the final state, a great multiplicity of lines and shape distortion in valence level related emissions due to weak selection rules.

Information about the chemical environment of the source ion can however be deduced by studying the energy position and shape of the Auger peak, since they may reflect the atomic energy levels that are involved, the loss structure and the valence band structure. In many cases chemically induced energy shifts in Auger peak positions (caused by intra- and extra-atomic relaxation effects) are greater than those of photoelectrons in XPS. Changes in the fine structure on the low kinetic energy side of major transitions might be dramatically different for metals compared to their oxides due to plasmon losses that are prominent in the metals, but absent in the oxides.

Line shape (and energy) changes are greatest for transitions involving valence band electrons, because the changes in the valence levels themselves are also reflected in the spectra (in addition to inter- and intra-atomic relaxation effects). Auger electron emission lines of good intensity usually involve at least one valence level and frequently two. To interpret changes in line shapes and energy values, the data obtained is usually compared with reference samples. The "fingerprint" spectra for the KLL (KVV) transition of carbon in different forms are shown in Figure 2.13.

2.9.6. Quantitative Analysis

Auger peak intensities are more difficult to predict than peak energy values, since several factors complicate quantitative analysis: Inelastic scattering and secondary ionization by backscattered electrons which affects the Auger current itself; the modulation voltage used for differentiation; and changes in peak shapes.

As with XPS the area under the Auger peak is proportional to the surface concentration. Moreover the peak-to-peak height in the differentiated spectrum is proportional to the area under the *N(E)-E* curve and can thus also be used to probe the surface concentration of an element.

The Auger electron yield is dependent on the electron-impact cross section and the fluorescence yield. The ionization cross section for excitation by electron impact is strongly dependent on the energy of the bound electron as well as the primary energy of the impinging electron beam. Since the fluorescence yield is greater than the Auger yield for heavier atoms, it is more difficult to measure Auger peaks of heavier elements. Equation 2.13 gives a full account of the different variables that influence the peak intensity:

$$I_x = I_P N_x \sigma_x \gamma_x (1+r) \lambda \cos\theta \, FTDR \qquad [2.13]$$

I_x = Auger intensity for the *ABC* transition of element X

I_P = Primary electron beam current

N_x = Number of atoms of element *X* per unit volume (total atom density × atomic concentration)

σ_x = Ionization cross section for the *A* level of element X

γ_x = Auger transition probability for the *ABC* transition of element X

r = Secondary ionization for the *A* level of element X by backscattered electrons

λ = Inelastic mean free path

θ = Angle between Auger electron and surface normal

F = Analyser solid angle of acceptance

T = Analyser transmission function

D = Detector efficiency

R = Surface roughness

Often all the variables required for this calculation are not known and measured yields are compared with external standards of known composition to calculate the surface concentration of a specific element. Ratios of the acquired data to standards can eliminate common terms, especially those related to experimental set up and the material analysed.

Another way to obtain an approximate compositional analysis is to use measured relative sensitivity factors from reference books. The mole fraction of a component A in a binary mixture of A and B is given by:

$$x_A = \frac{\left(\frac{I_A}{s_A}\right)}{\left(\frac{I_A}{s_A} + \frac{I_B}{s_B}\right)} \qquad [2.14]$$

Where I_x is the peak intensity and s_x the sensitivity factor of the relevant element. To calculate the absolute surface concentration, the peak can be related to a known concentration and the relationship should hold for coverages up to a monolayer.

2.10. Low Energy Electron Diffraction (LEED)[1, 23]

LEED is a very surface sensitive diffraction technique used to probe the periodicity (order) of a surface. In general, *diffraction* results from the interaction between the periodic oscillations of a wavefield and a periodic array of scattering centres. Electrons in the energy range ~20 – 200 eV are excellent probes of the surface structure because they possess de Broglie wavelengths of the same order of magnitude as the inter-atomic spacing between atoms/molecules at the surface, and will thus undergo diffraction if the atoms in the surface are arranged periodically (symmetrically). Furthermore electrons in this energy range have a IMFP of ~5 – 10 Å, which makes LEED very surface sensitive, since layers deeper than 3 or 4 atoms below the surface make virtually no contribution towards the detected signal.

The wavelength of electrons may be estimated from the de Broglie equation:

$$\lambda = \frac{h}{\sqrt{2mE}} \qquad [2.15]$$

Where λ is the wavelength of the electron, h is the plank constant, m is the electron mass and E is the electron energy. By substituting the constants, we get the expression for the electron wavelength:

$$\lambda(\text{Å}) = \sqrt{\frac{150.6}{E(eV)}} \qquad [2.16]$$

Yielding de Broglie wavelengths of 2.74 – 0.39 Å for kinetic energies of 20 – 1000 eV. LEED only measures elastically scattered electrons, so in essence all measured electrons have a kinetic energy of E_p, the kinetic energy of the primary beam.

The interaction between the scatter centres in the surface and the incident electrons is most conveniently described in reciprocal space. Figure 2.14 illustrates the scattering of electrons from a one-dimensional array of atoms. The scattering angle is θ_a and the lattice constant is a.

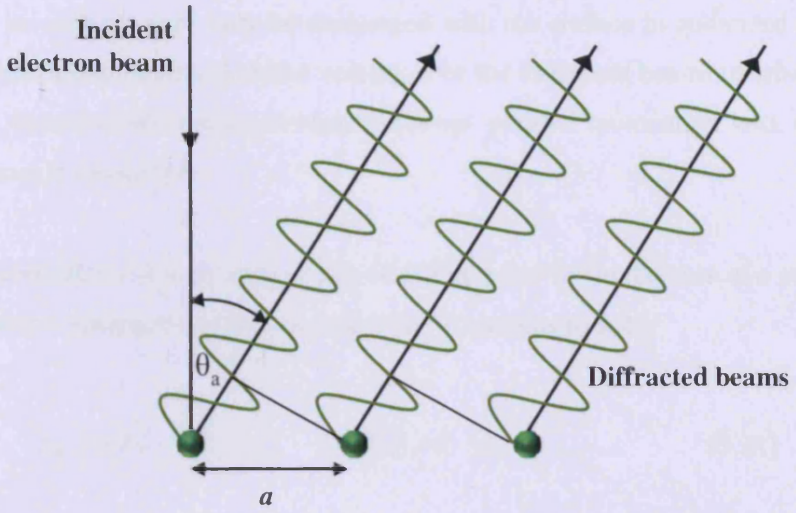

Figure 2.14 – Electron diffraction from a one-dimensional array of atoms.

For constructive interference between the scattered electron waves, the path length difference, Δ_a, must be equal to an integral number of wavelengths:

$$\Delta_a = n\lambda \quad (n = 0, \pm1, \pm2, \pm3, \ldots) \qquad [2.17]$$

Also, geometrically

$$\Delta_a = a \sin\theta_a \quad \text{or} \quad \sin\theta_a = \frac{n\lambda}{a} \qquad [2.18]$$

Equation 2.18 is a variation of the Bragg equation, $n\lambda = 2d \sin\theta_a$. For a one-dimensional array, the diffraction pattern consists of a set of parallel lines. The equation also indicates that the atom spacing is inversely related to the periodic spacing in the diffraction pattern. For fixed values of λ an increase in a leads to a decrease in $\sin\theta_a$ (and θ_a); *i.e.* the diffraction beams become more densely spaced. The wave vector of an electron is defined as

$$|\boldsymbol{k}_0| = \frac{2\pi}{\lambda} = \frac{2\pi}{h}(mv) \qquad [2.19]$$

Where mv is the momentum of the electron. By combining 2.18 and 2.19:

$$|\boldsymbol{k}_0| \sin\theta_a = \frac{2\pi}{a}(n) \qquad [2.20]$$

Which is the component of momentum parallel to the surface ($k_{//}$). Equation 2.20 specifies that parallel momentum may only be exchanged with the surface in quantized units of $2\pi/a$ (the magnitude of the reciprocal lattice vector). For the diffracted beams to arise (to undergo a change in direction) the electrons must exchange parallel momentum with the lattice so that momentum is conserved.

Introducing periodicity in a second, orthogonal dimension (as in the case of a surface) for an array with lattice constant b, leads to an equation analogous to 2.20:

$$|k_0| \sin\theta_a = \frac{2\pi}{b}(m) \qquad (m = 0, \pm1, \pm2, \pm3, \ldots) \qquad [2.21]$$

Both equations 2.20 and 2.21 need to be satisfied simultaneously for diffraction to be observed; *i.e.* diffraction is only allowed at the intersection of the one-dimensional reciprocal lattice rods generated in directions a and b respectively and the LEED pattern consists of a series of diffraction spots corresponding to the points of intersection. The exchange of parallel momentum is restricted to a two-dimensional reciprocal lattice vector **G**:

$$G = \Delta k_{//} = \frac{2\pi}{a}n + \frac{2\pi}{b}m \qquad [2.22]$$

Every real space lattice will generate an associated reciprocal lattice upon diffraction, and obey the following rules:

$$G = na^* + mb^*$$

$$|a^*| = \frac{2\pi}{|a|}; \qquad |b^*| = \frac{2\pi}{|b|}; \qquad a.b^* = a^*.b = 0 \qquad [2.23]$$

Where **G** is the reciprocal lattice vector; n, m are integers; a, b are the elementary vectors of the 2D surface unit; and a^*, b^* are the elementary vectors of the 2D surface unit. This means that for a large value of a (or b), a^* (or b^*) will be small and vice versa; that a is perpendicular to a^* and that that b is perpendicular to b^*.

The incoming primary beam is initially normal to the surface (*i.e.* it has no parallel component of momentum; $n = m = 0$) and is therefore not diffracted. On the other hand, the diffracted beams move towards the origin of the diffraction pattern with increasing beam

energy (and decreasing de Broglie wavelength), *i.e.* towards the (0,0). The diffraction beams are labelled according to the values of (*n*, *m*) that define their parallel momentum transfer. The intensities of the spots do not remain constant if the beam energy is varied; for each spot there are critical voltages which produce a maximum intensity, this can be ascribed to interference between the waves scattered by successive layers of atoms.[27]

Diffraction spot positions are thus indicative of the two-dimensional space lattice at the surface (the size and shape of the unit cell); which is used for evaluating the variation in unit cell size due to adsorption. Note that a LEED pattern itself cannot be used to distinguish between different adsorption sites; *e.g.* a $p(2\times2)$ structure of oxygen on Cu(100) can have the oxygen atoms adsorbed in the on-top, bridge or four-fold hollow sites.

On the other hand, the spot intensities are a function of the penetration depth of the electrons and the exact atomic coordinates within the unit cell; which makes it possible to determine the complete surface geometry, including bond lengths and angles.

Since the spacing in the reciprocal lattice is inversely proportional to the spacing in the real-space lattice, spots that are close together are associated with large surface unit cells and vice versa.

2.10.1. Experimental Setup and Operation

The experimental setup for LEED is shown in Figure 2.15. Note that the sample is grounded to prevent charging.

A monochromatic electron beam with variable primary energy E_p (0 – 1000eV) is generated by an electron gun which is incident on the grounded sample and as a result undergoes diffraction. The backscattered electrons travel towards a series of three or four concentric grids (mesh made from thin metal wire) in front of the fluorescent screen. Grid 1 (closest to the sample) is earthed to ensure that the electrons travel in a field free region and grids 2 and 3 are held at a negative potential ($-E_p+\Delta V$; $\Delta V = 0 - 10$V) to reject the inelastically scattered electrons (with $E_{kin} < E_p$) which otherwise contribute to bright, diffuse background on the screen; the potential can be adjusted to minimise the background. The screen (detector) itself is biased at a high positive voltage (~4 keV) to accelerate the electrons to a sufficient kinetic energy to cause light emission from the fluorescent coated glass. The diffracted

electrons give rise to a pattern consisting of bright spots on a dark background, which reflects the symmetry and crystalline order of the surface. The LEED pattern is captured by a video camera.

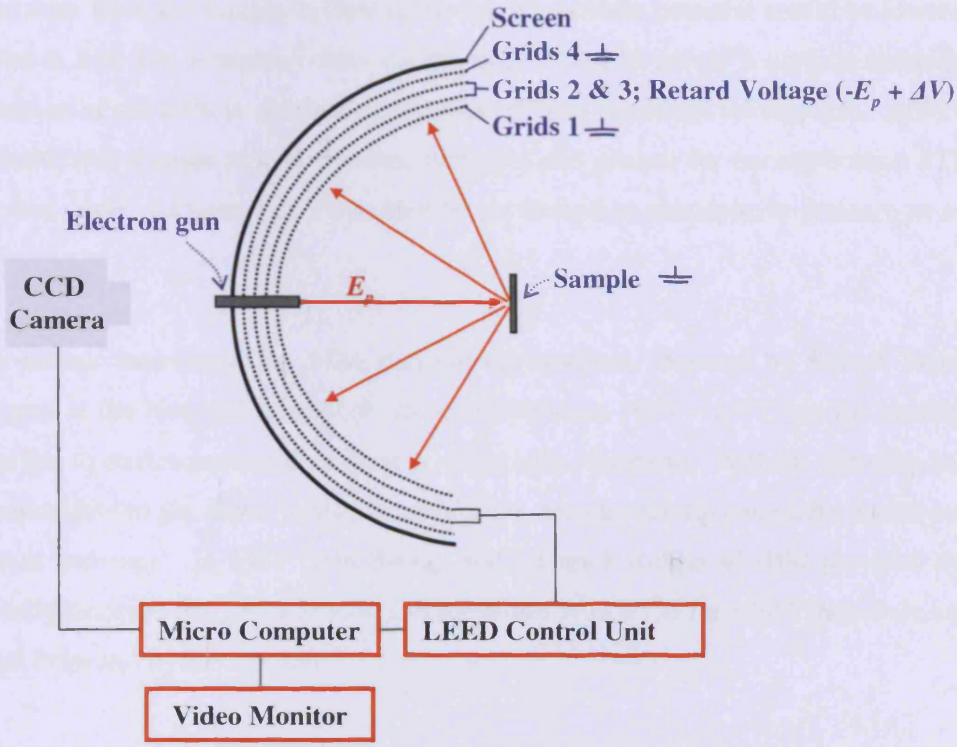

Figure 2.15 – Experimental set up for LEED.

2.11. Scanning Tunnelling Microscopy (STM)

2.11.1. General

The general principles on which STM is based is explained in the book of Attard and Barnes.[1] STM is a non-optical microscopy technique which is generally used to obtain atomically resolved images of electrically conducting (or semi-conducting) surfaces. In essence, STM allows one to visualize regions of high electron density and hence infer the position of individual atoms and molecules on the surface. The impressive resolution of the technique stems from the fact that the tunnelling current is a short range phenomenon (see section 2.11.2).

An atomically sharp electrical probe (brought within a few nanometers of the sample) is scanned across the surface to detect a weak electric current flowing between the tip and surface; this reveals the electron density distribution over the area and allows the surface to be "imaged". The tunnelling direction depends on the relative bias between the surface and tip. If the tip is biased positively relative to the sample, an energetic incentive is provided for electrons from the sample to flow to the tip, where their potential would be lowered (the opposite is true for a negative bias on the tip). STM is purely a surface technique (no information of the bulk is obtained) and provides only structural information. STM can be performed over a range of temperatures, pressures and phases; for our application STM was performed under vacuum, but it can also be performed at atmospheric pressure or even in liquid.

The precursor instrument for STM was the topografiner, invented by Russel Young and colleagues at the National Bureau of Standards between 1965 – 1971, but the machine was susceptible to environmental disturbances, especially vibrations. Without vibration isolation it is impossible to get down to atomic resolution, because the tip cannot be positioned with sufficient accuracy. In 1981 Gerd Binnig and Hienrick Rohrer of IBM provided the first atomically resolved images of silicon surface atoms with STM for which they were awarded a Nobel Prize in Physics in 1986.[28]

STM holds several advantages over other techniques in that it does not require laborious study of diffraction patterns or interpretation to obtain lattice structures; it is capable of higher resolution than AFM (Atomic Force Microscopy); images can be collected in times as short as 10 s, so it can be used to monitor kinetic reactions on the surface. The biggest disadvantage of the STM technique is the requirement that the surface needs to be a conductor or semi-conductor. STM cannot image insulators, because for tunnelling to happen, the electron needs an available energy state to tunnel into or out of and in insulators this is not available due to the band gap. To get around this problem, various other techniques have subsequently been invented since STM; AFM, for example, does not require a conducting surface.

2.11.2. Electron Tunnelling

In classical terms it is surprising that a current should flow across free space since electrons in the sample are bound within the solid and a minimum amount of energy, equal to the work

function of the sample, φ (typically a few eV) is required to dislocate them; at room temperature the average thermal energy available is a much smaller value; in the order of tens of meV. To resolve this problem, we turn to quantum mechanics. The wave function of an electron (a sine wave) can be obtained by solving the Schrödinger equation for a particle in a well. If the potential step at the edge of the well is infinite, the wave function drops to zero at the edge (*i.e.* the electron is bound in the solid and cannot escape from it). In a real metal, however, this barrier is finite and the wavefunction of the electron penetrates beyond the sample in such a way that the electron density gradually drops to zero a few nanometers outside of the surface. The same is true for the metallic tip, thus if the tip is brought within a few nanometers of the surface, the wave functions will overlap, creating a finite probability that the electron can tunnel from the sample to the tip where it will lower its energy. Figure 2.16 shows the process of electron tunnelling between the tip and sample.

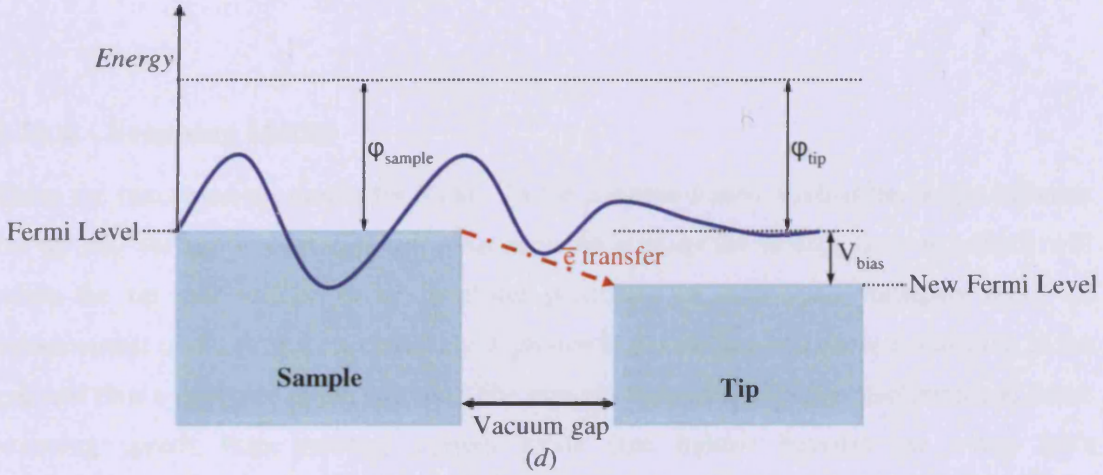

Figure 2.16 – Electron tunnelling from the sample to the tip.[1]

The steady flow of electrons between the sample and tip produces a small current with a magnitude exponentially dependent on the separation distance between tip and sample (a larger distance leading to a smaller current):

$$I(d) = C\exp(-d\sqrt{\varphi}) \qquad [2.24]$$

Where I is the tunnelling current, d is the distance between the sample and tip, φ is the work function of the sample and C is a constant. By measuring the magnitude of the current while moving it across the surface, a topographic image of the surface can be developed.

2.11.3. Manipulating Tip Movement[29]

The piezo-electric effect is used in STM to move the tip across and towards/away from the surface. The controller allows one to manipulate small movements with high precision. Piezo-electric transducers are crystalline materials containing structural units without point symmetry (tetrahedra). When a voltage is applied across the crystal, the charges inside move and cause a displacement of the atomic positions. All the equivalent structural units are orientated in parallel, leading to the contraction of the crystal along the bias and expansion perpendicular to it. In order for macroscopic polarisation to occur, piezo-materials need to be insulators. The most common piezo-ceramic used is $BaTiO_3$. Quartz was the first piezo-material used for commercial applications.

2.11.4. Scanning Modes

There are two scanning modes for STM: In the *constant height method* the height between the tip and surface is kept constant. An elevated area on the surface (*e.g.* an island) will cause the tip and surface to be in closer proximity of each other, bringing about an enhancement in the current. Conversely, a groove in the surface will cause a widening in the gap and thus a decrease in the current. The method can result in better resolution and faster scanning speeds than constant current mode (see below) because the z-axis isn't continuously adjusted, making it most suitable to detect fast changes (reactions) on the surface. The main disadvantage of the method is that an uneven or tilted surface can cause the tip to crash into it and be destroyed.

To avoid this, the *constant current method* can be used instead: the distance between the tip and sample is adjusted continuously to keep the tunnelling current at a constant level. This is accomplished with a third piezo-driven axis (in addition to the two scanning axes) and electronics with sufficiently fast response time to keep the tunnelling current constant. By measuring the height (which is directly related to the voltage applied to the piezo-element) one can model the surface structure under study. This method is thus better suited for relatively rough surfaces.

In practice the *Omicron* system has a variable feedback loop which allows one to use a combination of the two methods simultaneously. Depending on the *loop gain* value chosen, the type of scanning will be more characteristic of either the *z*-mode (constant current) or *I*-mode (constant height), producing superior quality images for one or the other. Since both types of images are saved during scanning, the best quality images can be selected afterwards during data processing.

2.11.5. Vibration Dampening[29]

For high-resolution scanning a high quality vibration decoupling system is essential. The SPM base plate is suspended by four soft springs protected by surrounding columns (see Figure 2.17).

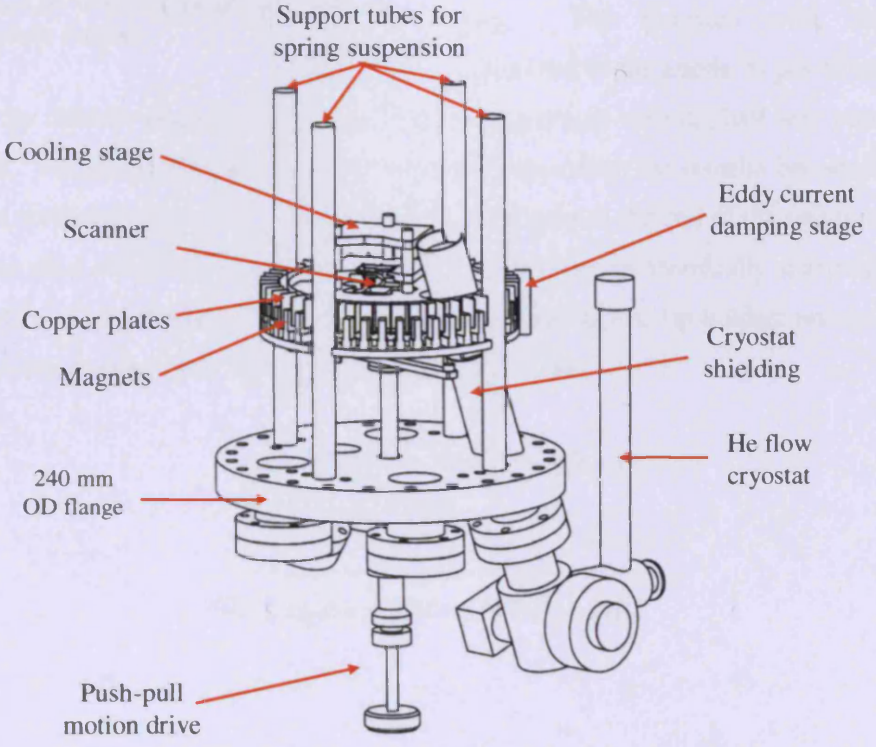

Figure 2.17 – The Omicron STM Instrument.[29]

Vibrations of the suspension system are intercepted by using a nearly non-periodic eddy current damping mechanism for which the base plate is surrounded by a ring of copper plates

which come down between permanent magnets. The spring suspension system can be blocked to allow tip/sample exchange etc. by using the push-pull motion feedthrough.

2.11.6. STM Tip Preparation[30]

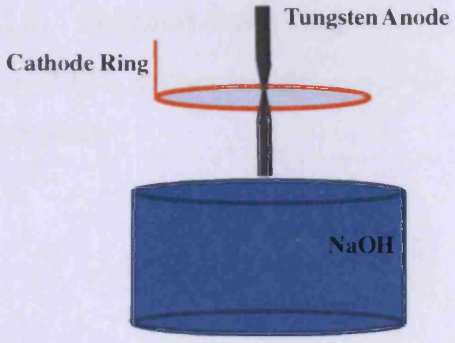

Figure 2.18 – STM tip preparation with the lamella method.

Tips are made by electrochemically etching tungsten wire (0.38 mm diameter) in a NaOH solution. For our purposes tips were prepared with the "Lamella" method (in contrast to etching in solution) illustrated in Figure 2.18. The cathode ring, which is connected to electronics set at a desired etching voltage, is dipped into the NaOH solution so that a lamella is formed in the ring. The tungsten wire, which is connected to the anode, is positioned in the middle of the cathode ring, in such a way that the ring aligns with the half way point of the wire length. As the etching proceeds, the wire in contact with the lamella becomes thinner and thinner, until the neck of the wire eventually can't support the end of the remaining wire, causing it to drop off (and the current to be cut off), leaving an atomically sharp tip at both ends. The tips are then washed with distilled water, clamped into tip holders and transferred into the vacuum system. The reactions at the electrodes are:

$$+ : \; W + 8OH^- \rightarrow WO_4^{2-} + H_2O + 6e^-$$

$$- : \; 6H^+ + 6e^- \rightarrow 3H_2$$

$$W + 2H_2O + 2\,OH^- \rightarrow WO_4^{2-} + 3H_2$$

2.12. The Molecular Beam Reactor[1, 31]

2.12.1. Introduction

Molecular beam reactors are used to investigate adsorption and surface reaction kinetics by measuring sticking probabilities; usually over a range of surface and/or gas temperatures and

surface coverages. A molecular beam is a collimated source of gas molecules of well-defined spatial distribution, particle flux and in certain cases energy distribution among the internal modes of freedom (translational, vibrational, rotational and electronic). Molecular beam reactors vary in complexity, thermal beams being the simplest and supersonic beams most complex. A thermal beam reactor was used for the purposes of this study.

2.12.2. Thermal Beam Reactors

Figure 2.19 is a schematic diagram of the thermal molecular beam reactor that was employed in this study.

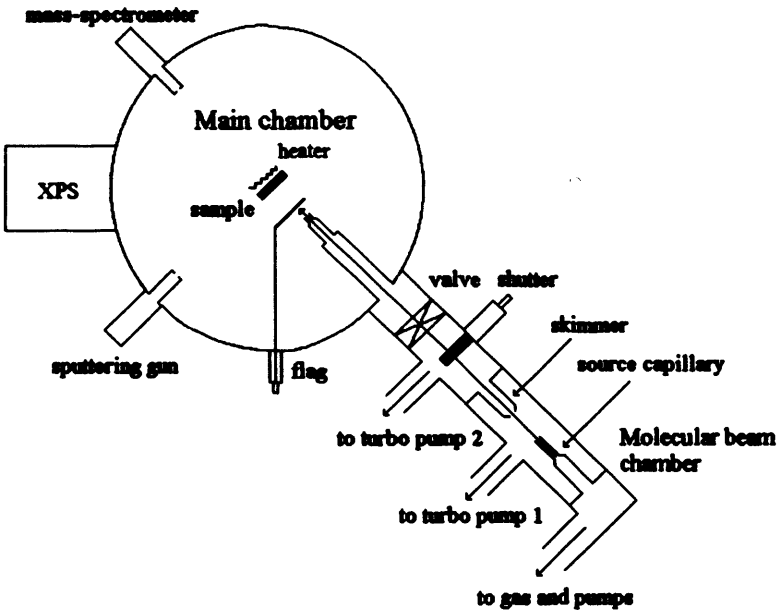

Figure 2.19 – Schematic diagram of the molecular beam reactor.

In this reactor the beam is formed by expansion of gas, typically at 0.1 atmospheres in the source chamber through a Pyrex capillary of diameter 0.1 mm. The molecules collide many times over with each other and with the capillary walls while passing through, which allows attainment of thermal equilibrium with the capillary (hence the name of the reactor). The gas may also be heated (through a wire around the source), to vary the mean kinetic energy of the gas particles. Along the gas source there are small chambers, each equipped with a vacuum pump for differential pumping of the gas that does not form a part of the beam, to ensure that UHV conditions are maintained in the main chamber. The first chamber contains

a *skimmer* (consisting of a small orifice) which is used to recollimate the beam, which expands in diameter as it moves further away from the capillary. The beam is again collimated as it enters the main chamber to produce a beam with a diameter of ~1mm and a flux of $10^{13} - 10^{14}$ molecules.cm^{-2}.s^{-1} (0.01 – 0.1 ML.s^{-1}). A *flag* is positioned directly in front of the sample to control gas impingement on the surface. Initially the flag blocks the gas beam during which time the initial pressure measurement is done. The flag is then removed, allowing the gas beam to hit the sample and adsorption to be measured. Upon hitting the sample, reflected particles are detected by the quadrupole mass spectrometer which is tuned to the charge-to-mass ratio of the gas in the beam and/or possible desorption products.

2.12.3. Supersonic Beams

As in the case of thermal beams, supersonic beam sources are formed by expansion of the gas through an orifice, but the source pressure is much higher (several atmospheres) and the orifice is much smaller (< 100 μm), which makes it possible to reach velocities faster than the local speed of sound. Due to the increased amount of incoming gas, much larger pumps are required, making the equipment more bulky and expensive than thermal beams.

Despite the high speed, the beams exhibit very cold temperatures. In fact, the considerable gas expansion causes the gas to cool to such a degree that the internal modes of vibrational/rotational/electronic freedom are frozen in their ground states, allowing the operator to control the exact quantum state of the molecules. It is possible to study highly activated adsorption processes which are not accessible to study with simpler thermal beams. The precise contributions to overcoming the activation energy barrier to dissociation may be resolved which leads to a molecular level understanding of the mechanisms involved in surface-catalysed reactions.

2.12.4. Sticking Probability Measurements with a Thermal Beam Reactor

Thermal molecular beams can be employed to measure the sticking probabilities for particular gas-substrate combinations of interest. The influence of the surface temperature, adsorbate coverage and the kinetic energy of the gas molecules may be determined. The

sticking probability at any particular adsorption time, *t*, may be calculated using the relationship

$$S(t) = \frac{P(f) - P(t)}{P(f) - P_0} \qquad [2.25]$$

Variables are defined in Figure 2.20. *P(t)* is the increase in partial pressure of the impinging gas over and above P_0, the initial pressure in the chamber and *P(f)* is the pressure when the surface is saturated with gas.

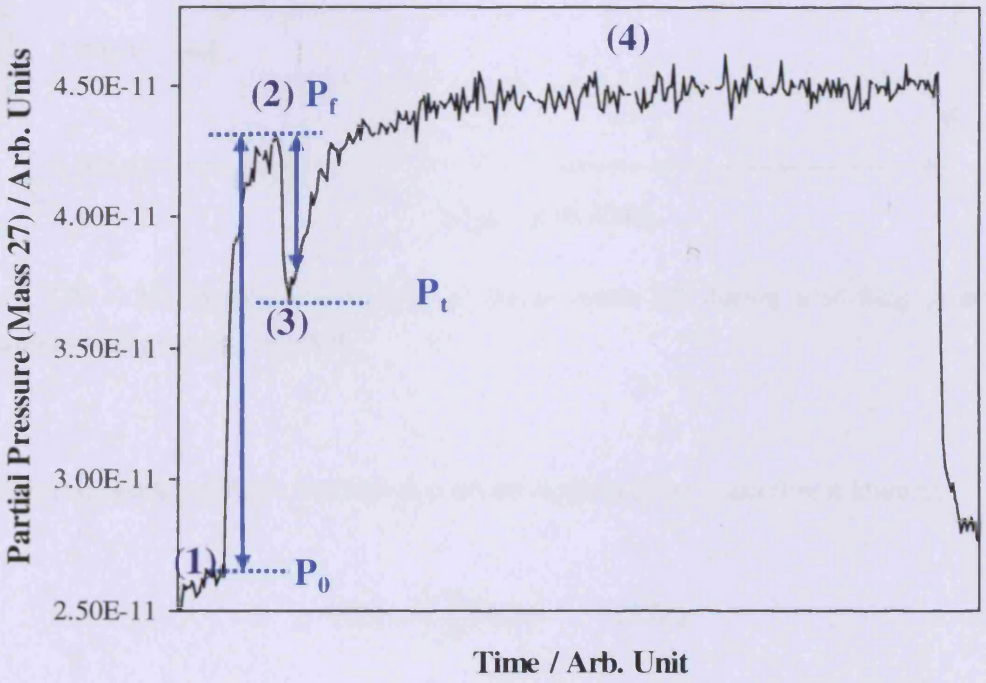

Figure 2.20 – MS signal measurement of ethene (mass 27) during a sticking probability measurement experiment at 373 K.

The numbers in Figure 2.20 correspond to the different stages of the experiment (Figure 2.19 shows the various components of the reactor): (*1*) Before the gas enters the chamber (cut off at the shutter); (*2*) The gas beam enters the chamber and hits the flag; (*3*) The gas beam hits the sample and is adsorbed; (*4*) The surface saturates and adsorption ceases. Instead of saturating, the surface can, given the right conditions, continue to adsorb gas as shown in Figure 2.21. In this case a *steady state sticking* measurement can be made.

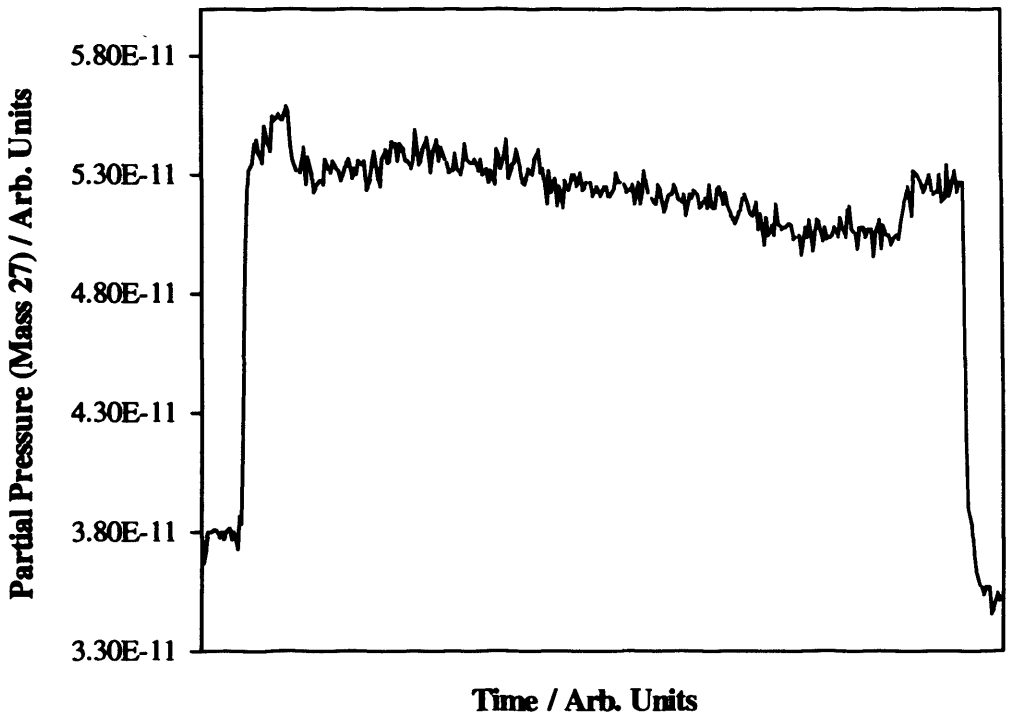

Figure 2.21 – MS signal measurement of ethene (mass 27) during a sticking probability measurement experiment at 723 K.

The corresponding surface coverage may be determined if the beam flux is known:

$$\theta(t) = F\int_0^t S(t)dt \qquad [2.26]$$

The data contained in the *P-t* plot obtained with the mass spectrometer may be converted to a sticking probability-coverage plot (as was shown in Figure 1.3) to give information about the adsorption mechanism (*e.g.* Langmuir *vs.* precursor type kinetics).

If a barrier for sticking exists, the sticking probability may be small, because the majority of the incoming molecules will not have enough energy to surmount the barrier. This barrier can be calculated if the sticking probability of the gas is measured at varied beam temperatures. As for the example shown in figure 1.4 the molecule needs to overcome the barrier E^a_{diss} before proceeding to a more thermodynamically favoured dissociated state (either directly or from a weak physisorbed state). The cross over point between the

physisorption and chemisorption wells represents a state in which the molecular bond is partially broken and the surface-atom bonds are partially formed. Transfer into the chemisorbed well is an activated process with the rate per collision given by the sticking probability for dissociative adsorption; it thus follows an Arrhenius-type response. The zero coverage sticking probability is

$$S_0 = S'\exp\left(\frac{-E^a_{diss}}{RT}\right) \qquad [2.27]$$

Or

$$\ln(S_0) = \ln(S') - \frac{E^a_{diss}}{R}\left(\frac{1}{T}\right) \qquad [2.28]$$

Where T is the absolute temperature of the incoming gas molecules and S' is the sticking probability in the absence of an energy barrier. By measuring S_0 for a range of temperatures and plotting $ln(S_0)$ against $1/T$ the activation energy can be calculated from the gradient.

Reactions involving two or more species can be studied by (*1*) pre-adsorbing a known coverage of reactant A on the surface and consecutively beaming reactant B on the surface or (*2*) using a mixed beam in which both reactants A and B are present, arrive at the surface simultaneously and are measured simultaneously by the quadrupole mass spectrometer.

2.13. Equipment

All experimental data was collected with one of three systems shown in Figure 2.22 – 2.27. Apart from the surface science techniques mentioned below, each system is also equipped for sputtering and annealing.

System A is a custom designed Multiprobe system supplied by *Omicron Vakuumphysik GmbH*. Figure 2.22 is a picture of the machine and diagrams are shown in Figure 2.23 and Figure 2.24. The system consists of different UHV chambers: The P-chamber is used primarily for surface preparation (cleaning and gas exposure). The A-chamber is used primarily for surface analysis and is equipped for XPS, ISS, LEED, UPS and EPR (electron paramagnetic resonance). Both chambers are also equipped with a quadrupolar Mass Spectrometer (from *MKS Instruments*) to monitor the gas composition. The STM-chamber is specifically suited for doing STM. Gate valves between the chambers allow isolation of each if required. The system is pumped by turbomolecular pumps (backed by rotary pumps), ion pumps and TSP's; a set for each chamber.

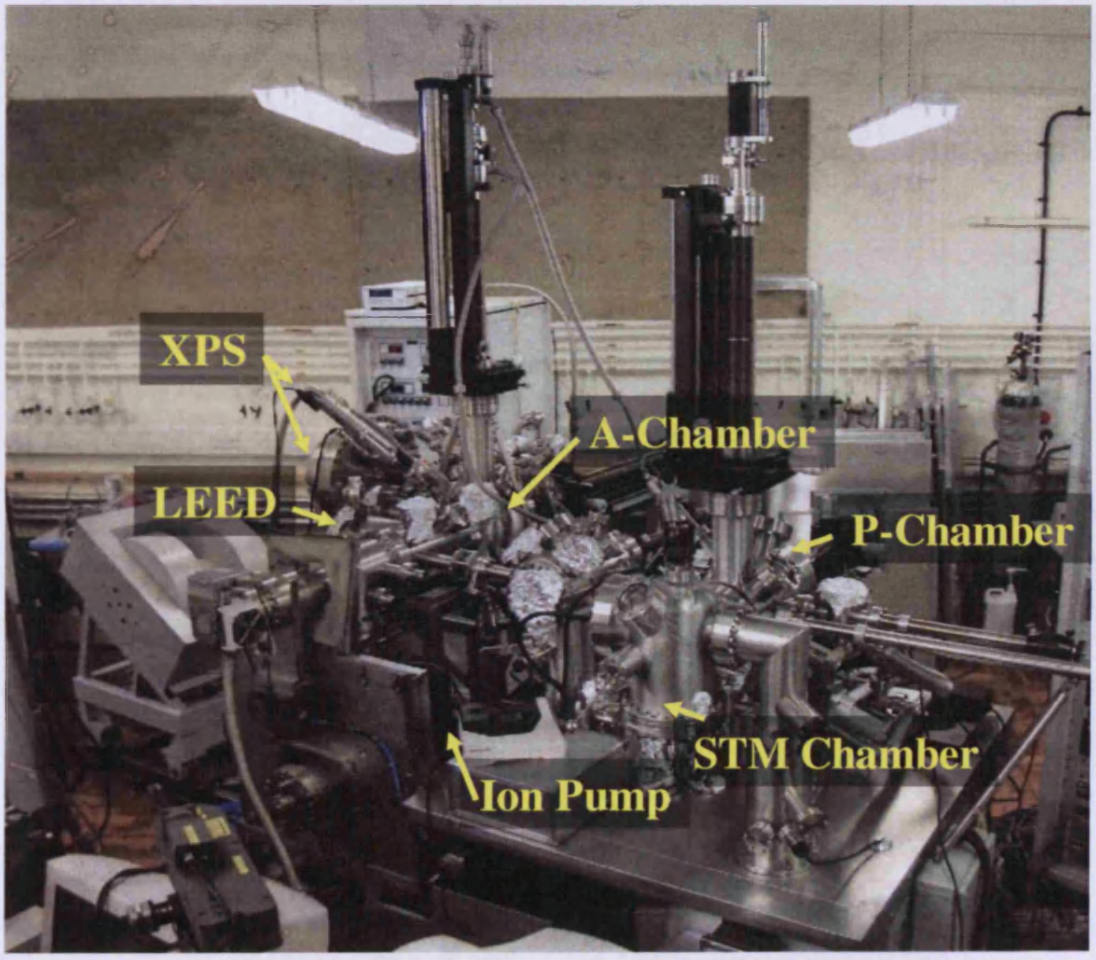

Figure 2.22 – System A facilitating STM, XPS and LEED.

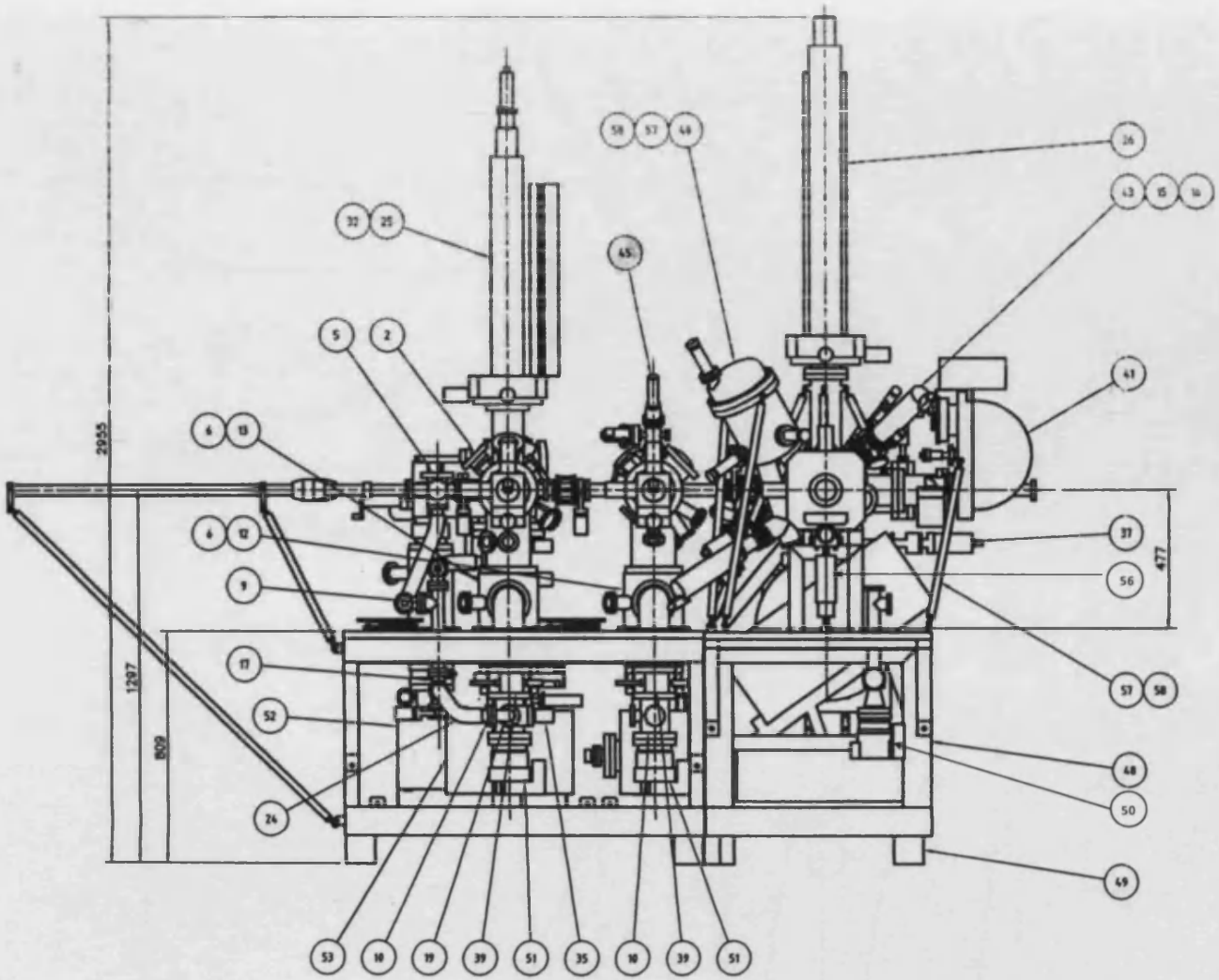

1. Analysis Chamber
2. Prep. Chamber
3. Central Chamber
4. STM Chamber
5. Fast Entry Lock
6,8-24. Connections
7. TSP Chamber
25,26. Manipulator Omniax
27, 28. Magn. transfer arm
29. Wobblestick
30, 31. Manipulators
32. Acceptance stage assy
33. Sample Heater Stage
34. All Metal Angle Valve
35-39. Gate Valves
40. Monochromator
41. Electrostatic Analyser 125
42. LEED Optics
43. X-Ray Source
44. UV Source
45. ISE 10
46. ISE 100
47. Evaporator
48. Bench Frame
49. Isolation Foot
50, 51. Turbo Pumps
52-54. Ion Pumps
55. Ion Pump Support Assy
56. Ominiax Support assy
57. Support Strut Set
58. Magprobe Retaining Brackt
59. Magprob Retainer
60. Bake Out Heater Assembly

Figure 2.23 – Side view diagram of System A; see Figure 2.20 for the top view.

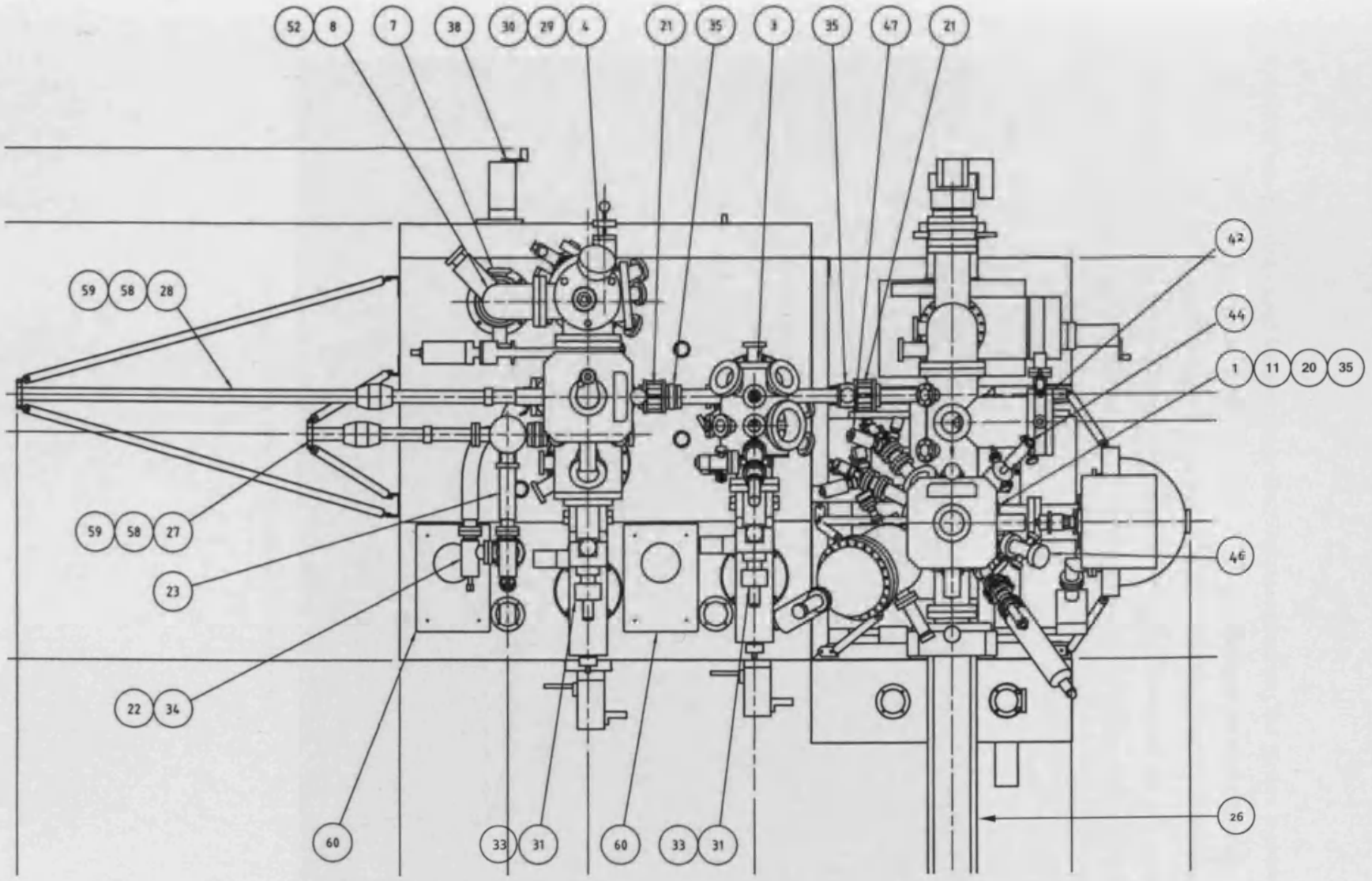

Figure 2.24 – Top view diagram of System A; see Figure 2.23 for description of parts.

System B was primarily used for sticking probability measurements; the picture is shown in Figure 2.25 and the diagram was shown in Figure 2.19. The machine consists of a molecular beam line and a main UHV chamber equipped with XPS (supplied by *PSP Vacuum Technology*) for surface analysis and a Quadrupole MS from *ThermoVG* for gas analysis. The sample is held in position and heated directly through two tungsten wires which pass through grooves in the edge of the crystal.

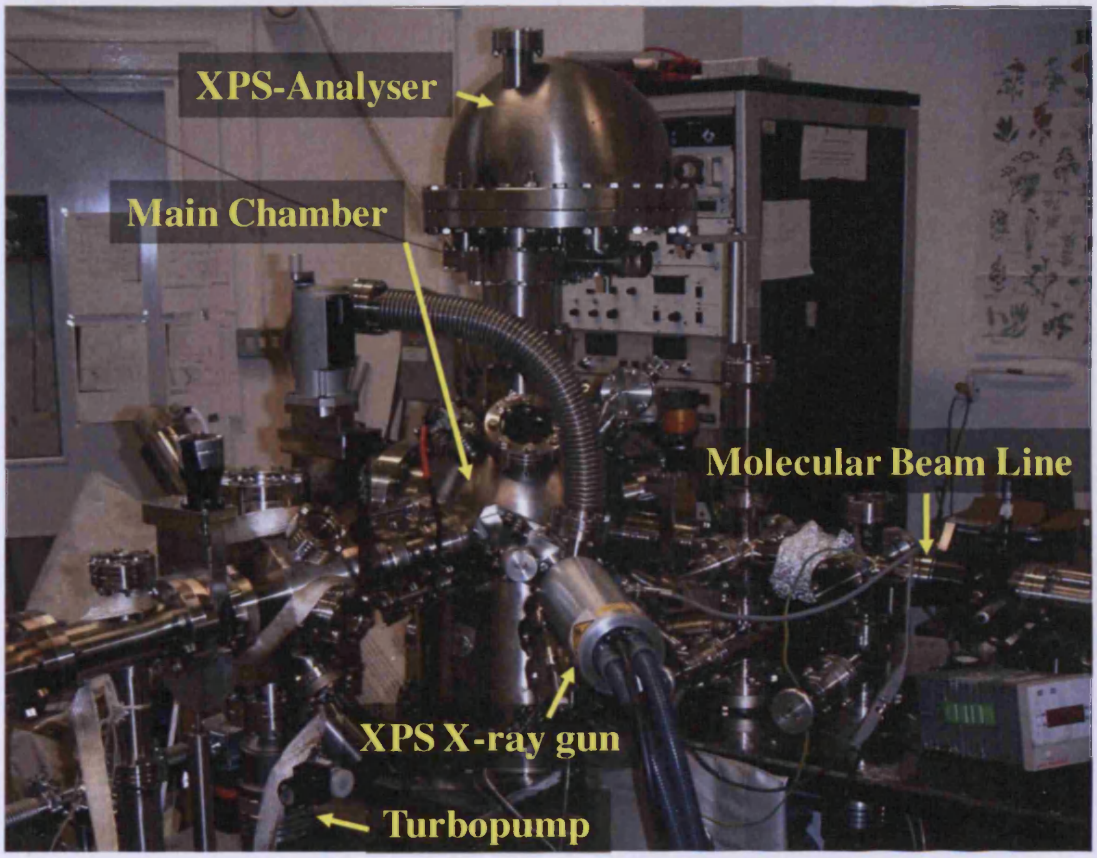

Figure 2.25 – System B: Molecular Beam Reactor.

System C is equipped for AES, LEED and TPD; Figure 2.26 is a picture of the equipment and Figure 2.27 is a schematic diagram. The small system is equipped with a LEED/AES system from *PSP Vacuum Technology* and a *Hiden* quadrupole MS used for TPD experiments and general gas analysis. The sample is heated by a heating box which is connected externally.

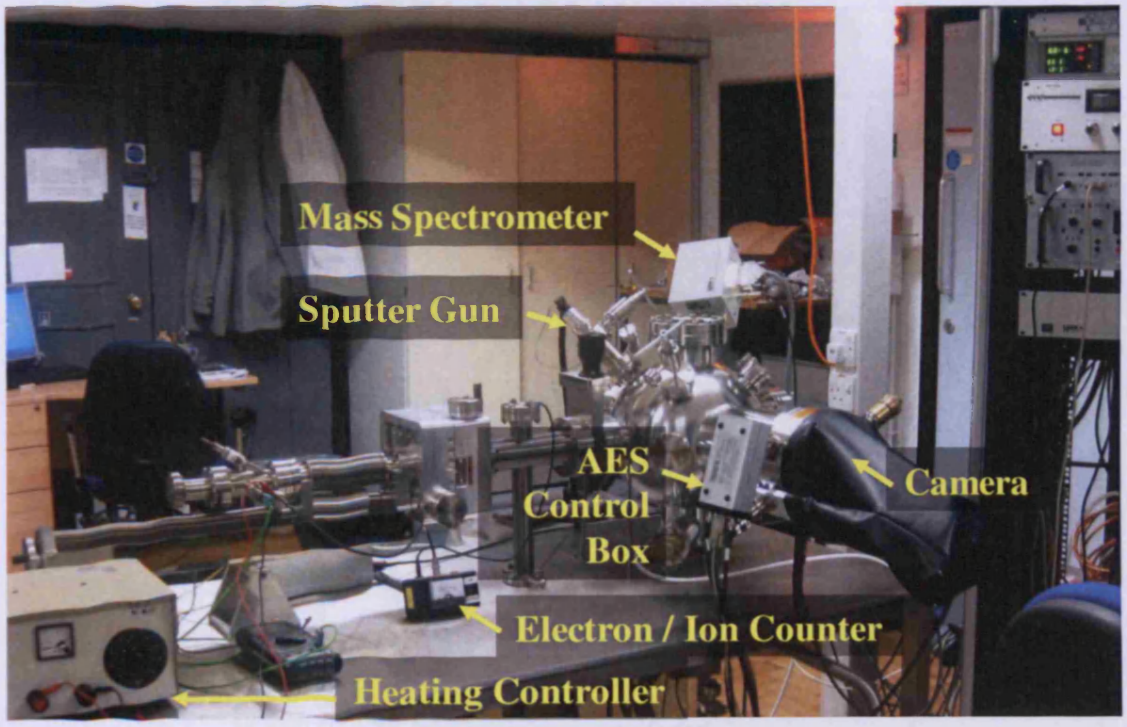

Figure 2.26 – System C equipped for AES and LEED.

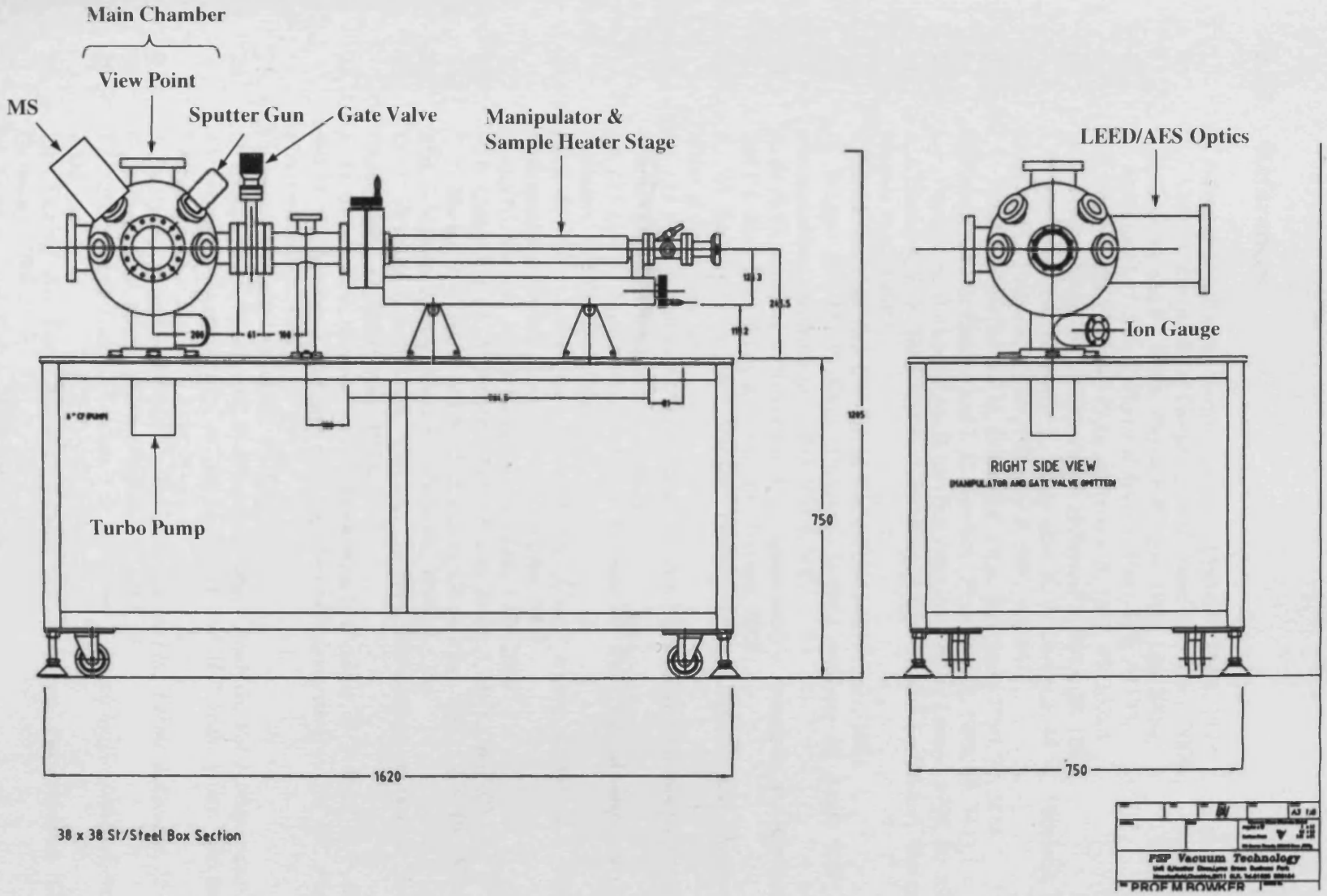

Figure 2.27 – Diagram of System C equipped for AES and LEED.

27. T. B. Rymer, *El*
28. G. Binnig and H
29. *VT SPM User'*
2002.
30. *Tip Etching K*
Germany, 1998.
31. M. Bowker, *App*

3.1.1. General Prin

Figure 3.1 shows the m
orbitals are shown on
molecular orbitals are
wavefunctions (+ or -) ar

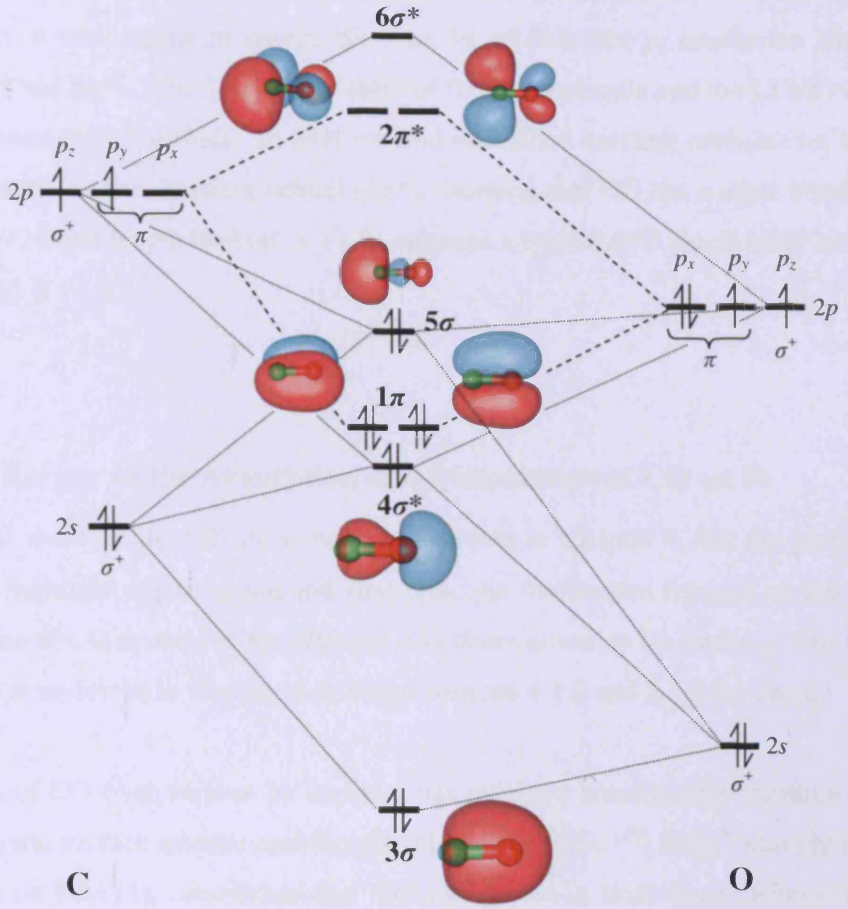

Figure 3.1 – Molecular orbital scheme of gas phase CO.[3]

CO has 10 valence electrons (4 from C and 6 from O) that fill the five lowest energy orbitals. The orbital with the lowest energy (at the bottom of the scheme) is the 3σ, which is formed by additive overlap of two *s* atomic orbitals from each atom. The anti-bonding $4\sigma^*$ orbital is formed by the subtractive overlap of the *s* atomic orbitals and is therefore higher in energy. The π orbitals lie above the σ orbitals and are formed from the atomic *p* orbitals. The p_x orbitals of C and O form the first 1π orbital (by additive mixing) and $2\pi^*$ orbitals (by subtractive mixing). Similarly the p_y orbitals form a second bonding (1π) and anti-bonding ($2\pi^*$) orbital at the same energy, but perpendicular to p_x. The p_z orbitals form the 5σ and $6\sigma^*$ molecular orbitals.

In CO the *s* and *p* orbitals are so close together that additional orbital mixing takes place: the *s* and p_z atomic orbitals contribute to all σ and σ^* orbitals respectively to form *sp* hybrids.

this frequency region, *a*
lowest CO coverages, c
when *c* also becomes
Bartosch and Whitman l
site, but also from the a_1

Several density function
bcc Fe surfaces are av

Fe(211),[14] Fe(310)[15] and Fe(710)[15] along with work on Fe carbides.[16,17,18] Early work, such as that of Mehandru,[19] used atomic clusters to represent Fe surfaces and studied the binding mode of CO on Fe(100), Fe(110) and Fe(111). Results on Fe(100) and Fe(110) were in agreement with experimental findings, but results on Fe(111) contradicted experimental studies in that it predicted that CO adsorbs in the order di-σ > OT > SH > DH.[4-6] More recently most investigators have turned to periodic DFT simulations using plane wave basis sets and the gradient corrected functional of Perdew, Becke and Ernzerhof (PBE)[20] or its revision (RPBE)[21] for the treatment of adsorbates on metal surfaces.

Sorescu *et.al.* studied the adsorption, diffusion and dissociation of CO on Fe(710) and Fe(310).[15] These two surfaces are likened to Fe(100) terraces separated by steps of atomic height. At low coverage the most stable site for CO on Fe(710) and Fe(310) is the tilted fourfold hollow at the top of the step $E_{ads\_Fe(710)}$ = -2.12 eV (PBE) and $E_{ads\_Fe(310)}$ = -2.09 eV (PBE); other configurations include bridged and end-on bonded modes. It was found that both the type of site and its position relative to the step edge affects the adsorption energy. The most favourable fourfold sites are highly tilted and exhibit frequencies as low as 1091 cm^{-1}.

The high indexed surfaces give low co-ordination Fe atoms and the above results suggest that these low co-ordination atoms enhance the adsorption of CO. However, since Fe is a bcc metal, Fe(111) (a low index surface) also presents low-coordination surface Fe sites. The particular surface is quite open with Fe atoms from three layers exposed at the surface as shown in Figure 3.2. This means that the top most atoms (Fe1, Figure 3.2*b*) have only four neighbours at the nearest neighbour distance (the three surrounding Fe2 atoms and the Fe4 atom directly beneath it) which is equivalent to a step edge atom on Fe(710).

Indeed the most stable site for CO adsorption on Fe(111), the SH, has reported adsorption energies of -2.45 eV (PBE),[7] -2.08 eV (RPBE)[9] and -2.09 eV, (RPBE)[15]. These values are even lower than those found for the high index stepped surfaces discussed above. The calculated adsorption energies for CO in the bridge like state (BL, tilting angle of 40°) are found to be slightly less favourable: E_{ads} = -2.35[7] / -1.94 eV (PBE),[15] -1.88 eV (RPBE).[9] Huo found the lowest energy pathway for CO dissociation to be BL to QP-C & QFFμ^3 with activation energy, E_a = 1.53 eV and reaction energy, E_r = -0.36 eV (RPBE).[9] Sorescu *et.al.* calculated a different pathway also from the BL site, with the C and O atoms ending up in two non-interacting QFF sites.[15] A barrier of 1.06 eV and a reaction energy of -0.28 eV was calculated.

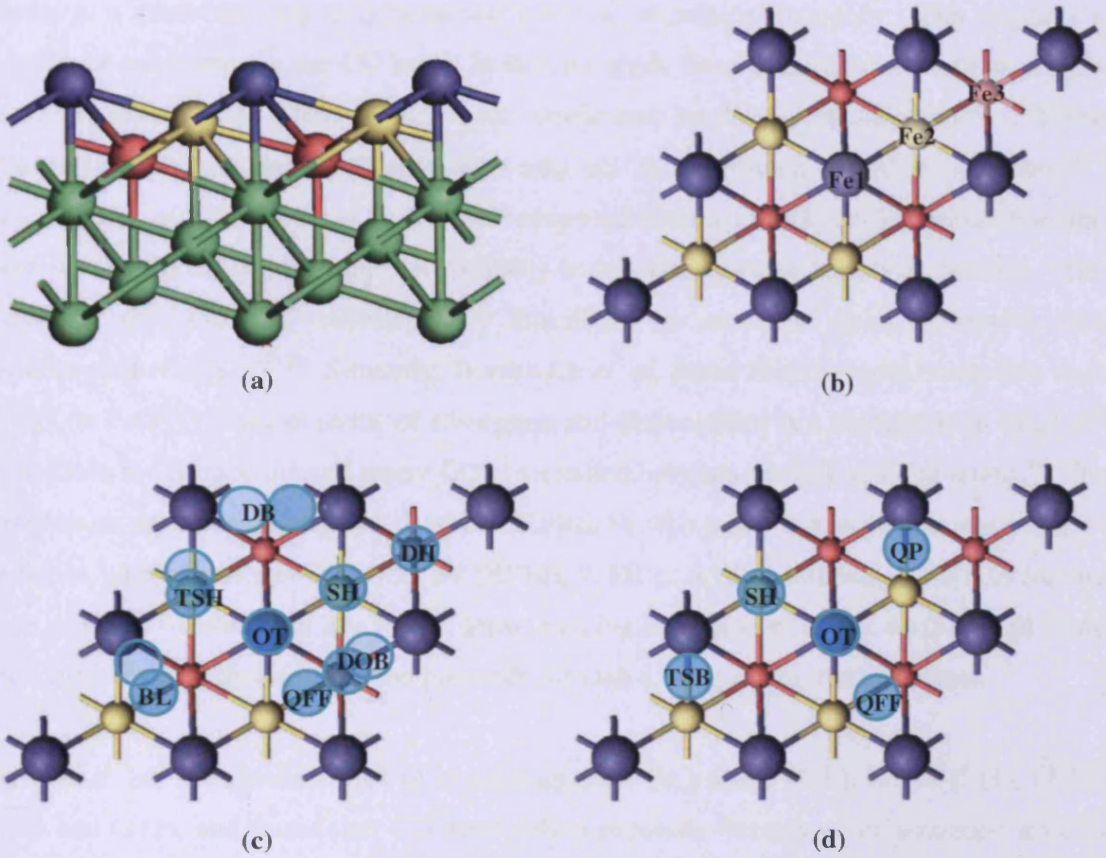

Figure 3.2 - Structure of Fe(111) and adsorption sites for molecular CO and atomic C/O *a*) **Side view of the Fe(111) simulation slab shaded to show the atoms of the different layers;** *b*) **Top view of Fe(111) 1st layer Fe1, large/purple, 2nd layer Fe2, medium/yellow and 3rd layer Fe3, small/pink.** *c*) **Adsorption sites of CO: DB – di-bridge, DH – deep hollow, TSH – tilted shallow hollow, SH – shallow hollow, OT – on top, BL – bridge like, DOB – deep hollow-on top bridge; lighter shaded circles represents oxygen in the cases where it is not directly above carbon.** *d*) **Adsorption sites for carbon or oxygen atomic species; SH and OT defined as for CO in** *c*, **QFF – quasi fourfold, QP – quasi plane, TSB – top-shallow bridge.**

Other low index surfaces are not as open as Fe(111) and correspondingly CO adsorption is found to occur with lower adsorption energies. The most favourable orientation on the close packed Fe(110) is the on-top position (E_{ads} = -1.88 eV, PBE[15]) while the most stable site on Fe(100) is the fourfold hollow with the CO axis tilted 51° away from the surface normal (E_{ads} = -2.12 eV (PBE)[15] / -2.54 eV, (PW91)[12] / -1.90 eV (RPBE)[11] at a ¼ ML coverage).

Similar conclusions ha
metal Ru. In this case
on the steps of the
Ru(0001) surface.[28]
intersection of (110) ar
step and facilitates C a

up. This particular adsorption site is often referred to as the B5 site since five surface atoms define the two atomic adsorption sites.

Sorescu *et. al.*[29] showed that C in the hollow or subsurface sites of Fe(100) increases stability of C/H/O atoms and CO/CH_x species adsorbed on the surface. It was also shown that dissociation of CO and H_2 are the rate determining steps in CH_4 formation. Jenkins[30] employed DFT calculations to study O, N and C induced surface reconstruction of Fe(211) and found that the surface will readily oxidise / nitridise, but carburisation is relatively retarded. Of the adatoms tested, charge transfer was least for C, which (like N) couples anti-ferromagnetically with the substrate; O on the other hand coupled ferromagnetically.

3.2. Method and Model

All calculations were performed in VASP (Vienna Ab Initio Simulation Package) version 4.6.28 which is based on the Density Functional Theory (DFT). The Kohn-Sham DFT equations were solved using a plane-wave basis set and periodic boundary conditions.[31,32] The gradient corrected functionals, PBE[20] and RPBE,[21] were used to calculate electron exchange and correlation energies as described below. The electron-ion interaction is described by Blöchl's PAW (projector augmented wave) method, which takes the exact shape of the valence wave functions into account and improves the description of magnetic transition metals considerably.[33] The use of gradient corrected density functionals and an all electron description of the metal cores are essential for an accurate description of magnetic properties of bcc Fe.[34] The Monkhorst-Pack scheme was used for *k*-point sampling.[35] The bulk bcc unit cell of Fe was optimized using an 8×8×8 *k*-point mesh with plane wave basis energy cut off of 400 eV.

Magnetism[36] arises from the spin of an electron, combined with its electric charge, which results in a magnetic dipole moment and creates a small magnetic field. Because of its unpaired d-electrons, Fe has a rich variety of magnetic states, of which three were considered here: non-magnetic (a calculation without spin polarisation); ferromagnetic and anti-ferromagnetic. Elements that contain atoms with partially filled orbitals, and therefore unpaired electrons, have the potential of being ferromagnetic. In ferromagnetic elements the spins of the unpaired electrons line up in parallel and their individual magnetic fields add together to create a measureable macroscopic field. In anti-ferromagnetic substances, neighbouring spins align in anti-parallel, to yield a zero net magnetic moment.

Figure 3.3 shows plots of the energy per atom calculated as a function of the cell volume (expressed as volume per atom) for each magnetic state. The methodology clearly identifies the ferromagnetic state as the ground state with an optimal cell volume (*i.e.* the curve minimum) much closer to the experimental value (indicated by the dotted line) than for either of the other two possibilities that were considered. A wider survey of magnetic ordering in the Fe bulk confirms that the ferromagnetic ground state is recovered by the spin polarised DFT methodology employed here.[37] The optimised bulk cell constant of 2.843 Å was extracted from a quadratic fit of the ferromagnetic data presented in Figure 3.3 and is in relatively good agreement with the experimental value of 2.86 Å[38] (see Table 3.1). This calculated cell constant was used to set the in plane cell dimensions of the slabs constructed for surface simulations.

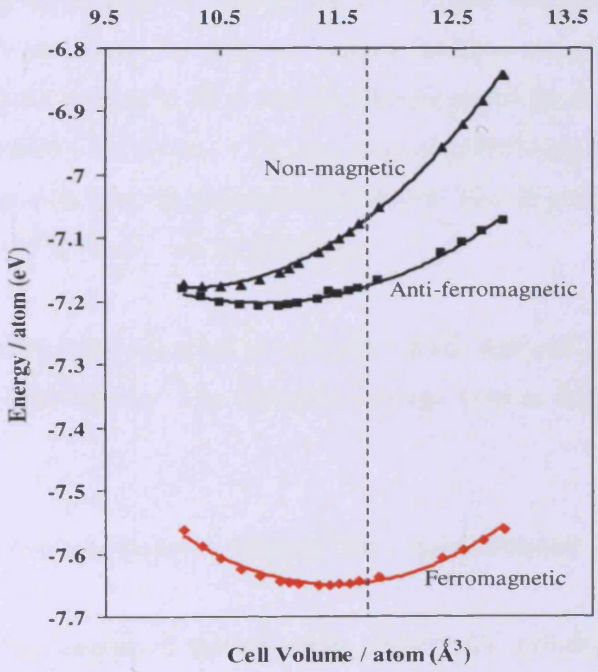

Figure 3.3 – Calculated bulk energy *vs.* volume per atom for different magnetic states of bcc Fe; the vertical dotted line indicates the experimental cell volume.

The RPBE functional (revised PBE), generally yields more reliable adsorption energies of atoms and molecules on transition metal surfaces and both PBE and RPBE perform better in this respect than the Perdew and Wang functional (PW91).[39] We therefore follow the procedure that the PBE functional is used to optimise the structure and then a single point RPBE calculation is performed so that quantities such as adsorption energies and C-O stretch

frequencies can be quoted with both PBE and RPBE functionals. The same method has successfully been applied by Jiang and Carter.[13]

Furthermore a frequency calculation was performed (with all atoms but CO constrained) to obtain a zero point energy (zpe) which was added to the adsorption energy to yield the final reported energy value.

A seven layer slab was used as a model for the Fe(111) surface. Increasing the number of layers to 8 caused a total energy change of only 0.04 eV. Fe atoms in the top three layers (as well as any adsorbates) were allowed to relax, while the bottom four Fe layers were constrained to simulate the bulk. For 1ML CO adsorption 1×1 unit cells were used, while all other calculations, which involved lower coverages, were performed using 2×2 unit cells. A 5×5×1 k-point mesh was used to optimise 1×1 unit cells and a 3×3×1 mesh to optimise 2×2 unit cells. Increasing the number of *k*-points for the 1×1 unit cell reduced the energy of the slab by only 0.009 eV per atom. To create an isolated surface a vacuum gap spacing of 10 Å was used. Increasing the spacing to 15 Å changed the energy of the slab by only 0.01 eV. The energy of an isolated C / O atom or CO gas was calculated by placing it in a 10 $Å^3$ box and performing a spin-polarized single-point calculation. The ^3P ground states of the atoms were considered, *i.e.* $2s^2 2p^2$ for C and $2s^2 2p^4$ for O.

Atoms and/or molecules were adsorbed on one side of the slab and a dipole correction was included for all slab calculations. The adsorption energy used in discussing surface species is defined as

$$E_{ads} = E(\text{Fe(111), adsorbates}) - (E(\text{Fe(111)}) + E(\text{adsorbates})) \qquad [3.1]$$

with E_{ads} the adsorption energy of the adsorbate, E(Fe(111), adsorbates) the energy of the slab with adsorbate (*i.e.* CO_{ads} / C_{ads} / O_{ads}), E(Fe(111)) the total energy of the clean slab and E(adsorbates) the energy of the free adsorbates in the gas phase. Each calculation is carried out using the same periodic box, with the same planewave cut off. Furthermore a frequency calculation was performed for both E(Fe(111), adsorbates) and E(adsorbates) (with all atoms but CO constrained) to obtain a zero point energy which was added to the adsorption energy to yield the final reported energy value. Table 3.1 contains the relevant bulk, surface and adsorbate parameters.

Table 3.1 – Structural and energy parameters of bcc Fe(111) and gas phase CO.

Bulk Parameters	This study	Litr (calc.)	Litr (exp.)
a (Å)	2.843		2.86[38]
Cohesive Energy (eV.atom^{-1})	4.81	4.88 (PBE) [40]	4.28 [36]
Bulk Magnetic Moment (μ_B)	2.19 (PBE) 2.22 (RPBE)	2.17 (FLAPW)[37a] 2.20 (LDA)[41b]	2.22 [36]
Bulk Modulus (GPa)	167	174 (PBE)[13]	168 [36]
Surface Parameters			
Surface Relaxation (%)		Ref [42] (GGSA)[c]	Ref [43]
$\Delta d_{12}/d_{12}$	-2.0	-6.3	-16.9 ± 3.0
$\Delta d_{23}/d_{23}$	-17.1	-16.9	-9.8 ± 0.3
$\Delta d_{34}/d_{34}$	12.4	12.0	4.2 ± 3.6
$\Delta d_{45}/d_{45}$	Constrained	Constrained	-2.2 ± 3.6
Surface Energy (J.m^{-2})	2.25 (RPBE)	2.54 (GGSA)[42c] 3.40 (FLAPW)[44b]	2.45 [45d]
Magnetic Moment (μ_B)	RPBE	Ref [46] (GGSA)[c]	
Fe1	2.884	2.82	---
Fe2	2.479	2.37	---
Fe3	2.560	2.54	---
Adsorbate Parameters		Ref [13] (PBE)	Ref [47]
CO_{gas} Bond Length (Å)	1.143	1.14	1.128
CO_{gas} E_{diss} (eV)	11.6	11.5	11.2
CO_{gas} ν_s (cm^{-1})	2115	2158	2143

Notes: *a)* Full potential linearized augmented-plane-wave total-energy method.
b) Local density approximation.
c) Generalized Gradient Spin Approximation.
d) For Polycrystalline Fe.

Transition state calculations were performed with the nudged elastic band (NEB) method which entails the generation of a number of configurations between the end points which are connected by springs and relaxed simultaneously. Figure 3.4 is an Energy *vs.* C-O bond length plot that illustrates the optimization. Because the images are constrained to be equally spaced, the true transition state can sometimes be located between the points and be missed. It was found that first round calculations were generally not accurate enough to yield the true

transition state, so to refine the search the process was repeated twice between points closer to the highest energy point along the pathway. The first NEB considers the whole dissociation pathway and eight structures along this route are identified; the C-O bond length changes by ~3 Å between the molecular and dissociated state. Figure 3.4 shows that the difference in bond length between some points on the red curve (especially *nr.* 3 & 4) are particularly large, which means that several structures in this region are initially not considered. The first refinement (the blue curve) spans less of the energy surface and so reduces the bond length gap between the three highest energy points from the initial calculation. The second refinement samples the energy surface near the maximum in even more detail, allowing accurate identification of the true transition state. Transition states were verified with frequency calculations which yielded a single imaginary frequency (all ground states only have real value frequencies). All geometry optimisations and NEB calculations were accepted as completed successfully once the calculated gradients fell below 10^{-3} eV.Å^{-1}.

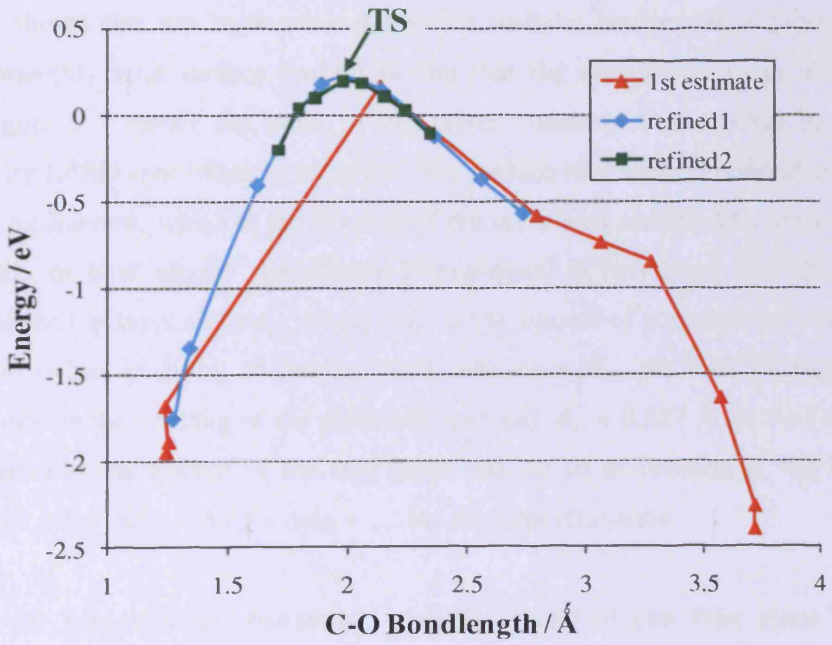

Figure 3.4 – Refinement of TS optimization for CO dissociation.

3.3. Results

3.3.1. Clean Iron

Surface Relaxation

Figure 3.2*a&b* show the simulation slab for Fe(111) from the side and from above. The coordination numbers of the surface atoms of Fe(111) are Fe1 = 4, Fe2 = 7, Fe3 = 7 & Fe4 = 8 (8 being equal to the bulk coordination). The structure is therefore much more open compared to Fe(100) for which Fe1 = 4 & Fe2 = 8 or Fe(110) for which Fe1 = 6 & Fe2 = 8. Because of the openness of its surface, Fe(111) is subject to considerable surface relaxation, particularly in the upper three layers.[43,44] Surface relaxation is the movement of the outer atomic layers of a crystal from their bulk positions due to the presence of the surface. All crystals exhibit some degree of surface relaxation in an attempt to stabilize low coordinated surface atoms. Surface relaxation should be distinguished from surface reconstruction, which changes the surface mesh dramatically; *i.e.* surface relaxation will preserve the periodicity defined by the bulk termination whereas reconstruction will not.

It has been shown that top layer relaxation of Fe surfaces (and metal surfaces in general) increases smoothly with surface roughness and that the relaxation can go several layers deep.[48] Figure 3.5 shows the trend in first layer contraction of several Fe crystals as determined by LEED spot intensity analysis. The surface roughness is defined as the inverse of the packing fraction, which is the fraction of the layer area occupied by atoms having the touching radii of bulk atoms. Relaxation is expressed in two ways: (1) The percentage relaxation of the top layer, $\Delta d_{12}/d_{12}$, where Δd_{12} is the amount of contraction (when negative) or expansion (when positive) of the top layer relative to d_{12}, the bulk interlayer spacing, which depends on the packing of the particular surface; d_{12} = 0.827 Å for Fe(111). (2) The total perpendicular movement of the first layer relative to its position in the bulk lattice, $\Delta d/d_{12}$, where $\Delta d = \Delta d_{12} + \Delta d_{23} + \Delta d_{34} + ...$, *i.e.* the total relaxation.

In addition to perpendicular relaxation, parallel relaxation can take place.[48] Parallel relaxation has been shown to shift first layer atoms toward more symmetric sites relative to the second layer so that the largest number of nearest neighbours in the second layer is obtained.

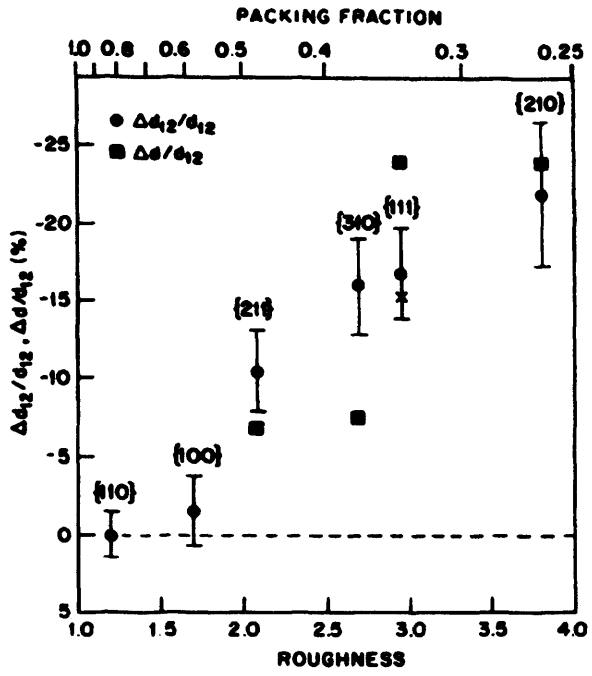

Figure 3.5 – Top-layer relaxation of Fe surfaces relative to the bulk spacing (0.827 Å) in % *vs.* surface roughness (which is the inverse of the packing fraction). • gives $\Delta d_{12}/d_{12}$ with the top three layers allowed to relax; × gives the same when only top layer relaxation is allowed; ■ gives $\Delta d/d_{12}$, the total relaxation of the top layer relative to the bulk spacing.[43]

Table 3.1 shows that the amount of relaxation of the first three layers calculated in this study. The values agree well with calculated values from literature and agree qualitatively with experimental results. The two topmost layers move toward the bulk and the third layer moves away from the slab centre. The openness of the surface (which leads to low coordination of the surface atoms) also affects the magnetic moment of the atoms in the surface layers which are all higher compared to bulk atoms by 0.26 – 0.66 μ_B (see Table 3.1).

Density of States

The density of states (DOS) plots for the top three layers of Fe(111) and bulk α-Fe are shown in Figure 3.6. The DOS of a system describes the number of states at each energy level that are available to be occupied. A high DOS at a specific energy level denotes that there are many states available for occupation, while a DOS of zero means that no states can be occupied at that energy level. The Fermi level is the highest occupied state in the valence band of the metal at 0 K, signifying that the states below the Fermi level are occupied, while those above it are empty. The Fermi level is indicated by the blue dotted line at zero energy in Figure 3.6.

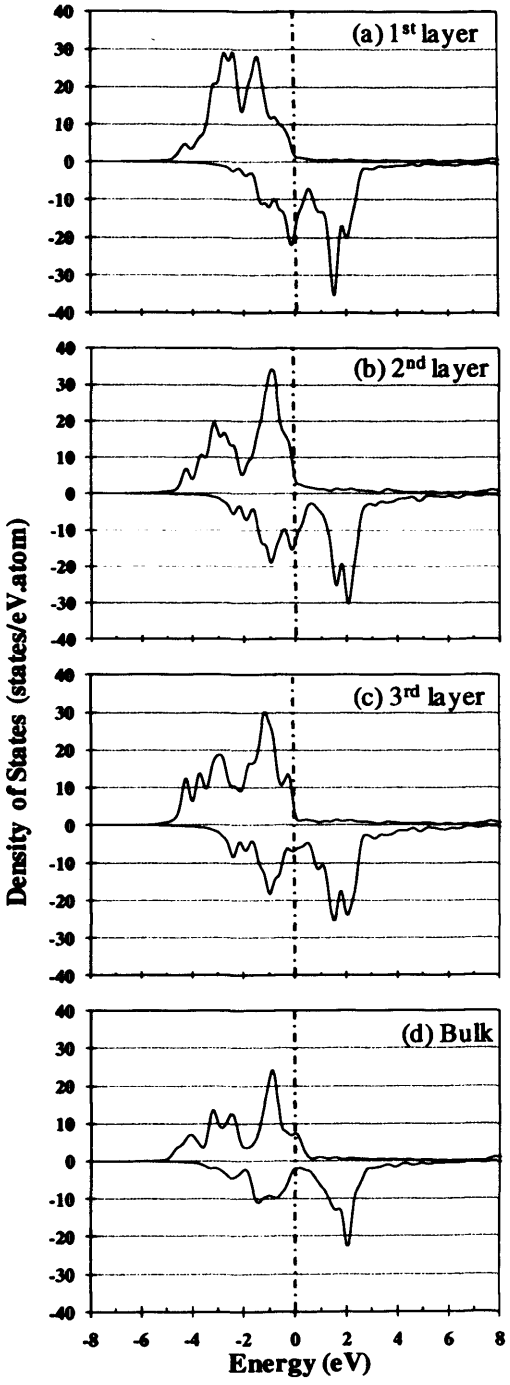

Figure 3.6 – *a* to *c*) DOS of the Fe(111) surface atoms, calculated from a 7 layer slab with a 15×15×1 k-point mesh. *d*) DOS of the bcc-Fe bulk, calculated with a 15×15×15 k-point mesh. The Fermi level is represented by the blue dotted line.

In each plot the majority up spin DOS is largely below the Fermi level while the minority down spin shows a large portion of unoccupied states, consistent with the ferromagnetic state of the material as was also seen in previous calculations.[41] The electronic distributions of the surface layers are clearly distinct from each other and from the bulk, due to the difference in coordination, which leads to relaxation and a change in the electronic distribution near the vacuum.

Some difference to take note of is the high (up spin) density at lower energy for the Fe1 atom (in the region of -2.5, -1.5 eV) which becomes progressively less pronounced for the layers lower down. The same can be said for the minority spin peaks around -0.2 & +1.5 eV. The filled energy states of Fe1 are positioned closer together compared to the other layers (roughly at -2.5, -1.5 eV *vs.* -3.5, -1.0 eV). The bulk atom possesses up spin states at the Fermi level and a few eV above zero, whereas these do not exist (or are very low) for the surface layers. As expected, the DOS of each surface layer resembles that of the bulk more closely in the order Fe1 < Fe2 < Fe3. These differences highlight the effects of the open surface structure of Fe(111); in the close packed Fe(110) surface atoms possess higher coordination, less relaxation occur and the DOS of the second layer already resembles that of the bulk closely.[41]

3.3.2. Adsorption of CO on Clean Fe(111)

Adsorption Energies and Geometries

CO adsorption was carried out at two coverages: ¼ ML and 1ML. Adsorption geometries are similar at the two coverages, although bond lengths and angles differ slightly. All of the structures at ¼ ML are shown together with their names and abbreviation in Figure 3.7 & 3.9. Adsorption energies, structural information and frequencies are summarized in Table 3.2 & 3.3 and compared with available values from the literature. The tables give PBE and RPBE data; in general the energetic ordering of the adsorbate sites is the same with either functional but the PBE data gives more favourable energies by between 0.3 and 0.5 eV. Zero-point energy (ZPE) corrections were calculated based on the vibrational frequency calculations discussed in the *Methodology* section and are added to the adsorption energy values; in general the ZPE-values changed the original value (shown in parentheses) by a maximum of 0.08 eV.

The frequency calculations verified that the SH, TSH, BL, DB and OT configurations (Figure 3.7*a-e*) are minima on the potential energy surface. The lowest energy binding site is the SH (Figure 3.7*a*), with the C atom of the molecule co-ordinated to a single second layer atom (Fe2) and the CO axis perpendicular to surface plane. Tilting the CO molecule in the SH site towards an Fe1 atom gives a second minimum only 0.11 eV (RPBE + ZPE) higher in energy. This tilted shallow hollow site (TSH, Figure 3.7*b*) has the CO axis inclined at an angle of 20° to the surface normal, placing the C atom 0.38 Å closer to the Fe1 atom than in the SH state. However, the CO bond length difference between TSH and SH is minimal and the vibrational frequency for the CO stretch in the two states differ by only ~20 cm^{-1}.

Adsorption of CO at the BL site gives an adsorption energy 0.21 eV (RPBE + ZPE) higher than the SH. Figure 3.7*c* shows that this structure has the C atom bridging two Fe1 atoms and close to a Fe2 atom which defines a SH site. In fact the BL adsorbate is only 0.1 Å further from the Fe2 atom than it would be in the SH position. However, the BL site also has a significant interaction between the oxygen atom of CO and one of the Fe1 atoms that is bridged by C ($d_{Fe1\text{-}C}$ = 2.139 Å *cf* $d_{Fe1\text{-}O}$ = 2.133 Å) and correspondingly the tilt angle away from the surface normal is significantly larger than for the TSH (40° *vs.* 20°).

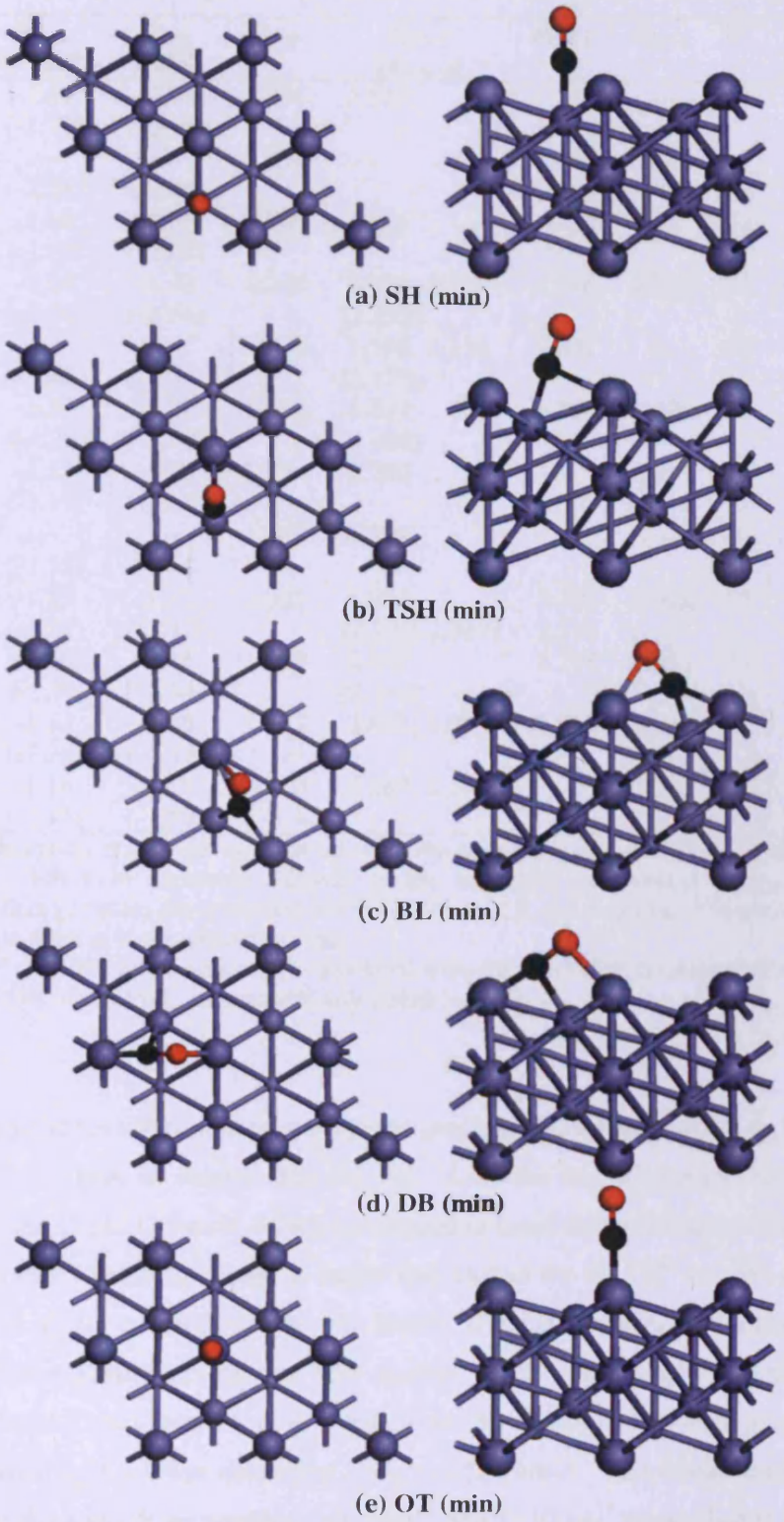

Figure 3.7 - Minimum (min) energy adsorption geometries for ¼ML-structures of CO on Fe(111) from above (left) and the side (right) in order of stability; *a*) SH (Shallow Hollow), *b*) TSH (Tilted Shallow Hollow), *c*) BL (Bridge Like), *d*) DB (Di-Bridge) & *e*) OT (On Top).

Table 3.2 – Adsorption energies, geometric data and stretch frequencies of ¼ ML of CO on Fe(111).[a]

¼ ML CO	E_{ads} (RPBE)	E_{ads} (PBE)	d_{C-O}	d_{Fe1-C} [d_{Fe1-O}]	d_{Fe2-C}	d_{Fe3-C}	θ^b	Freq[c] RPBE	Freq[c] PBE
SH (min)	-1.75 (-1.79)	-2.12 (-2.16)	1.201	2.523	1.750	---	---	1758	1764
SH[d]	--- (-2.08)	--- (-2.45)	1.191	---	1.749	---	---		
TSH (min)	-1.64 (-1.68)	-2.04 (-2.08)	1.204	2.145	1.754	---	20	1736	1740
BL (min)	-1.54 (-1.56)	-1.98 (-2.01)	1.244	2.036, 2.139 [2.133]	1.846	2.586	40	1467	1471
BL[d]	--- (-1.88)	--- (-2.35)	1.239	1.996, 2.134 [2.175]	1.841	---	40	---	---
DB (min)	-1.23 (-1.25)	-1.71 (-1.73)	1.255	1.812 [2.092]	2.053	2.693	57	1416	1422
OT (min)	-1.13 (-1.19)	-1.45 (-1.51)	1.174	1.772	---	---	---	1893	1900
OT[d]	--- (-1.35)	--- (-1.65)	1.167	1.791	---	---	---	---	---
DSB (ts)	-1.23 (-1.22)	-1.73 (-1.72)	1.327	1.963 [2.320, 2.337]	2.307 2.316	1.928	55	1096	1100
DOB (ts)	-1.20 (-1.19)	-1.65 (-1.64)	1.289	2.021 [2.116]	2.278	1.911	39	1232	1234
QFF (ts)	-1.17 (-1.18)	-1.65 (-1.67)	1.252	2.073, 2.093	1.969	2.017	4	1426	1429
DH (hsp)	-1.16 (-1.15)	-1.56 (-1.59)	1.230	2.367, 2.512	---	1.862	---	1523	1528

Notes: a) Adsorption states are in order of stability with minima listed first. Energy values are corrected for ZPE from harmonic analysis of the molecule; uncorrected values are shown in parentheses. Energy values are presented in eV, distances in Å and frequencies in cm^{-1}.
b) Tilting angle relative to the surface normal.
c) Both RPBE and PBE frequencies were calculated from the same PBE optimized structure.
d) Literature PBE[7] and RPBE[9] values were calculated at ⅓ ML.

We find an additional tilted state which has not previously been reported. The DB is 0.52 eV (RPBE + ZPE) higher in energy than the SH. Like the BL, it interacts with the surface through both the C and O atoms, which are placed in quasi threefold sites each consisting of Fe1, Fe2 and Fe3. The tilting angle is larger than that of the BL (57° *vs.* 40°) and as a result C and O are in closer contact with the Fe1 atoms. The DB could not be optimized at 1 ML coverage. The resulting structure is very similar to BL and is therefore called BL2 (see Table 3.3). In BL2 the C atom is positioned closer to Fe2 and further away from Fe3 than in BL1 which results in a lower frequency (υ_{1ML} = 1423 cm^{-1}). The frequencies for the C=O stretch in the BL and DB geometries (1467 cm^{-1} and 1416 cm^{-1} respectively) are also much lower than for the SH and TSH sites and the C=O bond is longer by 0.043 Å (BL) and 0.054 Å (DB) compared to the SH. This may suggest that the C=O molecule is activated for dissociation at these sites.

Table 3.3 – Adsorption energies, geometric data and stretch frequencies of 1 ML of CO on Fe(111).[a]

1ML CO	E_{ads} (RPBE)	E_{ads} (PBE)	d_{C-O}	d_{Fe1-C} [d_{Fe1-O}]	d_{Fe2-C}	d_{Fe3-C}	θ^b	Freq[c] (RPBE)	Freq[c] (PBE)
SH (min)	-1.63 (-1.68)	-2.00 (-2.05)	1.187	2.515	1.762	---	---	1807	1811
SH [d]	---	--- (-2.44)	1.187	---	1.761	---	---	---	---
BL1 (min)	-1.37 (-1.41)	-1.89 (-1.90)	1.244	1.981, 2.184 [2.095]	1.892	2.478	39	1500	
BL [d]	---	--- (-2.33)	1.221	2.111	1.824	2.128	---	---	---
BL2 (min)	--- (-1.43)	---	1.215	2.035, 2,173 [2.293]	1.846	2.617	30	1423	
OT (min)	-0.85 (-0.91)	-1.18 (-1.23)	1.164	1.784	---	---	---	1997	2003
OT [d]	---	-1.54	1.160	1.828	---	---	---	---	---
TSH (ts)	-1.53 (-1.61)	-2.04 (-2.08)	1.198	2.181	1.769	---	22	1783	1787
TSH [d,e]	---	--- (-2.41)	1.190	2.323	1.769	---	12	---	---
QFF (ts)	-0.94 (-1.10)	-1.56 (-1.57)	1.228	2.077, 2.098	1.923	2.139	10	1587	1590
μ^4 BR[d,f]	---	--- (-0.86)	1.240	2.072, 2.081	1.850	1.902	---	---	---
DH (ts)	-1.02 (-1.01)	-1.49 (-1.48)	1.227	2.338	---	1.852	---	1586	1589
DH[e]	---	--- (-1.79)	1.221	2.334	---	1.853	1	---	---
DOB (ts)	-0.99 (-0.99)	-1.65 (-1.64)	1.274	1.963 [2.163]	2.322	1.884	38	1326	1330
μ^3 BR[d,g]	---	--- (-1.22)	1.266	1.899	2.121	1.839	---	---	---

Notes: a) Adsorption states are given in order of stability with minima listed first. Energy values are presented in eV, distances in Å, frequencies in cm^{-1}. Values are corrected for ZPE from harmonic analysis of the molecule; uncorrected values are given in parentheses.
b) Tilting angle relative to the surface normal.
c) Both RPBE and PBE frequencies were calculated from the same PBE optimized structure.
d) Literature PBE values calculated at 1 ML.[7]
e) Named Bridge in ref. 7.
f) Fourfold bridge. Total adsorption energy at 2ML; adsorbed together with the μ^2-bridge state.
g) Threefold bridge. Total adsorption energy at 2ML; adsorbed together with the tilted OT state.

The fifth minima found for CO on Fe(111) is the OT site (Figure 3.7*e*). This structure has the C atom of the molecule coordinated to a single Fe1 atom with the molecular axis perpendicular to the surface plane. It lies 0.62 eV (RPBE + ZPE) higher in energy than the SH site. This OT structure has the shortest calculated CO bond length (1.174 Å) and highest calculated frequency (1900 cm^{-1}, PBE) of the minima identified, which is close to the corresponding values of the gas phase molecule ($bl_{CO\ gas}$ = 1.143 Å; C=O $\upsilon_{CO\ gas}$ = 2115 cm^{-1}, PBE).

Density of States

The PDOS of gas phase CO molecule is shown in Figure 3.8*a*. The plot gives similar information than the MO diagram (Figure 3.1) in that the molecular orbitals are arranged as a function of energy; the peaks in Figure 3.8*a* are labelled according to the orbitals that they correspond to. The filled orbitals shown in the MO diagram correspond to the states left of the Fermi level (which is represented by the dotted line at zero energy), while unoccupied orbitals correspond to states on the right. The contributions from the *s* and *p* orbitals in Figure 3.8*a* are coloured in orange and blue respectively to distinguish them from each other. Adsorption of CO in the different sites leads to three distinct PDOS plots, mainly dependent on the inclination angle of the C-O axis relative to the surface normal. The upright molecules (SH and OT; tilting angle θ = 0°) and TSH (θ = 20°) are represented by Figure 3.8*b*, while the PDOS of BL (θ = 40°) and DB (θ = 57°) are shown in Figure 3.8*c*&*d* respectively. Compared to the gas phase molecule the orbitals of the adsorbed species are shifted to the left, indicating that interaction with the surface leads to increased stabilization. Especially the 5σ and 2π* orbitals (labelled in Figure 3.8*a*) are broadened compared to that of the gas phase, due to the partial charge transfer that takes place. This is in agreement with the conventional model for CO bonding: the 5σ (HOMO) orbital of CO donates electrons to the d_z^2 and 4*s* orbitals of the metal, while the empty 2π* orbital (LUMO) overlaps with the d_{xy} and d_{yz} orbitals of the metal to accept electrons through back donation. In the tilted states the 1π orbitals are also involved

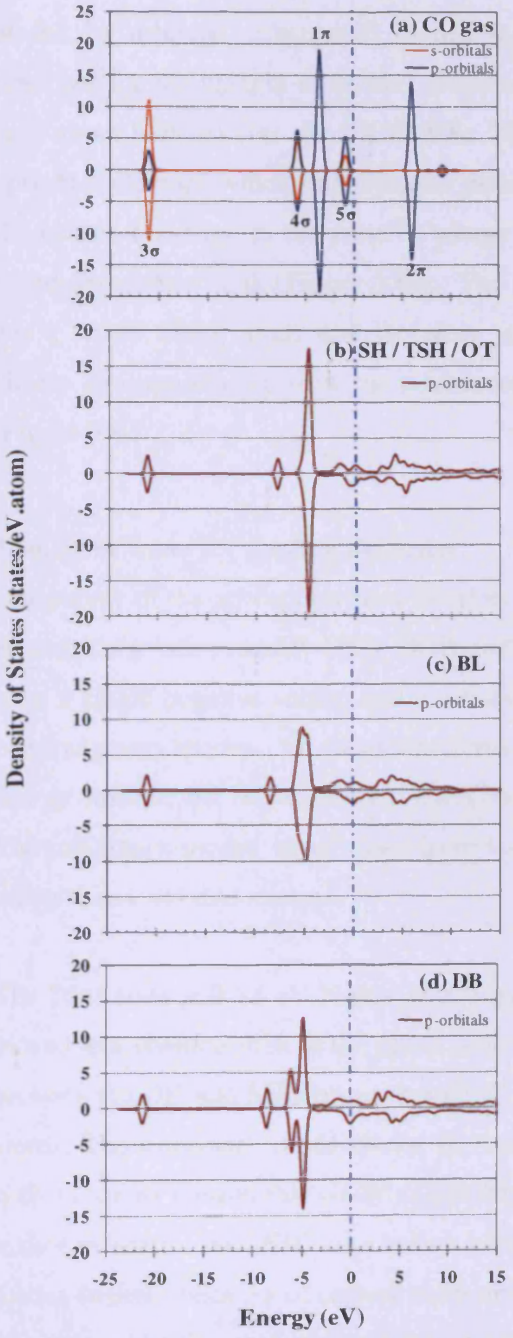

Figure 3.8 – PDOS of *a*) gas phase CO; contributions from s- & p-orbitals plotted separately and *b* – *d*) adsorbed CO; s- & p-contributions plotted together. The Fermi level is represented by the blue dotted line.

in donating electrons to the surface. The PDOS of the OT 1π orbitals are filled to a higher level than the SH and TSH, in accordance with the shorter C-O bond length (weaker interaction) of OT, which is closer to the bond length of the gas phase molecule.

The main difference between the PDOS of the different adsorption states is the appearance of the 1π orbitals. Compared to the gas phase molecule, no noteworthy difference is observed for the upright molecules (Figure 3.8*b*). For BL, however, 1π are broadened and only about half the size the SH PDOS. Whereas the two 1π orbitals are degenerate in the upright molecules which only interact through C, the additional interaction of O with Fe in BL causes a change in the relative energy levels of the 1π orbitals which translates into a broad unresolved peak (Figure 3.8*c*). The effect is even greater in DB (Figure 3.8*d*), which has a larger tilting angle and therefore stronger Fe...O interaction. Two peaks are now clearly distinguishable, with the additional peak being smaller and lying at lower energy (Figure 3.8*d*).

Transition States for Surface Diffusion

Our survey of the adsorption sites listed in Table 3.2 & 3.3 also identified a number of sites as transition states, namely DSB, DOB and QFF (Figure 3.9*a-c*) since frequency calculations gave a single negative mode; and a second order saddle point, the DH (Figure 3.10*d*) with two imaginary modes. Of these structures the DH is also the highest point on the potential energy surface, but the adsorption energies are all within a narrow range (-1.15 – 1.22 eV). The imaginary modes in all cases have to do with molecular migration across the surface rather than C=O dissociation.

The DSB state is 0.52 eV higher in energy than the SH. On optimisation the molecule has moved to a position that, in the plane view of Figure 3.9*a*, places it above a bridged position between the DH and SH sites so that the C atom is equidistance from two remaining SH Fe2 atoms. The imaginary mode shows the molecule moving between these two SH positions with a rocking motion that would create BL adsorption geometries. The DOB state (0.55 eV higher in energy than SH) also has an imaginary mode that switches between two BL-type modes (mainly because of carbon atom movement). The first mode is similar to the formal BL state, while the oxygen atom of the second is tilted perpendicularly relative to the first.

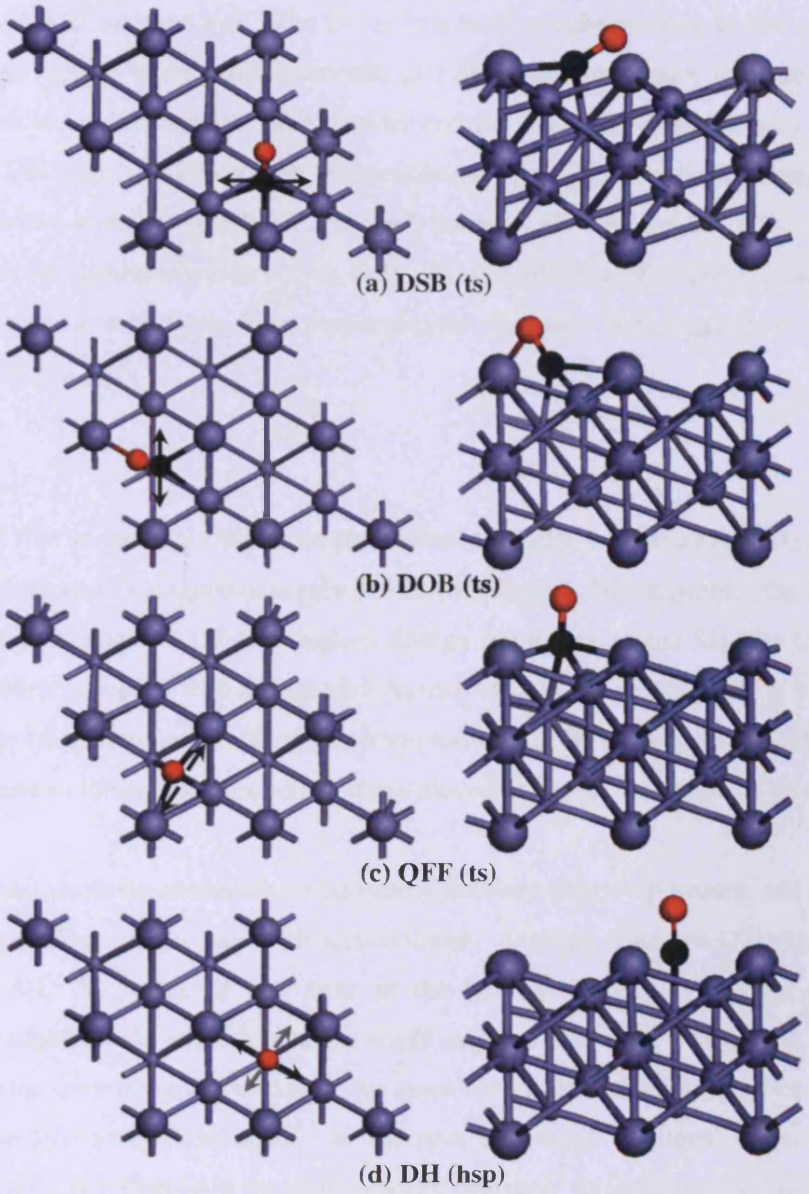

Figure 3.9 – Transition state geometries for molecular displacement found for ¼ML-structures of CO on Fe(111) from above (left) and the side (right) in order of stability; *a*) DSB (Deep Hollow – Shallow Hollow Bridge); *b*) DOB (Deep Hollow – On Top Bridge); *c*) QFF (Quasi Fourfold), *d*) DH (Deep Hollow). Geometries with single imaginary modes are classified as transition states (ts) the DH as a higher order saddle point (hsp), since 2 imaginary modes are found. The direction of motion of the C atom in eigenmodes corresponding to imaginary frequencies are indicated with arrows, for the DH case the lighter arrows are for the secondary mode.

The carbon atom of the QFF (0.58 eV higher in energy than the SH) is fourfold coordinated to two Fe1, one Fe2 and one Fe3. The CO is in a fully upright position at low coverage, but tilted 10° with regards to the surface normal at 1 ML. The imaginary frequency shows the molecule switching between two BL states by rocking back and forth between the two Fe1 atoms. The DH state is 0.59 eV less favourable than the SH. Its primary imaginary mode shows the carbon atom moving back and forth between the OT and SH sites, sampling the BL in the process (tilting towards Fe1 or Fe3); the second imaginary mode shows the carbon atom moving back and forth in a perpendicular direction with regards to the primary imaginary mode.

CO Migration

It was found that in general the diffusion barriers between the different minima are small, which should make CO migration across the surface facile. One example (shown in Figure 3.11) is migration from the OT (the highest energy minimum) to the SH (the lowest energy minimum) which proceeds with a negligible barrier of 0.03 eV. Figure 3.23 is a summary of some possible migration paths with the barriers indicated. Moving from the SH or BL to an adjacent minimum through the transition states shown in Figure 3.7 requires ~0.4 – 0.6 eV.

Figure 3.10*a&b* show the molecule transitioning between the two positions and Figure 3.10*c* is the corresponding energy plot with step number. Starting from the OT site progressing towards the SH, the molecule tilts over in the first seven steps (with the tilting angle increasing gradually). At point 5, where a slight increase in energy is observed, CO is in the process of tilting over towards Fe2 and at the same time pushes the adjacent Fe1 and two Fe2 atoms (on the left) away from itself. In the next step these Fe atoms move toward their original positions as reflected in the slight energy decrease; the energy continues to decrease up to step 8. At step 8 a local energy minimum is observed due to the bond formation between CO and Fe2. The molecule is now in an OT-SH bridge position (still tilted towards the SH site) and remains bridged up to the second last step. Between step 9 and 11 the position of O remains fairly constant, but C moves towards the Fe2 atom, causing the molecule to tilt over towards the Fe1 atom, *i.e.* it reconfigures to the TSH state; at the same time the Fe2 atom, to which it is now bound, moves slightly upwards. Initially (at step 9) a small barrier is overcome as CO moves out of the saddle point, but then the energy continues to decrease until the end of the transition. The molecule regains its upright position incrementally, which causes the Fe2 atom to move back to its original position. In the final step CO is fully upright and adsorbed directly above the Fe2 atom, *i.e.* in the SH site.

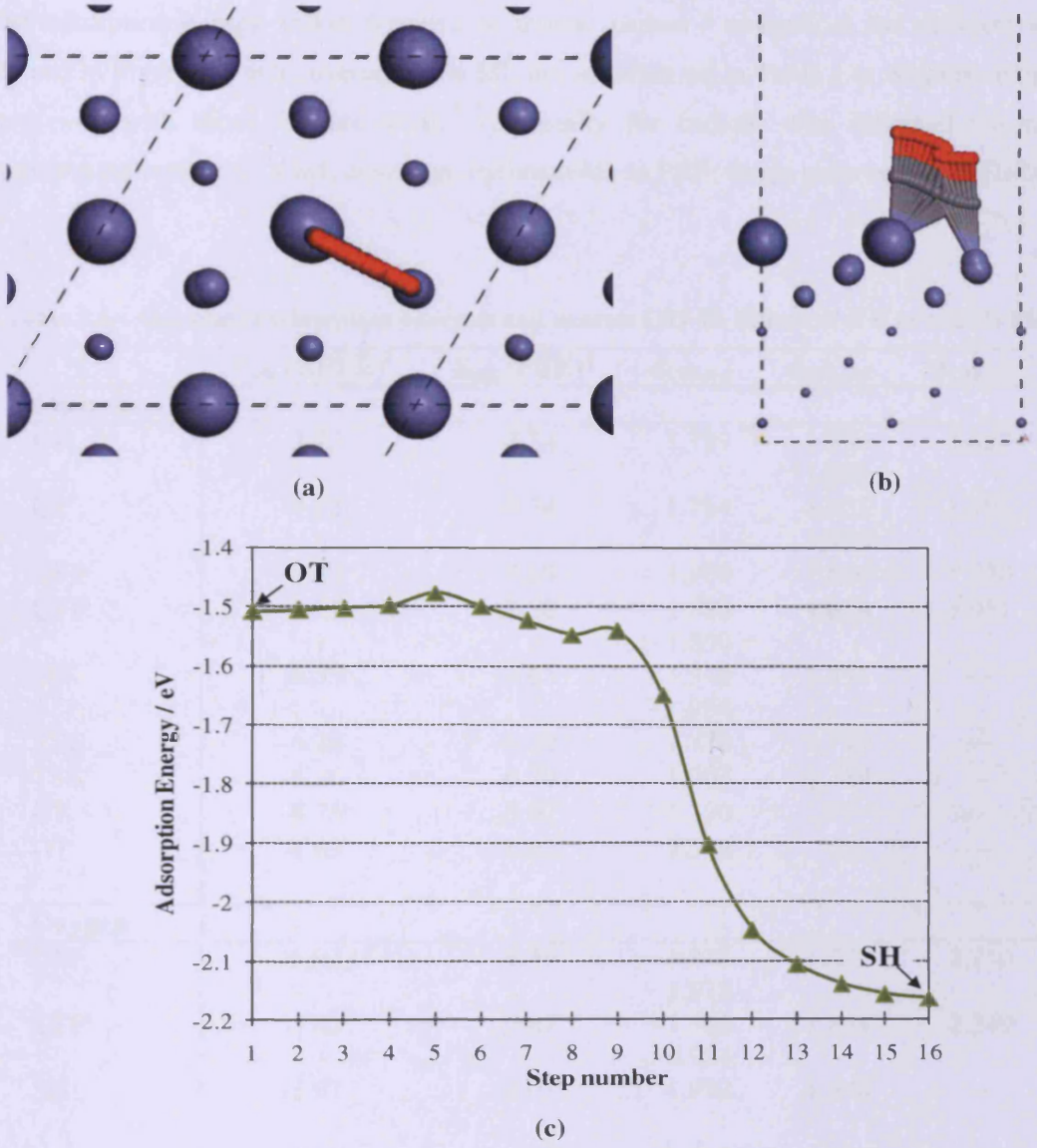

Figure 3.10 – CO diffusion from the OT to the SH site. *a*) Top view and *b*) side view of the transition. *c*) The corresponding energy plot (Energy calculated in PBE w/o ZPE corrections).

3.3.3. Adsorption of Carbon or Oxygen

In the nudged elastic band (NEB) method we require structures for both the initial, molecular adsorption states, and the possible post CO cleavage states, *i.e.* atomic C and O adsorption sites. In this section we discuss the adsorption of C and O atoms in isolation before moving on to their co-adsorption so that the influence of the atomic surface species on one another can be discussed. We then identify those structures which are likely end points for NEB calculations.

The adsorption energy values (relative to atomic carbon / oxygen) at the different sites defined in Figure 3.2 at a coverage of ¼ ML are summarized in Table 3.4. Results compare very well with those of Huo *et.al.*,[9] (especially for carbon) who followed the same optimization method at ⅓ML coverage (optimization in PBE; single point energy in RPBE).

Table 3.4 – Calculated adsorption energies and nearest C/O-Fe distances of C *or* O at ¼ ML.[a]

	E_{ads} (RPBE)[b]	E_{ads} (PBE)[b]	$d_{C/O\text{-}Fe1}$	$d_{C/O\text{-}Fe2}$	$d_{C/O\text{-}Fe3}$
Carbon					
QP	-7.23	-7.74	1.789	1.930 1.930	1.827
QP[c]	-7.22	-7.74	1.784	1.925 1.920	1.792
QFF	-7.19	-7.69	1.900	1.840	1.950
QFF[c]	-7.27	-7.80	1.890 1.890	1.818	1.951
SH	-6.33	-6.65	1.946 1.954	1.791	---
TSB	-6.28	-6.70	1.778	1.729	---
TSB[c]	-6.26	-6.70	1.707	1.769	---
OT	-4.75	-5.07	1.590	---	---
OT[c]	-4.63	-4.92	1.585	---	---
Oxygen					
QFF	-5.92	-6.39	1.976 1.978	1.829	2.240
QFF[c]	-5.42	-5.87	1.963 0.964	1.834	2.249
SH	-5.67	-6.03	1.992	1.846	---
TSB	-5.65	-6.14	1.722	1.803	---
TSB[c]	-5.24	-5.63	1.836	1.781	---
QP	-5.16	-5.44	1.827	2.039 2.041	2.081
QP[c]	-4.93	-5.33	1.872	2.134 2.191	1.955
OT	-5.07	-5.41	1.605	---	---
OT[c]	-4.44	-4.75	1.617	---	---

Notes: a) Energies are presented in eV and distances in Å.
b) Adsorption energies are taken relative to the atomic states and are not corrected for ZPE.
c) Literature values calculated at ⅓ML according to the same methodology.[9]

C bonds more strongly than O by ~1.3 eV. In general carbon atom adsorption at fourfold coordinated sites (QFF / QP) are lower in energy than two or threefold sites (TSB/SH*) by around 1 eV and lower than the OT site with a single Fe1...C interaction by 2.5 eV. For the oxygen atom this preference is less clear; the quasi fourfold is only 0.27 eV lower in energy than the twofold TSB site. This suggests that the end point of the reaction should place atomic C in a fourfold site but that the O atom may take up a position with either four- or twofold co-ordination.

3.3.4. Co-adsorption of Carbon and Oxygen

Based on the observed preferences of the C/O atoms discussed above, different end states for the CO dissociation reaction were created by considering co-adsorbed C and O atoms. Only the most stable adsorption sites for the individual atoms which place them within close proximity to one another were considered. The optimised structures of four alternatives from QP / QFF for carbon and QFF / TSB for oxygen are shown in Figure 3.11 following the order of adsorption energies relative to CO(*g*) given in Table 3.5. Other C(QP/QFF) & O(QFF/TSB) combinations were also optimised, but not used in NEB calculations, since they were higher in energy or, after optimization, very similar to states already considered.

In the most stable structure (QP-C & QFFμ^3-O, Figure 3.11*a*) the C and O atoms are practically opposite to one another on either side of an Fe1 atom. The Fe1 atom is displaced from its clean surface position toward the O atom which, although over the QFF site, co-ordinates to only two Fe1 atoms and the Fe2 atom and so the nomenclature QFFμ^3-O is adopted. If both atoms are placed in QFF sites so that they are on opposite sides of the same Fe1 atom (Figure 3.11*b*) the displacement of the Fe1 atom no longer occurs, but the calculated adsorption energy is 0.18 eV higher. For twofold co-ordinated O two alternatives were considered; with the C and O sharing an Fe1 atom (QFF-C & TSB-O, Figure 3.11*c*) and with them sharing the Fe2 atom of a shallow hollow site (QP-C & TSB-O, Figure 3.11*d*). The QFF-C & TSB-O is 0.38 eV lower in energy than the QP-C & TSB-O choice but 0.35 eV higher in adsorption energy than QP-C & QFFμ^3-O.

The three end states with the lowest energies, *i.e.* QP-C & QFFμ^3-O, QFF-C & QFF-O and QFF-C & TSB-O (Figure 3.11*a-c*), have C and O on opposite sides of an Fe1 atom,

* C in the SH position are more or less in line with the first Fe layer and attracts the three surrounding

suggesting a transition state in which both C and O interact with this top site. These structures are similar to three of the most stable configurations reported by Huo *et al.*,[9] but the QP-C & TSB-O end state (Figure 3.11*d*) was not considered in that study. It will be shown in the next section that pathways ending in this configuration have a bridged O atom in the TS, which make them significantly lower in energy than TS structures with terminally bonded O atoms.

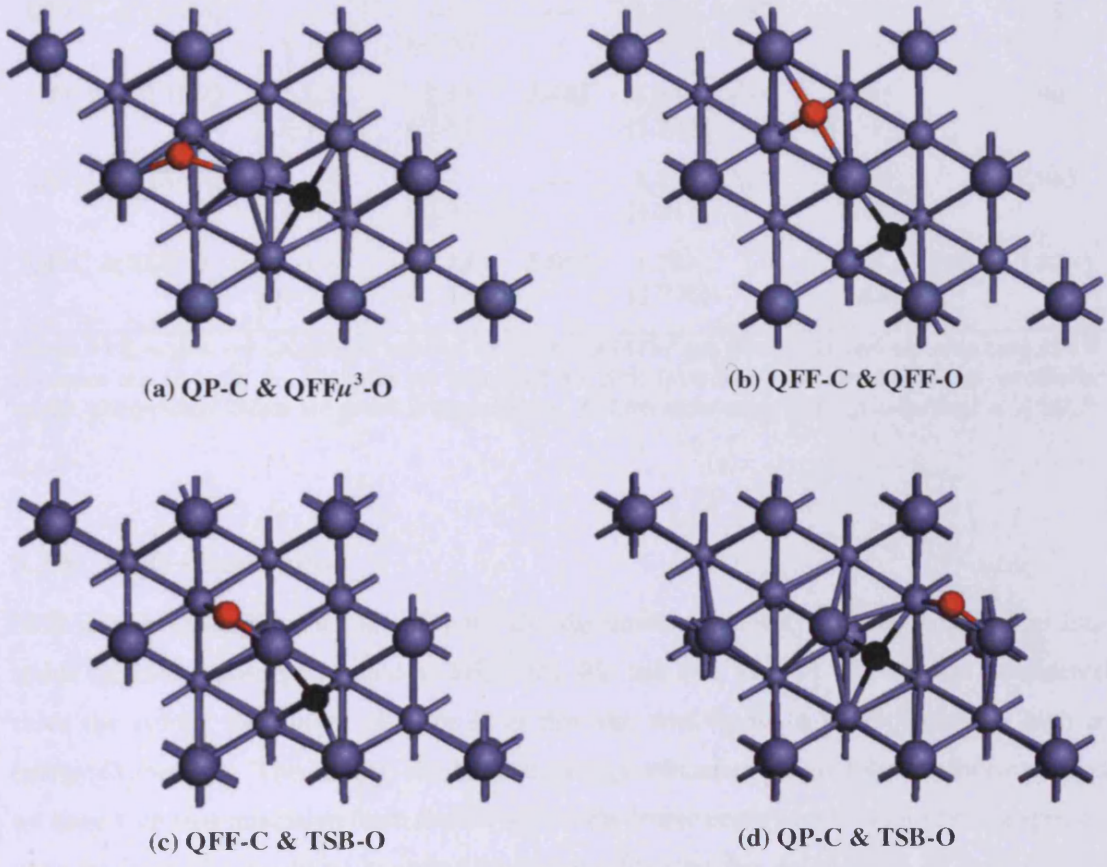

(a) QP-C & QFFμ^3-O (b) QFF-C & QFF-O

(c) QFF-C & TSB-O (d) QP-C & TSB-O

Figure 3.11 – Carbon and Oxygen co-adsorbed on clean Fe(111).

Table 3.5 – Adsorption energy values of ¼ ML dissociated CO on Fe(111).[a]

	E_{ads} (RPBE)	E_{ads} (PBE)	$d_{C\text{-}Fe1}$ [$d_{O\text{-}Fe1}$]	$d_{C\text{-}Fe2}$ [$d_{O\text{-}Fe2}$]	$d_{C\text{-}Fe3}$	$d_{C\text{-}Fe1}$ [$d_{O\text{-}Fe1}$]
QP-C & QFFμ^3-O	-1.87 (-1.89)	-2.47 (-2.48)	3.749	1.834 [1.894, 1.917]	1.934, 1.949 [1.920]	1.830
QP-C & QFFμ^3-O[b]	--- (-2.24)	--- (-2.87)	---	1.832 [1.900, 1.901]	1.939, 1.910 [1.916]	1.816
QFF-C & QFF-O	-1.69 (-1.69)	-2.33 (-2.33)	4.000	1.957, 1.958 [2.074, 2.088]	1.817 [1.819]	1.978 [2.131]
QFF-C & QFF-O[b]	--- (-1.86)	--- (-2.53)	---	1.916, 1.887 [1.956, 1.991]	1.814 [1.843]	1.987 [2.242]
QFF-C & TSB-O	-1.52 (-1.53)	-2.13 (-2.15)	3.481	1.876, 1.884 [1.779]	1.885 [1.790]	1.961
QFF-C & TSB-O[b]	--- (-1.72)	--- (-2.31)	---	1.887, 1.860 [1.817]	1.831 [1.792]	1.965
QP-C & TSB-O	-1.14 (-1.16)	-1.14 (-1.16)	2.992	1.793 [1.770]	1.900, 1.952 [1.818]	1.829

Notes: *a*) Energies are calculated relative to clean Fe(111) / gas phase CO and are presented in eV; distances are given in Å. Energies are corrected for ZPE from harmonic analysis of the coadsorbed atoms; uncorrected values are given in parentheses. *b*) Literature energy values calculated at ⅓ ML.[9]

3.3.5. CO Dissociation

NEB calculations were used to study the CO dissociation pathway starting from one of four stable molecular adsorption modes: SH, TSH, BL and DB. The OT site was not considered since the atomic adsorption of C or O at this site was found to be prohibitively high in energy (Table 3.4). This is also the highest energy minimum for molecular adsorption and we have seen that migration from the OT site to the lower energy adsorption sites is expected to be facile and so would be expected to precede dissociation. In addition, all experimental studies indicated that the so-called *b* site is the principal site from which CO dissociates,[4,5,6] so that pathways starting from SH/TSH should be important. Bartosch[5] and Whitman[6] suggested that the a_1 state, which we have used frequency calculations to assign to BL and/or DB positions, can also probably dissociate directly. In total sixteen combinations of molecular and dissociated states were considered.

Figure 3.12 shows the typical transition state structures for the reactions and Table 3.6 the relevant energy values and geometric data along with the available literature values. It has been noted that the lowest energy end points for co-adsorption of atomic C and O have the

atoms on opposite side of a Fe1 atom. We have also seen that the stable tilted structures in the molecularly adsorbed state (TSH, BL, and DB) place the O atom in close contact with the Fe1 atom and so these structures appear to suggest a transition state in which the O atom is moving over the OT site. The NEB calculations using any of these start/end points do find such a transition state.

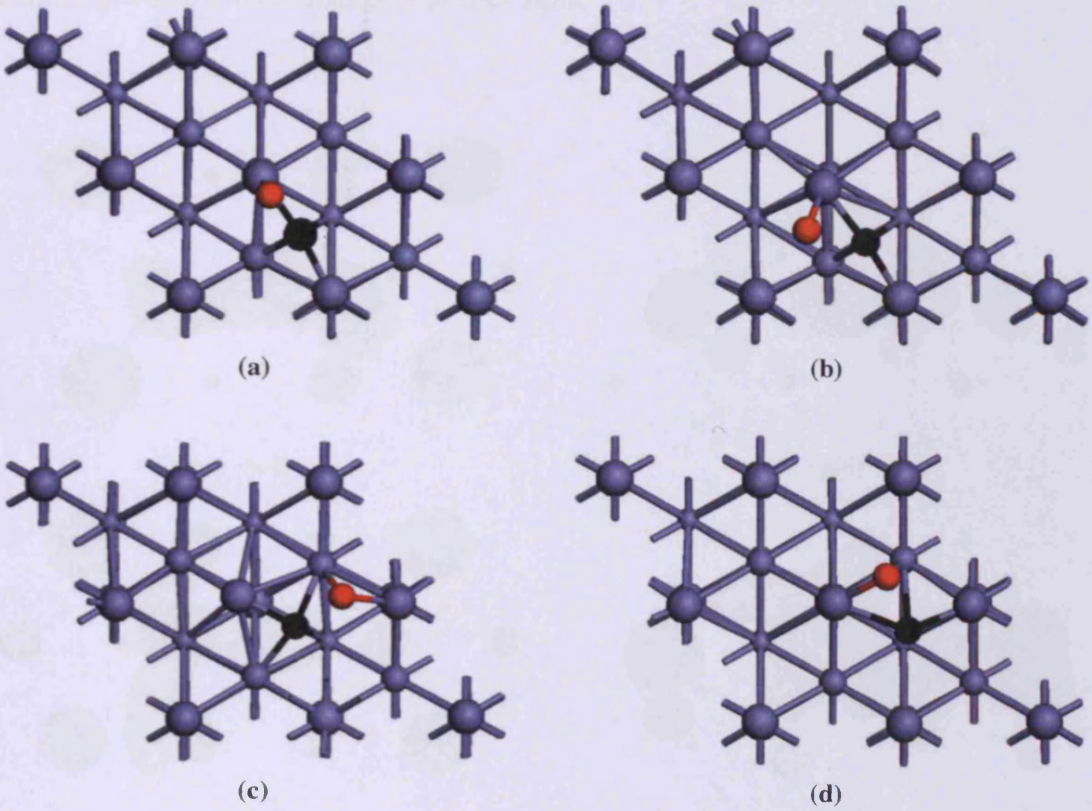

Figure 3.12 - Typical transition state structures for CO dissociation on clean Fe(111). *a*) C occupying a QFF site with O leaving toward the OT site. *b*) C occupying a QFF site with O moving around the OT site. *c*) C occupying a QP site with O leaving toward TSB. *d)* C moving into the DH site towards the QFF and O moving into the TSB site.

Two typical examples are shown in Figure 3.12*a* & *b*, in both cases the C atom has already moved to the fourfold co-ordinated position, but the O atom is either about to traverse the top site (*e.g.* BL to QP-C & QFFμ^3-O, Figure 3.12*a*). or is moving toward the QFF site (*e.g.* SH to QFF-C & QFF-O, Figure 3.12*b*). In the latter case the distortion of the position of the Fe1 atom common to C and O is seen in the end point structure (Figure 3.12*a*) has not fully taken

place in the transition state and the O atom is essentially co-ordinated to a single Fe1 atom. The movement of Fe1 away from its clean surface site occurs after bond cleavage along with the short migration of the C atom to the QP-C position. The individual adsorption calculations of atomic species (see Table 3.4) show that the single co-ordination of Fe1 by O is actually the highest energy position for an O atom, and correspondingly the transition states found for these processes are between 0.54 and 0.95 eV above the *CO(g) + clean Fe(111)* reference state (Table 3.6). Figure 3.13*a* shows an example of a CO dissociation pathway in which O transitions over the Fe1 atom.

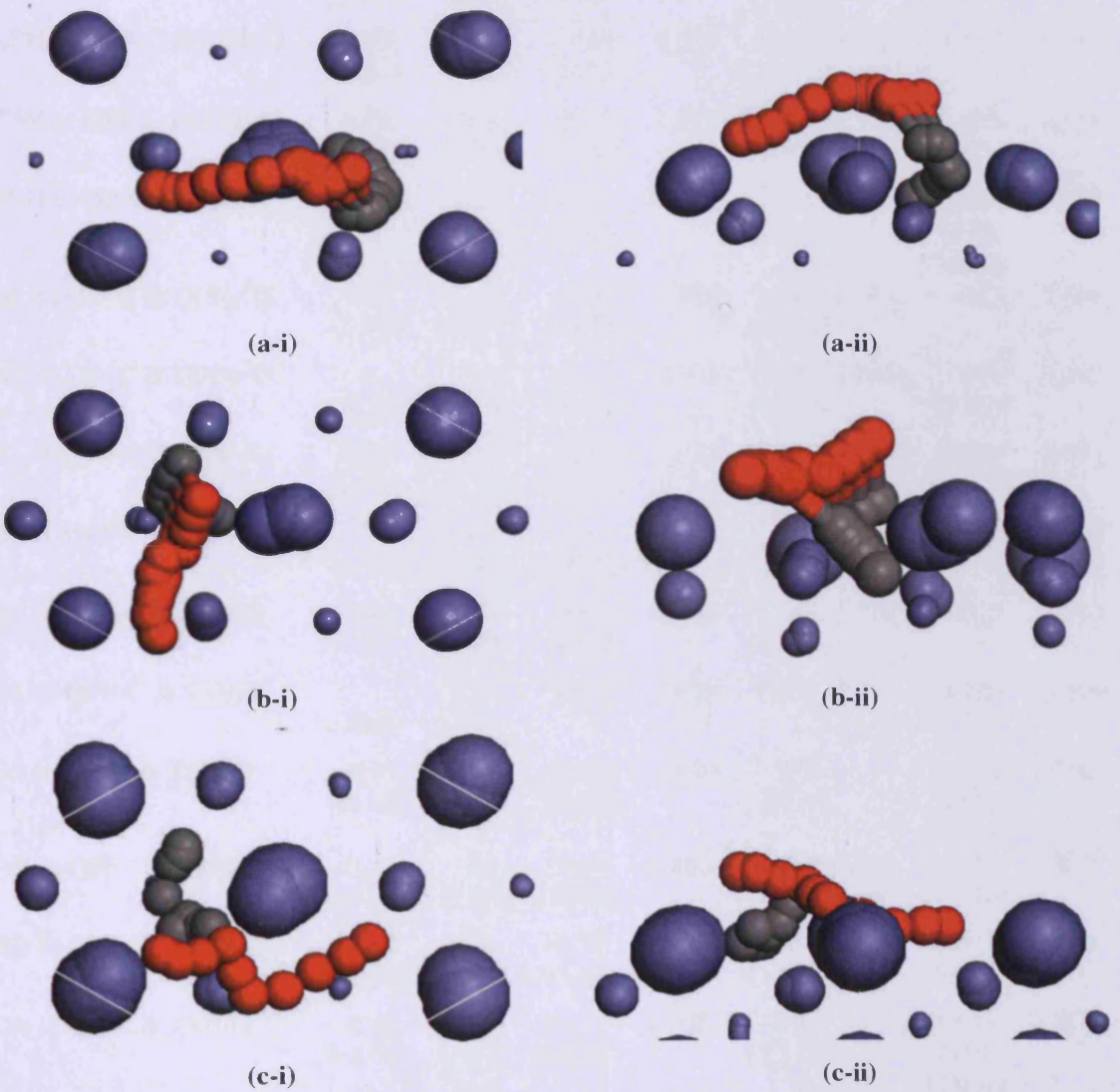

Figure 3.13 – *(i)* Top and *(ii)* side views of the CO dissociation pathways with *a)* the highest barrier (through TS with OT-O shown in Figure 3.12*a*) and the two lowest barriers: *b)* for the CO to QP-C & TSB-O pathways (corresponding to the TS shown in Figure 3.12*c*) and *c)* the DB to C+O pathways (corresponding to the TS shown in Figure 3.12*d*); the latter two pathways both avoid the OT site.

Table 3.6 – Energies and geometric data for CO dissociation transition states.[a]

	E_{ads_TS}	E_a[b]	ΔE[c]	$d_{C\text{-}O}$	$d_{C\text{-}Fe1}$ [$d_{O\text{-}Fe1}$]	$d_{C\text{-}Fe2}$ [$d_{O\text{-}Fe2}$]	$d_{C\text{-}Fe3}$
SH to QP- C & QFFμ^3O	0.95 (1.00)	2.70 (2.79)	-0.12 (-0.09)	1.926	1.865, 1.937 [1.785]	1.830	2.213
SH to QP- C & QFFμ^3O[d]	--- (0.63)	--- (2.71)	--- (-0.16)	1.992	2.181, 1.793 [1.719]	1.859	---
SH to QFF-C & QFF-O	0.85 (0.88)	2.60 (2.67)	0.06 (0.01)	2.000	1.883, 1.945 [1.681]	1.788	2.501
SH to QFF-C & TSB-O	0.74 (0.76)	2.49 (2.55)	0.23 (0.26)	1.988	1.861, 1.945 [1.700]	1.814	2.086
TSH to QP-C & QFFμ^3-O	0.91 (0.94)	2.55 (2.61)	-0.24 (-0.21)	2.014	1.852, 1.922 [1.699]	1.796	1.489
TSH to QFF-C & QFF-O	0.63 (0.64)	2.27 (2.32)	-0.05 (-0.01)	1.975	1.872, 1.952 [1.680]	1.812	2.087
TSH to QFF-C & TSB-O	0.64 (0.65)	2.28 (2.33)	0.12 (0.14)	1.979	1.869, 1.953 [1.690]	1.816	2.066
TSH to QP-C & TSB-O	-0.13 (-0.11)	1.51 (1.56)	0.50 (0.52)	1.849	1.834 [1.867]	1.932 1.996 [1.937]	1.855
BL to QP- C & QFFμ^3O	0.57 (0.58)	2.10 (2.14)	-0.34 (-0.32)	1.975	1.876, 1.968 [1.682]	1.823	2.006
BL to QP- C & QFFμ^3O[d]	--- (-0.35)	--- (1.53)	--- (-0.36)	2.002	2.309, 1.882 [1.835]	1.895 [1.884]	1.892
BL to QFF-C & QFF-O	0.49 (0.50)	2.15 (2.19)	-0.03 (0.00)	2.023	1.870, 1.990 [1.682]	1.829	1.951
BL to QFF-C & QFF-O[d]	--- (0.34)	--- (2.22)	--- (0.02)	1.862	1.822, 1.930 [1.692]	1.828	2.132
BL to QFF-C & TSB-O	0.54 (0.55)	2.07 (2.11)	0.03 (0.02)	2.042	1.863, 1.970 [1.674]	1.817	1.983
BL to QFF-C & TSB-O[d]	--- (0.64)	2.15	0.03	2.019	1.855, 1.923	1.805	1.960
BL to QP-C & TSB-O	-0.15 (-0.13)	1.39 (1.43)	0.40 (0.40)	1.920	1.847 [1.816]	1.982 2.021 [1.943]	1.862
DB to QFF-C & QFF-O	-0.23 (-0.19)	1.00 (1.06)	-0.46 (-0.44)	1.826	1.922, 2.230 [1.898]	2.252 [1.888]	1.877
DB to QFF-C & TSB-O	-0.16 (-0.14)	1.06 (1.12)	-0.29 (-0.28)	1.990	2.031, 2.068 [1.772]	1.954 [2.235]	1.891
DB to QP-C & TSB-O	-0.16 (-0.14)	1.07 (1.11)	0.09 (0.09)	1.915	1.843 [1.815]	1.973 2.010 [1.937]	1.864

Note: *a*) Energies are given in eV (RPBE) and are corrected for ZPE from harmonic analysis of reactant, transition state and products (uncorrected values in parentheses). Distances are given in Å.
b) Activation energies ($E_a = E_{TS} - E_{CO}$).
c) Reaction energies ($\Delta E = E_{C+O} - E_{CO}$) for CO dissociation at ¼ ML coverage.
d) Literature values calculated with RPBE at $^1/_3$ ML, without zero-point energy corrections from Huo *et. al.*[9]

Taking the alternative end point structure of QP-C & TSB-O does give transition states avoiding interaction with the OT Fe1 site (Figure 3.12*c*). In this transition state the C atom has already a QP position and the O atom is near to the twofold co-ordinate TSB site. Figure 3.13*b* shows this CO dissociation pathway. The TS occurs very late along the pathway and resembles the end-structure closely. After the TS only small changes occur; C is already in its final position and O moves from the quasi threefold site (consisting of Fe1, Fe2 and Fe3) to the TSB position (Fe1 and Fe2).

In Figure 3.12*d* the OT site is also avoided; this TS structure was obtained for DB to QFF-C & QFF-O / DB to QFF-C & TSB-O. Figure 3.12*d* shows that C is moving towards the DH site and O towards the TSB position; this specific structure was obtained for the DB to QFF-C & QFF-O pathway. In the case of DB to QFF-C & TSB-O, C is just exiting the DH site in the TS (not shown). Figure 3.13*c* shows the whole DB to QFF-C & QFF-O pathway which allows for high coordination of both atoms along the whole route, which is likely to contribute to the low energy barrier.

Figure 3.14 shows the PDOS of the most and least favourable transition states (the C and O atoms are shown separately in Figure 3.14*a* & *b* respectively); *i.e.* for the pathways CO to QP-C and QFFμ^3-O (least favourable, indicated by the green line in Figure 3.14 and corresponding to the state shown in Figure 3.12*a*), CO to QP-C & TSB-O (second most favourable, indicated by the purple line in Figure 3.14 and corresponding to the state shown in Figure 3.12*c*) and DB to C+O (most favourable, indicated by the blue line in Figure 3.14 and corresponding to the state shown in Figure 3.12*d*). The PDOS of the respective C atoms are more similar than the O atoms, but differences are noticeable: the most favourable TS has the highest population at low energy (at -5.5 eV) and relatively less filled states in the higher energy region (compare the three respective populations at ~ -4 eV & 4 eV for example). The reverse is true for the two remaining transition states, with the least favourable TS having the highest population at ~ -4 eV / 4 eV.

The differences for the O atoms are more pronounced, but the same principle holds. The CO to QP-C and QFFμ^3-O TS (least favourable) in which O is terminally bonded exhibits two large peaks above the Fermi level and the largest peaks at -3.5 eV, compared to the TS of DB to C+O (most favourable) of which the maximum peaks are again situated at lower energy (-5.5 eV).

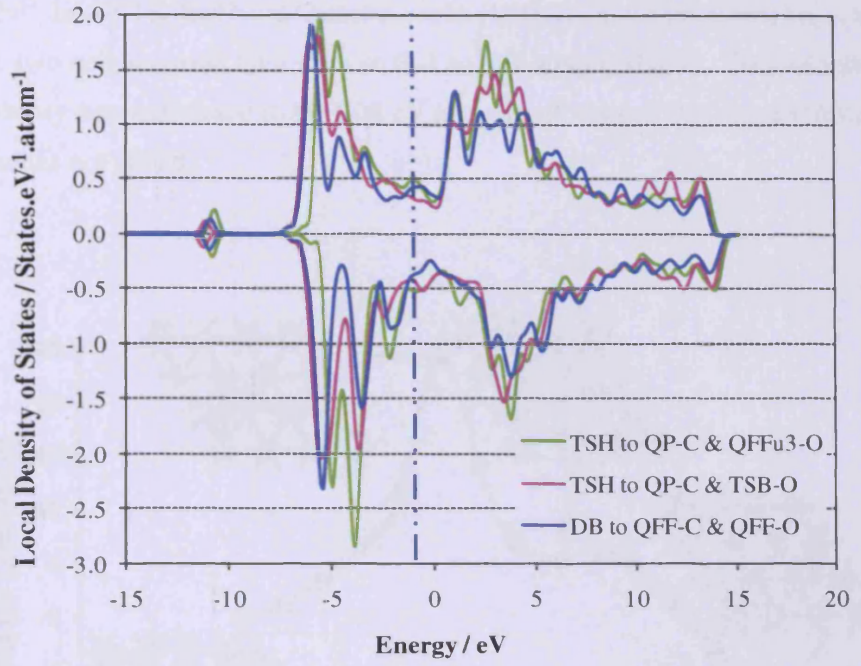

(a)

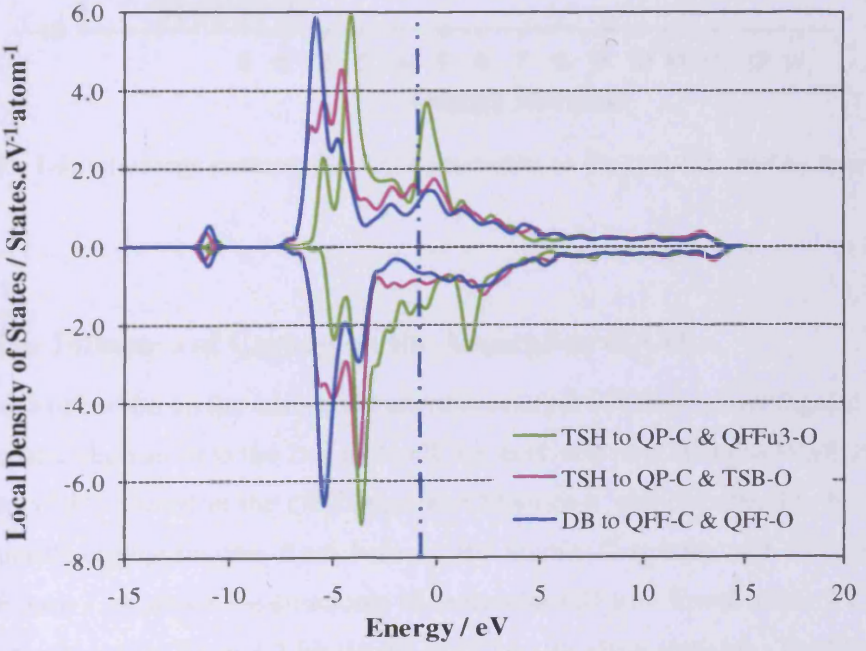

(b)

Figure 3.14 – Projected Density of states examples of the least and two most favourable generic TS structures: *CO to QP-C & QFFμ³-O >> CO to QP-C & TSB-O > DB to C+O*. The PDOS of carbon and oxygen are shown separately in Figures *a* and *b* respectively.

Sorescu *et.al.* simulated the dissociation of the BL site to an end state where C and O occupy two QFF sites which are separated so that no Fe atoms are shared; the pathway is shown in

Figure 3.15.[15] In the TS the C and O atoms are in relatively close proximity ($d_{C\text{-}O}$ = 1.802 Å) and occupy two neighbouring QFF sites so that an Fe1 atom is shared. The activation energy for this pathway was calculated to be 1.06 eV and overall the reaction is exothermic by 0.28 eV (ZPE values not added).

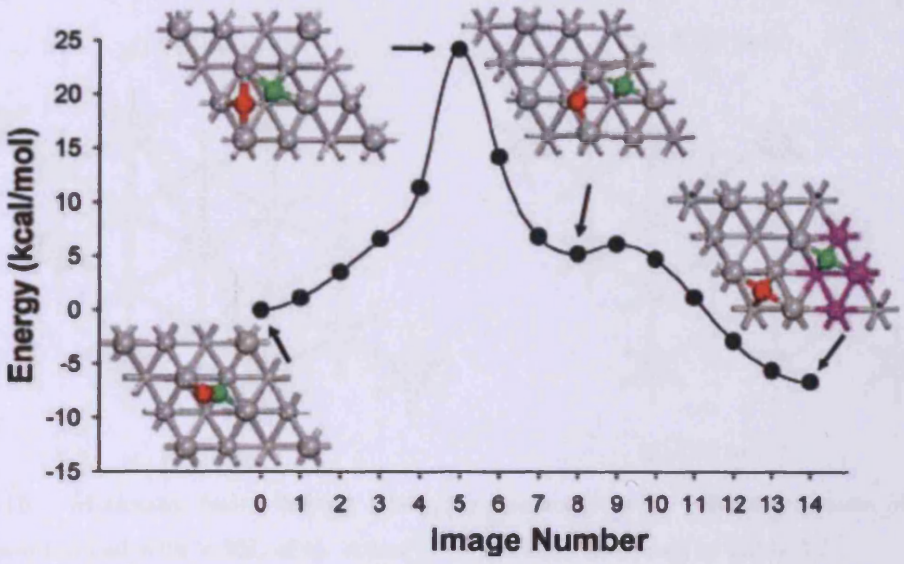

Figure 3.15 – Lowest energy pathway for CO dissociation on Fe(111) obtained by Sorescu *et.al.*[15]

3.3.6. The Influence of Carbon on the Adsorption of CO

The influence of carbon on the adsorption and dissociation of CO was investigated by adding one additional carbon atom to the 2×2 unit cell; *i.e.* each cell now contains ¼ ML of C and ¼ ML of CO. C was placed in the QFF opposite CO since it was calculated to be one of the most favourable configurations; from here on the atomic C species will be referred to as C(QFF). Figure 3.16 shows the structures of molecular CO with C and Table 3.7 shows the adsorption energies (see Table 3.2 for details of CO on the clean surface). The SH, TSH, BL and DB (the molecular states used for the CO dissociation study on the clean surface) were considered here. In the presence of additional atomic carbon the DB state moved to the BL site during optimisation and is thus not discussed separately. On the other hand the DH, which is a hsp on the clean surface is a minimum in the presence of C and is thus also considered in this section.

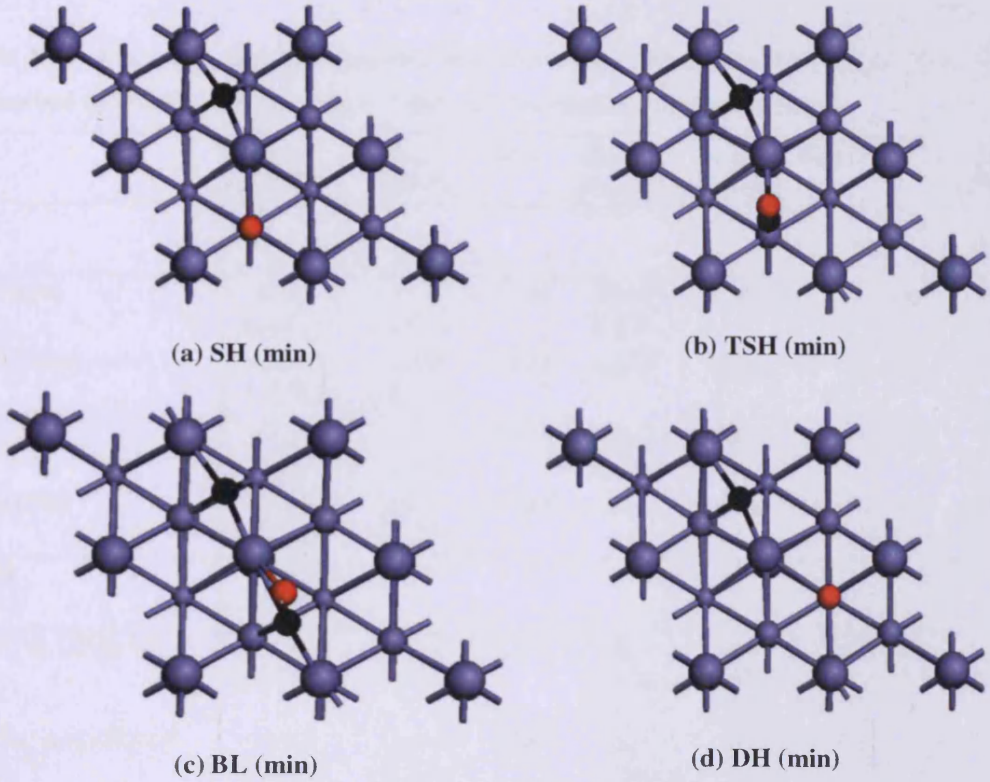

Figure 3.16 – Minimum (min) energy adsorption geometries for ¼ML-structures of CO on Fe(111) co-adsorbed with ¼ ML of C. Adsorption energies are listed in Table 3.7.

Except for the BL, the molecular CO geometries co-adsorbed with C(QFF) are similar to the clean surface equivalents; furthermore the respective C(QFF) atoms do not move from their starting positions during optimization, both of which indicates that no significant steric interaction occurs. The adsorption energies, bond lengths and C-O frequencies do not generally change significantly; CO adsorption is enhanced slightly in the presence of C by an average of 0.12 eV. The largest change is observed for the BL state which is more tilted in the presence of carbon (θ = 44° *vs.* 40°) and accordingly the C-O bond length is longer by 0.013 Å. This increased interaction leads to a stronger adsorption energy (ΔE = -0.25 eV); in fact the BL is now almost as stable as the TSH state, which is second most favourable after the SH (according to the PBE calculation the BL is as favourable as the SH). The DH is now a minimum with no imaginary vibrational modes where as on the clean surface it only existed as a hsp.

Table 3.7 – Adsorption energies, geometric data and stretch frequencies of ¼ ML of CO on Fe(111) coadsorbed with ¼ ML of C. Compare Table 3.2 for data of the clean surface.[a]

	E_{ads} (RPBE)	E_{ads} (PBE)	d_{C-O}	d_{C-Fe1} [d_{O-Fe1}]	d_{C-Fe2} [d_{O-Fe2}]	d_{C-Fe3}	θ^d	Freq (RPBE)
CO								
SH (min)	-1.92 (-1.88)	-2.25 (-2.21)	1.191	2.495 2.556	1.761		---	1819
TSH (min)	-1.83 (-1.78)	-1.92 (-2.10)	1.202	2.183	1.763		20	1754
BL (min)	-1.79 (-1.74)	-2.23 (-2.18)	1.257	1.977 2.296	1.890	2.398	44	1409
DH (min)	-1.29 (-1.19)	-1.75 (-1.65)	1.218	---	---	1.850	---	1041
C+O								
QP-C & QFFμ^3-O	-1.38 (-1.31)	-1.95 (-1.88)	3.717	1.846 [1.864] [1.887]	1.947 1.970 [1.944]	1.838		---
QFF-C & TSB2-O[b]	-1.54 (-1.47)	-2.14 (-2.07)	4.987	1.856 1.889 [1.789]	1.856 [1.797]	1.971		---
QP-C & TSB-O	-1.26 (-1.19)	-1.87 (-1.80)	3.047	1.805 [1.808]	1.890 1.941 [1.807]	1.826		---
QFF-C & OT-O[c]								
From SH	0.29 (0.37)	-1.17 (-0.09)	2.725	2.021 2.040 [1.580]	1.800	1.878		---
From BL	0.35 (0.43)	-0.13 (-0.05)	2.781	1.967 2.018 [1.632]	1.769	1.967		---
From BR	0.31 (0.39)	0.15 (0.23)	2.725	1.971 2.056 [1.614]	1.765	1.899		---
QFF-C & TSHμ^3-O[c]								
From DH	-1.13 (-1.05)	-1.72 (-1.64)	2.766	1.933 2.033 [1.963] [2.099]	1.766 [1.809]	1.975		---

Notes: *a)* Energies (in eV) are relative to clean Fe(111), gasphase CO and atomic C. Values are zpe-corrected from harmonic analysis of molecule / atoms; values without zpe-corrections are given in parentheses. Frequencies are given in cm^{-1} and distances in Å.
b) Equivalent to QFF-C & QFF-O on the clean surface.
c) Equivalent to QFF-C & TSB-O on the clean surface.
d) Tilting angle relative to the surface normal, presented in degrees.

The presence of C does not bring about a noticeable change in the PDOS of C & O in the SH molecule. TSH with C(QFF) is also similar to TSH without C, with the main difference being the reduction in the states attributed to the 1π orbitals (see Figure 3.8 for the peak assignment). Corresponding to the change in structure and adsorption energy with the addition of C, the biggest difference in the PDOS is observed for BL, as shown in Figure 3.17. The energy position and size of the peaks are the same on the two surfaces, but while the clean surface exhibits one broad peak, the peak of BL on Fe(111)/C is split, in accordance to the larger tilting angle (44° w/o C(QFF) *vs.* 40° with C(QFF)) which increases the Fe...O interaction and changes the local environment of the respective orbitals. This is in agreement with results on the clean surface (Figure 3.8) where molecules with larger tilting angles also exhibit broader or more distinct 1π peaks.

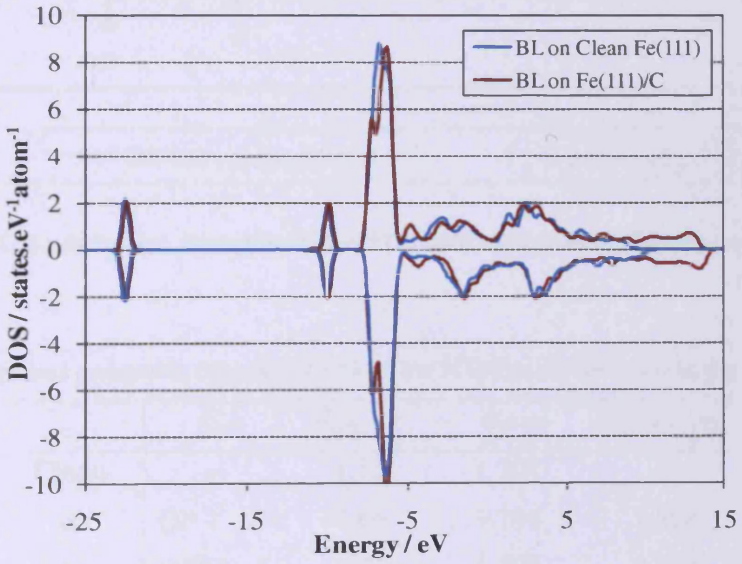

Figure 3.17 – PDOS of BL adsorbed with and without C(QFF).

Even though these results show that C(QFF) stabilizes CO, the adsorption site of C(QFF) and its relative position with regards to CO also needs consideration. Figure 3.18 shows a series of figures in which the position of atomic C was varied along with the respective adsorption energies. Table 3.8 contains the adsorption energies and geometric data of the CO + C(QFF/QP) systems.

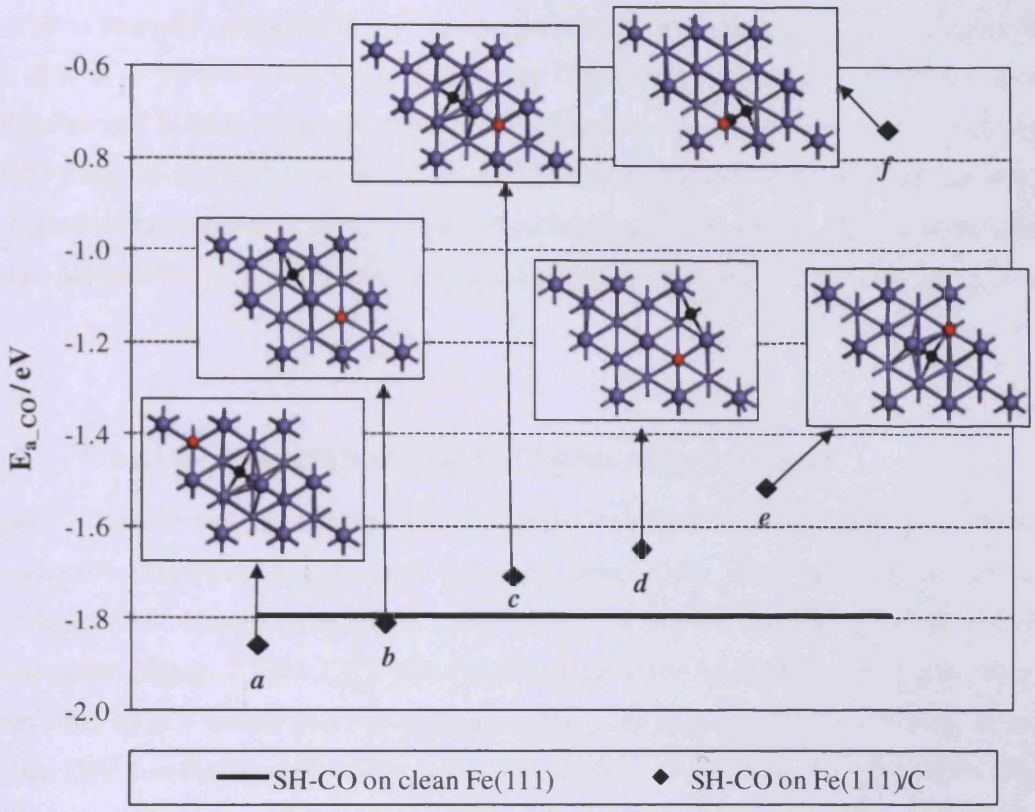

Figure 3.18 – CO adsorption energy on C/Fe(111) with variation in the position of atomic C.

Table 3.8 – Energy and geometric data of SH CO on Fe(111)/C with variation in the position of C.[a]

	C	E_{ads_CO}	$d_{C\text{-}O}$	$d_{C(QFF)\text{-}CO}$[b]
Clean	---	-1.79	1.201	---
a	QP 1	-1.86	1.194	3.908
b	QFF1	-1.81	1.197	4.263
c	QP2	-1.71	1.210	3.995
d	QFF3	-1.65	1.193	3.124
e	QP3	-1.51	1.184	2.743
f	QFF4	-0.73	1.223	1.425

Notes: a) Energy values calculated in RPBE and presented in eV; zpe corrections not added. Distances are presented in Å.
b) Measured from C(QFF/QP) to C in the molecule.

In general shorter C(QFF)-CO distances lead to higher adsorption energies. In structures *a* and *b* where C(QFF/QP) is adsorbed in a site one Fe-atom away from CO ($d_{C(QFF/QP)\text{-}CO} > 3.9$ Å), the overall energy of the system is lower than CO on the clean surface, in agreement with

results in the preceding section. The remaining structures, on the other hand, have higher adsorption energies compared to CO on the clean surface. The energy of *c* is higher than that of *a* & *b* by ≥ 0.1 eV even though the C(QFF)-CO distance is 4.263 Å. In this configuration CO also interacts with the displaced Fe1 atom, which causes it to move slightly from the optimum SH site. Similarly the CO configuration is somewhat distorted in the higher energy structures (*e* & *f*), which should influence the energy of the system. Direct contact between the C atoms results in a significant rise in overall energy (structure *f*).

3.3.7. Co-adsorption of Dissociated CO with Atomic Carbon

Figure 3.19 shows the structures of dissociated CO co-adsorbed with C(QFF) and Table 3.6 the relevant adsorption energies and structural parameters. The influence of carbon on dissociated CO is more pronounced than on the molecule. In the QP-C & QFFμ^3-O configuration (Figure 3.19*a*), C(QFF) forces O closer to the fourfold position (even though it doesn't end up in a formal fourfold site) and at the same time C(QFF) moves away from the original QFF towards the DH which is less favourable. The QFF-C & QFF-O state (Figure 3.19*b*) also undergoes a change in the presence of carbon: C(QFF) remains in its original QFF site, but O moves into a TSB position further away from C(QFF). This configuration on the C/Fe(111) surface will be referred to as QFF-C & TSB2-O to distinguish from the non-related QFF-C & TSB-O state on the clean surface where O is coordinated to a different TSB site.[†]

O again is forced into a less coordinated site in the QFF-C & TSB-O configuration (Figure 3.19*c*), namely the OT position between the two C-atoms, since C(QFF) fills the closeby QFF site; this end-structure is thus more aptly described as a QFF-C & OT-O state. The QFF-C & OT-O end state was obtained when starting from the BL, SH or TSH. The adsorption energies of these QFF-C & OT-O states on the C/Fe(111) surface are higher by ~1.95 eV than the clean surface equivalents, QFF-C & TSB-O, presumably mainly due to the decrease in coordination of the O atom and the close proximity of the three atoms.

[†] For the QFF-C & QFF-O structure on the C/Fe(111) surface the C(QFF) was adsorbed in the top right QFF site of the unit cell instead of the top left, to leave this site open for O and keep consistancy with the clean surface (compare QFF-C & QFF-O on the clean surface in Figure 3.11).

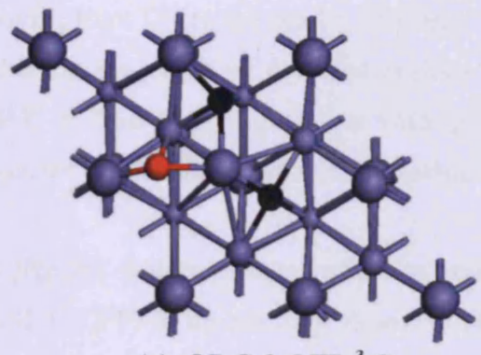

(a) QP-C & QFFμ^3-O

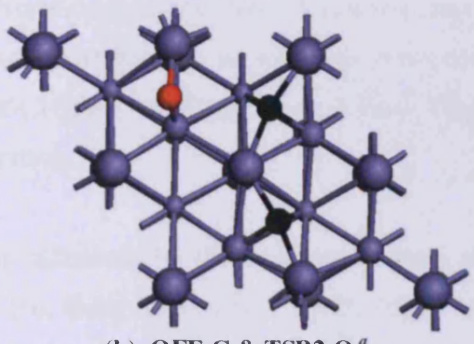

(b) QFF-C & TSB2-O [a]

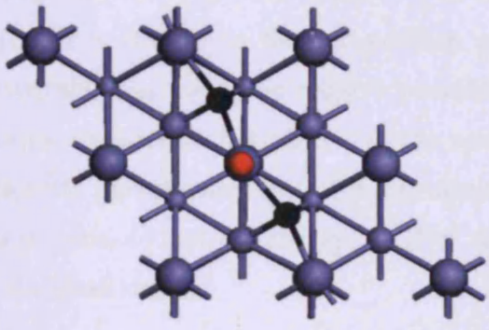

(c) QFF-C & OT-O [b]

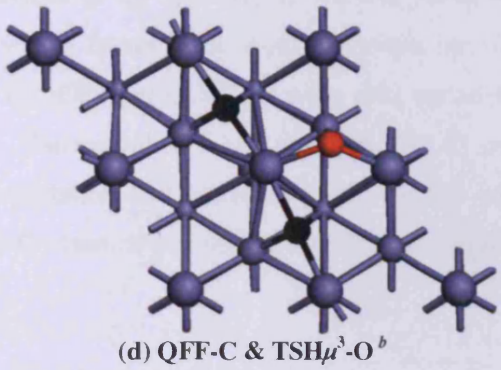

(d) QFF-C & TSHμ^3-O [b]

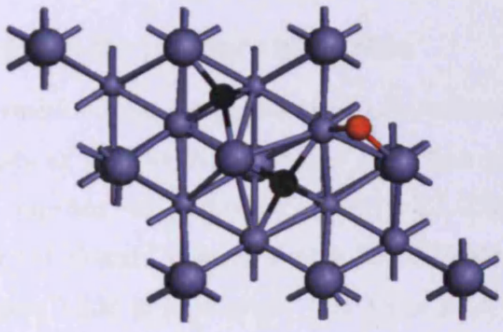

(e) QP-C & TSB-O

Figure 3.19 – Minimum adsorption configurations of dissociated CO coadsorbed with ¼ ML of C; adsorption energies are listed in Table 3.7. Compare equivalent clean surface structures in Figure 3.11.

Notes: a) Equivalent of QFF-C & QFF-O on the clean surface.
b) Equivalent of QFF-C & TSB-O on the clean surface.

very similar to Figure
SH to QP-C & QFFμ^3-O
bridged between two Fe1
to other CO to QP-C &
structure of CO to QP-
equivalent and therefore a

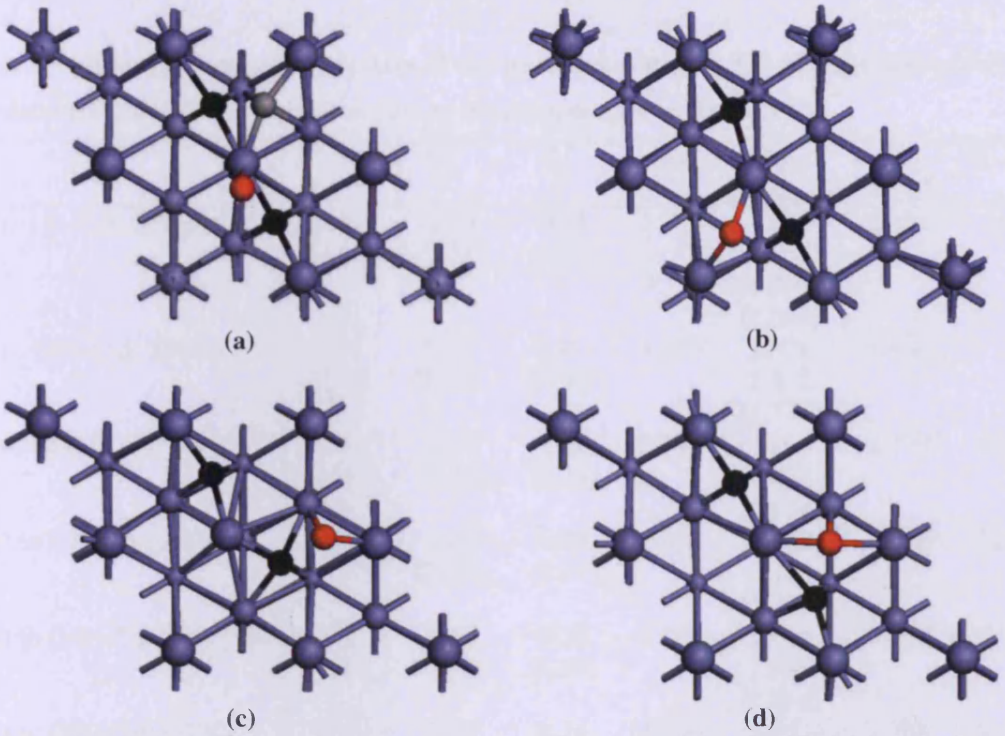

Figure 3.20 – Typical transition state structures for CO dissociation on Fe(111)/C: *a*) C occupying a QFF site with O leaving towards the OT site. Pathways sampling this TS are BL/TSH to QP-C & QFFμ^3-O, BL/SH/TSH to QFF-C & OT-O^b and CO to QFF-C TSB2-O (C(QFF) for the CO to QFFμ^3-O / OT-O pathways are shown in black while C(QFF) for the CO to QFF-C & TSB2-O pathways are superimposed in light grey). *b*) C & O occupying adjacent QFF sites (fourfold and twofold bonded respectively), O leaving toward the QFFμ^3 position. The TS is sampled in the SH to QP-C & QFFμ3-O pathway. *c*) C occupying a QP site with O leaving towards TSB; the TS is sampled in the CO to QP-C & TSB-O pathways. *d*) C in a QFF position moving away from the DH site; O in a QFFμ^3 position moving towards the TSHμ^3 position.

Notes: a) Equivalent of QFF-C & QFF-O on clean surface.
b) Equivalent of QFF-C & TSB-O on clean surface.

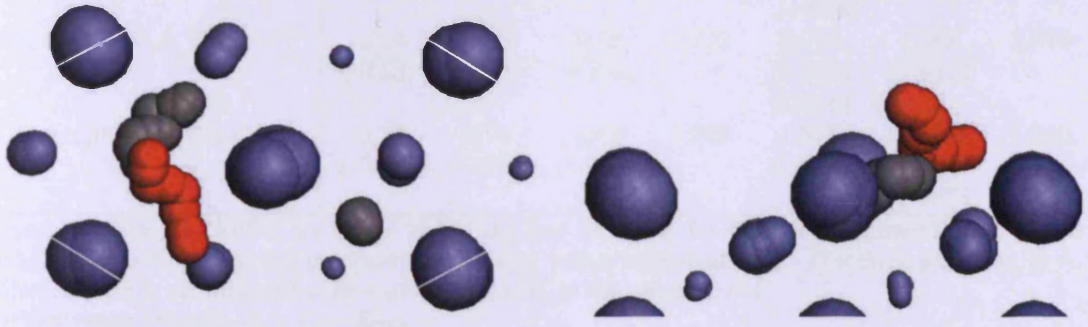

Figure 3.21 – *i*) Top and *ii*) side view of the CO dissociation pathway DH to QFF-C & TSH μ^3-O on C/Fe(111); the pathway has the lowest barrier of all clean or C-modified surfaces.

Table 3.9– Energies and geometric data of the transition states for CO dissociation on Fe(111) co-adsorbed with ¼ ML C; compare data of the clean surface in Table 3.6.[a]

	E_{ads_TS}	E_a[b]	E_r[c]	d_{C-O}	d_{C-Fe1} [d_{O-Fe1}]	d_{C-Fe2} [d_{O-Fe2}]	d_{C-Fe3}
SH to QP-C & QFFμ^3-O	0.33 (0.46)	2.25 (2.34)	0.53 (0.57)	1.999	1.991 2.062 [1.893] [2.005]	1.804	---
SH to QFF-C & TSB2-O[d]	0.74 (0.85)	2.63 (2.70)	0.35 (0.38)	1.925	1.878 1.912 [1.732]	1.801	---
SH to QFF-C & OT-O[e]	0.51 (0.60)	2.43 (2.48)	2.21 (2.24)	2.247	1.914 2.236 [1.648]	1.770	1.900
TSH to QP-C & QFFμ^3-O	0.81 (0.93)	2.63 (2.71)	0.44 (0.47)	1.962	1.982 2.132 [1.752]	1.794	2.174
TSH to QFF-C & TSB2-O[d]	0.50 (0.60)	2.32 (2.37)	0.28 (0.30)	2.015	1.864 1.922 [1.686]	1.799	2.046
TSH to QFF-C & OT-O[e]	0.51 (0.60)	2.33 (2.38)	2.14 (2.17)	1.906	1.992 2.150 [1.771]	1.788	2.048
TSH to QP-C & TSB-O	-0.28 (-0.18)	1.55 (1.60)	0.57 (0.59)	1.886	1.841 [1.865]	1.932 2.023 [1.930]	1.839
BL to QP-C & QFFμ^3-O	0.56 (0.65)	2.35 (2.20)	0.41 (-0.08)	2.166	1.922 [1.658]	1.781	1.898
BL to QFF-C & TSB2-O[d]	0.58 (0.67)	2.20 (2.24)	0.08 (0.09)	2.036	1.859 2.022 [1.673]	1.801	1.979
BL to QFF-C & OT-O[d]	0.43 (0.53)	2.23 (2.38)	2.15 (2.17)	2.163	1.924 2.221 [1.667]	1.782	1.912
BL to QP-C & TSB-O	-0.29 (-0.19)	1.51 (1.60)	0.54 (0.56)	1.880	1.854 [1.828]	1.960, 2.022 [1.957]	1.847
DH to QFF-C & TSB2-O[d]	0.62 (0.71)	1.79 (1.79)	-0.37 (-0.40)	2.066	1.863 2.032 [1.664]	1.803	1.949
DH to QFF-C & TSHμ^3-O[e]	-0.66 (-0.53)	0.63 (0.66)	0.16 (0.14)	1.971	2.328 [2.603] [2.016]	1.868 [1.917]	1.910
DH to QP-C & TSB-O	-0.33 (-0.22)	0.96 (0.97)	0.03 (0.00)	1.805	1.870 [1.848]	2.031, 1.991 [1.967]	1.860

Notes: *a*) Energies RPBE are given in eV and are corrected for ZPE from harmonic analysis of reactant, transition state and products (uncorrected values in parentheses). Distances are given in Å. The DB state is not included since it revert to the BL in the presence of C.

b) Activation energies ($E_a = E_{TS} - E_{CO}$).

c) Reaction energies ($E_r = E_{C+O} - E_{CO}$) for CO dissociation (¼ ML, RPBE).

d) Equivalent of QFF-C & QFF-O on clean surface.

e) Equivalent of QFF-C & TSB-O on clean surface.

Figure 3.21 shows the movement of the C & O (and Fe) atoms during dissociation along the DH to QFF-C & TSHμ^3-O pathway, showing that O avoids the OT position and that C & O both remains highly coordinated along the whole pathway. Especially the Fe1 atoms move from their original positions as C & O migrate towards the equilibrium positions. The CO to QP-C & TSB-O pathways (second most favourable) and those sampling the OT-O site (least favourable) are similar to the clean surface equivalents and are not shown again (refer to Figure 3.13).

CO Dissociation and Variation of the Relative Position of Atomic C

The position (and type of site) of the C(QFF) atom was varied with regards to CO in order to determine the influence on the adsorption configuration of CO, as well as the pathway and energy barrier of CO dissociation on Fe(111)/C; only the BL to QP-C & QFFμ^3-O dissociation pathway was considered. Table 3.10 shows the relevant structures as well as the respective adsorption, activation and reaction energies.

The configuration of CO in the CO + C(QFF/QP) structures are similar to that on the clean surface, but the C-O bond lengths of BL are all somewhat longer (by 0.02 – 0.17 Å). The adsorption energies were equal to or lower than (by up to 0.26 eV) 0 BL on the clean surface and correlate to the C-O bond lengths (stronger adsorption with longer bond length) and if only the structures with C(QFF) are considered, also the tilting angles (stronger adsorption with larger tilting angle). The CO + C(QP) structure has the largest tilting angle (48°), but not the longest C-O bond length. This might be because of the movement of the Fe1 atom caused by the interaction of C(QP).

All the end structures are less favourable compared to the clean surface equivalents by 0.02 – 0.49 eV, as was also found for other structures (Figure 3.19). The difference in adsorption energies can be related to the stability of the surface species. In some cases repulsion between O and C(QFF) forces the atoms into less favourable positions, *eg.* CO + C(QFF1/QFF3), which causes the overall energy of the system to increase.

Table 3.10 – Starting, transition state and end structures of the dissociation reaction BL to QP-C & QFFμ^3-O on C/Fe(111) with C(QFF/QP) in different adsorption sites (QFF1, QFF2, QFF3 and QP).[a]

	C_{QFF1}	C_{QFF2}	C_{QFF3}	C_{QP}
Start	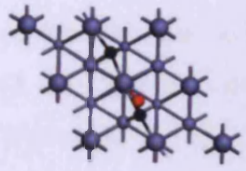	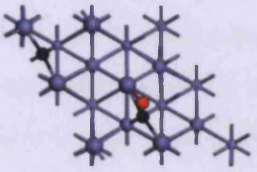	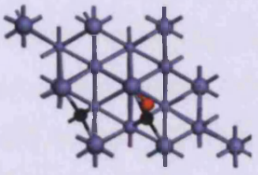	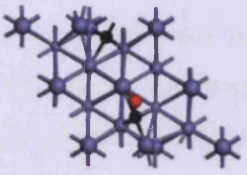
	E_{ads} = -1.80 (-1.74)	E_{ads} = -1.54 (-1.48)	E_{ads} = -1.58 (-1.52)	E_{ads} = -1.72 (-1.67)
	d_{C1-O} = 1.257	d_{C1-O} = 1.241	d_{C1-O} = 1.243	d_{C1-O} = 1.247
	d_{C2-O} = 3.672	d_{C2-O} = 6.576	d_{C2-O} = 4.102	d_{C2-O} = 4.655
	d_{C1-C2} = 4.226	d_{C1-C2} = 6.822	d_{C1-C2} = 3.797	d_{C1-C2} = 5.159
	θ = 44	θ = 40	θ = 41	θ = 48
TS	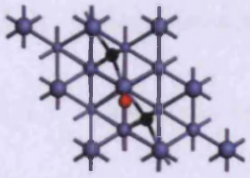	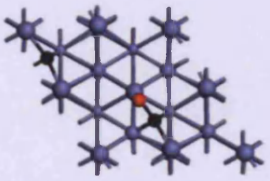	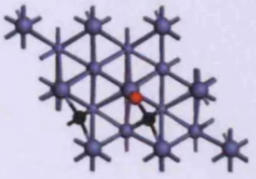	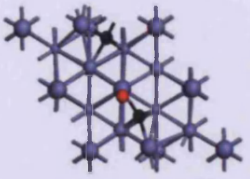
	E_{ads} = 0.56 (0.65)	E_{ads} = 0.63 (0.73)	E_{ads} = 0.61 (0.71)	E_{ads} = 0.43 (0.53)
	d_{C1-O} = 2.027	d_{C1-O} = 2.135	d_{C1-O} = 2.517	d_{C1-O} = 2.009
	d_{C2-O} = 3.109	d_{C2-O} = 5.781	d_{C2-O} = 4.102	d_{C2-O} = 4.040
	d_{C1-C2} = 4.141	d_{C1-C2} = 6.910	d_{C1-C2} = 3.797	d_{C1-C2} = 4.895
End	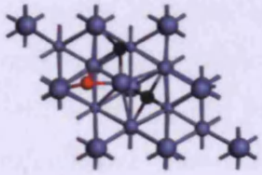	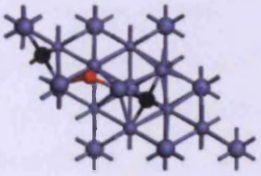	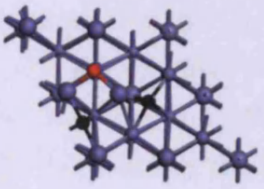	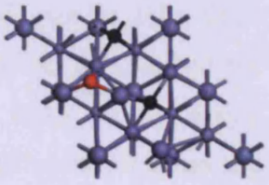
	E_{ads} = -1.38 (-1.31)	E_{ads} = -1.85 (-1.78)	E_{ads} = -1.71 (-1.63)	E_{ads} = -1.83 (-1.75)
	d_{C1-O} = 3.682	d_{C1-O} = 3.720	d_{C1-O} = 3.713	d_{C1-O} = 3.717
	d_{C2-O} = 2.776	d_{C2-O} = 3.020	d_{C2-O} = 2.944	d_{C2-O} = 3.187
	d_{C1-C2} = 3.214	d_{C1-C2} = 6.409	d_{C1-C2} = 3.870	d_{C1-C2} = 4.128
	E_a = 2.35	E_a = 2.17	E_a = 2.19	E_a = 2.15
	E_r = 0.41	E_r = -0.30	E_r = -0.14	E_r = -1.11

Notes: *a*) Adsorption energies (E_{ads}), activation energies (E_a) and reaction energies (E_r) are presented in eV and were calculated relative to clean Fe(111), gas phase CO and atomic C. Values are ZPE-corrected and values without zpe-corrections are given in parentheses. Distances are given in Å; θ is the tilting angle of the C-O axis relative to the surface normal in degrees.

The TS structures themselves are all similar to each other and to the clean surface TS: C is still in the original QFF position and O is terminally bonded to Fe1 making its way over (or around) it. TS + C(QP) is lower in energy than the other structures (by 0.13 – 0.20 eV) and the clean surface TS (by 0.14 eV). The remaining structures are all similar in energy compared to the clean surface. The activation energies of all the CO+C(QFF/QP) pathways (2.15 – 2.35 eV) are even higher than the clean surface value (2.10 eV); due to the lower adsorption energy of CO + C and/or the higher TS energy. Reaction energies are also higher compared to the clean surface, E_r = -0.34 eV (although CO + C(QFF2) is only slightly higher, E_r = -0.30 eV); but three out of the four reactions are still exothermic. The pathway starting from CO + C(QFF1) is endothermic by 0.41 eV due to the relatively high energy end structure.

3.4. Discussion

3.4.1. CO Adsorption on Clean Fe(111)

Adsorption Geometries and Energies

The geometries of our calculated minima (SH, TSH, BL, DB & OT) agree well with the earlier work by Chen,[7] but the adsorption energies are higher by ~0.3 eV (PBE), possibly due to our use of the projector augmented wave (PAW) representation of the core states rather than pseudopotentials. For CO in other systems use of the PAW method to represent core states has been shown to improve the treatment of magnetic transition metals considerably compared to ultra-soft pseudopotentials.[34] At low coverage (⅓ ML and ½ ML) Chen optimised only three stable adsorption states, OT, SH and BL;[7] and the TSH (called the *bridge site* in ref 7) and DH could only be optimized at 1ML (note that frequency calculations were not performed in that study). We find that the TSH and DH states are stable at both ¼ ML and 1 ML; however the DH is only a second order saddle point at both coverages. The QFF ts state seems to be similar to the μ^4-bridged CO optimized by Chen at 2 ML (the state was co-adsorbed with a μ^2-bridged CO state). The DOB ts state correlates to the triply capped CO that Chen optimized at 2 ML, co-adsorbed with a tilted OT state; the carbon atom is bonded to a Fe atom in each of the three surface layers and the oxygen atom interacts with a second Fe1 atom.

The DB state, calculated in this study, has not previously been reported. The state was obtained from a starting structure where the CO axis is completely parallel to the surface, as

optimized in the cluster calculations of Mehandru *et. al.*;[19] however, in our calculations the CO moved into a more upright position during optimization to have a final tilting angle of 57°. Nevertheless, according to our knowledge this state still has the largest tilting angle of any CO-Fe system calculated in DFT, with the nearest value found for CO on Fe(100), θ = 51°[12] (experimentally estimated values vary between 45 – 55°[23,25,26]).

C–O Stretch Frequencies

The C-O stretch frequencies calculated at ¼ ML & 1 ML are compared graphically with experimental values from HREELS[4-6] at low and high coverage in Figure 3.22. The calculated frequencies are in good agreement with the experimental values, even though the systems are somewhat different: Only one adsorption configuration was considered in calculations, while the experimental values correspond to mixed systems, especially at higher coverage.

The frequency values calculated for the SH ($\upsilon_{1/4ML}$ = 1758 cm^{-1} and υ_{1ML} = 1807 cm^{-1}) as well as the TSH ($\upsilon_{1/4ML}$ = 1736 cm^{-1} and υ_{1ML} = 1783 cm^{-1} (ts)) compare well with the experimental HREELS measurements (between 1760 – 1823 cm^{-1}) of the so-called *b* state obtained after 0.05 – 8.4 Langmuir[‡] gas exposure. Our data thus suggests that CO in the SH can easily tilt away from vertical and so is probably undergoing the corresponding rocking motion even at low temperatures so that both SH and TSH contribute to the experimental band.

The calculated frequency of the OT state ($\upsilon_{1/4ML}$ = 1893 cm^{-1} and υ_{1ML} = 1997 cm^{-1}) is in agreement with that of the experimentally defined *c* site, with a reported frequency of between 1940 and 2000 cm^{-1} (at low and high coverage).

[‡] 1L corresponds to an exposure of 10^{-6} torr for 1 second.

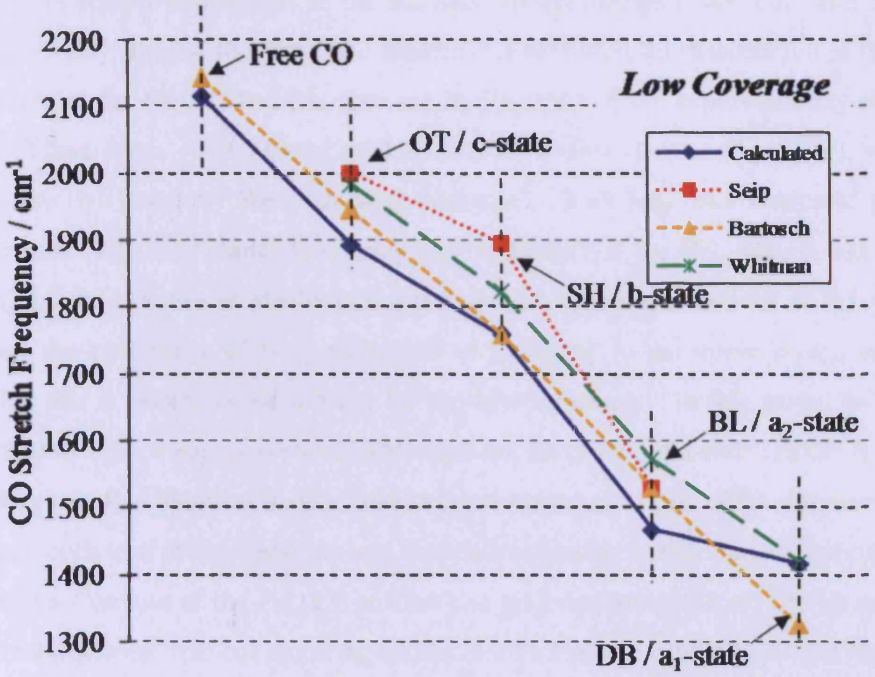

(a)

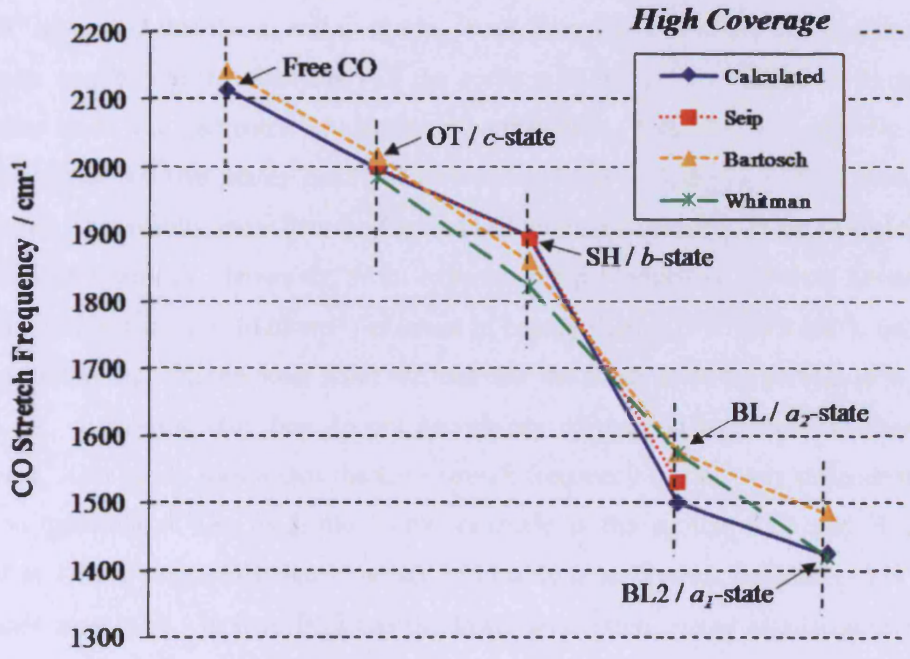

(b)

Figure 3.22 – *a*) Calculated CO stretch frequencies at ¼ ML compared to low coverage HREELS values.[4-6] *b*) The same at 1 ML (calculated) and high coverage (HREELS).

The low C–O stretch frequencies of the BL and DB geometries (1467 cm^{-1} and 1416 cm^{-1} respectively) may suggest that the C=O molecule is activated for dissociation at these sites. The frequencies for the BL and DB sites are in the range of the experimentally observed *a* states.[5, 6] These states yield a broad peak in HREELS (first observed by Seip[4]), which was resolved into two bands by Bartosch[5] and Whitman[6]. Both Seip[4] and Bartosch[5] postulated that the *a* state (with C-O stretch frequency near 1500 cm^{-1}) is the DH, since it was estimated that the CO would fit almost ideally into this hole with minimum diameter of 2.5 Å; the DH also offers the possibility of O coordination to Fe atoms in the upper layers, and it was argued that this is necessary to account for the low frequency. In this study, the DH state was calculated to be a *hsp*, and should therefore not be observable with HREELS (although our results show that the state is stabilized in the presence of ¼ ML of C). However, the BL and DB are both true minima and possess stretch frequencies in this range. Our calculations show that the structure of the Fe(111) surface can give rise to significant CO tilt angles, and so Fe...O interactions, without requiring access to a Fe3 atom. Both the BL and the DB sites actually place the molecule closer to second layer Fe atoms where the most favourable SH adsorption sites are located.

Bartosch[5] suggested that the a_1 and a_2 modes result from the same site with the difference in frequencies ascribed to the occupancy of the *c* site with the latter at higher coverages; this presumably leads to a geometric or electronic perturbation. This idea was supported by the observation that the two states readily inter-convert with a change in either coverage or temperature. Our results show that the BL and DB are indeed similar, in agreement with the postulation of Bartosch. However, from experiments performed at different coverages, it was suggested that a_1 ($\nu \sim 1420$ cm^{-1}) is lower in energy than a_2 ($\nu \sim 1573$ cm^{-1}), because a_1 populates before a_2. On the other hand we find that the BL is more favourable than the DB by ~0.3 eV, suggesting that they do not necessarily correspond to a_1 and a_2 observed in experiment. Our study shows that the C-O stretch frequency can be very dependent on the exact configuration of the molecule. One example is the similar BL1 and BL2 states obtained at 1 ML; suggesting that a variety of closely related states possessing low stretch frequencies may exist. In fact, BL2 has the lower adsorption energy and frequency (-1.43 eV RPBE, 1423 cm^{-1} *vs.* -1.41 eV RPBE, 1500 cm^{-1}) and this pair therefore reflects the experimental trend better (although a larger energy difference would be expected from experimental results).

It also needs to be emphasized that the experimental and calculated systems are different, in that surface impurities resulting from CO dissociation at low coverage will be present in

practice and will influence adsorption configurations and energies. This is especially noticeable in the calculated DH state, which is only a *hsp* on the clean surface, but a formal minimum in the presence of ¼ ML of C. This suggests that the DH might well exist under experimental conditions, since the first amount of incoming CO gas will most likely dissociate to atomic C & O even at low temperatures.

Transition States for CO Migration

The DSB, DOB and QFF were calculated to be transition states and the DH a higher order saddle point (for CO diffusion). The tilting angles and bond lengths of the DOB state are very similar to the threefold coordinated state on Fe(211)[14] calculated at ½ ML coverage: 39° *vs.* 40°; 1.289 Å *vs.* 1.280 Å. However, the DOB state is significantly less stable than the state on Fe(211): -1.19 eV (RPBE) *vs.* -1.92 eV (RPBE); ZPE not included. This might be due to the difference in the position of C: Carbon prefers highly coordinated sites; and on Fe(211) C is in close contact with three Fe atoms, whereas C in the DOB state is essentially in a DH position, which is a less favourable site for C. Saying that, the adsorption energy of this particular CO state on Fe(211) (-1.92 eV; RPBE at ½ ML) is lower than all of the values that we calculate for Fe(111) (-1.15 eV to -1.79 eV; RPBE, ZPE values not included).

CO Migration

In general it was found that barriers for CO diffusion across the surface are small, which should make movement between minima facile. Bartosch and Whitman proposed that site occupation at low temperature is a function of the relative sticking probabilities of the states and not a restriction to mobility. Only one diffusion barrier was estimated (through heating rate variation analysis), namely the OT to the SH. A barrier of 0.20 ± 0.02 eV was calculated, which is higher than the value we find (see Figure 3.10), but there was some uncertainty regarding the experimental measurement, especially since a very low pre-exponential factor was calculated ($\nu_1 = 10^{11\pm2}$ s^{-1}).

The following profile was constructed to illustrate potential paths that CO can follow across the surface and to show how the different states might relate to each other (however, diffusion is not restricted to these routes).

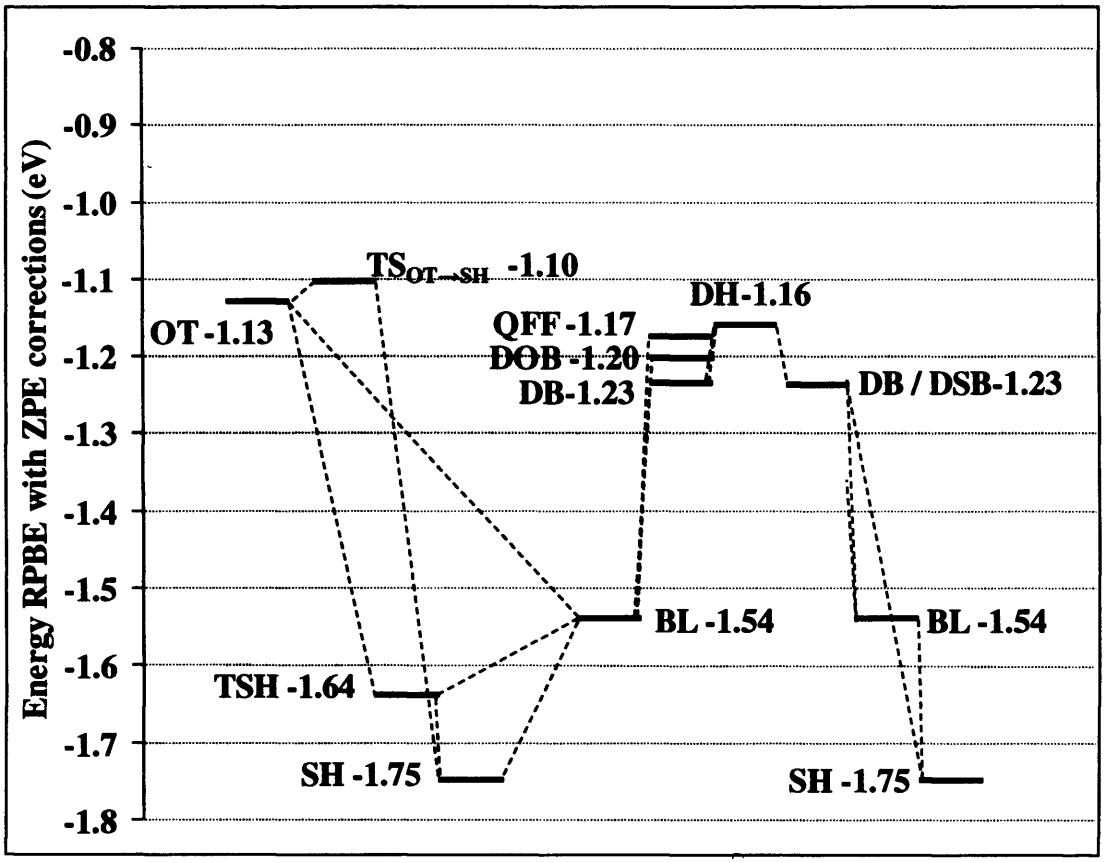

Figure 3.23 – Possible routes for diffusion of molecular CO across the surface.

3.4.2. The Adsorption of Atomic Carbon & Oxygen and CO Dissociation

Our results show that C prefers highly coordinated sites, in agreement with other studies on Fe surfaces. Sorescu *et.al.*[11] similarly found that on Fe(100) the stability of C decreases in the order fourfold > twofold > onefold sites; the strongest bound species had an adsorption energy of -8.07 eV (PW91), which is ≥ 1.4 eV lower in energy than other sites. O follows the same trend on Fe(100), but the adsorption energy difference between the fourfold and twofold species is only ~0.56 eV (-6.29 eV *vs.* -5.72 eV respectively). Adsorption of O is weaker than C by ~1.78 eV, whereas the difference calculated here is ~1.31 eV. Jiang[49] found that C on Fe(110) prefers the long bridge site (which again provides the highest coordination) while the short bridge and on top sites are not minima.

For CO dissociation we find that the starting structure does not generally affect the structure or energy of the transition state significantly (except in the case of the DB molecular state, which will be discussed shortly), but there is a connection between the TS structure/energy and the end state. Figure 3.24 illustrates the respective energies of the starting, TS and end

structures of the different pathways. The TS structures are divided into two groups in terms of energy. The higher energy group (E_{TS} = 0.54 – 0.95 eV) consists of pathways from SH, TSH or BL toward QFF-C & QFF-O, QFF-C & TSB-O or QFF-C & QFFμ^3-O. All of these pathways have TS structures with O in a terminally bonded position (represented by Figure 3.12*a* or *b*). This means that CO dissociation via these pathways is unlikely to be competitive with CO desorption except at high partial pressures of CO. The tilted molecular adsorption geometries all involve O interacting with the Fe1 surface atom and simply stretching the "activated" bond along the C=O direction would move along these high energy pathways.

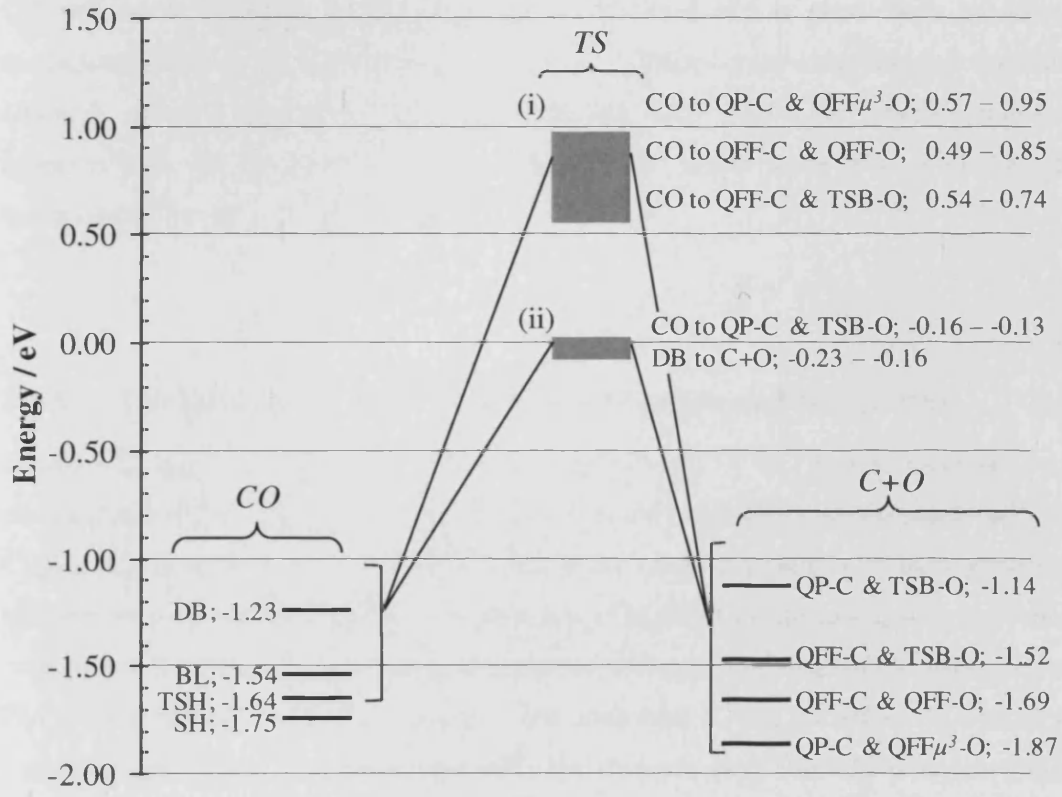

Figure 3.24 – Reaction barriers for CO dissociation on Fe(111). Energy values are relative to clean Fe(111) & gas phase CO; see Table 3.6 for specific values.

Figure 3.24 shows that the CO to QP-C & TSB-O TS is practically iso-energetic with the *CO(g) + clean Fe(111)* reference state so that the dissociation process via this pathway is competitive with molecular desorption. The lower energy group (E_{TS} = -0.23 – -0.13 eV) consists of all pathways towards this end state and all pathways from the DB starting structure. The distinguishing property of this low energy group is the fact that O in the TS

structure is in a bridged position. This notion is further supported by the fact that TS structures of type *d* in Figure 3.12 are also of low energy, despite the fact that adsorption of C in the DH site is expected to be highly unfavourable (DH C on its own could not be optimized, but move to the QFF site during optimisation). We also note that the barriers to migrate between molecular adsorption sites are significantly lower than any CO dissociation barrier so that the molecular sites will be in thermal equilibrium under conditions for which CO cleavage is observed. Given that the DB is the highest energy starting point the estimated barrier for the CO bond cleavage reaction is 1.07 eV. This is actually in remarkable agreement with that reported at low coverages by Whitman, 0.87 ± 0.22 eV.[6] The relative energies of the molecular and atomic adsorption states are quite close, suggesting a similar reverse barrier for CO reformation. At low coverages, then, molecular CO will move between the various minima identified and is most likely to enter the dissociation pathway from the DB site. However, Whitman gave a much higher estimate for atomic C and O to recombinatively desorb at 760 K (E ~ 2.08 eV) which would not be expected from the barriers illustrated in Figure 3.24, unless some process closes off the lower barrier for QP-C & TSB-O to CO.

3.4.3. The Influence of Carbon on CO Adsorption and Dissociation

Figure 3.18 indicates that the adsorption energy of the C + CO system increases as C is placed closer to CO. In Figure 3.18*f* (E_{ads} = -0.73 eV *vs.* -1.79 eV on the clean surface) the C(QFF)-C_{CO} bond length is 1.425 Å, which is in the range of a single C-C bond expected for hydrocarbons. The rise in energy with decreasing C(QFF)-C_{CO} distance is in agreement with experimental studies that have shown that the co-adsorption of C and CO results in weaker Fe-CO interaction.[50] Our results suggest that additional C will not affect the Fe-CO bond strength negatively if C is positioned a sufficient distance away from the molecule (which is likely at low coverage). In fact, in several cases the Fe-CO was strengthened in the presence of C. This is in agreement with results of Sorescu *et.al.*,[29] who found that C in the hollow site or subsurface of Fe(100) stabilises CO (as well as other co-adsorbates, such as C, O, H and CH_x). However, we find that placing the C and CO species too close together (which is inevitable at higher coverages) will result in a rise in energy of the system due to crowding.

Figure 3.25 shows the transition state barriers for CO dissociation in the presence of C. The group *ii* and *iii* transition states follow the same trend as the clean surface equivalents in terms of structure and energy. In addition the DH (which is now a formal minimum in the

presence of C) dissociates to QFF-C & TSHμ^3-O with the lowest energy barrier of all transitions on the clean and C modified surfaces.

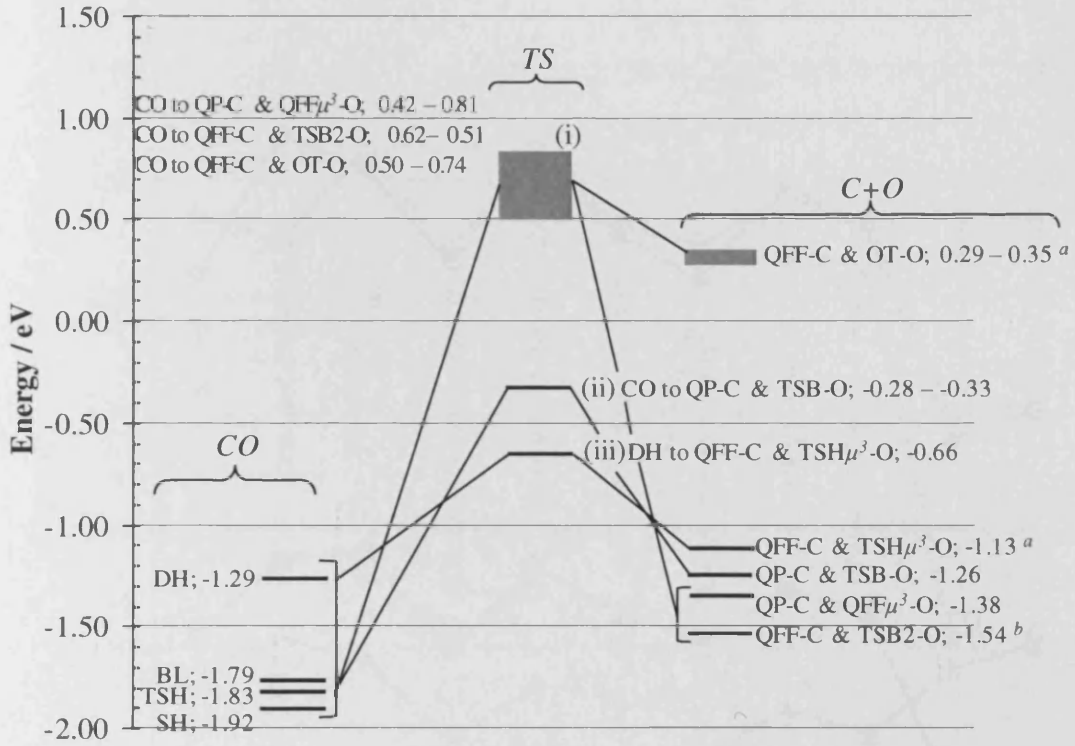

Figure 3.25 – Reaction barriers for CO dissociation on Fe(111) co-adsorbed with ¼ ML C. Energy values are relative to the carbided Fe(111) surface and gas phase CO; see Figure 3.24 to compare barriers on the clean surface.[a]

Notes: a) QFF-C & OT-O is equivalent to QFF-C & TSB-O on the clean surface.
b) The QFF-C & TSB-O (obtained when starting from SH, TSH or BL) and QFF-C & QFFμ^3-O (obtained when starting from DH) is equivalent to QFF-C & QFF-O on the clean surface.

Figure 3.26 is a graphic representation of the influence of carbon on the activation energy, TS adsorption energy and reaction energy of CO dissociation; the pathways starting from the DH or DB are not considered, since they do not exist on both surfaces. In general the TS adsorption energies are very similar to the clean surface equivalents (slightly higher or lower in some cases) and the pathways with the same end structures yield similar TS structures. The SH to QP-C & QFFμ^3-O pathway is the exception, since it has a lower TS adsorption energy compared to the clean surface (ΔE = -0.62 eV); on the C modified surface O is bridged, compared to being terminally bonded on the clean surface.

As on the clean surface the activation energy barriers for the CO to QP-C & TSB-O pathways are the lowest on the Fe/C surfaces (since the DH to QFF-C & TSHμ^3-O pathway

is not considered at present), but the values are somewhat higher in the presence of carbon. The reaction energies of the pathways on Fe(111)/C are all endothermic and considerably higher than on the clean surface, where some pathways are exothermic.

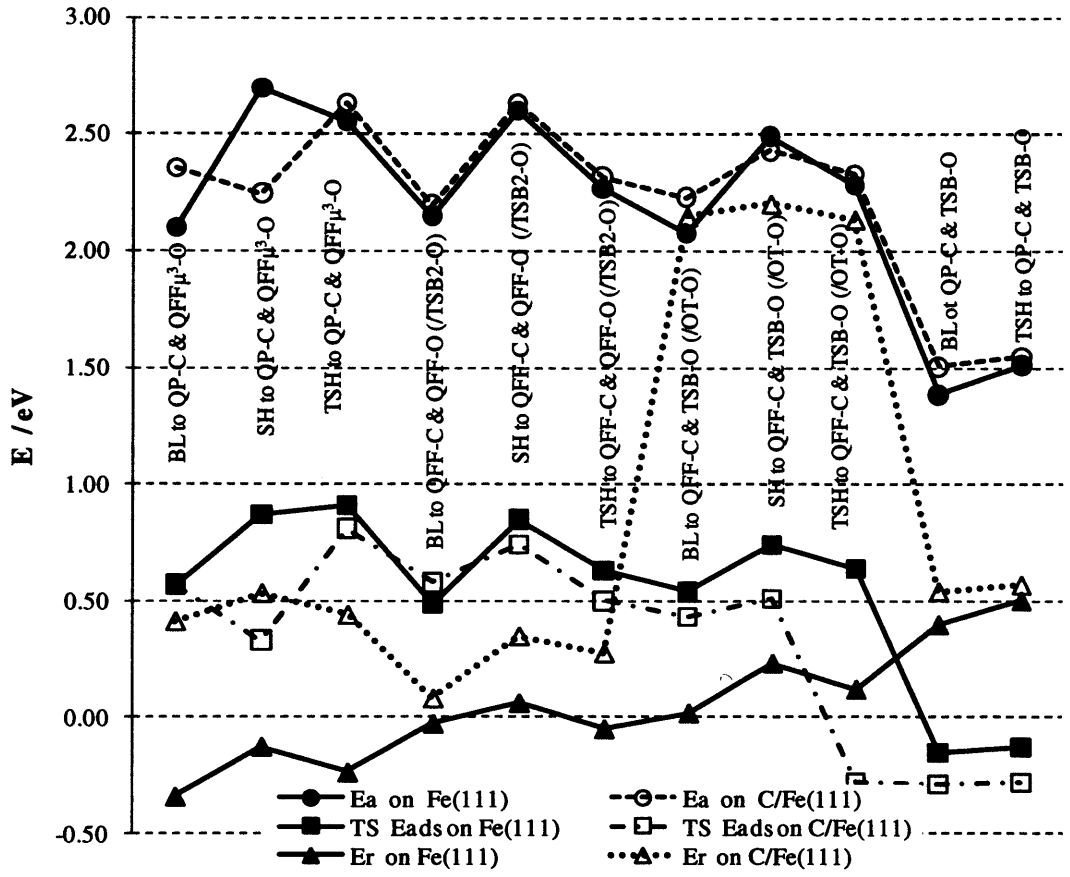

Figure 3.26 – TS adsorption energy (E_{ads}), activation energy (E_a) and reaction energy (E_r) of CO dissociation on Fe(111) with/without carbon.

Variation of the position of C(QFF/QP) (shown in Table 3.10) indicates that that C can either increase or decrease the adsorption energy of co-adsorbed CO (with ¼ ML C + ¼ ML CO on the surface). The most prominent influence of C is on the configurations of the dissociated species. Steric interaction between C(QFF/QP) and especially O can cause the atoms to move into less favourable adsorption sites, which increases the energy of the system. CO dissociation is more activated in the presence of C, even at ¼ ML coverage.

3.5. Summary

The first principle study in this chapter explored the adsorption, diffusion and dissociation of CO on Fe(111) with or without additional C. In accordance to previous studies the SH is found to be the most stable adsorption site for the molecular species. In addition, four other states are also minima: the TSH, BL, DB and OT (listed in order of stability). The DB has not previously been reported and exhibits the largest tilting angle (57°) of all states on this and the other Fe surfaces that have been studied with DFT up to date. CO migration across the surface is found to be facile. The barrier for CO dissociation is mainly a function of the configuration of the O atom in the TS – bridged states are more stable than terminally bonded configurations, which translate into lower activation energy barriers for dissociation. Pathways which meet this criterion are the CO to QP-C & TSB-O routes as well as all routes starting from the DB state; the latter proceed with activation energies of ~1 eV (RPBE).

¼ ML of additional C was shown to stabilize the CO molecule if close interaction is avoided, but C has a destabilizing effect on the dissociated species, since it frequently blocks the most favourable site for O adsorption, which forces both atoms into less favourable configurations. Barriers for dissociation pathways with / without C are generally similar, but since the DB state (which gives the lowest barrier on the clean surface, E_{act} ~ 1.00 eV) converts to the BL on the C/Fe(111) surface, these pathways are not available on the C/Fe(111) surface. On the other hand, The DH is a formal minimum in the presence of C and the barriers for at least two pathways from this state are significantly lower than the remaining routes. The barrier for DH to QFF-C & QFFμ^3O is only 0.63 eV, which is ~0.4 eV lower than the next lowest pathway on either the clean or carbided surface. This is due to the short, highly coordinated pathway that the atoms follow to reach the end states. The reaction energies of all CO dissociation pathways on C/Fe(111) are endothermic and significantly higher compared to the clean surface mainly due to the unfavourable end states, which should make CO dissociation on this surface rather improbable.

3.6. References

1. A. Steynberg and M. Dry, *Fischer-Tropsch Technology*, 2004, **Elsevier**.
2. A. P. Steynberg, R. L. Espinoza, B. Jager and A. C. Vosloo, *Appl. Cat. A*, 1999, **186**, 41-54.
3. D. Willock, *Molecular Symmetry*, Wiley, 2009.
4. U. Seip, M. C. Tsai, K. Christmann, J. Kuppers and G. Ertl, *Surface Science*, 1984, **39**, 29-42.
5. C. E. Bartosch, L. J. Whitman and W. Ho, *J. Chem. Phys.*, 1986, **85**, 1052.
6. L. J. Whitman, L. J. Richter, B. A. Gurney, J. S. Villarrubia and W. Ho, *J. Chem. Phys.*, 1989, **90**, 2050-2062.
7. Y.-H. Chen, D.-B. Cao, Y. Jun, Y.-W. Li, J. Wang and H. Jiao, *Chem. Phys. Lett.*, 2004, **400**, 35-41.
8. Z. Y. Ma, C. F. Huo, X. Y. Liao, Y. W. Li, J. Wang and H. Jiao, *J. Phys. Chem. C*, 2007, **111**, 4305-4314.
9. C.-F. Huo, J. Ren, Y.-W. Li, J. Wang and H. Jiao, *J. Cat.*, 2007, **249**, 174-184.
10. Y. Aray and J. Rodriguez, *Surface Science*, 1998, **405**, L532-L541.
11. D. C. Sorescu, D. L. Thompson, M. M. Hurley and C. F. Chabalowski, *Phys. Rev. B*, 2002, **66**, 035416.
12. T. C. Bromfield, D. Curulla Ferré and J. W. Niemantsverdriet, *ChemPhysChem*, 2005, **6**, 254-260.
13. D. E. Jiang and E. A. Carter, *Surface Science*, 2004, **570**, 167-177.
14. D. Borthwick, V. Fiorin, S. J. Jenkins and D. A. King, *Surf. Sci.*, 2008, **602**, 2325-2332.
15. D. C. Sorescu, *J. Phys. Chem. C*, 2008, **112**, 10472-10489.
16. X.-Y. Liao, D.-B. Cao, S.-G. Wang, Z.-Y. Ma, Y.-W. Li, J. Wang and H. Jiao, *Journal of Molecular Catalysis A: Chemical*, 2007, **269**, 169-178.
17. D.-B. Cao, F.-Q. Zhang, Y.-W. Li and H. Jiao, *J. Phys. Chem. B*, 2004, **108**, 9094-9104.
18. D.-B. Cao, F.-Q. Zhang, Y.-W. Li, J. Wang and H. Jiao, *J. Phys. Chem. B*, 2005, **109**, 10922-10935.
19. S. P. Mehandru and A. B. Anderson, *Surface Science*, 1988, **201**, 345-360.
20. J. P. Perdew, S. Burke and M. Ernzerhof, *Phys. Rev. Lett.*, 1996, **77**, 3865.
21. B. Hammer, L. B. Hansen and J. K. Nørskov, *Phys. Rev. B*, 1999, **59**, 7413.
22. S. D. Cameron and D. J. Dwyer, *Langmuir*, 1988, **4**, 282-288.
23. D. W. Moon, S. Cameron, F. Zaera, W. Eberhardt, R. Carr, S. L. Bernasek, J. L. Gland and D. J. Dwyer, *Surf. Sci. Lett.*, 1987, **180**, L123-L128.
24. D. W. Moon, S. L. Bernasek, J. P. Lu, J. L. Gland and D. J. Dwyer, *Surface Science*, 1987, **184**, 90-108.
25. R. S. Saiki, G. S. Herman, M. Yamada, J. Osterwalder and C. S. Fadley, *Physical Review Letters*, 1989, **63**, 283.
26. D. J. Dwyer, B. Rausenberger, J. P. Lu, S. L. Bernasek, D. A. Fischer, S. D. Cameron, D. H. Parker and J. L. Gland, *Surface Science*, 1989, **224**, 375-385.
27. S. Vendelbo, M. Johansson, D. Mowbray, M. Andersson, F. Abild-Pedersen, J. Nielsen, J. Nørskov and I. Chorkendorff, *Topics in Catalysis*, 2010, **53**, 357-364.
28. E. Shincho, C. Egawa, S. Naito and K. Tamaru, *Surface Science*, 1985, **149**, 1-16.
29. D. C. Sorescu, *Phys. Rev. B*, 2006, **73**, 155420.
30. S. J. Jenkins, *Surface Science*, 2006, **600**, 1431-1438.
31. P. Hohenber and W. Kohn, *Phys. Rev.*, 1964, **136**, B864.
32. W. Kohn and L. J. Sham, *Phys. Rev.*, 1965, **140**, A1133.
33. P. E. Blöchl, *Phys. Rev. B*, 1994, **50**, 17953.
34. G. Kresse and D. Joubert, *Phys. Rev. B*, 1999, **59**, 1758.
35. H. J. Monkhorst and J. D. Pack, *Phys. Rev. B*, 1976, **13**, 5188.

36. C. Kittel, *Introduction to Solid State Physics, 7th Ed.*, 1996, **Wiley, NY**.
37. H. C. Herper, E. Hoffmann and P. Entel, *Phys. Rev. B*, 1999, **60**, 3839.
38. M. Acet, H. Zahres, E. F. Wassermann and W. Pepperhoff, *Physical Review B*, 1994, **49**, 6012.
39. F. Abild-Pedersen and M. P. Andersson, *Surface Science*, 2007, **601**, 1747-1753.
40. T. Asada and K. Terakura, *Phys. Rev. B*, 1992, **46**, 13599.
41. A. Stibor, G. Kresse, A. Eichler and J. Hafner, *Surface Science*, 2002, **507-510**, 99-102.
42. P. Blonski and A. Kiejna, *Vacuum*, 2004, **74**, 179-183.
43. J. Sokolov, F. Jona and P. M. Marcus, *Phys. Rev. B*, 1986, **33**, 1397.
44. R. Wu and A. J. Freeman, *Phys. Rev. B*, 1993, **47**, 3904.
45. H. Wawra, *Z. Metallk.*, 1975, **66**, 395 & 492.
46. P. Blonski and A. Kiejna, *Surface Science*, 2007, **601**, 123-133.
47. K. P. Huber and G. Herzberg, *Molecular Spectra and molecular Structure, 4: Constants of Diatomic Molecules, Van Norstrantd Reinhold Co., NY*, 1979.
48. J. Sokolov, F. Jona and P. M. Marcus, *Solid State Commun.*, 1984, **49**, 307.
49. D. E. Jiang and E. A. Carter, *Phys. Rev. B.*, 2005, **71**, 045402.
50. J. Benziger and R. J. Madix, *Surf. Sci.*, 1980, **94**, 119-153.

CHAPTER 4

Surface Science of Fe(111) & Fe(110)

P.T.O.

4.1. Introduction

Iron is an active catalyst for FT synthesis. The nano-crystalline material consists of a variety of facets, some more effective than others in yielding the desired hydrocarbon products. However, it is impossible to determine the relative contributions of the different surfaces on the product spectrum under normal reaction conditions and to achieve this single crystals are studied. UHV surface science studies of single crystals allow one to monitor the characteristics of the metal itself as well as the individual facets, *i.e.* the structure, composition and reactivity of the particular surface can be examined. The influence of adatoms can also be studied in a controlled way.

This chapter presents results for two such single crystals, namely Fe(110) and Fe(111). In the first section the general structural features of the surfaces are reviewed followed by a literature survey of studies concerning the interaction of adsorbates relevant to this study.
In the first part of the *Results* section, the influence of common bulk contaminants on the structural properties of these surfaces will be discussed. The latter part of the results section describes the adsorption of ethene and oxygen. Ethene is a FT product and evidence have shown that methylene ($-CH_2$) and methylidyne ($-CH_3$) surface intermediates play a key role in chain growth processes.[1,2] Ethene is the smallest alkene and therefore useful in establishing some basic principles of alkene-iron interaction. Iron can easily be oxidized and it is thought that iron oxide plays a part in the production of certain FT products. The influence of oxygen on the oxidation state of iron will be illustrated.

4.1.1. Structural Parameters

The (111)-plane of iron is one of the more open single crystal surfaces with a lattice parameter of $a = b = 0.405$ nm and an angle of $\theta = 60°$ between the base vectors (as shown in Figure 4.1). The surface unit cell is unusually large; the diameter is >0.7 nm along the long diagonal between two Fe1 atoms (*i.e.* iron atoms in the top most surface layer) and the Fe2 / Fe3 atoms are also exposed to the environment. The density of the top layer is considerably lower than most other low-index single crystal metal planes as shown in the calculation below.

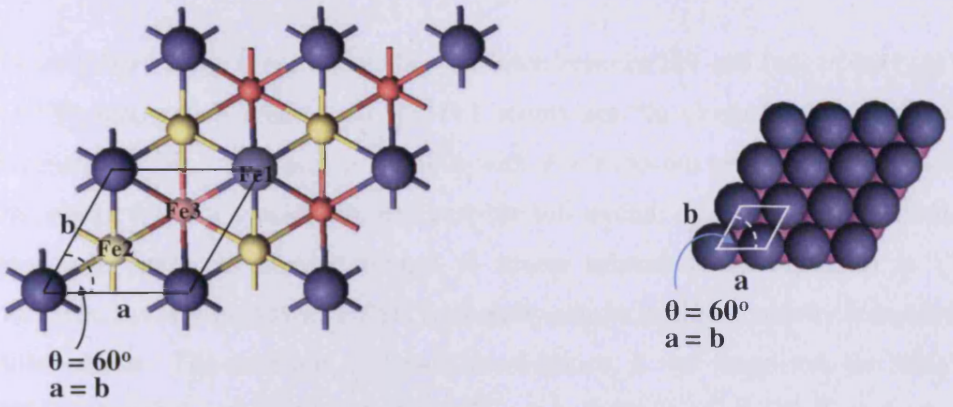

(a) (b)

Figure 4.1 – *a*) Diagram of the bcc(111) surface of iron; the solid black lines indicate the unit cell. The large purple balls represent topmost layer atoms (Fe1), yellow medium sized balls the second layer atoms (Fe2) and pink small balls the atoms in the third layer down (Fe3). *b*) The fcc(111) surface of iron. The surface is more dense than bcc(111) due to the smaller lattice parameter ($a_{fcc\_Fe(111)}$ = 0.254 nm *vs.* $a_{bcc\_Fe(111)}$ = 0.405 nm) and lower layers are therefore not exposed.

The shape of the bcc(111) unit cell is a rhombus, of which the area can be calculated by the equation

$$\text{Area} = a \times b \sin\theta \quad [4.1]$$
$$= 0.405 \text{ nm} \times 0.405 \text{ nm} \sin 60^\circ$$
$$= 0.142 \text{ nm}^2$$

Where a and b are the lattice parameters and θ the angle between them (see Figure 4.1*a*). Each unit cell contains one Fe1 atom, and the surface atom density, σ, is therefore

$$\sigma = \text{Nr. of atoms / Unit cell area}$$
$$= 1 / 0.142 \text{ nm}^2$$
$$= 7.04 \times 10^{18} \text{ atoms/m}^2$$

The fcc(111) iron surface is also a rhombus, with the same value for θ as bcc(111), but the lattice parameter is smaller, $a = b = 0.254$ nm (see Figure 4.1*b*). By substituting these values into equation 4.1 and calculating the surface atom density, one get $\sigma = 1.79 \times 10^{19}$ atoms/m^2. The iron fcc(111) surface is thus 2.54 times as dense as the corresponding bcc(111) surface. The Fe(100) surface, which is the second most open in the bcc series Fe(111) > Fe(100) > Fe(110), has a surface atom density of 1.22×10^{19} atoms/m^2.

The inter-layer spacing (*i.e.* the vertical distance between Fe1 and Fe2) of Fe(111) is small, d = 0.083 nm, which means that the Fe1 atoms are "in closer contact" with Fe2 atoms compared to other surfaces, *e.g.* Fe(100) with d = 0.143 nm or Fe(110) with d = 0.203 nm. The small interlayer spacing coupled with the low overall coordination number of the atoms themselves make the surface subject to severe relaxation (as explained in Chapter 3). Moreover, the low density of Fe(111) generally results in higher activity compared to denser Miller planes. For ammonia synthesis, for instance, it was found that the relative rate on Fe(111), Fe(100) and Fe(110) is 418 : 25 : 1.[3] In the case of CO dissociation however, surface geometry has a less severe effect. On Fe(100)[4] and Fe(111)[5] CO dissociates readily at room temperature (at small exposures), but on Fe(110)[6] CO will initially chemisorb molecularly and then dissociate slowly.

In contrast to the (111)-plane, the (110)-plane is the most closely packed of the bcc-surfaces (unit mesh shown in Figure 1.7 *c*). The structural parameters are a = 0.248 nm; θ = 70.52°, d = 0.203 nm; σ = 1.73×10^{19} atoms/m^2. As a consequence the surface relaxation (and generally also the reactivity) of Fe(110) is significantly less compared to Fe(111).

4.1.2. The Interaction of Adsorbates with Low Miller Index Fe Single Crystals[†]

Adsorbate Induced Reconstruction of the Metal Surface[7]

Before the development of the appropriate analysis techniques, the surface was seen as a rigid lattice, but surface science studies have revealed that the interface region (the top few layers of the surface) is mobile and responds to the presence of adsorbate atoms or molecules through structural modifications. The formation of a chemical bond between an adsorbate and a metal atom in the surface layer alters the local charge density experienced by the metal atoms. Moreover the effect on the surface will be dependent on the nature and density of the adsorbed layer. In general the surface layer atoms will restructure to reduce the local charge density.

Many atomic adsorbates prefer highly coordinated adsorption sites and both long and short range effects are driving forces for reconstruction. The adsorption of adsorbates can lead to changes in the lateral and vertical atomic arrangements of the first few atomic layers of the

[†] All XPS binding energy values reported are corrected against a Fe $2p_{3/2}$ at 706.7 eV.

substrate[8,9] or even more radical changes.[10] The resulting structure will be determined by the balance between the increase in adsorption energy on the reconstructed surface and the increase in surface energy caused by the adoption of a less than ideal configuration. Fe single crystal surfaces have been shown to reconstruct in the presence of adsorbates,[8,11,12] as discussed further below.

Carbon

The understanding of the interaction of Fe with carbon/hydrocarbons are of fundamental importance in fields such as Fisher-Tropsch catalysis and the steel industry. A relatively large body of work is reviewed here, since holds relevance for subsequent chapters too. For the purposes of this discussion the interaction of carbon with Fe is discussed separately from hydrocarbons or carbon oxides, but in practice of course the latter always leads to the former given the appropriate conditions. C dissolution in Fe is discussed further in Chapter 4.

α-Fe and C can coexist in one of two states depending on the C concentration and temperature of the system: a stable equilibrium state between α-Fe and graphite, or a metastable equilibrium state between α-Fe and Fe_3C. On clean iron surfaces (under UHV conditions) carbon is present as atomic (chemisorbed) carbon or graphite.[13-15] Graphite generally forms on the surface at particularly high C coverages and below the dissolution temperature.[15] Wiltner[16, 17] formed Fe_3C at the interface of a Fe single crystal and a C film that was deposited through vapour deposition from a graphite rod. Arabczyk[14] observed that when the Fe(111) surface is saturated with sulphur, graphite is prevented from nucleating on the surface; instead a three dimensional Fe_3C phase forms underneath the S layer.

Several authors have carried out XPS studies of C on Fe. Graphitic, chemisorbed and carbidic carbon are distinguishable with XPS, due to binding energy differences.[‡] Assuming that relaxation effects can be neglected for the C 1s level, the chemical shift to lower binding energies exhibited by chemisorbed/carbidic carbon (compared to graphite) suggests an electron transfer from Fe to C. Comparison of these binding energies indicates that the charge transfer is stronger for chemisorbed carbon (~2 eV) than for carbon in carbides (~0.9 – 1.3eV) and no charge transfer occurs for graphitic carbon on Fe. However, the interaction with secondary metals in (Fe, Cr) and (Fe, Mn)-carbides also needs to be taken into account.

[‡] Some authors refer to chemisorbed carbon as carbide, but the term chemisorbed carbon is used here (as in ref. 13 to distinguish the phase from bulk carbide, which has a higher XPS binding energy. Chemisorbed carbon may be thought of as surface carbide

Some reported binding energies for carbon species obtained with XPS are reported in Table 4.1.

Table 4.1 – C 1s binding energies (eV) reported in literature.

Chemisorbed	Carbidic	Graphitic	Dosing Method and Surface	Ref
282.6	283.5 – (Fe,Cr)C;[a] 283.1 – (Fe,Mn)C[a]	284.6	Gas-phase carburization, segregation on Fe(100)	13
282.6[b]	283.5 "phase II", carbidic C layer with bonded H	284.3	CO hydrogenation on Fe(110)	18
—	—	284.7	Solid graphite	19
282.7	283.5 – Fe_3C[a]	284.1	Gas-phase carburization, segregation on Fe(111)	14
	283.4 – Fe_3C[a]		Graphite vapour deposition on Fe(100)	16

Notes: a) C 1s BE values of natural iron carbide samples used as comparison for carbon doped iron crystals. *b)* This species was referred to as carbidic in the reference.

Studies of Arabczyk *et. al.*[20] have shown that defect sites in an α-Fe monocrystalline sample are more favourable for accommodating carbon than the surface sites. This is in contrast to sulphur, which prefers the surface sites.

Carbon segregation in an α-Fe(111) single crystal was studied with AES (to investigate the chemical composition and local density of states of the surface), XPS (to analyze the chemical binding states) and LEED (to characterize the surface structure).[21] Carbon was introduced into the sample by methane ion bombardment. The segregation process changed with increasing carbon coverage: θ = 1 resulted in adsorption of atomic carbon; θ = 2 resulted in the formation of chemisorbed molecules, C_2^*; and higher coverages resulted in three-dimensional graphite. The graphite domains on the Fe surface are oriented in a manner where an angle of 13.5° between the $[1\bar{1}0]$ Fe and $[10\bar{1}0]$ graphite is formed.

A STM/LEED investigation by Fujii showed that segregated carbon (or phosphor) can form surface structures with short and long range order on Fe(100); some STM and LEED images

from the study are shown in Figure 4.2.[22] Carbon caused a c(2×2) reconstruction at 573 K (as indicated by LEED). Between 650 – 850 K a $c(2\sqrt{3}\times\sqrt{2})$ reconstruction, based on carbon lines in a zigzag arrangement, was observed. The chains of carbon were typically 2 nm long after which it either broke or changed direction by 90°. AES showed that carbidic carbon was present on the surface.

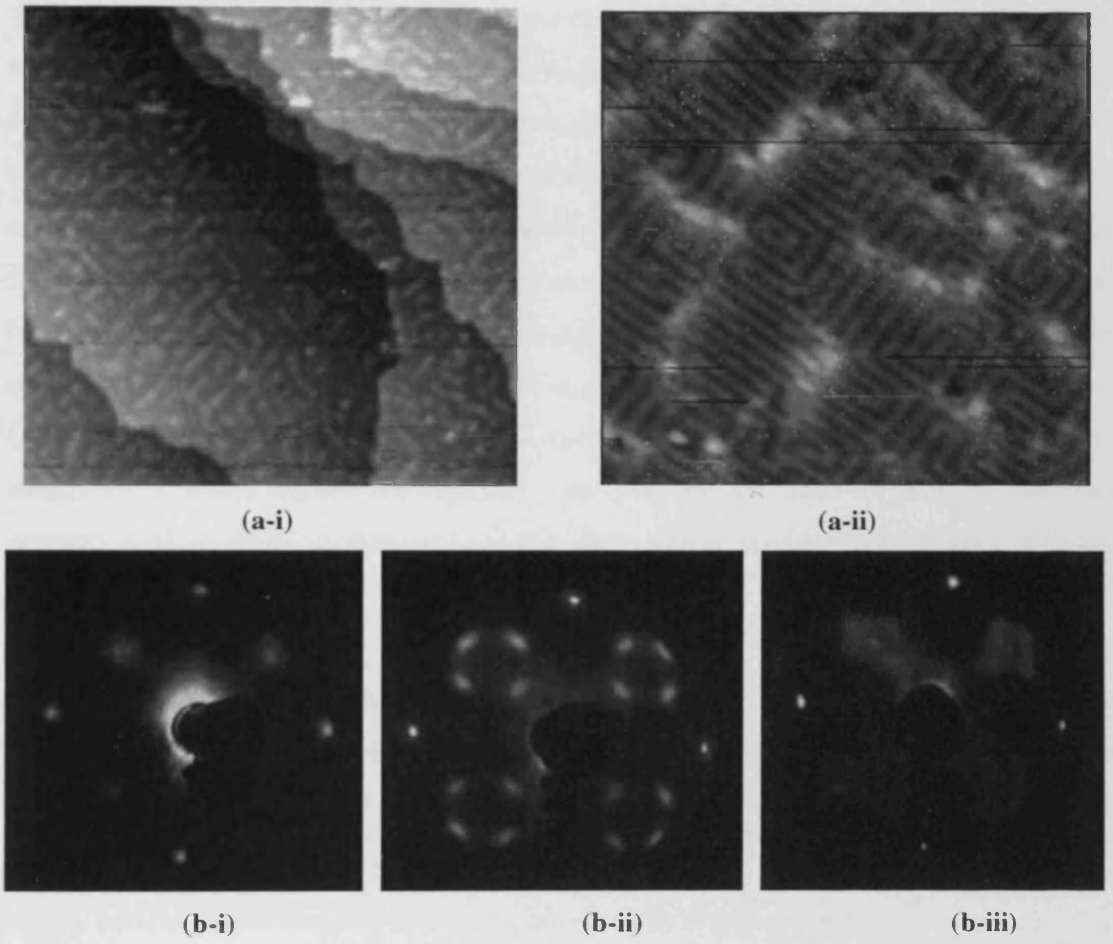

Figure 4.2 – *a*) STM images of ordered C structures on Fe(100) consisting of zigzag chains. *a-i*) size = 82.5 nm^2, *a-ii*) size = 16.5 nm^2. *b*) LEED images of the surface after annealing to different temperatures; *b-i*) broad c(2×2) structure after annealing at 573 K; *b-ii*) $c(3\sqrt{2}\times\sqrt{2})$ after annealing at 823 K; *b-iii*) after annealing to 948 K.[22,23]

On Fe(100) the only LEED pattern observed for C, N or S within the solid solution range was c(2×2); indicating that only one adsorption structure is thermodynamically stable for each system.[24] The additional diffraction spots of S were very sharp, but those of C and N were diffuse and split into a square of four spots. The splitting indicates that the c(2×2) structures are not as well ordered as in the case of S, but include many anti-phase domain

boundaries. Since only the additional spots are split, it can be concluded that adatoms occupy sites of the same symmetry as the basic lattices. It is most probable that the C atoms are placed in the fourfold hollow sites to be embedded between four iron atoms. These sites are large enough to accommodate the C atoms and would result in the closest interaction with Fe. This notion is supported by reaction kinetics of the carburization of the Fe crystal and from the low "shadowing effect" of carbon on the low energy Auger electrons from Fe.

Wiltner *et. al.*[16] studied carbide formation on various metals including W, Ti, Si and Be which showed exothermic carbide formation as well as Fe and Ni (with Fe(100) and Ni(111) used as substrates), which exhibited endothermic carbide formation. The onset of carbide formation and the amount of carbide detected depends on both the thermodynamic properties and the structures of the respective elements and carbides. Fe and Ni have similar carbide structures (comparing Ni_3C and Fe_3C) and metal substrates have to rearrange during carbide formation. Fe rearrange from bcc into a complex orthorhombic structure with C in a trigonal site. Ni rearrange from fcc into a trigonal structure with hexagonal close packing of Ni and C in the octahedral sites. Even though carbide formation is endothermic for these two substrates, a small amount of carbide was observed on both Fe and Ni after vapour deposition of graphite at 300 K; however the carbide fraction was smaller than on the exothermic carbides.

Several authors have reported a complex LEED pattern of C on Fe(110) for a range of coverages (*e.g.* AES C/Fe = 0.2 – 0.6);[6, 25,26,15,27] the pattern has later become known as the "carbon ring" pattern and the notation $\begin{vmatrix} 4 & 0 \\ -1 & 3 \end{vmatrix}$ was assigned to it. Atomic N results in a similar pattern, but in the case of C the spots are split in two or four.

Hydrocarbons

Yoshida *et. al.* reported that adsorption of C_2H_2 at ~270 K caused the integral diffraction pattern of Fe(111) to weaken.[27] The diffraction spot intensities became successively weaker on heating up to 600 K. At 600 K the spots became well-defined again and a new streak pattern appeared which converted to a diffuse (3×3) pattern. Flashing to 850 K resulted in the (1×1) pattern, but AES showed that the surface contained a lot of C. Repeated adsorption and flashing resulted in a (5×5) pattern which converted to the (3×3) upon heating. Both C_2H_2 and C_2H_4 gave the same flash desorption peaks – a C_2H_2 peak at 370 K

and a broad H_2 peak at 400 K. CO and CO_2 produced flash desorption peaks at ~370 K, 420 K and 700 K.[27]

C (as well as O) only had a site-blocking effect on the adsorption of C_2H_2 on Fe(111) – the total uptake was reduced without any further noticeable influence on the thermal or vibrational properties of the adsorbed species.[28] Pre-adsorbed C prevented dissociation of C_2H_4 on the surface; EELS spectra after C_2H_4 adsorption indicated at least two bonding geometries for the molecule. The dissociation energy of C_2H_4 was lowered and in parallel the activation energy for decomposition was increased. The change in the TPD spectrum indicates a change in the electronic structure of the surface due to the pre-adsorbed C. The presence of the strongly bonded C_2H_4 state indicates that adsorbed C atoms still allow some C_2H_4-Fe interaction. The weakly bonded C_2H_4 state was correlated to adsorption on the Fe1 atom; C blocks these sites and therefore only allows weak π-interaction. The weakly bonded state existed at adsorption at 120 K. Flashing the surface to 190 K caused the weakly adsorbed state to desorb and flashing to 250 K resulted in the complete desorption of C_2H_4. It was concluded that relatively small differences in geometric and electronic properties of both the hydrocarbon and the metal surface influence the chemisorption behaviour of the hydrocarbons.

Yoshida *et. al.* & Somorjai *et. al.* both studied the chemisorption of CO, CO_2, C_2H_2, and C_2H_4 on Fe(111) and Fe(110) with LEED and TPD.[27] These adsorbates readily decompose to fragments (mostly carbon) which lead to the same sequence of surface structures as function of temperature. C-C bond scission occurs at ~300 K in both C_2H_2 and C_2H_4. The complexity of the structural chemistry would suggest the co-existence of different hydrocarbon segments and successive changes of bonding position as the temperature is increased.

Benziger *et. al.* dehydrogenated C_2H_4 on Fe(100) by adsorbing it at 200 K and heating to 400 K. This resulted in the evolution of H_2 from the surface and the formation of a c(2×2)-C overlayer (θ = ½ ML).[29] Continued heating above 400 K caused C to diffuse into the crystal as evidenced by a decrease in the intensity of the half-order diffraction spots in the LEED pattern and a decrease in the C 1s photoelectron emission.

Adsorption of C_2H_2 and C_2H_4 on Fe(100) occurs with C-C bond scission, even at low temperatures to yield CH_n (n = 1,2) surface species.[30] A weakly bonded molecular layer can adsorb above the layer of chemisorbed fragments or pre-adsorbed C / O atoms.

Perturbations of the nonbonding σ-levels were observed with UPS, implying geometrical distortions due to the stretching and bending of the weakly chemisorbed molecules. The degree of distortion serves as a measure of the reactivity of the surface toward the unsaturated molecules. It was proposed that π forward and back-bonding interactions with clean Fe weaken and stretch the C-C bonds of simple olefins to such an extent that C-C scission is induced.

Unlike on Fe(100) UPS studies of C_2H_2 adsorbed on Fe(110) at room temperature showed that the molecule adsorbs without geometrical distortion or rehybridization.[6] The molecule dehydrogenates when heated (dehydrogenation is complete by 473 K) and results in a carbidic C Auger-peak (C/Fe = 0.2) and the complex LEED pattern. C_2H_2 dosed at ~500 K resulted in graphite formation on the surface – a large C peak with graphitic line shape appeared in the Auger spectrum (C/Fe = 2.6) and the LEED pattern showed two concentric, continuous rings similar to that found for graphite on Pt.[6] The AES signal did not change with increased exposure or temperature up to 673 K. Heating at 718 K for 300 s caused the LEED to revert to the complex pattern and the Auger carbide line shape to reappear (C/Fe = 0.6). The process could be repeated and reversed, but the carbide surface did inhibit graphite formation from acetylene dehydrogenation and the decomposition of the surface carbide somewhat. Monitoring the C signal with temperature suggested that surface graphite facilitates carbide dissolution.

In contrast to the findings of Bróden,[6] HREELS studies of C_2H_2 and C_2H_4 on Fe(110) by Erley[31] suggested a strong distortion of C_2H_2 and C_2H_4 close to the sp^3 hybridization state. Both species bonded molecularly in the triangular adsorption site at 120 K. Above 340 K C_2H_2 starts to decompose leading to the formation of CH_x intermediates and a complete loss of hydrogen above 540 K; C_2H_4 starts to decompose into C_2H_2 and H_2 below 300 K, which is complete by ~315 K. The thermal desorption peaks of H_2 were found at lower temperatures than reported by Yoshida *et. al.*; 340 K and 440 K (*vs.* 400 K and 470 K) and in addition a peak at 630 K was obtained;[27] the latter was correlated to the complete rupture of the C-H bonds. The peak at 440 K was attributed to C-C bond scission which leads to the formation of CH surface species.

Adsorbed on Fe(110) at 270 K – 320 K C_2H_2 or C_2H_4 yielded poorly ordered $p(2\times2)$ surface structures that do not change with increased exposure.[6, 15, 27] Adsorption at 400 K produced a streaky (1×3) structure (and a poorly ordered (1×1) structure with increased exposures).[27] Flashing the surface to 600 K produced a coincident pattern and flashing to 700 K caused

conversion to the carbon ring pattern. Flashing to 1050 K didn't cause the carbon to diffuse into the bulk or be removed in any other way in contrast to CO which recombined above 800 K and desorbed from the surface. Flash desorption peaks for C_2H_4 included that of molecular C_2H_2 at ~320 K and H_2 at 400 K and 470 K; a similar profile was obtained after adsorption of C_2H_4 and the desorption of molecular C_2H_4 could not be established.

Bonzel studied the chemical nature of carbonaceous deposits on Fe(110).[18] The single crystal was exposed to continuous flow of CO/H_2 at 1 bar total pressure in a micro-reactor. The crystal was heated to a certain temperature to synthesize hydrocarbons and carbonaceous layers in the process. After a certain amount of time (15 sec – 10 min) the crystal was cooled and immediately transferred to a UHV system equipped with AES and XPS. Three significantly different carbonaceous layers were observed depending on the process conditions. Characterization was done with AES and XPS and the phases were distinguished in terms of the C 1s XPS binding energy and the C AES peak shape: a CH_x phase with a C 1s binding energy of 283.2 eV; a carbidic carbon-hydrogen phase at 283.5 eV; and graphitic carbon at 284.0 – 284.3 eV (depending on the amount of intercalated hydrogen. The CH_x phase was unstable in UHV after a period of 50 min and very unstable under electron irradiation. Both the CH_x and carbidic phases were active toward hydrogenation whereas the graphitic carbon was inactive under the chosen experimental conditions.

Carbon Oxides

The interaction of CO/CO_2 with Fe surfaces has also been the subject of many fundamental studies, since it is crucial to reactions like Fischer-Tropsch synthesis, methanation and water-gas shift (WGS).

Dissociation of adsorbed CO on Fe(111) leads to the formation of a 'carbide-oxide' layer.[32] Low exposures (< 1L) results in a single XPS C 1s peak at 282.8 eV, the same as for surface carbide. The valence orbital spectrum shows an increase in emission at -5.7 eV. This value corresponds to that of a carbide layer which is formed by heating adsorbed C_2H_4 to 650 K; while the value for molecularly adsorbed CO is 2 eV higher. Molecular adsorption occurs at higher exposure on single sites, when pairs of adjacent sites on the surface are no longer vacant to allow CO dissociation to proceed. Yoshida *et. al.* reported that CO adsorption at 300 K resulted in a broadening of the iron integral order spots, suggesting that CO forms

small domains of (1×1) structure.[27] The same series of LEED patterns were observed as for C_2H_2 and C_2H_4.

When the Fe(111) surface with a complete layer of CO (some dissociated, some molecular) was exposed to 4×10^{-6} mbar of H_2 at 300 K no reaction or change occurred.[32] This was repeated at 470 K, which caused the C 1s peak of molecular CO to decrease rapidly, but the C 1s peak of dissociated CO remained unchanged.

Benziger *et. al.* found that several molecular binding states of CO as well as dissociated CO co-exist on Fe(100) at room temperature, but only dissociated CO was found above 400 K.[4] Dissociated CO gives C 1s / O 1s binding energies of 282.0 eV and 529.9 eV respectively; whereas these values are higher for molecular CO: 284.5 eV and 531.0 eV. The activation energy for dissociation of adsorbed molecular CO was determined as 105 kJ/mol.

Benziger *et. al.* also studied the effect of pre-adsorbed C on the adsorption of CO and H_2 (on Fe(100)) [4] A C adlayer posed a barrier for CO adsorption and reduced the sticking probability of CO at 150 K from ~1 on the clean surface to ~0.2 on the c(2×2)-C surface. However, the effect of C was much smaller than that of the c(2×2)-S surface, which resulted in a sticking probability < 10^{-4}. The strength of the CO-Fe bond was weakened by the presence of pre-adsorbed C as shown by the XPS binding energy which increased from 284.0 eV on the clean surface to 284.5 eV on C/Fe(100). The greater effect of S on CO adsorption compared to that of C or O was said to be due to the size difference between the adatoms. Sulphur, which is a large atom, is positioned higher above the surface plane and can therefore interact strongly with adsorbed CO. C and O are much smaller and sit deep in the plane of the surface, causing them to interact only weakly with adsorbed CO.

The adsorption of CO or CO_2 on Fe(110) resulted in a split c(2×2) pattern at 300 K and a super structure of c(2×2) and split c(2×2) at 400 K. Increased exposures caused c(2×2) to convert to a (1×4) pattern.[27] Flashing to ~500 K after CO adsorption resulted in the $\begin{vmatrix} 4 & 0 \\ -1 & 3 \end{vmatrix}$ pattern which disappeared at 800 K to give way to (1×1)-C,O or (2×2)-C,O structures. Flash desorption peaks of CO was observed at 320 K, 400 K and 700 K; and CO_2 gave a similar profile.

CO chemisorbs molecularly on Fe(110) at 320 K and dissociates slowly over time.[6] Only dissociative CO adsorption was observed at 385 K. In contrast, dissociative adsorption

occurs on Fe(100) at and even slightly below room temperature.[4] When CO was adsorbed on Fe(110) at low temperatures, no additional spots were seen in the LEED pattern, however, subsequent heating to > 450K or adsorption > 400K led to a well-developed c(2×2) LEED pattern. Further heating to > 800K led to the desorption of molecular CO and restoration of the clean surface.[29] LEED intensity analysis concluded that the c(2×2) LEED structure is due to the random occupation of C/O atoms in every second fourfold hollow site. The binding energy values of C 1s and O 1s was the same as for a surface carbide and oxide.

Oxygen

Iron oxidation studies are numerous due to the wide application of the oxides, *ex.* catalysis, paint pigments, the polishing of precious metals, and the insulation of magnetic tapes and low-capacity disks in the computer industry.[33] Iron oxides can take on many forms depending on the relative amount of O and Fe in the compounds. Oxide growth is sensitive to surface temperature and exposure and a variety of oxide structures can form depending on the conditions.[34-36] Some of these phases are wustite (FeO), magnetite (FeO + Fe_2O_3 or Fe_3O_4) and haematite (Fe_2O_3).

Seip *et. al.*[28] reported that exposure of Fe(111) to 1L of O_2 followed by annealing at 550 K leads to complete oxidation of the surface; a (6×6) LEED pattern was observed. Arabczyk[37] reported the Fe(111)(1×1)-O LEED pattern and Qin[38] reported a $(2\sqrt{3}\times 2\sqrt{3})$ pattern for 0.1 ML of oxygen; Lin[11] also reported this LEED pattern for a similar O coverage. Qin[38] showed that the oxidation of Fe(111) (P ~ 5×10^{-7} mbar) results in the formation of a Fe_2O_3-Fe_2O_3 mixture at 300 K, but predominantly Fe_3O_4 was formed at 500 K. STM showed that oxidation at 300 K resulted in a uniformly covered surface with relatively small oxide islands (5 – 15 nm in diameter), while oxidation at 500 K resulted in large oxide islands of width 100 – 300 nm.

Benziger *et. al.* reported a (1×1)–O LEED pattern on Fe(100) that was obtained by dosing O_2 while maintaining a surface temperature of 800 K.[29] No change in LEED pattern, Auger spectrum or XPS intensity was observed with further exposure to O_2 at this temperature. No trace of Fe^{2+} or Fe^{3+} was indicated by XPS; however exposure at room temperature resulted in the formation of Fe_2O_3. LEED intensity analysis of the (1×1)–O LEED structure showed the oxygen atoms to occupy every fourfold interstitial site.

LEED studies have shown that ¼ ML of O on Fe(110) produces a $p(2\times2)$ structure at room temperature[6] (labelled c(2×2) by some);[39, 40, 41] while EELS experiments indicted that the O-atoms are adsorbed in the long bridge sites.[42] At ~0.34 ML coverage a (3×1) pattern is formed of which the spots split between 0.34 – ½ ML. Wight *et. al.* reported that oxygen coverages higher than 0.34 ML results in a diffuse (1×1) pattern.[39] UPS measurements suggested that oxygen chemisorbs onto the Fe surface when the coverage is lower than 0.4 ML; but at higher coverages it starts to penetrate into the bulk to form an oxide.[40] EELS indicated that the O atoms are situated in the threefold hollow sites at these higher coverages. Erley reported a (5×12) LEED pattern almost identical to that of FeO(111) and attributed it to a mixed Fe-O surface structure.[42]

Hodgson *et. al.*[43] showed that the dissociative chemisorption of O_2 on Fe(110) is facile with an initial sticking coefficient of ~0.3 (translational energy of 50 meV) at room temperature. The sticking probability is sensitive to the surface temperature – at room temperature the saturation coverage is ~1ML while at 160K it is nearly 4ML.

Wight *et. al.*[39] studied the chemisorption of O_2 on Fe(110) by means of STM, LEED and sticking measurements. The sticking probability of O_2 decreases steadily with coverage to a minimum of 0.03 – 0.06 at $\theta = 0.4$, which coincided with the onset of FeO nucleation. At higher coverages the sticking increases slightly and then decreases at $\theta > 1$. STM images of the surface with O coverage > ¼ ML showed small single step features which were attributed to FeO. Above 0.4 ML the size and density of the FeO islands increased and developed into a surface with a LEED pattern characteristic of FeO(111).

Sulphur hinders the oxidation of Fe, but the presence of potassium cancels this inhibiting effect.[37,47] On the other hand the presence of potassium on Fe(110) without sulphur has been shown to cause an increase in the sticking probability of O_2 from 0.13 to 1. Co-adsorption of 0.28 ML of K and ½ ML of O gave an ordered c(4×2) LEED pattern. The chemisorption may be followed by the penetration of oxygen into the subsurface region prior to oxide formation regardless of the presence of K.[40]

Sulphur

Sulphur is a common contaminant found in Fe and also a severe poison for Fe catalysts (whether from the bulk or gases like H_2S).[44-46] For this reason, the S-Fe system has been the subject of many surface science/catalytic studies.

Lin *et. al.*[11] reported S induced faceting of Fe(111). At low coverages of S (adsorbed with N & O) a complex clock LEED structure was observed and STM showed that the surface consisted of triangular terraces and mounds. Terraces were typically ~140 nm in diameter and separated by steps as high as 5 nm. Annealing the crystal above 700 K increases S segregation from the bulk and results in a (1×1)-S LEED pattern. The surface now consists of planes with monatomic steps spaced ~10 nm apart. Further annealing and higher S coverages transforms the (1×1) LEED pattern into a $(2\sqrt{3}\times1)$ structure. STM revealed that the surface had a "staircase topography". Triangular pits of varying sizes, as deep as 5 nm and as long as 80 nm were aligned along the <110> directions of the surface.

Benziger *et. al.* reported a Fe(100)-c(2×2)-S LEED structure for ½ ML of surface S obtained through segregation from the bulk.[4]

Kelemen[21] deposited S onto Fe(110) through H_2S decomposition at 423K. The initial sticking probability was near unity and the coverage was limited to the surface. At low H_2S exposures a *p*(2×2)-S LEED pattern was obtained with a corresponding maximum AES S/Fe ratio of 2.5; the actual coverage was assumed to be ¼ ML. At higher exposures the c(3×1)-S pattern was obtained (AES S/Fe = 3.9); the actual coverage was assumed to be $^1/_3$ ML. Intermediate exposures led to the superposition of the two structures (coverage calculated to be 0.67). Sulphur segregation from the bulk was also employed, but coverages were less controlled and structures less stable; presumably due to the formation of a three dimensional sulphur phase. Several LEED structures were obtained as a function of S concentration (in agreement with the findings of Gafner *et. al.*[26]) with streaking and extra spots in the c(n×1) direction indicating the existence of a number of poorly ordered phases.

LEED diffraction intensity analysis by Shih *et. al.*[8] showed that ¼ ML of S on Fe(110) leads to a 2×2 reconstruction. The S atom is situated in a fourfold hollow site which is enlarged by contracting other fourfold hollow sites.

A pre-carbided Fe(110) surface readily adsorbs sulphur (from H_2S),[15] but no change in LEED structure was observed other than the increased background intensity. The C AES signal decreased almost linearly with sulphur coverage up to saturation at $^1/_3$ ML. It was established that the enthalpy of C segregation decreases with S coverage from a maximum of 117 kJ/mol to a minimum of 88 kJ/mol. As for S on the clean surface, the c(3×1) pattern was obtained at $^1/_3$ ML. The only other ordered surface observed was the c(18×3) at θ_S = 0.78. When this surface was heated to 633 K a reversible change in C concentration

occurred accompanied by the transformation of the c(18×3) to the c(3×1) structure, implying interaction between C, Fe and S can produce novel states not predicted by thermodynamics. In agreement with these results, Arabczyk *et. al.* found that C segregation does not influence S segregation, but S segregation influences C segregation strongly.[21] If the Fe surface is covered with S, C is prevented from reaching the surface and nucleating. Instead C segregation toward the surface results in the formation of a three dimensional cementite structure underneath the S layer.

4.2. Aims and Difficulties

One of the main aims of this work was to study the adsorption and reactivity properties of Fe(111). As can be seen from the literature review above there are actually relatively little previous work on Fe(111), and on iron single crystals in general. One of the reasons for this may be the great difficulty of cleaning iron single crystals,[47] which are of intrinsically low purity compared to many other single crystals. In some ways the peak of research on Fe was in the late 1970's and 1980's which includes work of Ertl *et. al.*[5,28,48-56] and Somorjai *et. al.*, [3,12,27,57-60] which mostly focused on N_2 and NH_3 adsorption. Moreover, the subject of many of the remaining studies has been the bulk contaminants themselves.[11, 15,20, 36, 61-67] Accordingly a large part of this chapter deals with the difficulties of working with Fe (and maybe especially Fe(111)) and in getting the surface clean, which proved to be a frustrating, difficult target. Nevertheless, we made some progress in that direction and also carried out some adsorption measurements to try and understand the effect of individual contaminants on the Fe surface structure.

4.3. Experimental

The intention at the start of this project was to perform all experiments on Fe(111), but upon ordering a second crystal, a Fe(110) sample was sent by mistake. This was only realized after a few weeks (and hours of cleaning), since the surface symmetry of the two facets (as observed by LEED) are quite similar and especially difficult to distinguish for a new, dirty crystal. Nonetheless, the dense Fe(110) surface provides a good comparison for the more open Fe(111) surface; therefore some interesting surface structures and limited adsorption studies on Fe(110) are reported here. The remainder of the thesis is dedicated to the Fe(111) surface.

The iron crystals were cut from iron in the body centred cubic (bbc) phase, also known as α-Fe or ferrite, which is the most stable phase below 1180 K.[68] Above this temperature a phase transition occurs to the face-centred cubic (fcc) phase, a.k.a. γ-Fe or austenite. For this reason, annealing temperatures were always kept below 1180 K. All cleaning was performed under UHV conditions. The Fe single crystals were obtained commercially from *Metal Crystals and Oxides* and have a reported purity of 99.8 %; the samples are 10 mm wide and 2mm thick.

All experiments were performed on one of three machines that are shown in Figures 2.21 – 2.27 (pictures and diagrams) and described in section 2.13. The background pressures of *Systems B & C* were ~2×10^{-10} mbar and 5×10^{-10} – 1×10^{-9} mbar respectively, but the background pressure in *System A* was higher; typically 1×10^{-9} – 5×10^{-9} mbar. The higher pressure in *System A*, along with prolonged transfer periods (due to equipment design) made it especially difficult to obtain/sustain clean surfaces; however, this is possible, as shown in section 4.5.

All STM results reported were performed at room temperature in the UHV-STM chamber of *system A* which has a lower pressure than the rest of the system, P ~ 1×10^{-10} mbar. The sample in use was welded onto a molybdenum plate and heating was done with a resistive heater. *System B & C* did not require sample transfer; but in *System A* sample transfer between the various chambers was done with manipulators. Gases were supplied by *Argo Int.* and purity levels were 99.999% for Ar / O_2 and 99.7% for C_2H_4.

Data collection and processing were done with the help of several programs: *EIS*[69] for XPS data acquisition and *CasaXPS*[70] for data processing; *Scala Pro*[71] for STM data acquisition and *WSxM*[72] for data processing; and *Spectraview*[73] for LEED data acquisition. *LEEDpat*[74] was often used to interpret LEED patterns. XPS binding energies were calculated against the value of the Fe 2p peaks with $BE_{Fe\ 2p3/2}$ = 706.7 eV. Monolayer coverages were calculated relative to the number of atoms in the topmost layer of the relevant surface, *i.e.* 7.08×10^{14} atoms/cm^2 for Fe(111) and 1.73×10^{15} atoms/cm^2 for Fe(110).[75] The base vectors indicated on the LEED patterns of the clean surfaces in Figure 4.31 were used in defining the directions of all other reciprocal lattices.

Coverages calculated from XPS data with the Carley and Roberts equation (see equation 2.5) resulted in unrealistically high values for even seemingly clean surfaces; *e.g.* the lowest O

coverage calculated was ~0.5 ML. Extensive effort was spent in resolving this issue, but with limited success. However, LEED/AES data of O on clean Fe(111) proved to be an effective way of calibrating the surface oxygen concentration, from which other adsorbate coverages were calculated by using relative sensitivity factors that incorporates both the dependence on the photo-ionic cross sections and asymmetry parameters (see section 2.7.5). Oxygen coverages were calculated as follow:

In several independent experiments Fe(111) was dosed at different exposures of O_2 (2 – 70 L) at room temperature, which leads to a bright background in the LEED and the disappearance of the integral spots. A brief period of annealing restores order to the surface and leads to the formation of the (6×6) LEED pattern. It was found that this LEED pattern is always obtained regardless of the initial oxygen dose (given that the dose exceeds a minimum value of ~2 L) and the Auger peak-to-peak height of O compared to Fe at which this pattern first appears also spans a narrow range, AES O/Fe = 0.6 – 0.7. This value was taken as 1 ML of O on Fe(111). The (4×4)-O LEED pattern was not frequently obtained, but if so, at a lower O coverage. From the relative ratios it was determined that the pattern corresponds to 0.27 ML (~ ¼ ML) of O on Fe(111). This pattern was used to calibrate all XPS data accordingly and marked with the subscript 6×6 (*eg.* ¼ $ML_{6\times6}$), to distinguish these calculated values from coverages determined with alternative methods.

4.4. Working Towards Obtaining Clean Fe Surfaces: Impurity Surface Segregation

4.4.1 General

Iron is notorious for containing high concentrations of bulk contaminants that can be difficult to remove. Figure 4.3 compares a series of Auger spectra of the Fe(111) surface that was initially sputtered at room temperature then annealed in stages to show the temperature at which each of the bulk contaminants segregate to the surface or desegregate into the bulk (each spectrum was taken as soon as the surface temperature has stabilized at the required temperature).

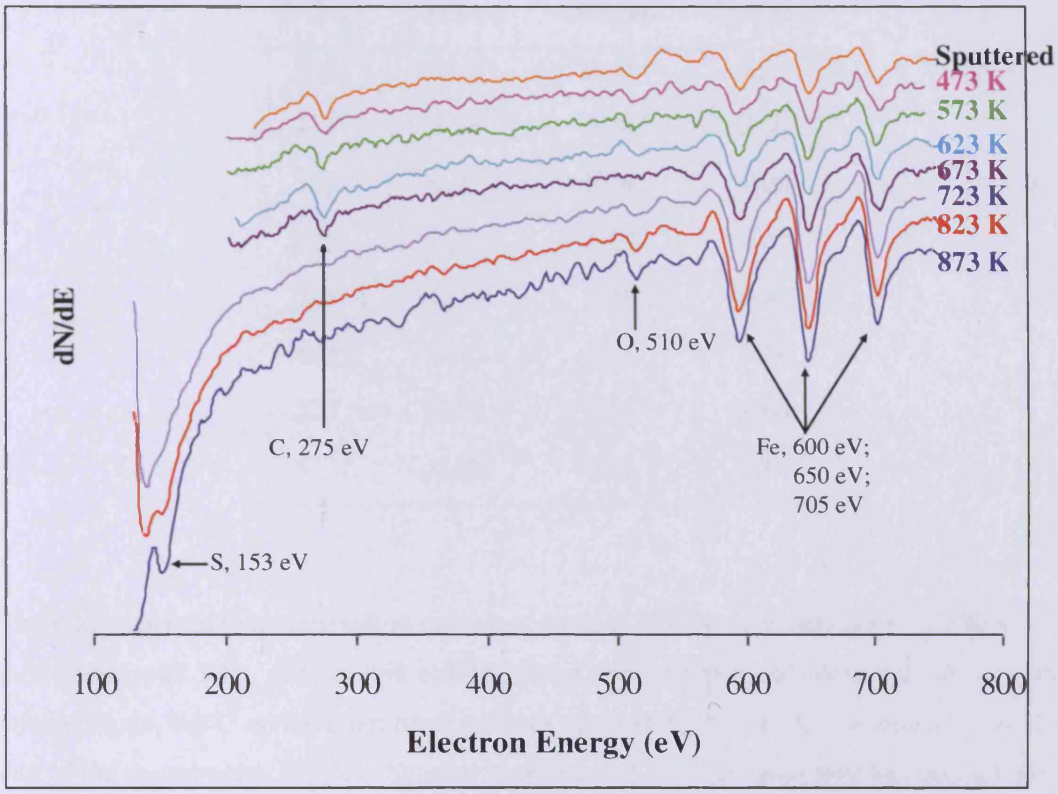

Figure 4.3 – Auger spectrum of Fe(111) that was annealed in stages, causing bulk contaminants to segregate to the surface or desegregate into the bulk.

Table 4.2 indicates the type/amount of contaminants present at each temperature in terms of the Auger peak-to-peak height ratio of the relevant adatom compared to Fe (the Fe-peak at 650 eV was used for this purpose).

At the start of the experiment O and C is present on the sputtered surface at room temperature. The C concentration initially decreases with temperature up to 573 K, but further annealing causes the concentration to increase and peak at 623 K. At 673 K only C is present on the surface, but above this temperature the C coverage decreases quickly and by 723 K the C signal has disappeared completely.

Table 4.2 – Contaminant levels derived from the AES in Figure 4.3. Relative concentrations are given as a peak-to-peak height ratio, *i.e.* X/Fe_{650eV}, X = C, O, N or S.

T (K)	Carbon	Oxygen	Sulphur
298	0.61	0.44	0.00
473	0.44	0.28	0.00
573	0.39	0.30	0.00
623	0.53	0.23	0.00
673	0.33	0.00	0.00
723	0.00	0.07	0.00
823	0.00	0.13	0.03
873	0.00	0.21	0.19

The initial surface O concentration decreases steadily with temperature up to 673 K at which point none was left. Above this temperature C has disappeared from the surface not to emerge again, but O on the other hand surfaces again and increases in concentration up to the end of the experiment (873 K). Sulphur surfaced at 823 K and increased in concentration at 873 K at which stage the experiment was terminated.

It is important to note that there is an interdependence between the different contaminants and that concentrations will vary according to the presence and concentrations of co-adsorbates. For example, depending on the relative amounts of C and O on the surface between 673 – 773 K, the minor contaminant would be depleted by the desorption of CO gas while the excess of the other would remain on the surface. Bearing these segregation properties and literature procedures in mind, the following cleaning method was applied:

The crystal was cleaned by a combination of sputtering and annealing cycles as generally prescribed in the literature. Sulphur was cleaned off first, as also advised by Arabczyk,[61] who studied the segregation properties of contaminants in an Fe(111) single crystal. The new crystals used in this study contained a significant amount of sulphur, which was cleaned off by sputtering hot for several hours at temperatures between 773 – 873 K. It was found that the degree of sulphur segregation to the surface increases with temperature and becomes significant >773 K, in agreement with the findings of others.[11] The equilibrium surface concentration of sulphur on Fe is virtually independent of the solute concentration and even small bulk concentrations leads to a large amount of sulphur on the surface if the crystal is

annealed to sufficiently high temperature.[24, 61] After some cleaning, the concentration of sulphur in the bulk decreased and the appearance of sulphur on the surface could be avoided by keeping annealing temperatures lower than 773 K. The presence of sulphur on the surface was not affected by other contaminants, but a large amount of surface sulphur prevented other contaminants to segregate to,[21] or adsorb onto,[37] the surface.

Although not shown in Figure 4.3, nitrogen occasionally surfaced at temperatures ≥ 673 K. Bulk O started segregating to the surface at ~723 K and the degree of segregation increased with temperature. Like S, N and O could be removed from the surface through sputtering.

Carbon proved to be very difficult to remove as also experienced of others.[29] The most effective way to remove surface C was to burn it off with O at temperatures between 673 – 723 K (O originated from the bulk or a small amount was dosed at room temperature). However, O_2 needs to be applied very carefully since Fe can easily oxidize, which is then in itself difficult to remove. The maximum amount of C on the surface was obtained by heating the crystal to 573 K, as also observed by others.[76]

4.4.2 Fe(110)

Sulphur Contaminated Surfaces

Figure 4.4 shows LEED patterns of Fe(110) containing S with either C or O that all originated from the bulk. S with C resulted in at least three distinguishable patterns. A (1×1) pattern was obtained for AES S/Fe = 1.5, C/Fe = 0.18 (not shown). The c(3×1) pattern, in matrix notation $\begin{vmatrix} 2 & -1 \\ 1 & 1 \end{vmatrix}$, is shown in Figure 4.4*a-i* and was obtained for AES S/Fe = 2.8, C/Fe = 0.4. Kelemen[15] reported the c(3×1) pattern for $^1/_3$ ML of sulphur on Fe(110) with and without carbon. Closer inspection of the pattern (especially at 68 eV, shown in Figure 4.4*a-ii*) reveals additional rows of spots along the (1, 1) direction.

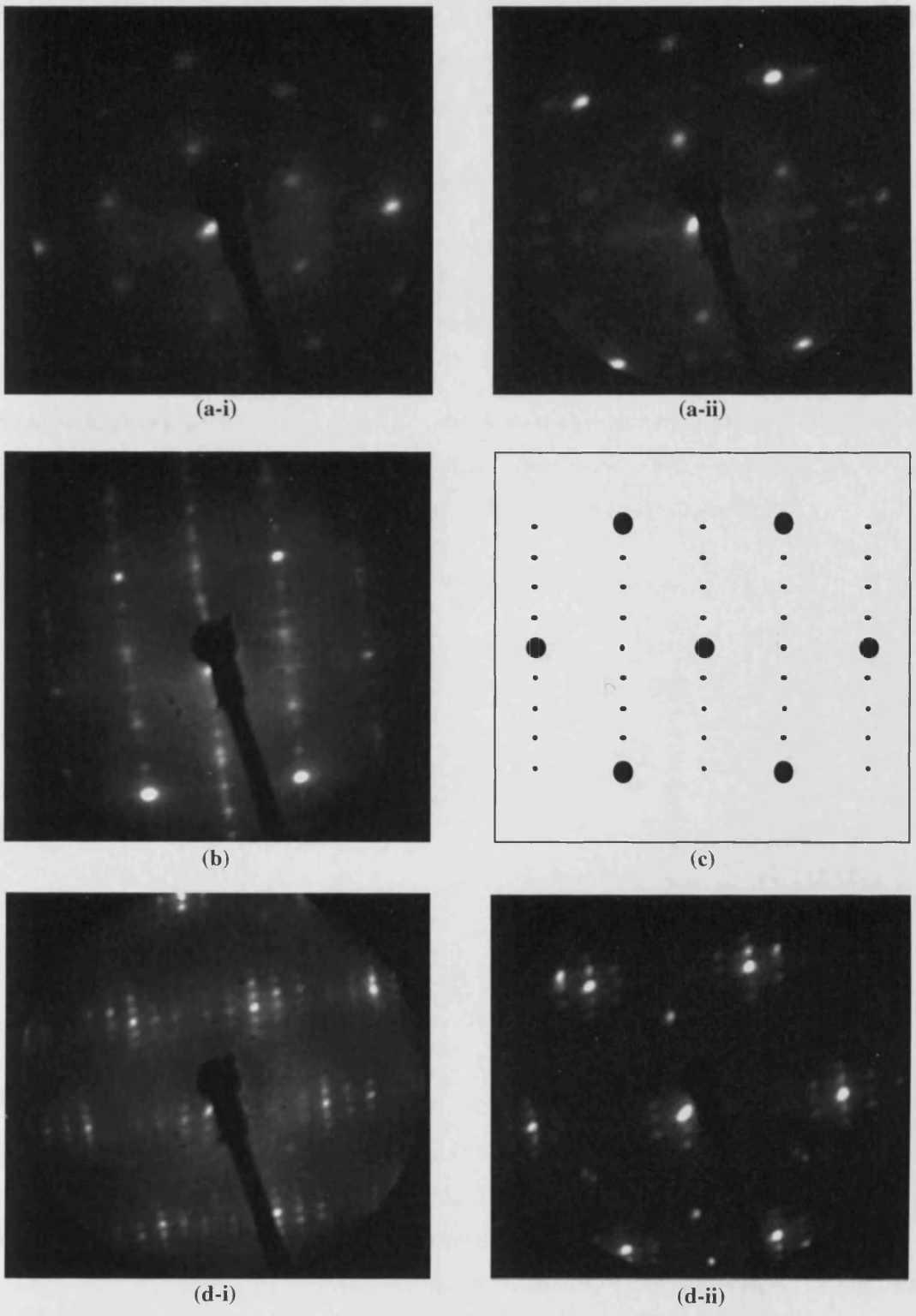

Figure 4.4 – Fe(110) surfaces with sulphur and carbon/oxygen: *a-i*) c(3×1); AES S/Fe = 2.80, C/Fe = 0.4; E = 80 eV. *a-ii*) The same structure as in *a* at 68 eV. *b*) Pattern consisting of a super position of the c(3×1) and $\begin{vmatrix} 1 & 1 \\ -5 & 3 \end{vmatrix}$ structures; AES S/Fe = 1.01, C/Fe = 0.32; E = 116 eV. *c*) Diagram of the $\begin{vmatrix} 1 & 1 \\ -5 & 3 \end{vmatrix}$ structure. *d*) AES S/Fe = 0.58, O/Fe = 0.42 at *d-i*) E = 100 eV and *d-ii*) E = 58 eV.

The c(3×1) pattern can also be distinguished in Figure 4.4*b* (AES S/Fe = 1.01; C/Fe = 0.32) and is in fact brighter than the other non-integral spots. Furthermore the spots in the (1, -1) direction are unevenly spaced and the pattern may be interpreted as a superposition of the c(3×1) and $\begin{vmatrix} 1 & 1 \\ -5 & 3 \end{vmatrix}$ structure (diagram shown in Figure 4.4*c*). Gafner[26] and Kelemen[15] also obtained several c(n×1) patterns for S on Fe(110) with or without C. The pattern obtained by Gafner[26] for S on Fe(110) is shown in Figure 4.5; no further interpretation of the pattern was provided.

Figure 4.4*d* shows the LEED for a surface with both sulphur and oxygen (S/Fe = 0.58, O/Fe = 0.42). The pattern exhibits a great number of spots arranged in rows along the (1, -1) direction, which suggests that the unit cell of the overlayer is particularly large.

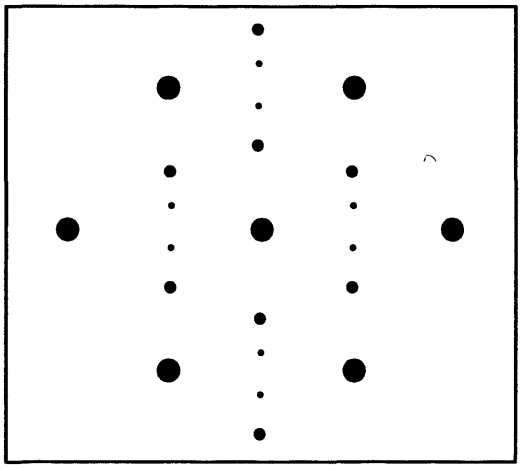

Figure 4.5 – Diagram of the LEED pattern obtained by Gafner for S on Fe(110).[26]

Carbon Contaminated Surfaces

Figure 4.6 shows LEED patterns of C on the Fe(110) surface. Carbon at high coverages (AES C/Fe = 0.55 – 0.75) gave a (1×1) pattern (Figure 4.6*a*). The *p*(2×2) pattern shown in Figure 4.6*b* was obtained for a surface containing carbon and oxygen (O/Fe = 0.2 and C/Fe = 0.35); the *p*(2×2) pattern has previously been attributed to ¼ ML of oxygen.[6] The LEED pattern in Figure 4.6*c* was taken at 453 K and AES C/Fe = 1.06, O/Fe = 0.32. Streaking of some rows in the (1, 1) direction is visible – the rows form groups of three, so that every second group of three rows are streaked, while the remaining rows are not. Streaking is generally associated with loss of order in one direction, because the structural units on the surface are out of phase or randomly spaced in that direction. The pattern showed in Figure 4.6*c* converted to the "carbon ring" pattern (Figure 4.6*d*) after being cooled further (T < 358 K).

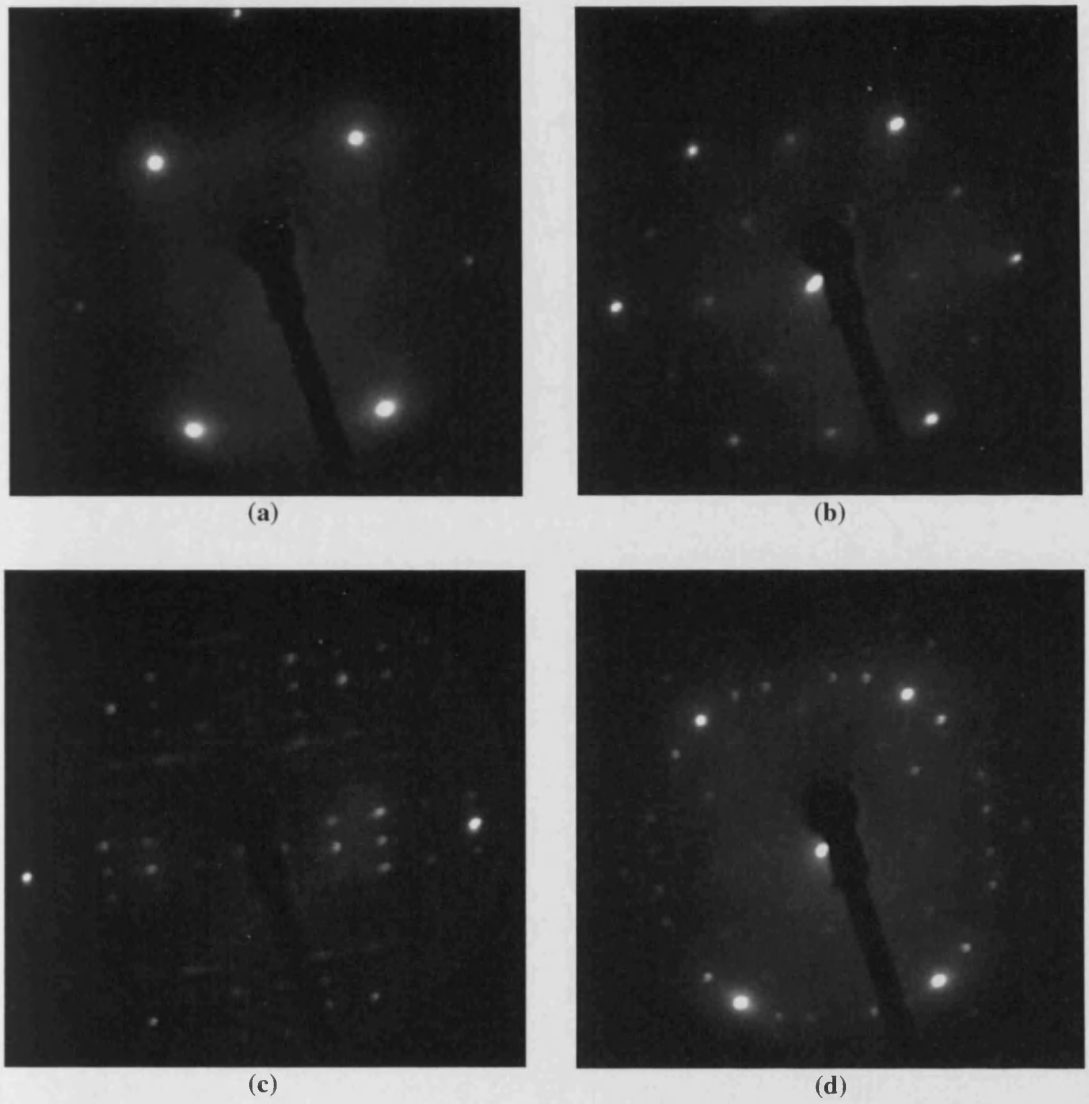

Figure 4.6 – LEED patterns of Fe(110) with predominantly carbon on the surface: *a*) (1×1); C/Fe = 0.75, O/Fe = 0.13, E = 100 eV. *b*) *p*(2×2); O/Fe = 0.21, C/Fe = 0.35; E = 94 eV. *c*) C/Fe = 1.06, O/Fe = 0.32; T = 453 K; E = 113 eV. *d*) The "carbon ring pattern" obtained from the same surface as *b* after being cooled further; T = 358 K; E = 83 eV.

The carbon ring pattern has also been observed by others,[6, 19,26,15] and was attributed to the presence of atomic carbon. The pattern is also shown in Figure 4.7*a*, at a slightly higher electron beam energy to reveal some additional spots. The diagram of the pattern (Figure 4.7*b*) shows that it is made up out of two unique sub-structures (coloured in pink and blue respectively) which are rotated 70.5° with regards to each other; one of these domains is shown on its own in Figure 4.7*c*. The real space lattice is shown in Figure 4.7*d*; the unit cell is a rectangle. This model was utilised to derive the matrix notation and dimensions of the superlattice.

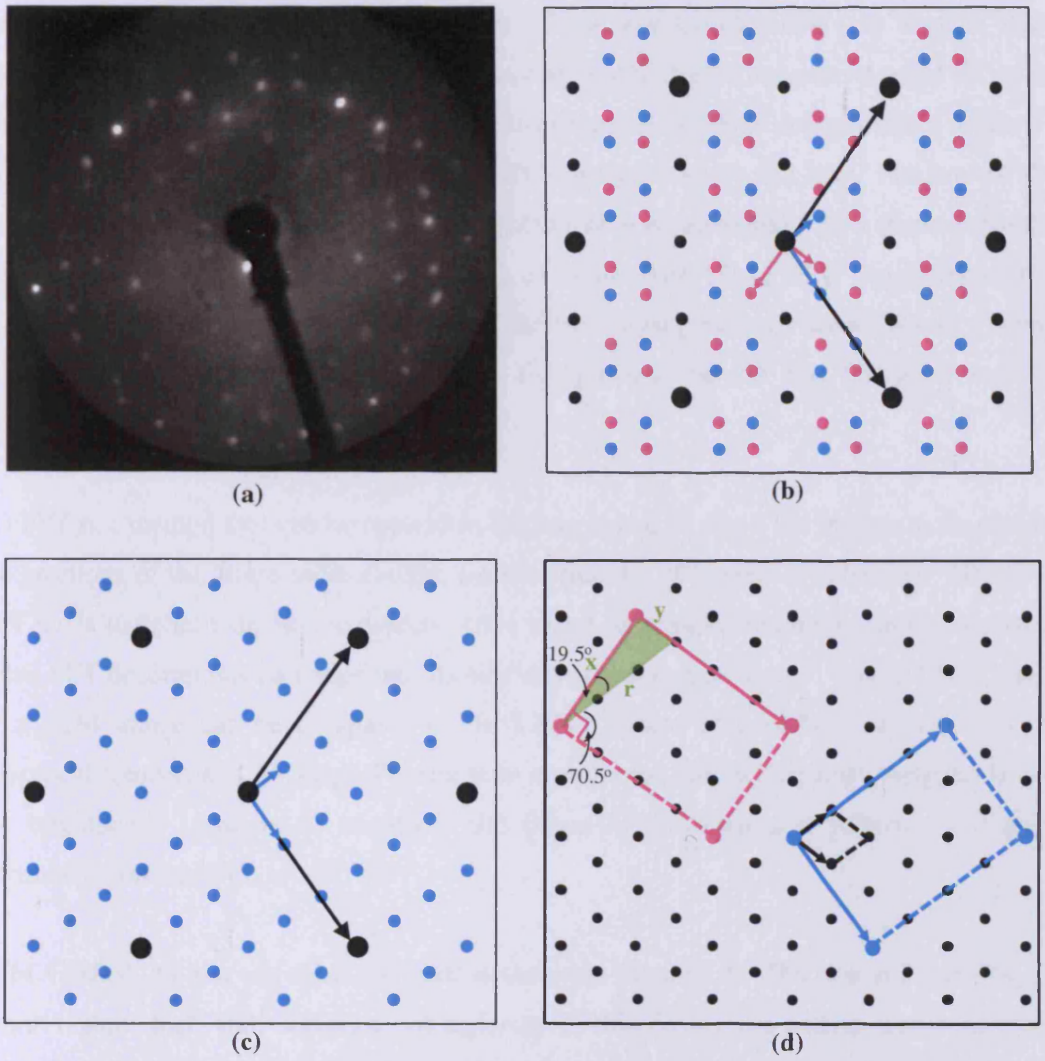

Figure 4.7 – *a*) The "carbon-ring" LEED pattern at E = 90 eV. *b*) Diagram of the LEED pattern which consists of two coincident domains (unique points are indicated by blue or pink dots and coincident points by small black dots). *c*) One of the reciprocal domains shown on its own. *d*) Real space unit cells of the substrate (black rhombus) and the adsorbate overlayers (blue and pink squares).

The matrix $\begin{vmatrix} 4 & 0 \\ -1 & 3 \end{vmatrix}$ is found to satisfy the relationship between the overlayer and substrate structure. The unit cell dimensions were calculated as follow: Since the lattice vector of the substrate is a_s = 0.248 nm, the corresponding lattice vector of the overlayer structure is calculated to be a_o = 0.992 nm ($a_o = 4*a_s$). The second lattice vector of the overlayer, b_o, is:

$$b_o = x = r\cos(90^\circ - 70.5^\circ)$$
$$= (3*0.248\text{ nm})\cos 19.5^\circ$$
$$= 0.701\text{ nm}$$

Some near atomic resolution STM images of the contaminated Fe(110) surface were obtained (Figure 4.8), however, no obvious connection to the C-ring pattern could be made. This result emphasises the fact that LEED is an averaging technique and analyses a relatively large surface area, while a high resolution STM image portrays the local structure of the surface (which is not necessarily altered / contaminated by adatoms). XPS showed that the surface contained approximately 0.12 $ML_{6\times6}$ of O and 0.64 $ML_{6\times6}$ of C and as mentioned before the LEED pattern was identified as "the carbon ring pattern" shown above. Figure 4.8 shows the STM images along with its line profiles and 2D Fast Fourier Transform Analysis (FFT).

2D FFT is a method that can be applied in the processing of raw STM images to emphasise the positions of the atoms more clearly, *i.e.* the structure of interest is enhanced. However, FFT tends to "eliminate atomic defects" (like steps) on regular structures. In mathematical terms FFT decomposes an image into its sine and cosine components.[77] The 2D FFT image of a STM image can be compared to the LEED pattern of a surface structure (*i.e.* its reciprocal counterpart). A single Fourier term encodes the spatial frequency, magnitude (*i.e.* the brightness – positive or negative) and phase of the sinusoidal pattern. For more information on this tool, see ref. 77.

STM verified that the surface is ordered, as shown in Figure 4.8. The step in Figure 4.8*a* is about 1 atom high and, although not apparent in this figure, the pattern was continuous across steps, as shown in Figure 4.8*b*. The step in Figure 4.8*b* is approximately ~0.5 nm high (as measured from the corresponding *Z*-image). The features visible in both figures were measured to be spaced ~0.8 nm apart along line *i* (Figure 4.8*a-i*) and ~0.9 nm apart along line *ii* (Figure 4.8*a-ii*). The FFT image is somewhat difficult to interpret due to the large number of spots and the, perhaps artificial, variation in spot brightness, but the Fe(110) unit cell might be discerned in the image. The rectangular unit cell of the C-ring LEED pattern is not apparent.

Summary

A variety of LEED patterns was obtained for S / C / O overlayers on Fe(110). Some patterns are complicated and each comprises of two or more superimposed structure. The C-ring pattern that has frequently been observed for C on Fe(110) has been shown to possess a rectangular unit cell. The pattern consists of the superposition of two domains which are rotated 70.5° with respect to each other.

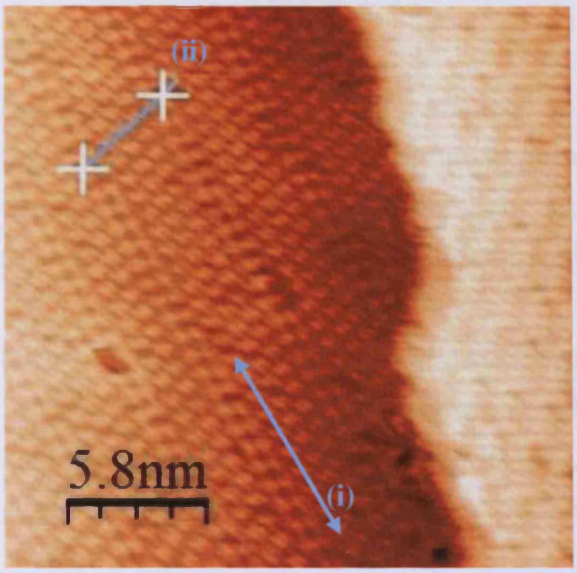

(a)

Figure 4.8 – *a*) Z-image of Fe(110) with C & O; sample bias = 0.38 V, feedback set = 0.11 nA. *a-i* & *a-ii*) Line profiles along lines *i* & *ii* in *a*; the nearest neighbour distance along line *i* is ~0.9 nm and along line *ii* ~0.8 nm. *b*) *I* image of a different region. *c*) FFT of the surface.

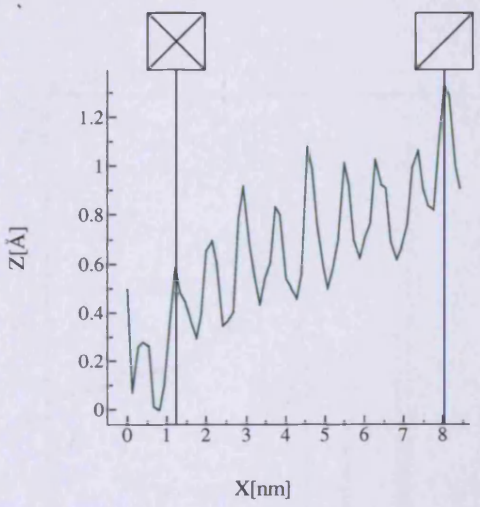

(a-i)

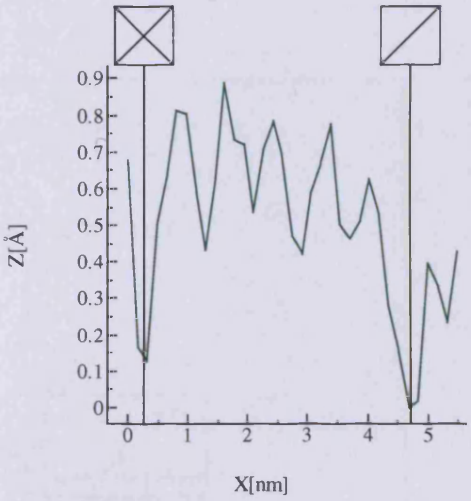

(a-ii)

(b)

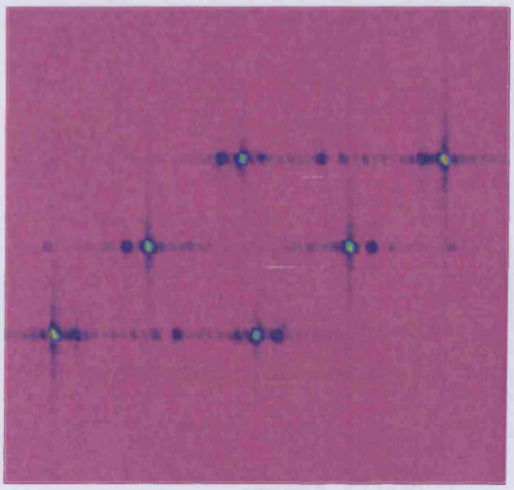

(c)

4.4.3 Fe(111)

Sulphur Contaminated Surfaces

Due to its open structure, Fe(111) is morphologically relatively unstable and therefore more likely than denser surfaces to undergo adsorbate induced restructuring. STM characterisation studies of clean Fe(111) could not be found in literature, but work on sulphur or oxygen covered Fe(111) surfaces has been done.[11, 38, 66, 67]

Figure 4.9 is a XP spectrum of Fe(111) contaminated with low coverages of S, O and N; Figure 4.10 – Figure 4.12 are the corresponding STM images and the LEED pattern is shown in Figure 4.13. It was estimated that 0.09 $ML_{6\times6}$ S and less than 0.05 $ML_{6\times6}$ N and O were present on the surface. The surface was prepared by sputtering and annealing at 873 K for 30 min.

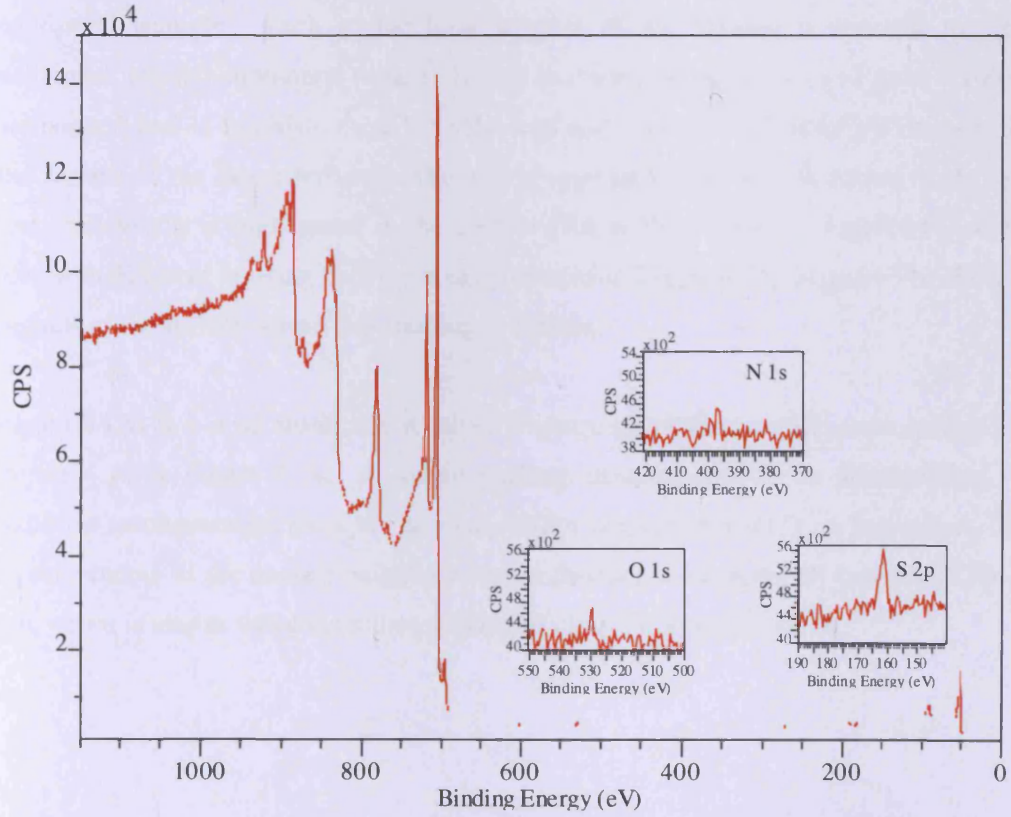

Figure 4.9 – XPS spectrum of Fe(111) with 0.09 $ML_{6\times6}$ S, 0.05 $ML_{6\times6}$ O and 0.05 $ML_{6\times6}$ N; see Figure 4.10 – Figure 4.12 for the corresponding STM images and Figure 4.13 for the LEED structure.

Figure 4.10 shows a region of the surface with sharp triangular mounds and some triangular terraces. The structures are generally aligned with the step edges, noticeable especially in Figure 4.10*a*. The steps in Figure 4.10*a* were measured to be ~150 nm apart and ~5.5 – 8.0 nm high (see Figure 4.10*a-i*). Figure 4.10*b* shows a flatter area which for most part comprises of similar structures. The line profile along line *i* (Figure 4.10*b-i*) emphasises that the features are pointed and generally very similar in shape and size (40 nm wide and ~2 nm high); the average slope of the facets is ~6°. These pointed features dominate the surface, but some terraces are also present. The largest terrace in Figure 4.10*b* is shown at *ii*. As the steps in Figure 4.10*a*, the edges of this terrace are lined with multiple smaller facets. The line profile in Figure 4.10*b-ii* emphasises this further and shows that the smaller facets are more or less as high as the larger structure itself. The flat plane is ~80 nm wide and the diameter of the whole structure (along line *ii*) is ~140 nm. Figure 4.11 shows terraces that were present on the same surface. Figure 4.11*a* shows a triangular terrace of roughly the same size as the one shown in Figure 4.10*b*; the corresponding line profile and contour plot is shown in Figure 4.11*a-i* & *b*. The shape of the terrace parallel to the surface is a perfect equilateral triangle. Each of the three corners of the triangle is elevated to form an additional, smaller equilateral terrace. Unlike the facets on the terrace in Figure 4.10*b* which are pointed and ~1 nm high, these have flat tops and are only half the height (measured from the surface of the larger terrace). The highly symmetric and smooth nature of the terraces and shallow pits is highlighted in the contour plot in Figure 4.11*b*. Figure4.11*c* shows an area with different faceting than the areas presented in Figure 4.10. Figure4.11*d* show flatter regions of the surface where less faceting is evident.

Figure 4.12*a* & *b* is an atomically resolved Z-image of a terrace on the same surface seen in Figure 4.10 & Figure 4.11. A square packing arrangement can be distinguished, which indicates reconstruction, since the original surface unit cell of Fe(111) is hexagonal. Several measurements of the nearest neighbour repeat distance were done, all between 0.78 – 0.92 nm, which is almost twice the lattice spacing of clean Fe(111), 0.405 nm.[78]

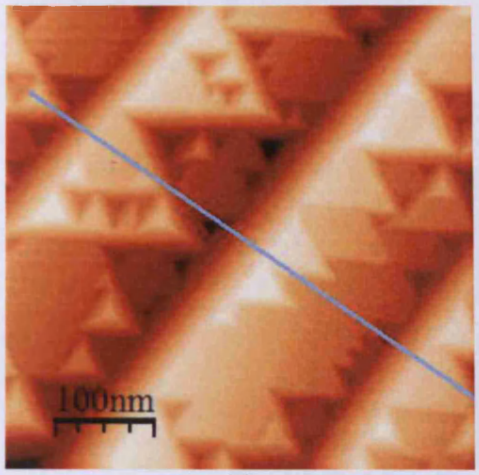

(a)

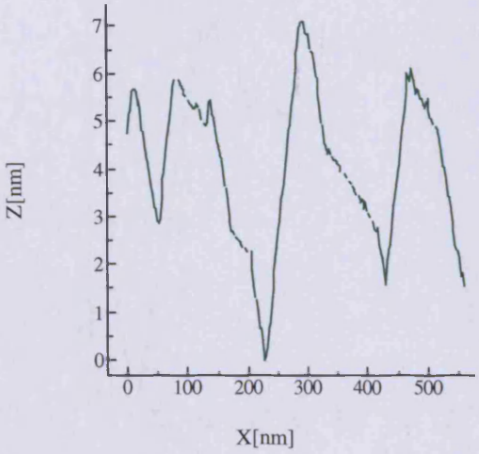

(a-i)

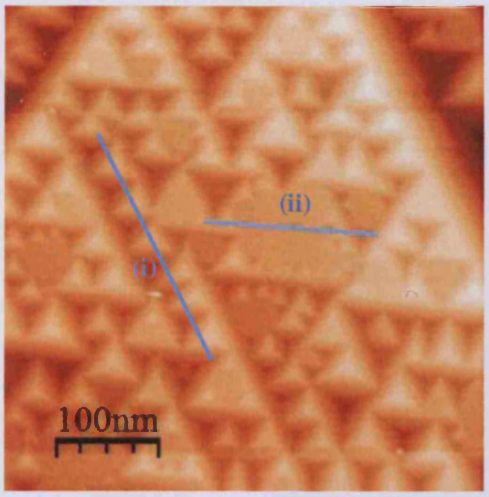

(b)

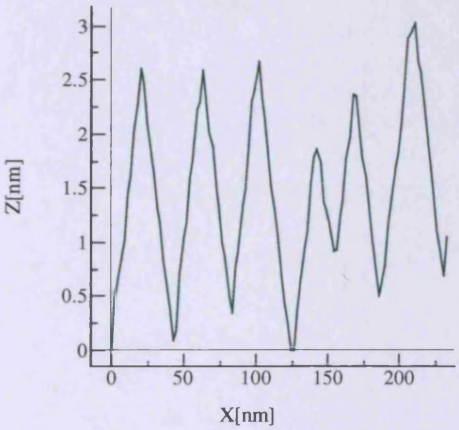

(b-i)

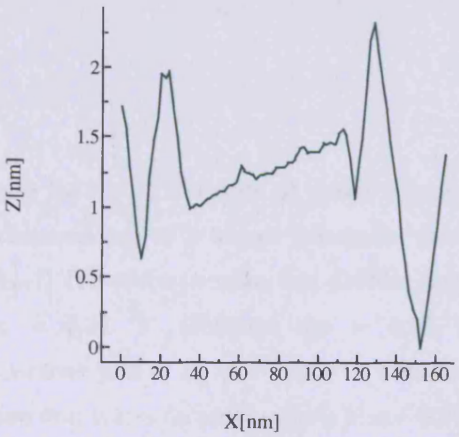

(b-ii)

Figure 4.10 – Z-images and line profiles of the Fe(111) surface with S, N and O; sample bias = 0.82 V, feedback set = 0.35 nA. *a*) Steps on the surface; *a-i*) Line profile of *a*, steps are ~150 nm wide and ~6 – 8 nm high. *b*) Triangular terrace with triangular mounds stacked on the edges; *b-i* and *b-ii* are line profiles of *b*.

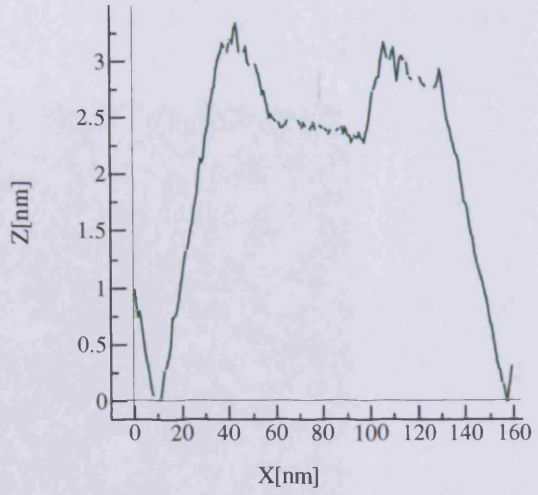

(a) (a-i)

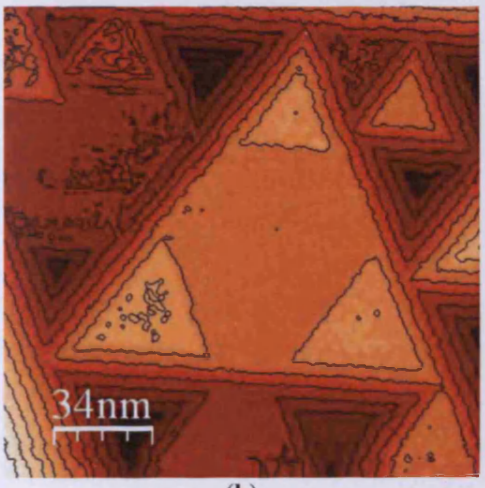

(b)

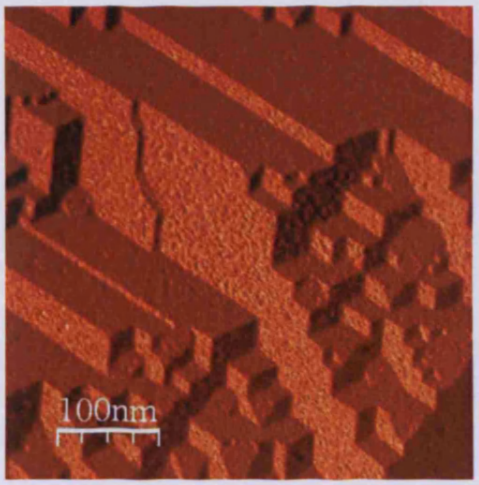

(c)

(d)

Figure 4.11 – *a*) *Z*-image of small triangular terraces on top of a larger triangular terrace and *a-i*) The corresponding line profile; sample bias = 0.81 V, feedback set = 0.43 nA. *b*) Contour plot of *a*. *c*) *I*-image of a different region that is less faceted; sample bias = 0.81 V, feedback set = 0.47 nA. *d*) A third region where no faceting is evident; sample bias = 0.82 V, feedback set = 0.35 nA.

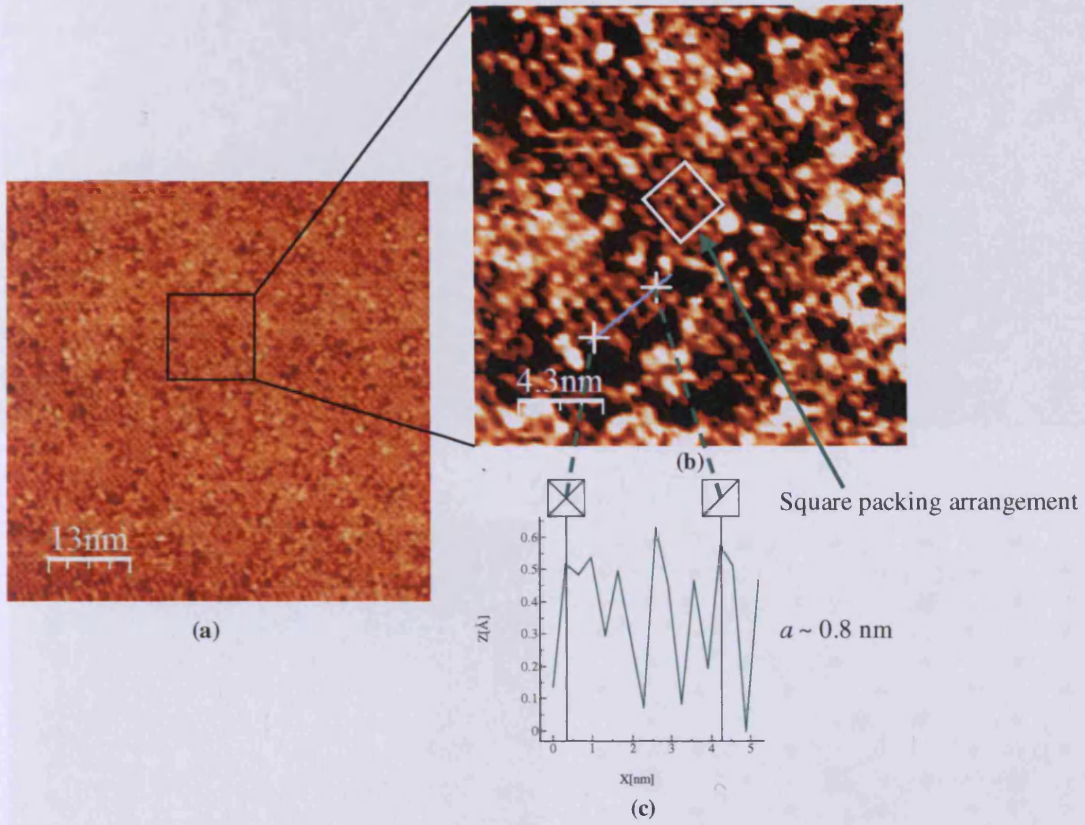

Figure 4.12 – *a*) Atomically resolved *Z*-image of the same surface shown in Figure 4.10 & 4.11; size = 49nm^2; sample bias = 0.8 V, feedback set = 0.49 nA. *b*) The square packing arrangement. *c*) Line profile of *b*, the nearest neighbour spacing is measured to be ~ 0.8 nm.

Figure 4.13 shows the so-called "clock structure" LEED pattern at different electron energies that was obtained for the surface shown in Figure 4.10 – 4.12. The term was coined by Lin *et. al.*[11] who observed it earlier and named it according to the rings around the integral spots which consist of 12 spots each and therefore look like clocks. The pattern is very complicated and a simple overlayer structure could not be derived. The pattern was also obtained at higher oxygen coverages (with a trace amount of S/C/N again being present), as for the surface of which the XPS spectrum is shown in Figure 4.32-*iv*. These observations suggest that the different impurities create distinct, co-existing structural domains on the surface.

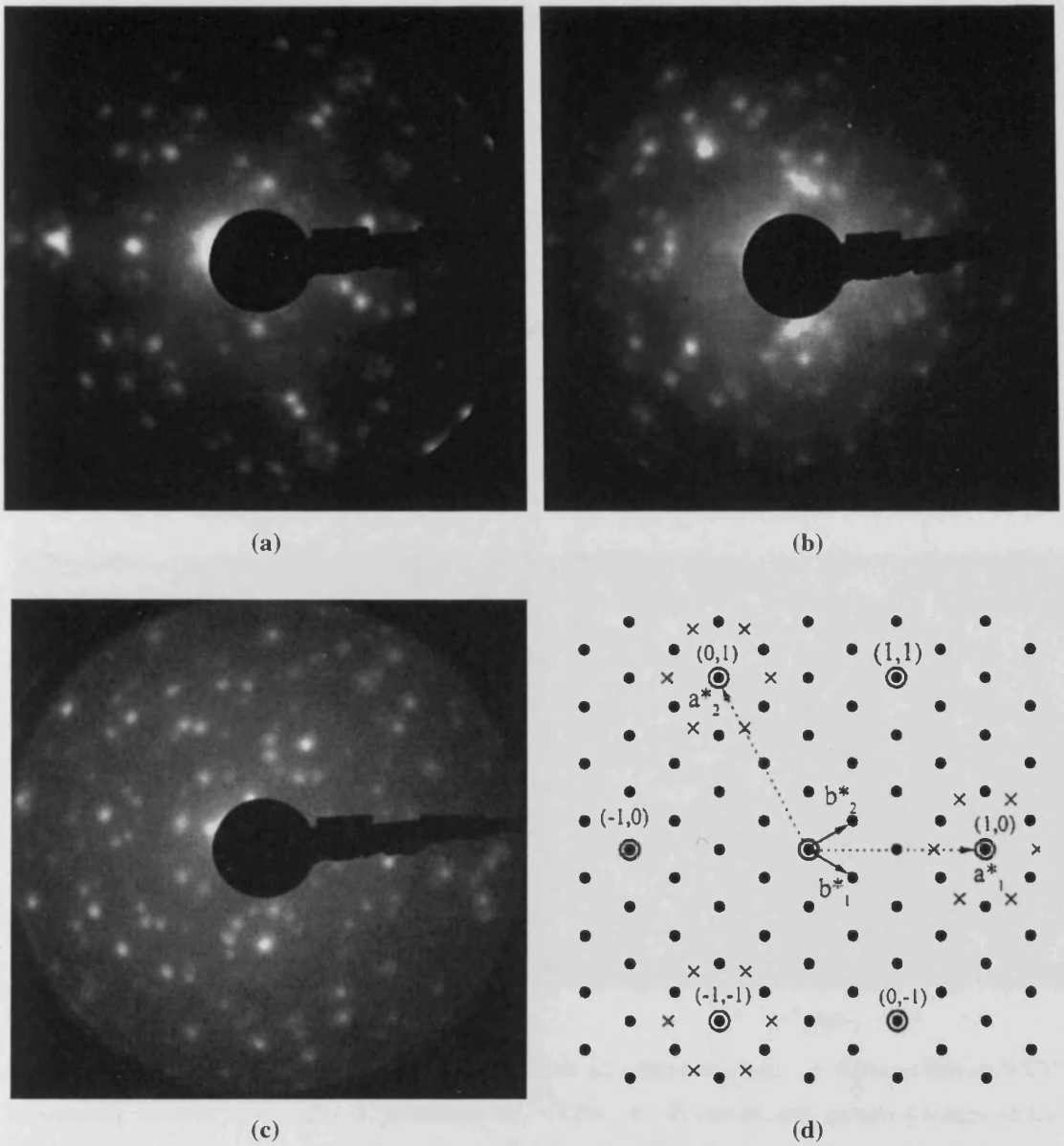

Figure 4.13 – The "Clock-structure" LEED pattern for Fe(111) with low levels of S, O and N at *a*) E = 45 eV; *b*) E = 76 eV and *c*) E = 87 eV. *d*) Diagram of the LEED structure[11] – the reciprocal net of Fe(111) is indicated by ○, the $(2\sqrt{3}x2\sqrt{3})$ overlayer structure is indicated by • and additional spots of clock pattern are indicated with x.

All the results discussed above resemble observations of Lin closely.[11] N, O and S were observed with AES and it was estimated that the concentrations of the individual species were 0 – 8 at%, while the total coverage was lower than 20 at%. The LEED ring pattern with 12 spots can be obtained by superposition of the $(2\sqrt{3}\times 2\sqrt{3})$ structure and additional spots from other structures (see diagram in Figure 4.13*d*). The diagram presented by Lin shows "clock rings" around three of the integral spots, but we found that all the integral spots

possess these rings (compare Figure 4.13*a* & *b*/*c*). It was reported that an increase in O coverage (> 8 at %) caused the clock structure to transform into the $(2\sqrt{3}\times 2\sqrt{3})$R30° structure (indicated by the black dots in Figure 4.13*d*) with faint spots of the clock structure; we did not observe the $(2\sqrt{3}\times 2\sqrt{3})$R30° structure on its own. STM images from that study are shown in Figure 4.14. The steps on that surface were measured to be 140 nm wide and 5 nm high, in good agreement with measurements done in this study (width ~150 nm; height 5 – 8 nm). It was said that annealing led to more regular steps and a less rough surface. Lin measured the nearest neighbour repeat distance of the pseudo square to be ~0.8 nm, again in good agreement with our measurements (0.78 – 0.92 nm).

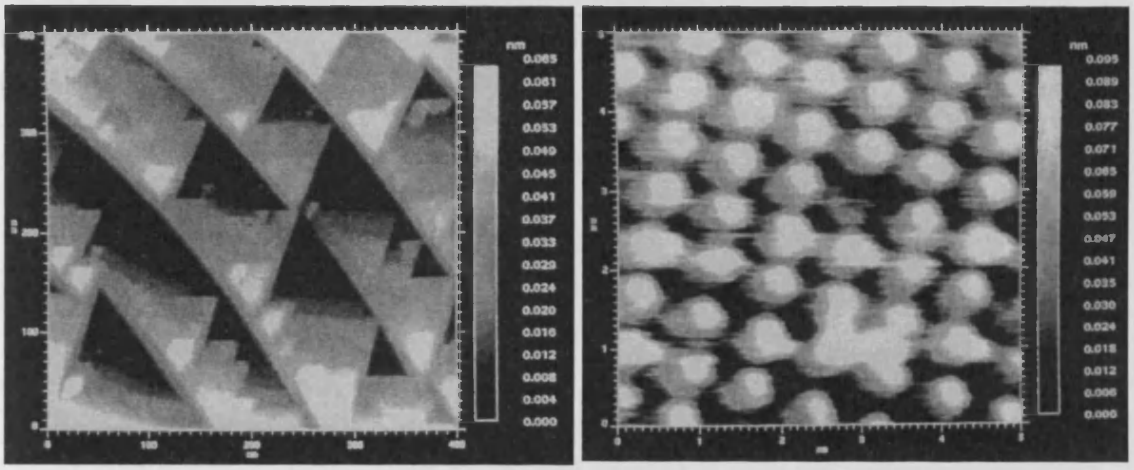

(a) (b)

Figure 4.14 – STM images of Lin[11] for the clock structure surface: *a*) 400nm×400nm STM topograph, sample bias = -0.1 V, feedback set = 1.00 nA. *b*) Atomically resolved image of the clock phase. A pseudo-square unit cell with lattice vector ~0.7 × 0.8nm; sample bias = 0.1 V, feedback set = 3.0 nA.

Based on the dimensions and symmetry, Lin tentatively assigned the surface to Fe(100)c(4×4);[§] a diagram of the surface structure is shown in Figure 4.15. The overlayer lattice vector, a_o, written in terms of the substrate lattice vector, a_s, is

$$\begin{aligned} a_o &= 2\sqrt{2}a_s \\ &= 2\sqrt{2}\times 0.2866 \text{ nm} \\ &= 0.811 \text{ nm} \end{aligned}$$

[§] Centered (4×4) structure.

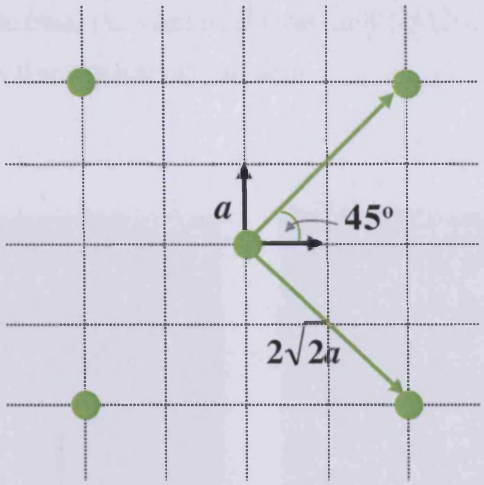

Figure 4.15 – Surface unit cell of Fe(100)c(4×4) to which the contaminated Fe(111) surface is thought to reconstruct to. The surface unit cell is represented by the dotted lines while the green dots represent the adsorbate atoms.

The reconstruction was attributed to the presence of the low level adsorbate(s), but the species responsible could not identified, nor could a complete structural model for the clock structure be presented. It is concluded that the clock structure is a thermodynamic phase, since annealing is required to bring it about.

Strongin and Somorjai[12] have shown that nitrogen can cause restructuring of all three low Miller index planes of bcc iron as evidenced by scanning electron microscopy (SEM) images, TPD spectra and measurements of the ammonia synthesis activity. The single crystal surfaces were treated with ~6.7 mbar of ammonia for 30 min at 723 K, which resulted in the surface structures shown in Figure 4.16 & 4.17. The restructured Fe(111) surface contains triangular facets, not unlike the pits that were observed in the current study, *e.g.* Figure 4.11*b*. In contrast to the surface reported here, the N-faceted Fe(111) surface does not contain mounds, and triangular pits are separated by clean featureless planes. The angle at which plane *i* in Figure 4.17*b* intersects the (111) plane were estimated to be ~18.2 ± 0.5°. This value agrees most closely with the value expected for the (112) face, which intersects the (111) plane at 19.5°. It was suggested that {211} surface planes develop on the N-treated Fe(111) surface. This notion also matches the catalytic activity, in that the activity of the Fe(111) surface decreases only slightly after treatment in ammonia, in agreement with the ammonia synthesis activity trend of the clean surfaces Fe(111) > Fe(211) >> Fe(100) >

Fe(210) > Fe(110). In contrast, the faceted Fe(100) and Fe(110) surfaces are more active toward ammonia synthesis than the original surfaces.

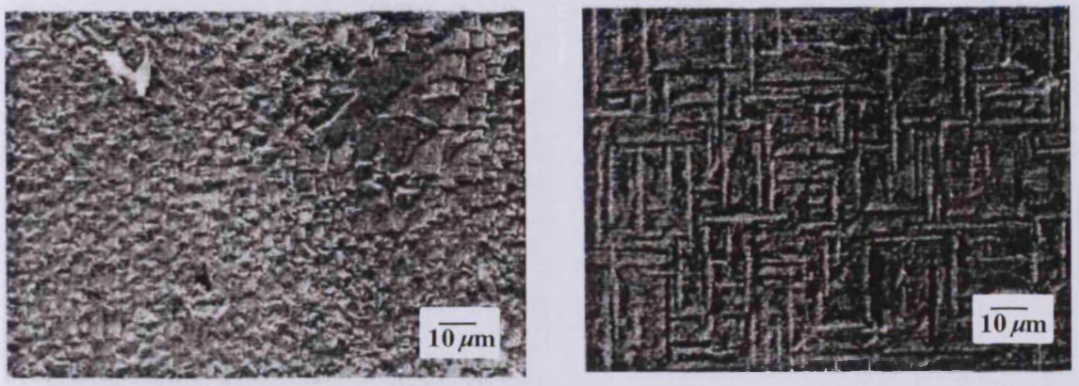

(a) (b)

Figure 4.16 – SEM images showing the reconstruction of *a*) Fe(110) and *b*) Fe(100) after being treated in 6.7 mbar of ammonia at 723 K for 30 min; before treatment the surfaces appear smooth and featureless.[12]

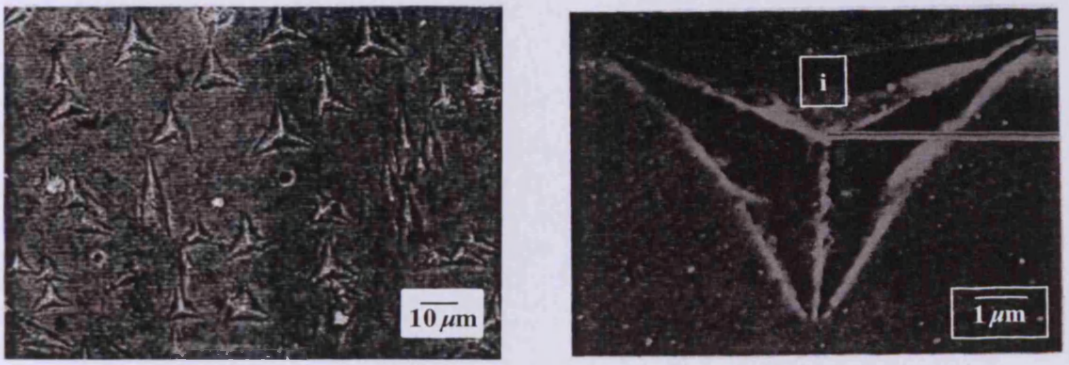

(a) (b)

Figure 4.17 – SEM images of the reconstructed Fe(111) surface after being treated in 6.7 mbar of ammonia at 723 K for 30 min; before treatment the surface appears smooth and featureless. [12]

LEED Patterns attributed to Sulphur

Figure 4.18*a* shows, what at first glance looks like, the (1×1) Fe(111) LEED pattern; however, especially at lower electron energy one can see that the integral spots are split and each seems to consist of a group of three spots. The matching XPS in Figure 4.18*b* shows that sulphur is present on the surface; the coverage was calculated to be 0.11 $ML_{6\times6}$. The surface was prepared by sputtering and annealing at 873 K for ~30 min.

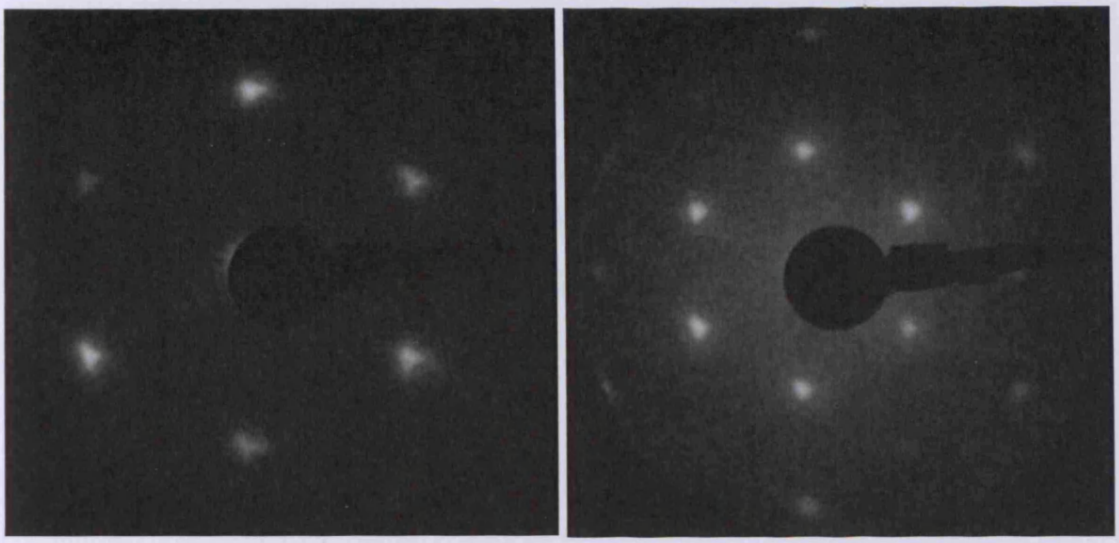

(a-i) (a-ii)

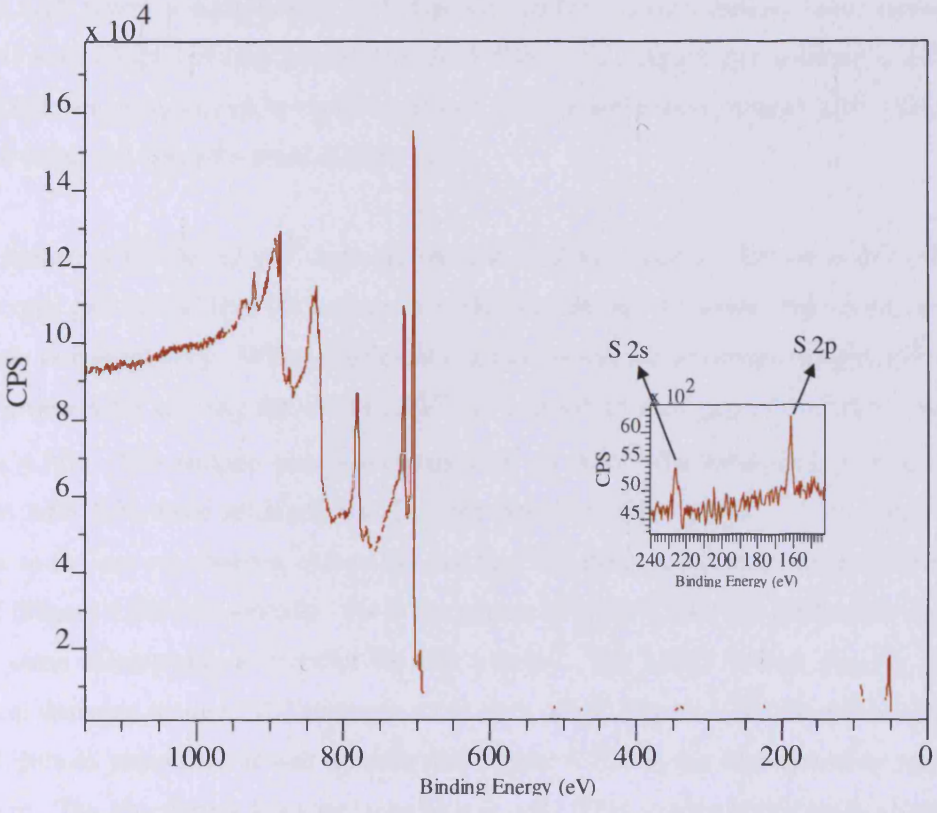

(b)

Figure 4.18 – *a*) LEED pattern of Fe(111) at *a-i*) E = 38V and *a-ii*) E = 84V. *b*) The corresponding XPS showing the presence of a small amount of sulphur.

From the literature it is known that 1ML of S on Fe(111) gives a (1×1) pattern, which implies that the overlayer has the same periodicity as the substrate.[11, 79] Sulphur atoms presumably occupy the threefold shallow hollow sites in each unit cell (above Fe2,

surrounded by 3 Fe1 atoms; see Figure 4.1 for the unit cell of Fe(111)). Overlayer structures of lower sulphur coverages on Fe(111) could not be found in literature.

In this study, spot splitting was frequently observed in the LEED patterns of Fe(111) with surface contaminants like sulphur (Figure 4.18 & 4.19) and oxygen (Figure 4.26). In these patterns, some or all of the integral spots consisted of a group of three or six spots each. In general the extent of spot splitting can be related to the step separation of the sample with a regular array of steps as well as the angle between the terraces relative to the average surface orientation.[80, 81] The observed spot splitting of Fe(111) is perhaps not surprising when considering the relative ease by which Fe(111) reconstructs to form trigonal facets and pits to varying extend, depending on factors like the type of contaminant and its concentration. The spot splitting observed in LEED is therefore attributed to these trigonal planes and pits which intersect the (111) surface at an angle to give rise to different scattering angles.

Figure 4.19 shows a complicated LEED pattern and the corresponding Auger spectrum of Fe(111) with a high coverage of sulphur; AES S/Fe = 6.2. Again spot splitting is evident in the LEED; the groups of spots each consists of three brighter spots, rotated 120° with regards to each other and similarly three dimmer spots.

STM studies of Cabibil *et. al.*[66] have shown that sulphur causes the formation of equilateral, nanoscopic pits on the Fe(111) surface at 1 ML; the pits are 11 atoms wide along the edges and only one atom deep. With a sufficient increase in sulphur coverage, the pitting becomes more pronounced causing the (1×1) LEED to convert to the $(2\sqrt{3}\times1)$ structure (shown in Figure 4.20). The surface was associated with an AES S/Fe ratio greater than 1.4; the highest AES S/Fe ratio achieved was 2.1 (the ratio we obtain is 6.2). The pattern is very similar to the one we observe, except that we find that the spacing of the spots do not fit the model (Figure 4.20*b*) completely. From the picture (Figure 4.20*a*) it is difficult to determine if the same discrepancy is relevant for that pattern. The LEED pattern consists of three identical domains rotated 120° with respect to each other. Figure 4.20*c* shows the schematic LEED pattern expected for *one* domain and Figure 4.20*d* is the corresponding real space structure. The superlattice has a rectangular unit cell. STM images in that study showed that the surface was severely reconstructed and contained triangular pits as long as 80 nm (along the edges) and as deep as 5 nm.[11, 66] Vertically displaced atomic rows was observed and a periodicity of 0.14 nm was measured ($2\sqrt{3}\times a_{Fe(111)} = 0.14$ nm, $a_{Fe(111)} = 0.405$ nm); the same periodicity was also found inside the pits.

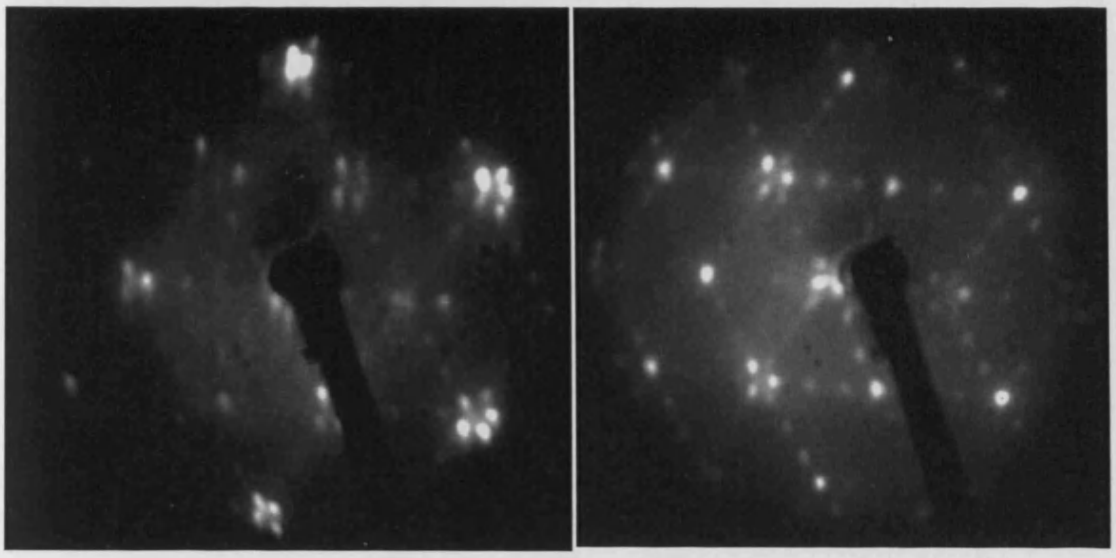

(a-i) (a-ii)

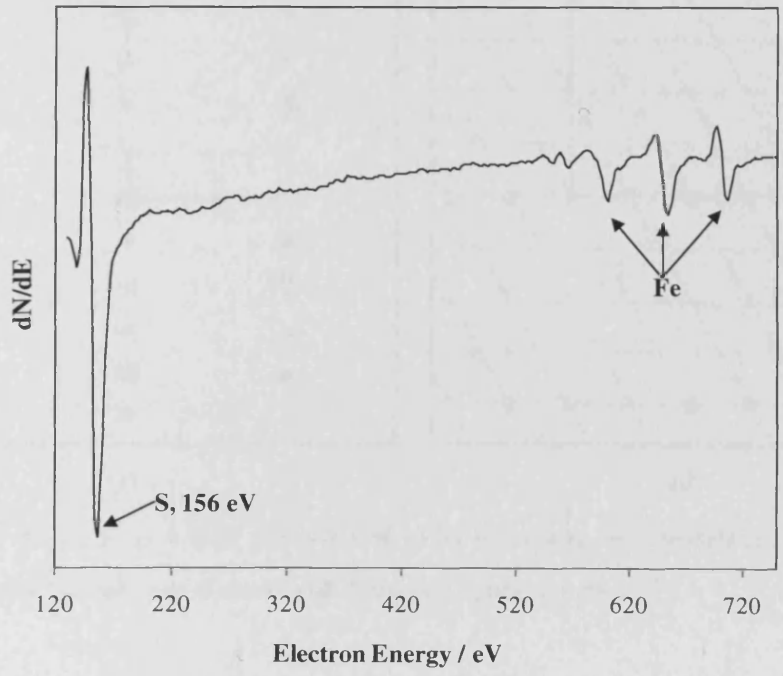

(b)

Figure 4.19 – *a*) LEED pattern of Fe(111) with S at *a-i*) E = 110 eV and *a-ii*) E = 123 eV. *b*) The corresponding AES; S/Fe = 6.2.

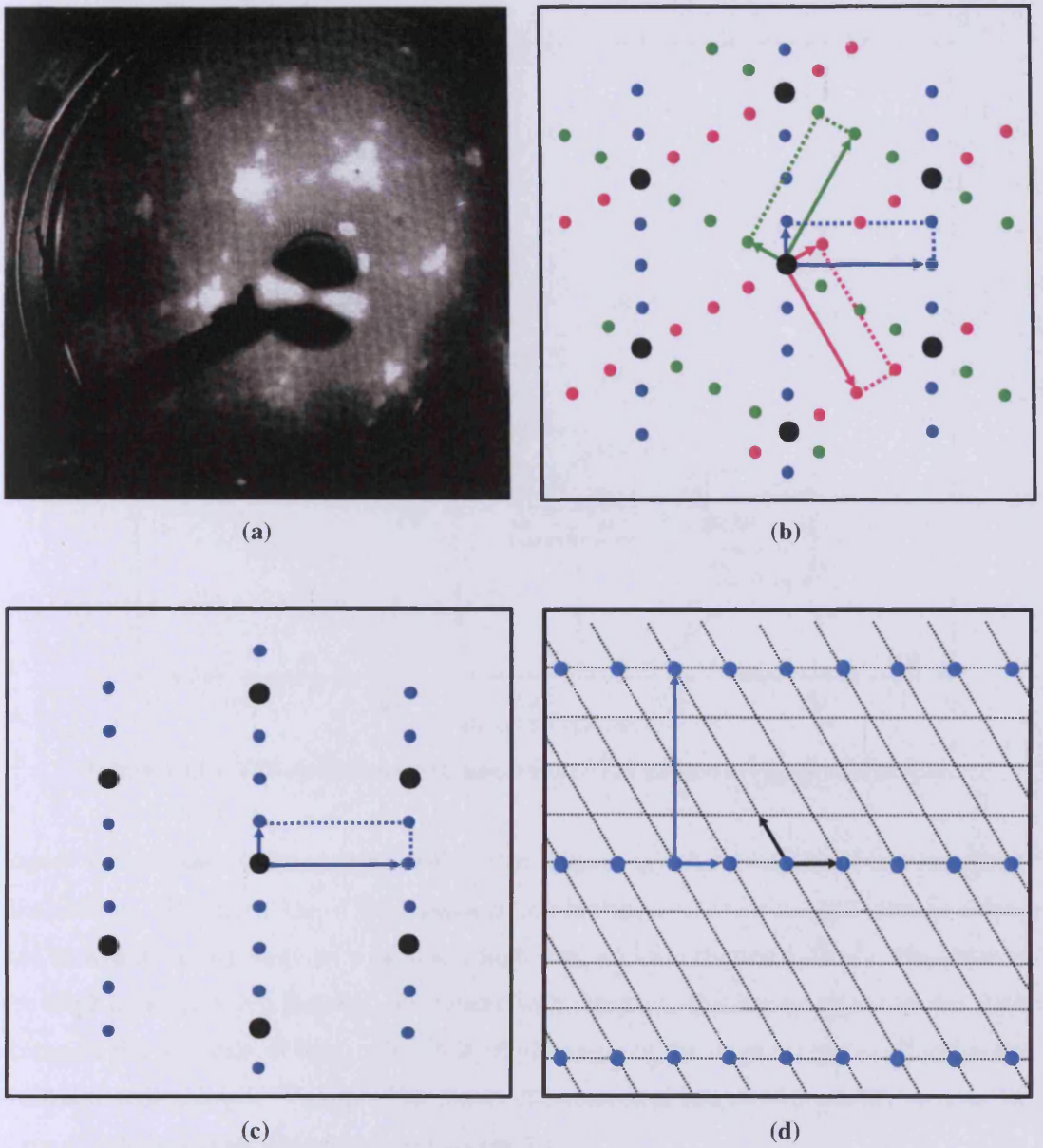

Figure 4.20 – *a*) $(2\sqrt{3}\times1)$ LEED pattern and *b*) its schematic representation. *c*) The LEED pattern expected for only one domain and *d*) the real space structure.[53]

Oxygen, Carbon and/or Nitrogen Contaminated Surfaces

The STM results in this section could not be complemented with LEED, since the equipment was being repaired at the time. Figure 4.21 is a XPS spectrum of Fe(111) with 0.05 $ML_{6\times6}$ of O and 0.06 $ML_{6\times6}$ of N; Figure 4.22 & 4.24 present STM images of the same.

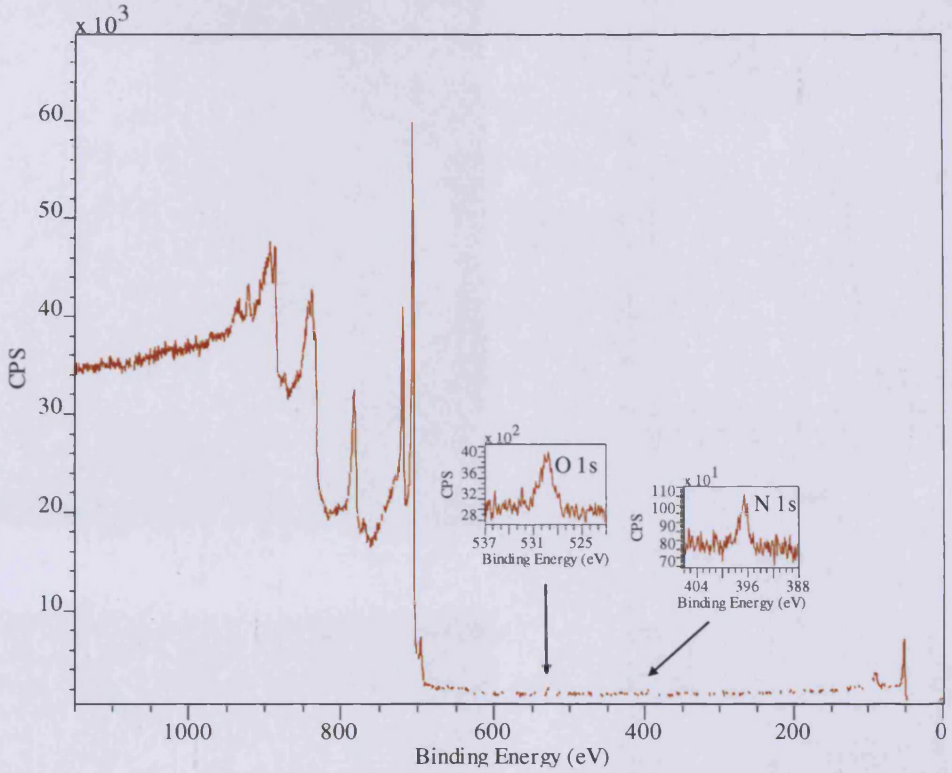

Figure 4.21 – XPS spectrum corresponding to STM images in Figure 4.22 & 4.24.

Figure 4.22*a* shows a large terrace with round features which are organised in a hexagonal like fashion. The direction of the pattern is continuous across two parallel terraces (along line *i*), which are separated by a relatively high step, ~0.7 nm (Figure 4.22*a*-*i*). The order on the slope (at *ii*) is also hexagonal, but rotated with regards to the domain on the terrace itself (compare the direction of line *i* relative to *ii*); the angle of the slope is only ~1.4° relative to the plane (not shown). Figure 4.22*b* shows the correlated image of a smaller area on the terrace with the hexagonal lattice superimposed on it.

Self correlation is a method applied in image processing to emphasise periodicity. Self-correlation[82] is defined as

$$G(k1,k2) = \sum f(x,y)f(x+k1,y+k2)$$

Where *f(x,y)* is the image matrix. The equation takes the image and the same image shifted a distance *k1* and *k2* in the x- and y-axis with respect to the centre of the image. The resulting image, *G(k1,k2)* is a measure of how different the two images are. The highest value in self-correlation is obtained at the centre of the image, where *k1* and *k2* are zero; any periodicity in the original image will be shown as a periodic pattern in the self correlation.

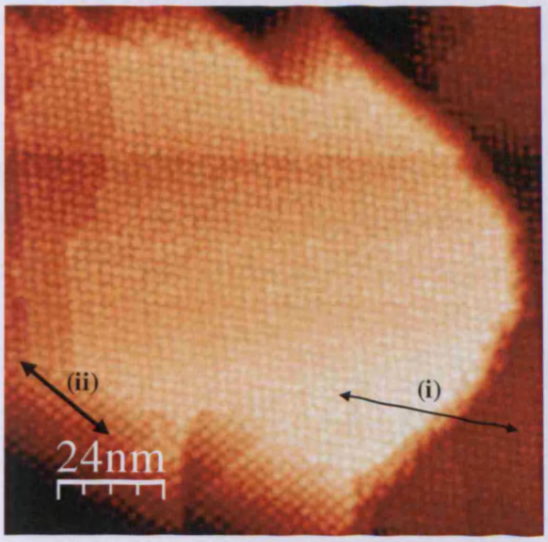

(a)

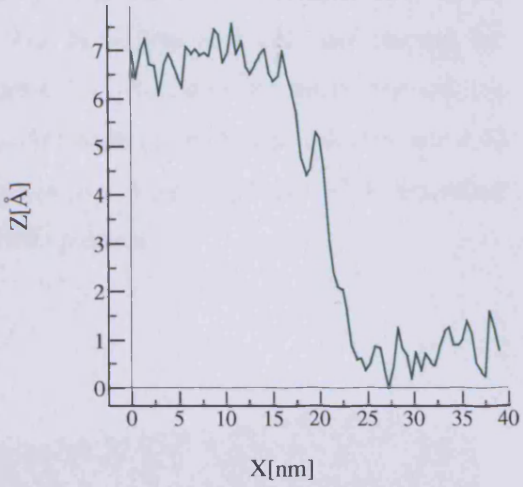

(a-i)

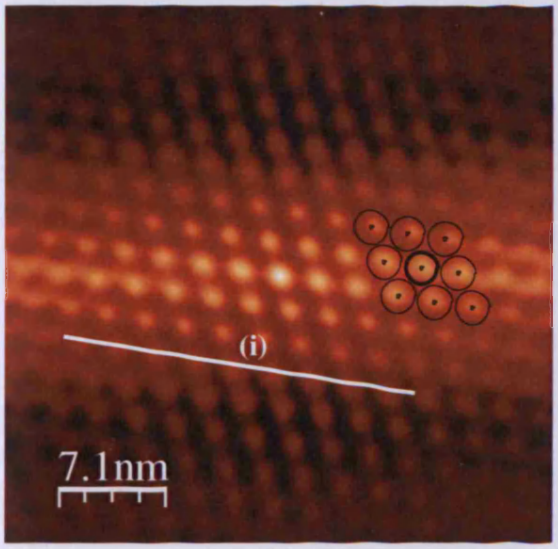

(b)

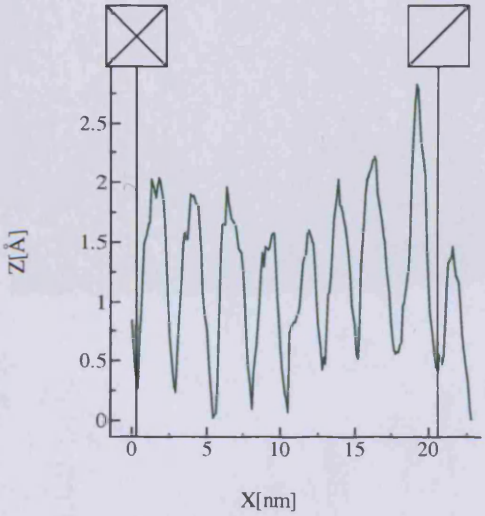

(b-i)

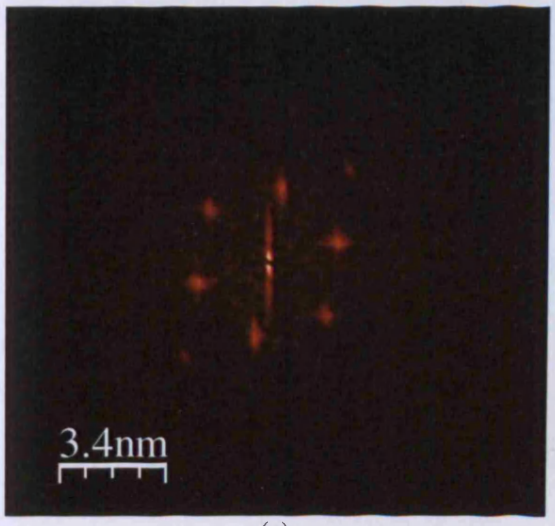

(c)

Figure 4.22 - STM images and measurements of Fe(111) with surface O and N. ***a*****) Z-image of a large terrace; sample bias = 0.63 V, feedback set = 0.17 nA.** ***a-i*****) Line profile across the step edge in** ***a.*** ***b*****) Correlated image of a smaller region on the terrace with the hexagonal lattice superimposed.** ***b-i*****) Line profile along line** ***i*** **in** ***b.*** ***c*****) 2D FFT image of** ***b*** **showing the hexagonal unit cell. Also see Figure 4.24 for different images of the same surface.**

According to the line profile (Figure 4.22*b-i*) the spacing between the features is ~2.5 nm and the array is only one atomic layer thick. The hexagonal unit cell and spacing are confirmed by the 2D FFT analysis shown in Figure 4.22*c*. Based on the symmetry and line profile measurement, it is suggested that the supperlattice has a (6×6) unit cell ($6 \times a = 2.43$ nm; $a_{Fe(111)} = 0.405$ nm). Exposing Fe(111) to oxygen (*e.g.* 1L of O_2 followed by annealing at 550 K[28]) has been known to result in a (6×6) LEED pattern.

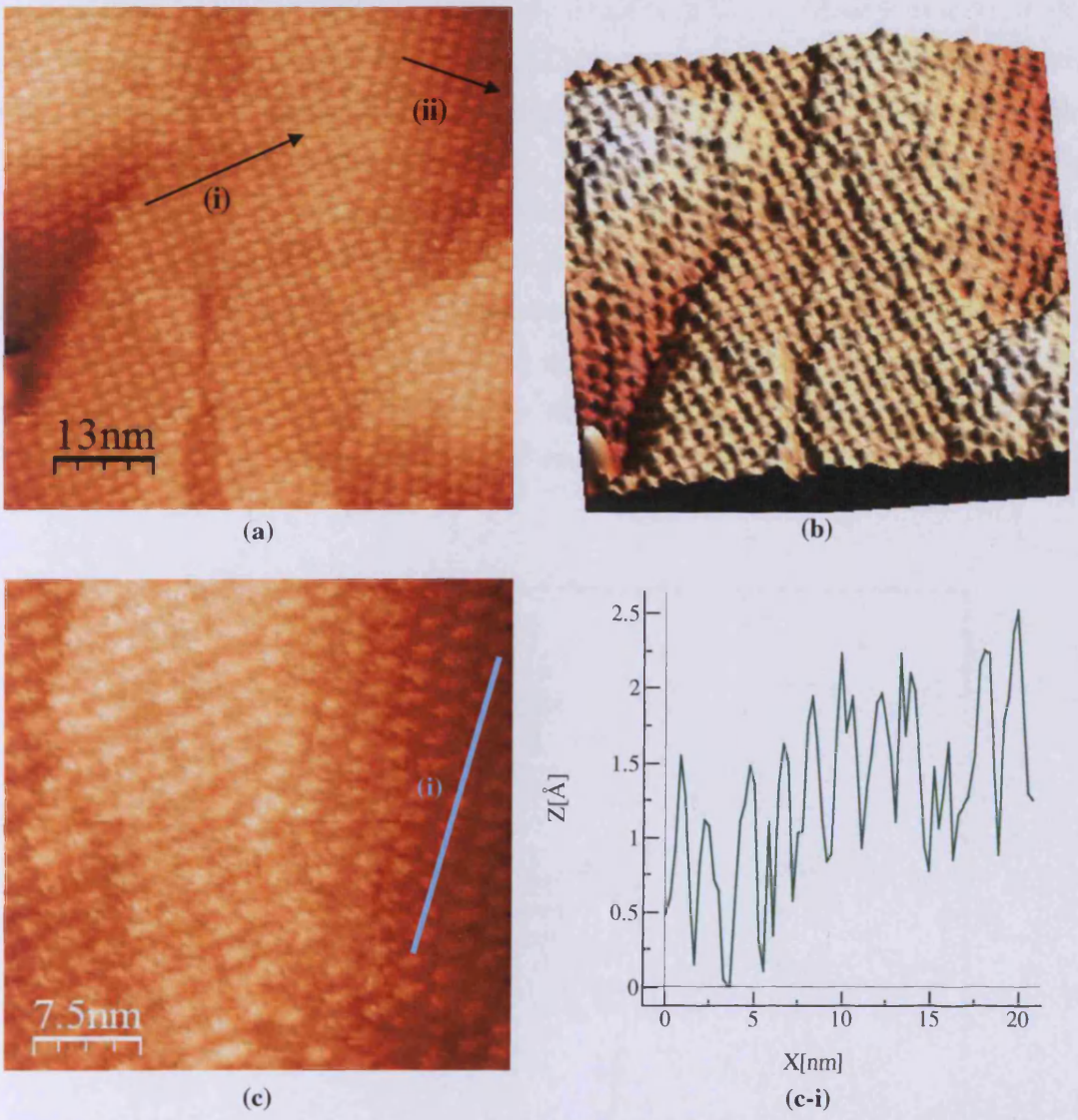

Figure 4.23 – STM images and corresponding line profiles of the same surface as shown in Figure 4.22; sample bias = 0.70 V, feedback set = 0.73 nA.

Figure 4.23 shows a more uneven area of the same surface where the packing arrangement is not hexagonal like in Figure 4.22, but square. The direction of the pattern changes across the different slopes of the surface as indicated by the arrows in Figure 4.23*a*; plane *i* is fairly flat, while plane *ii* intersects plane *i* at an angle of ~4.5°. Figure 4.23*b* is the corresponding 3D image to show the surface terrain more clearly. Figure 4.23*c* is a close up of the same area and Figure 4.23*c-i* is the line profile along line *i* in *c*; the features are spaced ~1.9 nm apart. The domains were not large enough to yield a good quality FFT image.

Figure 4.24 shows the XPS of a surface with ~0.11 $ML_{6\times6}$ O and 0.60 $ML_{6\times6}$ C that have segregated from the bulk. The C 1s peak is positioned at 282.7 eV and the O 1s at 529.7 eV, indicating that atomic C and O are present. STM images of the surface are shown in Figure 4.25. The surface consists of evenly sized triangular structures of a mere atomic layer high. Some regions are more ordered than others. The close up of the area indicated in Figure 4.25*b* shows an ordered region; the nearest neighbour repeat distance is ~2.2 nm along line *i* (see Figure 4.25*b-i*) and ~1.9 nm along line *ii* (see Figure *b-ii*); and the angle indicated in Figure 4.25*b* is ~73°, which is close to that expected for Fe(110), $\theta = 70.5°$. Figure 4.25*c* is a correlated image of the region that shows the symmetry more clearly. A centered rectangle, the non-primitive unit cell of Fe(110), was obtained in the FFT analysis (Figure 4.25*d*). Both the value of θ and the spacing were confirmed by the correlated and FFT images.

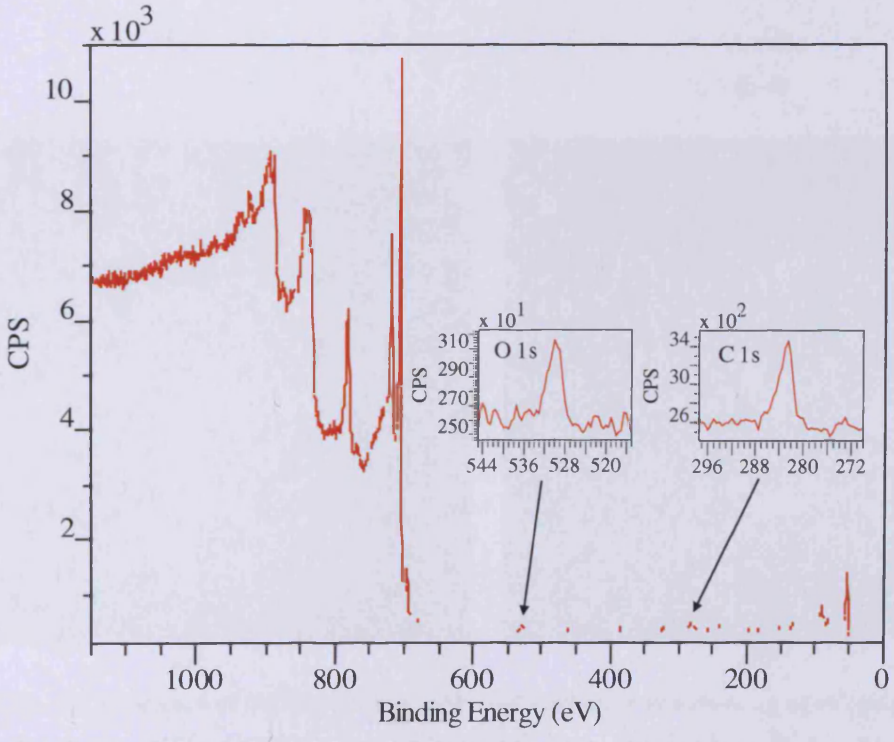

Figure 4.24 – XPS of Fe(111) contaminated with oxygen and carbon.

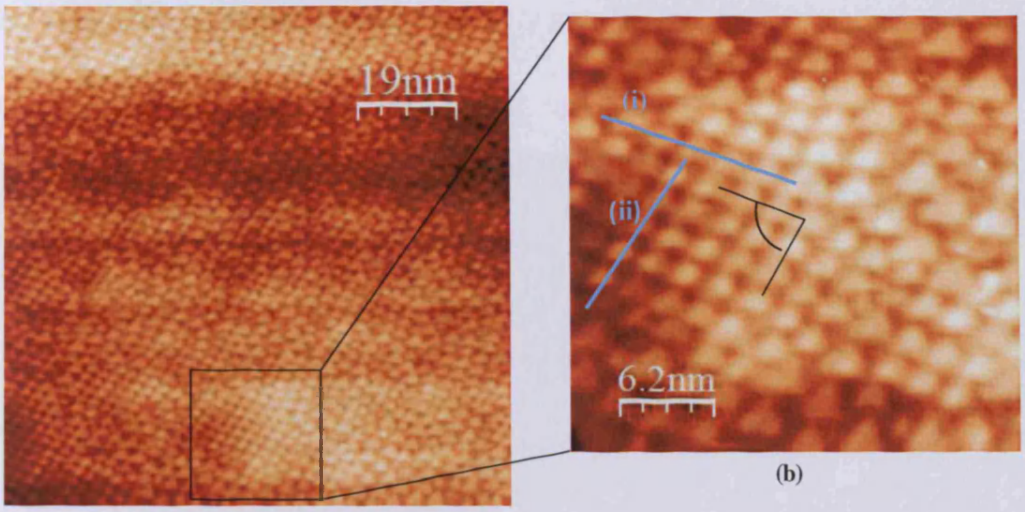

(a) (b)

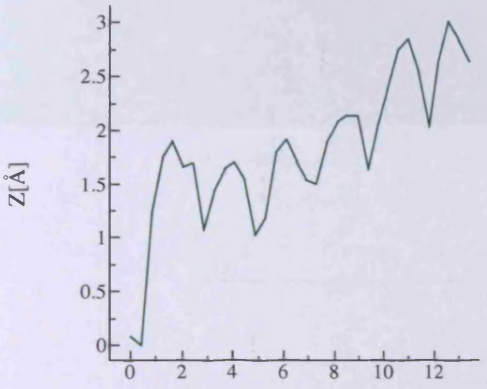

(b-i)

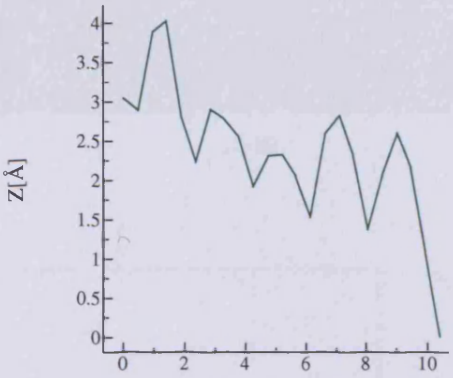

(b-ii)

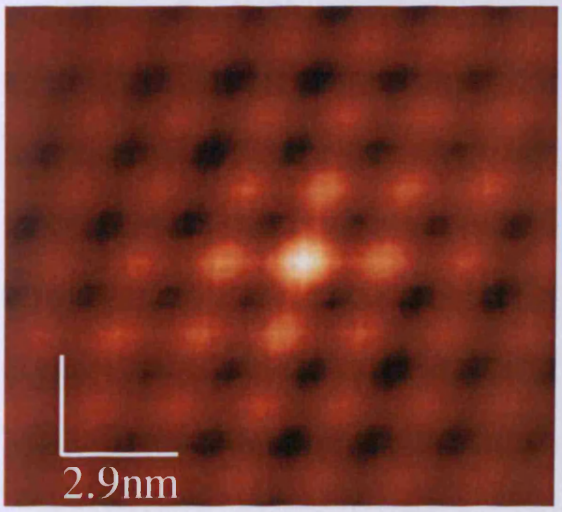

(c)

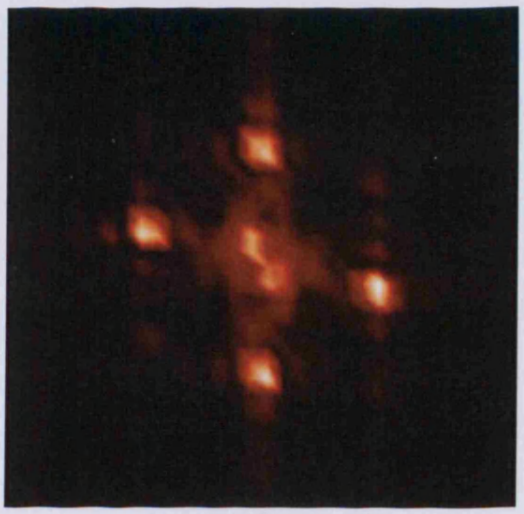

(d)

Figure 4.25 – STM images of Fe(111) with oxygen and carbon; *b* is a close up of *a*; sample bias = 1.0 V, feedback set = 0.26 nA; *b-i* & *b-ii* are line profiles of *b*. *c*) Correlated image of an ordered region and *d*) the FFT image.

LEED Patterns Resulting from the Segregation of Bulk Oxygen

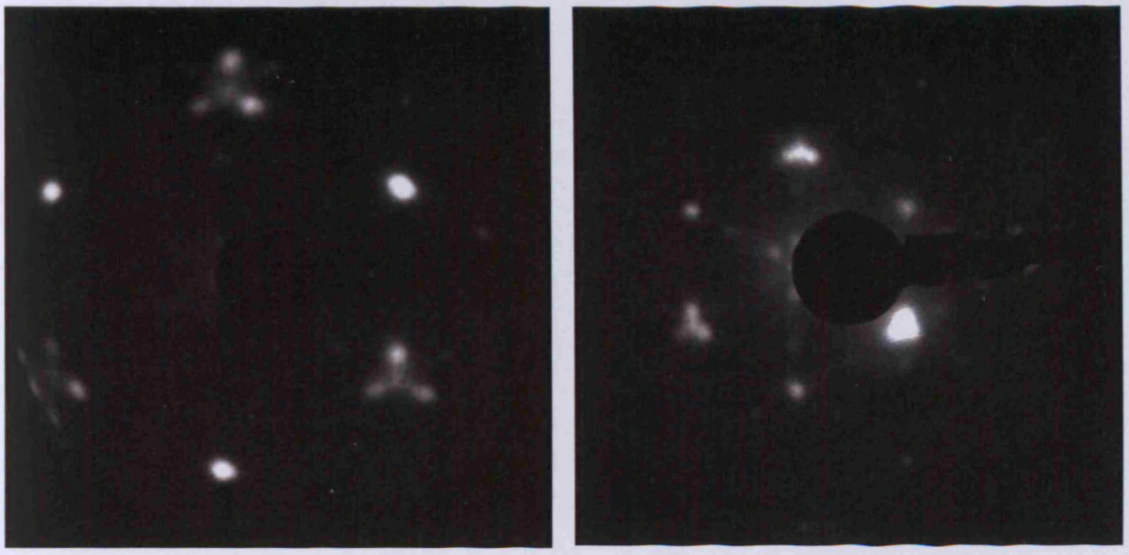

(a-i) (a-ii)

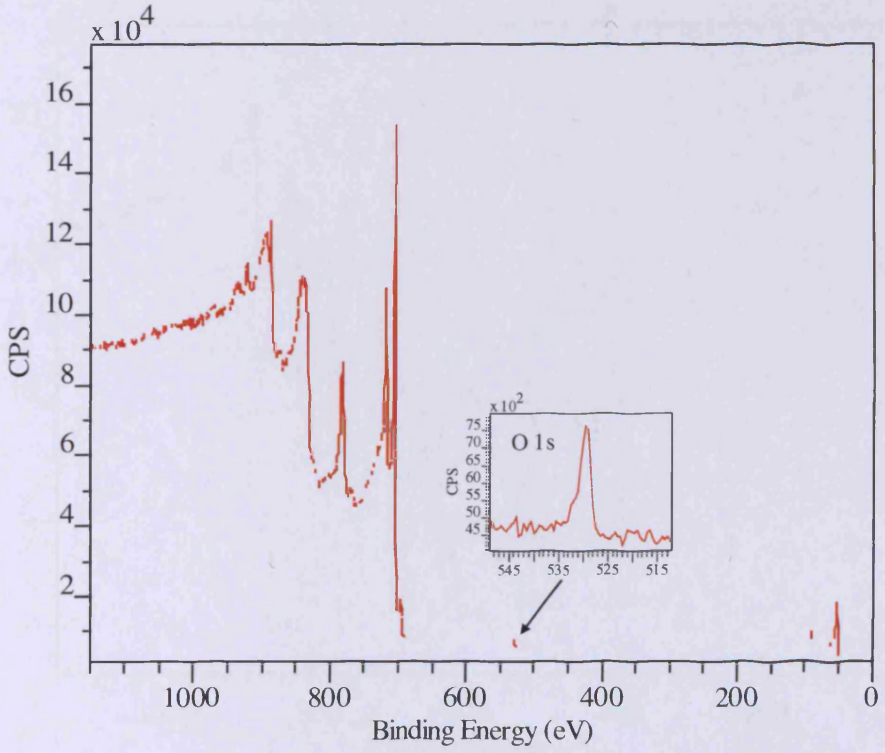

(b)

Figure 4.26 – *a*) LEED of Fe(111) with 0.15 $ML_{6\times6}$ of surface oxygen at *a-i*) 36 eV and *a-ii*) 89 eV. *b*) The corresponding XPS.

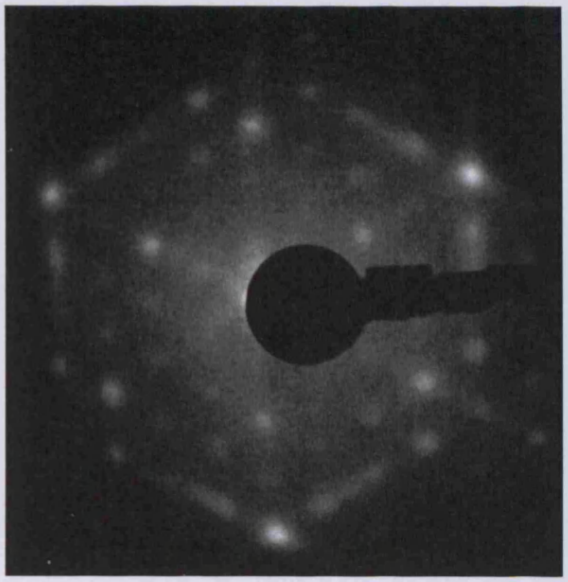

(a)

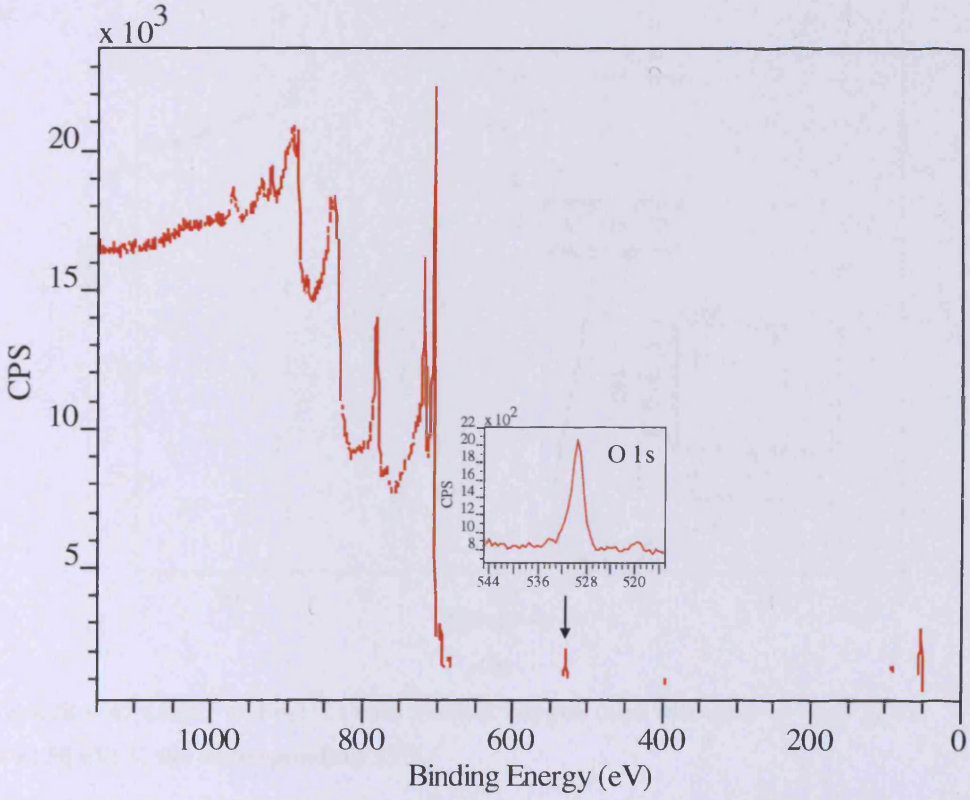

(b)

Figure 4.27 – *a*) (4×4) LEED pattern of Fe(111) with 0.27 $ML_{6\times6}$ of surface oxygen; E = 29 eV. *b*) The corresponding XPS spectrum.

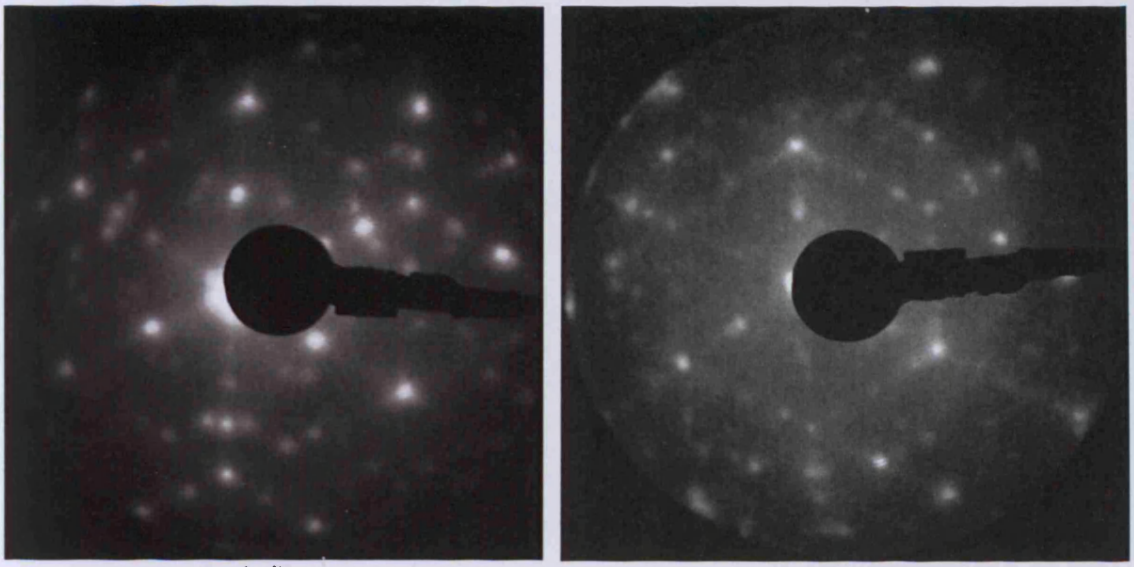

(a-i) (a-ii)

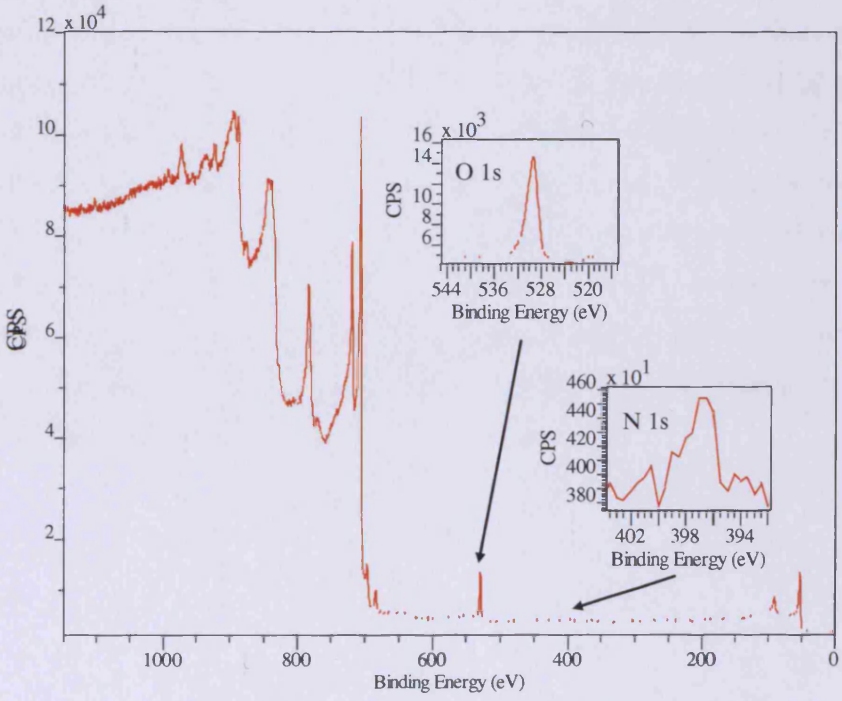

(b)

Figure 4.28 – *a*) LEED of Fe(111) with surface oxygen (and nitrogen) at *a-i*) 37 eV and *a-ii*) 58 eV; *b*) the corresponding XPS.

Figure 4.26 – 4.28 show LEED patterns that were obtained for Fe(111) with only/mainly oxygen that originated from the bulk during cleaning.

The LEED pattern in Figure 4.26*a* was obtained for a surface with 0.15 $ML_{6\times6}$ of oxygen. Three of the six integral spots exhibit extensive spot splitting, while the remaining three spots are quite broad. The overall pattern resembles (two coincident domains of) the (2×1) pattern, but the non-integral spots are not positioned exactly halfway between the integral spots.

The (4×4) structure in Figure 4.27*a* was obtained for a surface with 0.27 $ML_{6\times6}$ of oxygen. The same pattern was also obtained when clean Fe(111) that was dosed with oxygen (see Figure 4.36). The complicated pattern shown in Figure 4.28*a* was obtained for a surface with 0.43 $ML_{6\times6}$ of O and 0.06 $ML_{6\times6}$ of N; the pattern comprises of more than one (possibly several) sub-patterns.

Summary

It has been shown that Fe(111) is very susceptible to restructuring when ad-atoms are present, even at low levels. This is conceivable given the open structure of the surface, which should make it more reactive than denser surfaces. STM imaging of the surface suggests that the (111)-plane reconstructs to the more stable (100) or (110)-facets, as recognized by the symmetry; different packing arrangements can exist on the same surface. A variety of complicated LEED patterns, consisting of two or more sub-patterns, also allude to heterogeneous surfaces. In independent LEED experiments, split spots with threefold symmetry were observed, in agreement with the triangular pits and terraces observed with STM in independent experiments.

4.5. The Clean Surfaces

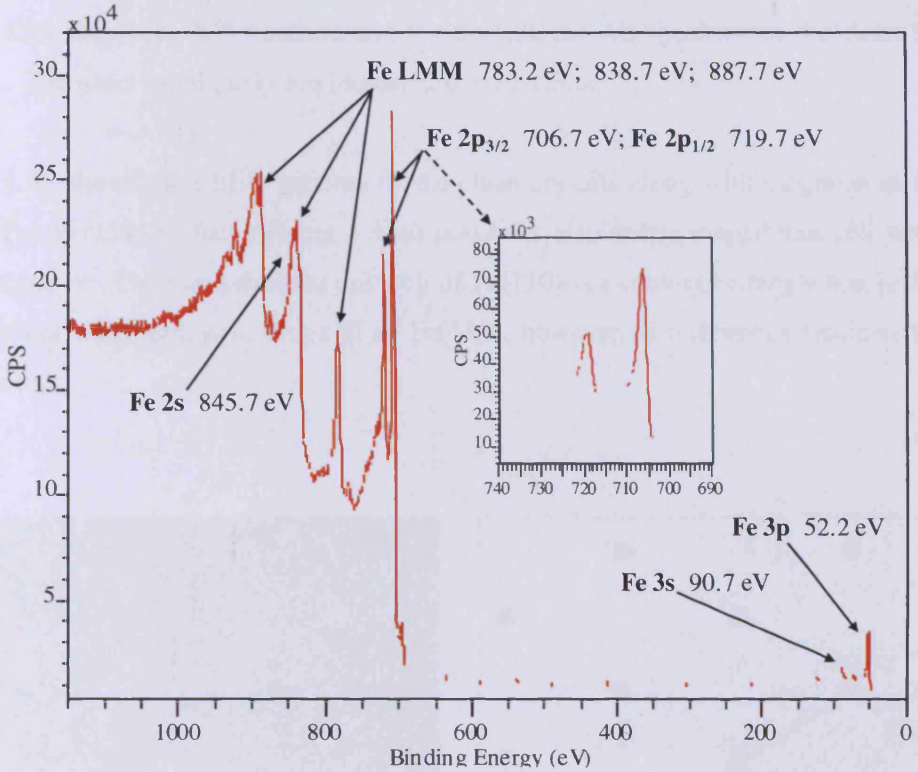

Figure 4.29 – XPS of Fe(111) after cleaning; Fe 2p peaks are used for quantification purposes.

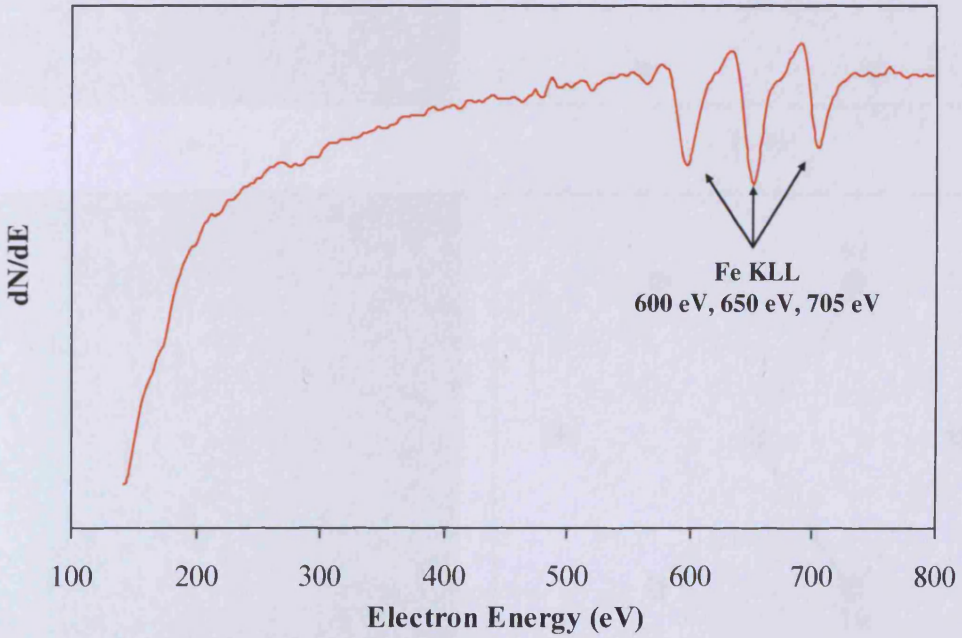

Figure 4.30 – AES of Fe(111); the Fe peak at 650 eV was used in peak-to-peak height measurements.

Clean surfaces of both crystals could be obtained by following the procedure described in section 4.4 and avoiding high temperatures which lead to the segregation of bulk sulphur. Figure 4.29 shows the XP spectrum and Figure 4.30 the AE spectrum of the clean Fe(111) surface. The main metal peaks are indicated in both cases.

Figure 4.31 shows the LEED patterns of the clean crystals along with diagrams of the unit cells. The Fe(111) surface (Figure 4.31*a*) possesses a rhombus shaped unit cell with three fold symmetry. The non-primitive unit cell of Fe(110) is a centred rectangle that is two-fold symmetrical. The primitive unit cell of Fe(110), however, is a rhombus (indicated by the base vectors).

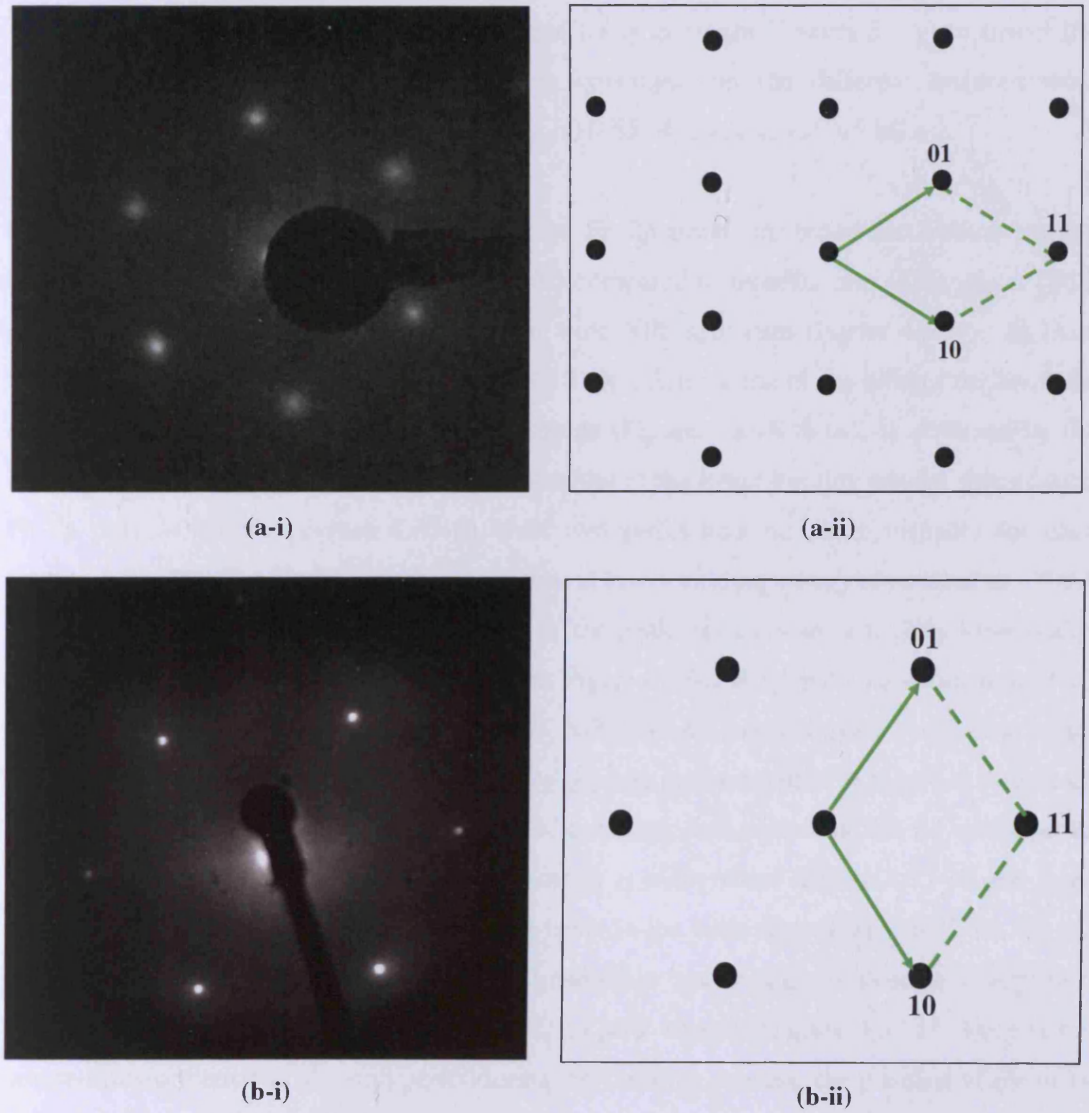

(a-i) (a-ii)

(b-i) (b-ii)

Figure 4.31 – (1×1) LEED pattern of *a*) clean Fe(111); E = 82 eV and *b*) Fe(110); E = 124 eV and the corresponding diagrams showing the base vectors.

4.6. Adsorption Studies

4.6.1 Adsorption of O_2 on Fe(111)

The effect of oxygen on the composition and oxidation state of the Fe(111) surface was investigated by dosing it with oxygen (5×10^{-6} mbar for 10 min at 473 K) and then cleaning it off in cycles of sputtering and annealing (at 673 – 873 K). The experiment was performed on a relatively new crystal and additional contaminants were therefore generally also present on the surface, as discussed below. Figure 4.32 – 4.35 show the gradual de-oxidation of the surface. The peak at ~685 eV in spectra *i – iii* is attributed to fluorine contamination.

Treating Fe(111) in oxygen led to severe oxidation of the surface as observed by the reduction and shift of the Fe 2p peaks and the increase in O 1s and O auger peaks (Figure 4.32-*i*). The oxidized film was then sputtered away in stages (figures *ii* - *v*) to reveal the metal surface again. The relative oxygen coverages on the different surfaces were *i*) 1.47 $ML_{6\times6}$; *ii*) 1.21 $ML_{6\times6}$; *iii*) 1.09 $ML_{6\times6}$; *iv*) 0.55 $ML_{6\times6}$; and *v*) 0.05 $ML_{6\times6}$.

For the initial oxidized surface (Figure *i*), the Fe 2p peaks are broad and shifted toward higher binding energies ($BE_{Fe\ 2p3/2}$ = 710.2 eV) compared to metallic iron ($BE_{Fe\ 2p3/2}$ = 706.7 eV). Large oxygen peaks are visible in the wide XPS spectrum (Figure 4.32-*i*): O 1s at 529.7 eV, O 2s at 21.7 eV and O KLL at 973.7 eV. After some of the oxide film has been sputtered away the metal surface starts to emerge (Figure 4.33-*ii & iii*), as observed by the change in the Fe 2p peaks. At first only a shoulder at the lower binding energy side of each Fe 2p peak is visible (Figure 4.33-*ii*), then two peaks become distinguishable for each (Figure 4.33-*iii*). The Fe $2p_{3/2}$ peak component at lower binding energy is situated at ~706.7 eV expected for Fe^0. The oxide component of the peak shifts toward a slightly lower value from 710.2 eV in Figure 4.33-*i* to 709.9 eV in Figure 4.33-*ii & iii*, but a component at 710.2 eV is still visible in both Figure 4.33-*ii & iii*. In Figure 4.33-*iv* this oxide component is not as pronounced: notice that especially the Fe $2p_{1/2}$ peaks are very broad in Figure 4.33-*ii & iii*, but narrower in Figure 4.33-*iv*. After more sputtering and annealing the Fe metal peaks dominate, but a shoulder at higher binding energy is still present (Figure 4.33-*iv*) and large oxygen features (O 1s and O KLL) are still visible in the wide scan (Figure 4.32-*iv*). In the last spectrum the higher binding energy Fe 2p shoulder and O auger peak have disappeared and only the iron metal features and a small O 1s peak remains (Figure 4.32-*v*). Despite the severe transformation of the iron peaks during the cleaning process, the position of the O 1s peak remains at 529.7 eV throughout (see Figure 4.34).

For surface *i* no LEED pattern was observed – the integral spots of the Fe(111) have disappeared completely and only a bright background was visible. Annealing the surface at 873 K for 1 min did not cause any change to occur; longer annealing times were not employed at that time. Sputtering and annealing caused the weak (1×1) pattern to become visible on a bright background (surface *iii*). The LEED pattern of surface *vi & v* was the "clock structure" which was shown in Figure 4.13.

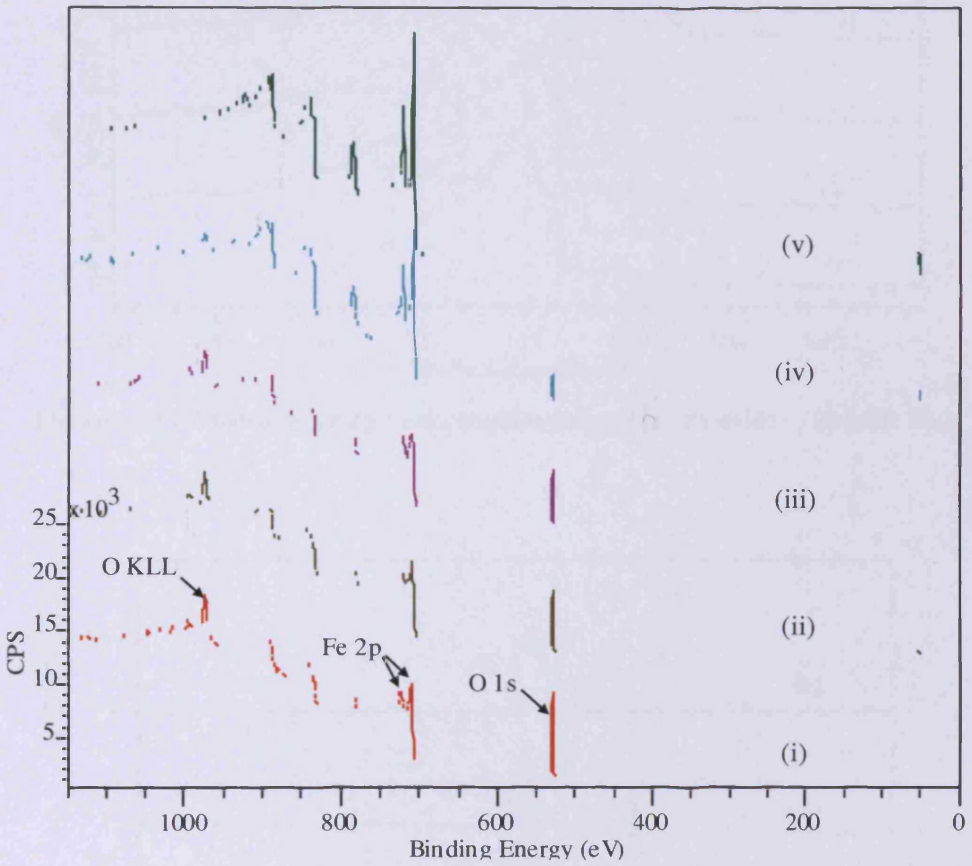

Figure 4.32 – Wide scan XPS spectra showing the de-oxidation of Fe(111); see Figure 4.34 & 4.35 for corresponding scans of the Fe and O peaks.

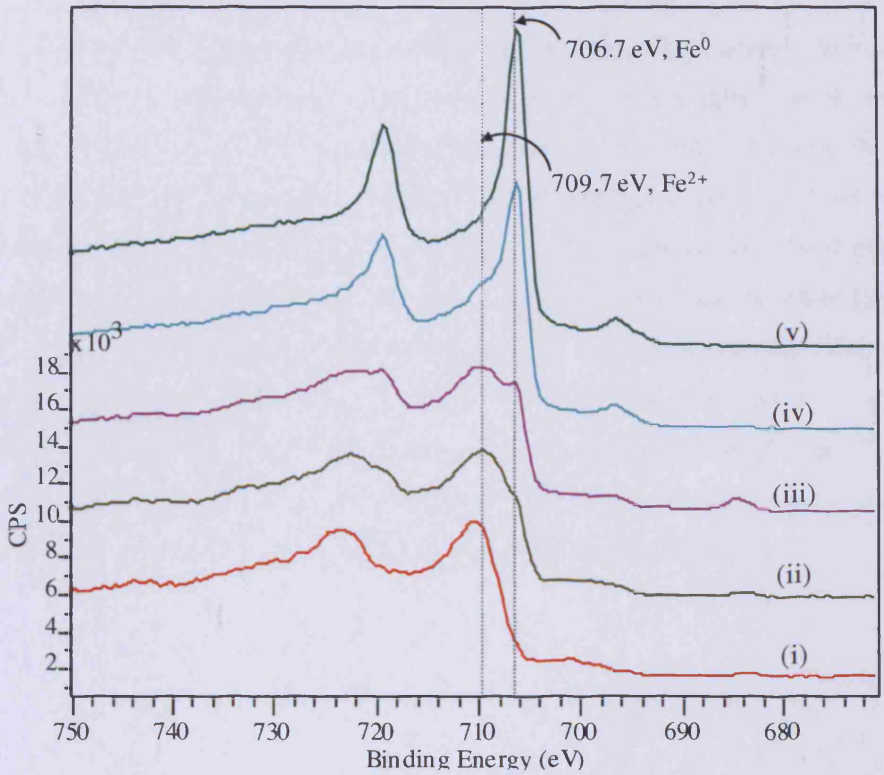

Figure 4.33 – Change in Fe 2p peak shape in going from Fe oxide to metallic Fe.

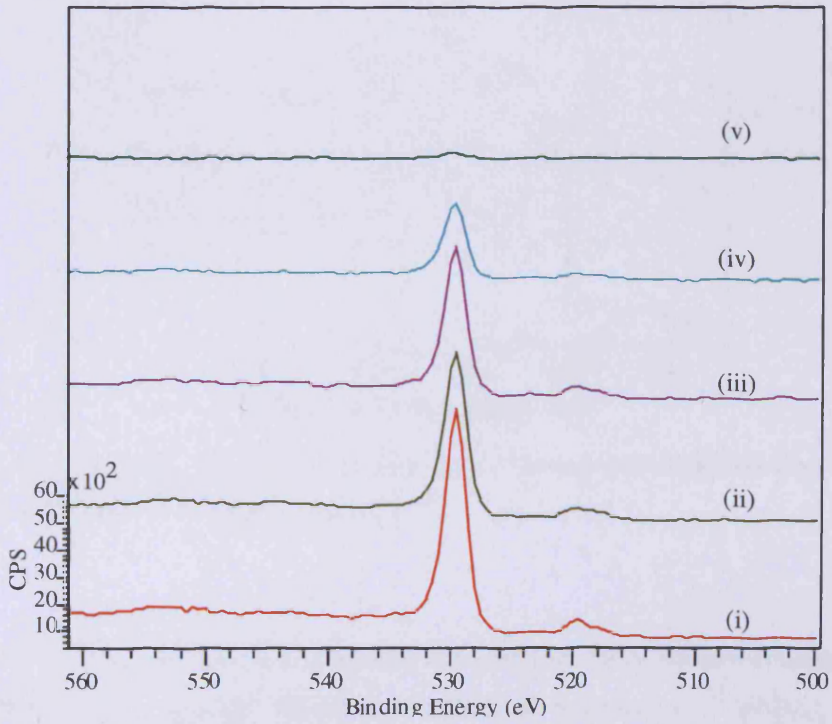

Figure 4.34 – Diminishing O 1s peak in going from iron oxide to iron metal.

Literature binding energy values for iron oxides vary greatly, which makes identification of the current oxide species difficult; some complications are the difference in calibration methods and sample types used in independent studies. For these reasons the Fe $2p_{3/2}$ binding energy values will be compared with those reported by Graat *et. al.*[83] who analyzed three oxidation states from pure reference samples: polycrystalline iron, FeO powder and Fe_2O_3 powder. The XPS spectra of the Fe region from that study are shown in Figure 4.35. The value of the pure iron sample (706.8 eV) is in good agreement with our reference value of 706.7 eV. A value of 709.8 eV and 711.2 eV was obtained for Fe^{2+} and Fe^{3+} respectively. The characteristic satellite peaks of Fe^{2+} and Fe^{3+} are clearly distinguishable at ~715 eV and 719 eV (indicated by arrows); these features are not visible in our spectra, most likely because the oxide layer isn't thick enough to give strong satellite features.

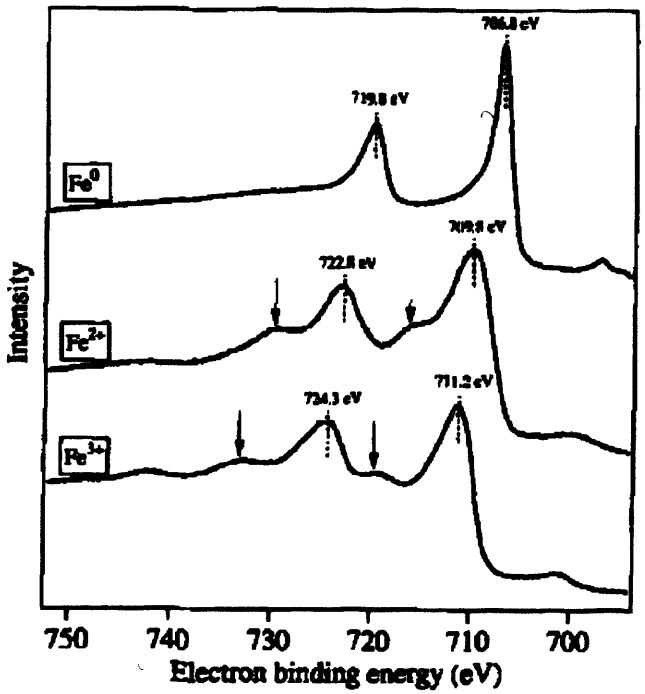

Figure 4.35 – Fe 2p spectra from reference samples: Fe^0 from a polycrystalline iron crystal, Fe^{2+} from FeO powder and Fe^{3+} from Fe_2O_3 powder.[83]

The value of $BE_{Fe\ 2p3/2}$ = 710.2 eV obtained here for the initial surface (Figure *i*) falls in between that of the Fe^{2+} and Fe^{3+} reference samples, but is closer to Fe^{2+} ($\Delta BE_{Fe(111)\ oxide\ -\ FeO}$ ~ 0.5 eV and $\Delta BE_{Fe(111)\ oxide\ -\ Fe2O3}$ ~ 0.9 eV). Given this binding energy value and the fact that the peaks themselves are broad, it is most likely that an oxide mixture exists on surface *i*.

For the intermediate surfaces the mixture of oxides is apparent from the Fe 2p peak shapes as discussed above (Figure 4.33-*ii & iii*). The value of the Fe $2p_{3/2}$ peak maximum of these surfaces, 709.9 eV, corresponds very well with that of the Fe^{2+} reference sample. Furthermore the higher oxidation state component ($BE_{Fe\ 2p3/2}$ ~710.2 eV) is reduced in these surfaces and even more so in the cleaner surface (Figure 4.33-*iv*).

In agreement with these findings, Graat observed a mixture of Fe^{2+} and Fe^{3+} after oxidation of the polycrystalline iron sample.[83] Different oxidation temperatures were employed, which affected the oxide ratio. A Fe^{2+}/Fe^{3+} ratio of 0.69 : 0.31 was obtained at 298 K and a ratio of 0.87 : 0.31 at 573 K. Qin[38] concluded from STM/AES results that oxidation of Fe(111) at 300 K leads to the growth of thin Fe_3O_4 or FeO islands at lower exposures; and at higher exposures Fe_2O_3 forms on top of these islands. Oxidation at 500 K causes the formation of thicker islands, with Fe_3O_4 being the dominant species.

Despite the apparent change in oxidation state of iron, the O 1s peak position remained unaffected; indicating that the oxygen binding energy is independent of the relative concentration / bonding configuration. Pirug also found that the O 1s peak position is unaffected by a change in oxygen coverage in a study on Fe(110) (only submonolayer coverages of oxygen were tested).[40] The O 1s binding energy reported in that study was 529.5 eV (corrected against $BE_{Fe\ 2p3/2}$ = 706.7 eV), which agrees well with our value, 529.7 eV. In the study of Graat the O 1s peak positions of the oxide samples were adjusted to 529.9 eV so that it matches the value of oxidized samples that has previously been reported.[84]

Oxidation of Fe(111) at 300 K has been shown to result in oxide island formation.[38] The surface was uniformly covered as judged by STM imaging and conduction measurements; both the islands and the areas in between displayed insulating behaviour. As in this study (surface *i*) no LEED pattern was observed for the oxidized surface, indicating the lack of long range order in these oxide islands. The clock structure, obtained for surfaces *iv & v* has previously been attributed to a combination of low level impurities such as S, N and O; and indeed S was also present on surface *iv* and N & C were present on surface *v*.

Oxidation of the clean Fe(111) surface leads to simpler patterns, as shown in Figure 4.36 & 4.38. The (4×4) pattern shown in Figure 4.36*a* has been exposed to ~0.1 L of oxygen at RT and then annealed at 773 K for 15 min; the AES O/Fe ratio was 0.19, which was approximated to be equal to ~0.27 $ML_{6\times6}$ of oxygen (calibrated to an estimation of 1 $ML_{6\times6}$

of surface oxygen which gives an AES O/Fe ratio of 0.7). Figure 4.37*a* shows a (6×6) structure that could be obtained by exposing the surface to 2 – 70 L of oxygen and then annealing at 773 K. The resulting O-Fe Auger ratio was between 0.33 – 0.7; the surface shown in Figure 4.37*a* has an AES O/Fe ratio of 0.33, which was approximated to be ~0.50 $ML_{6\times6}$ of oxygen. A Fe(111)(6×6)-O LEED pattern was also reported by Seip *et. al.*[28] **

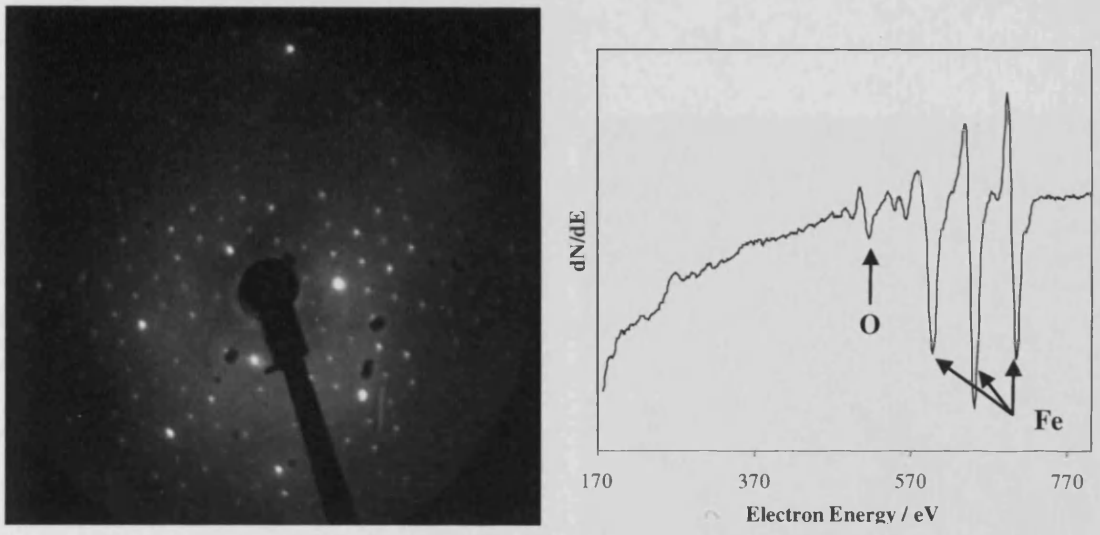

(a) (b)

Figure 4.36 – *a*) LEED pattern of Fe(111) with surface oxygen; E = 120 eV. *b*) The corresponding AES; O/Fe = 0.16 (corresponding to 0.27 $ML_{6\times6}$ of O).

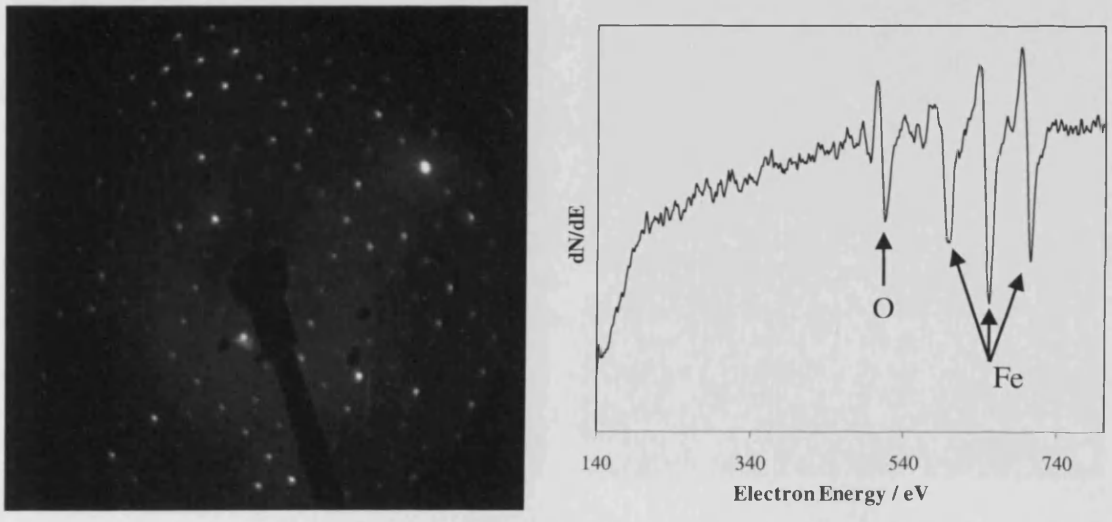

(a) (b)

Figure 4.37 – *a)* (6×6) LEED pattern of Fe(111) with a higher concentration of surface oxygen; E = 100 eV. *b*) The corresponding AES; O/Fe = 0.60; ~1.0 $ML_{6\times6}$ of O.

** LEED / AES in Figure 4.36 & Figure 4.37 were supplied by Robert Davies.

4.6.2 Adsorption of C_2H_4 on Fe(110)

The adsorption of C_2H_4 on Fe(110) was investigated with STM, LEED and XPS. C_2H_4 was initially dosed at room temperature (34 L, P = 1×10^{-7} mbar), followed by annealing at 423 K for 10 min to dissociate the reactant without causing bulk carbidization.

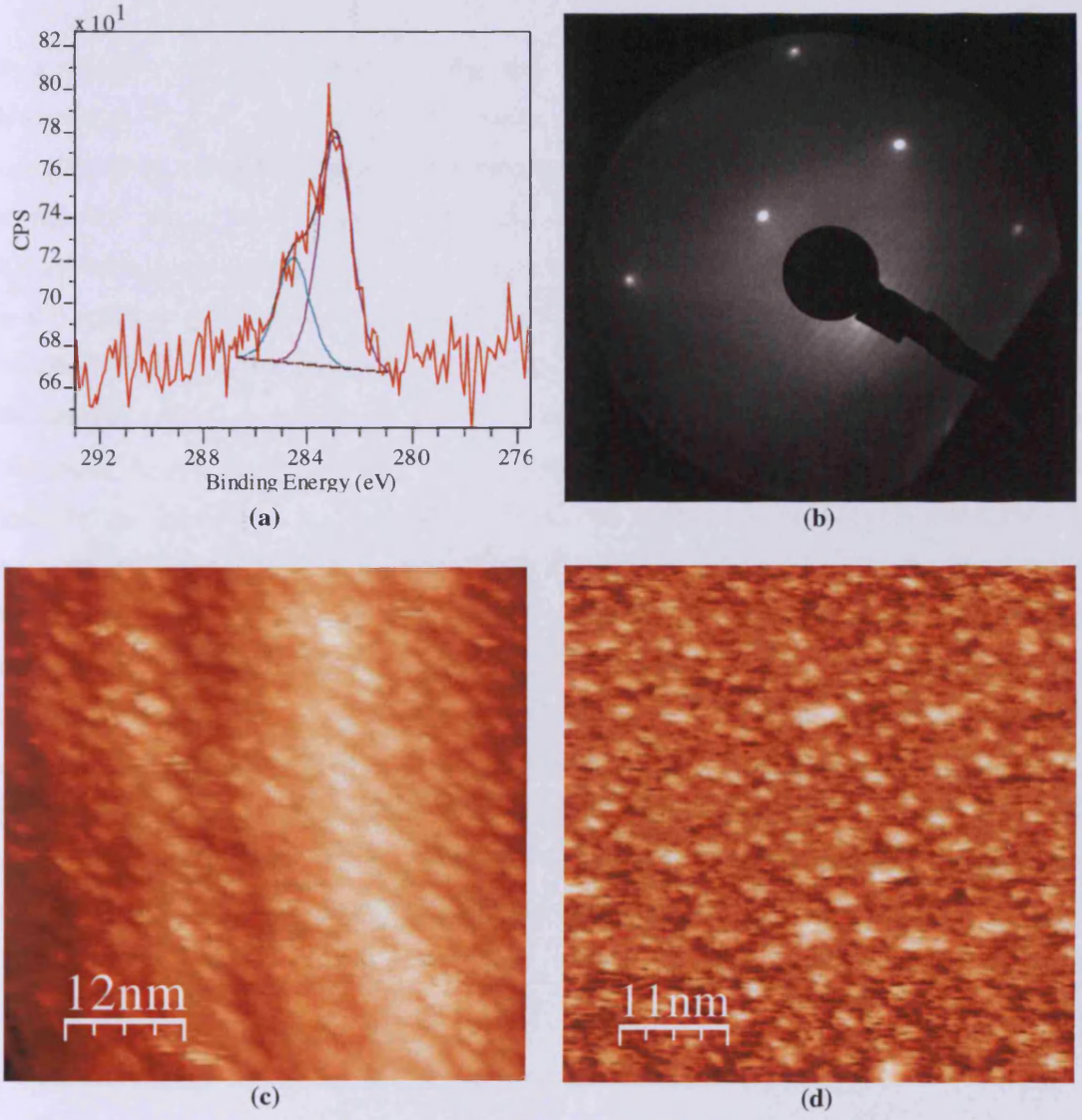

Figure 4.38 – *a*) C 1s XPS peak obtained from Fe(110) that was dosed with 34 L of C_2H_4 at RT and then annealed at 423 K for 10 min. *b*) The corresponding LEED pattern; E = 100eV. *c*) The resulting STM image. *d*) STM after annealing further for an hour at 423 K.

Figure 4.38*a* shows the resulting XPS spectrum of the C region. The C peak consists of two sub-peaks; the main peak is situated at ~282.9 eV and translates into ~0.18 $ML_{6\times6}$ of C. The shoulder at the higher energy side of the peak is situated at ~284.6 eV and is attributed to contamination from background CO; in agreement with the amount of oxygen that was also present. The Fe(110) unit cell can be recognized in the LEED pattern (shown in Figure 4.38*b*), but the bright background indicates a high degree of disorder. STM also shows that the surface is relatively disordered (Figure 4.38*c*). One hour of additional annealing at 423 K did not improve the order (Figure 4.38*d*).

In a separate experiment, 6 L of C_2H_4 was dosed onto the clean surface at the higher temperature of ~473 K (P = 1×10^{-7} mbar). The position of the XPS C 1s peak was comparable to that in the previous experiment (~282.8 eV) and the coverage was estimated to be ~0.23 $ML_{6\times6}$ (again some CO was also present); the LEED also looked the same as before (showing the integral spots on a bright background). In contrast to the surface dosed at RT and annealed at 423 K, however, STM images of this surface show smooth terraces of which some are covered with groups of islands aligned in parallel rows. Figure 4.39*a* shows the features being continuous over some step edges, but other terraces are not covered even though the heights of the respective steps separating the terraces are comparable. The island indicated in Figure 4.39*c* was measured to be 6.4 nm wide and 33 nm long (Figure 4.39*c-i* & *c-ii*), while some of the smallest ones were 5 – 8 nm in diameter. The height of these features is a mere ~ 0.2 nm, *i.e.* a single layer of atoms. The features are generally grouped together and the larger islands don't have smooth surfaces (Figure 4.39*c-i*), suggesting that the bigger islands might have been formed out of a number of smaller islands. An alternative explanation of the uneven island surfaces is that they actually contain some residual CH groups; see discussion on p.214 – 215. The difference in STM images at 423 K and 473 K (random distribution in the former *vs.* island formation in the latter) suggests that the surface species is more mobile at the higher temperature.

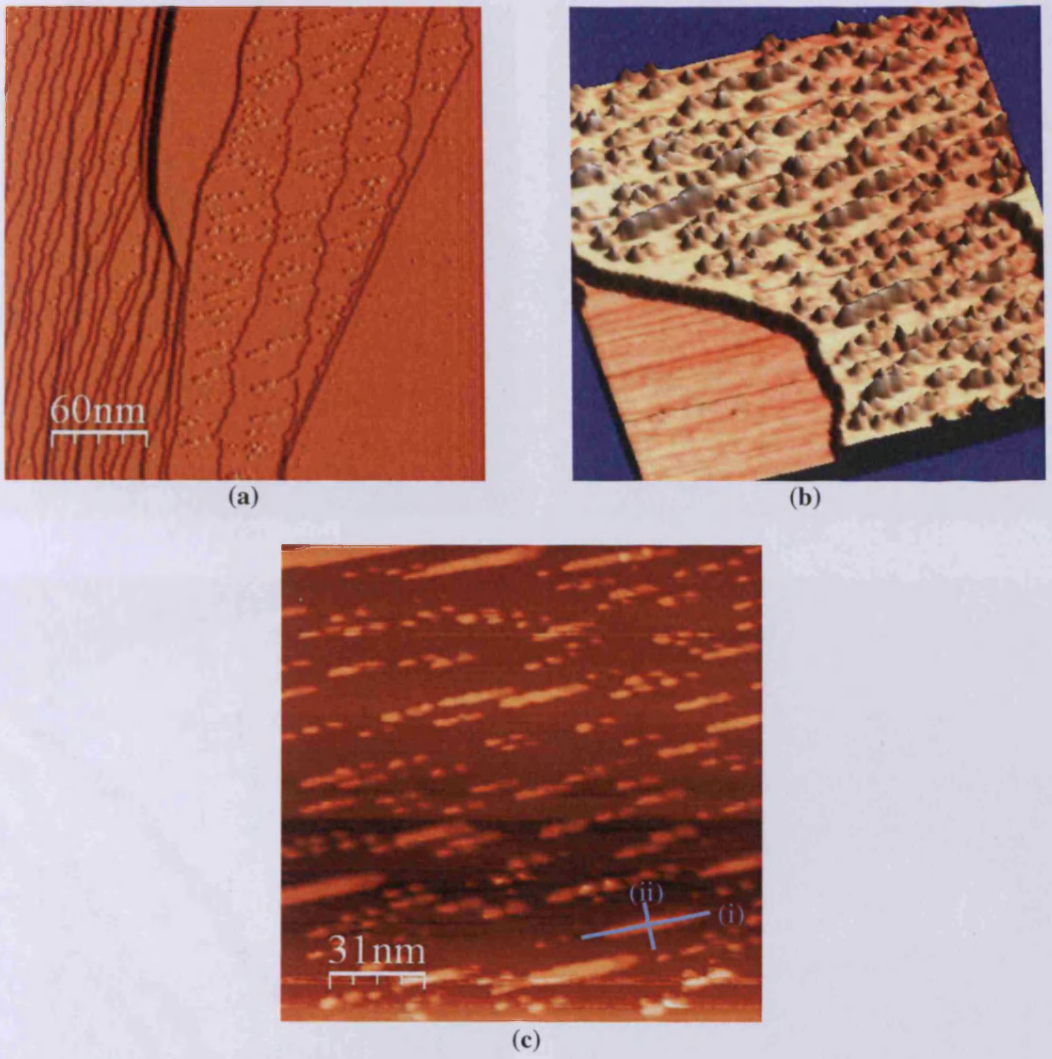

Figure 4.39 – STM images of Fe(110) after being dosed with 6 L of C_2H_4 at 473 K. ***a*) 2D *I*-image of the terraces, some with parallel rows of islands, others bare; sample bias = 0.52 V, feedback set = 0.31 nA.** ***b*) 3D view of a smaller area.** ***c*) *Z*-image; sample bias = 0.44 V, feedback set = 0.34 nA;** ***c-i* & *c-ii*) Line profiles across the length and width of the island shown in *c*.**

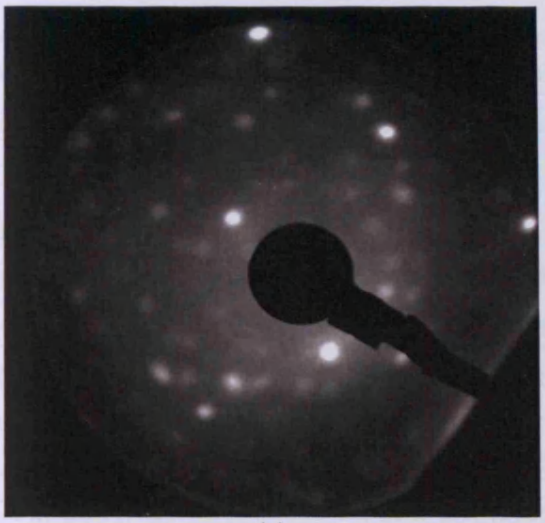

(a)

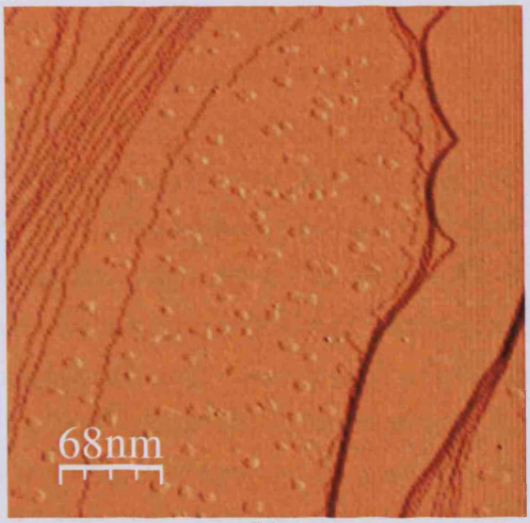

(b)

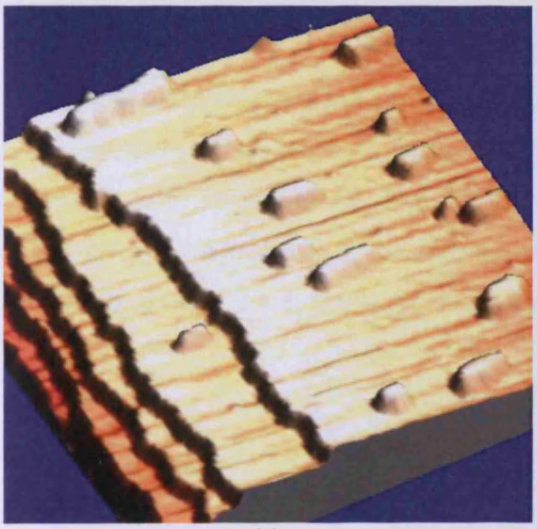

(c)

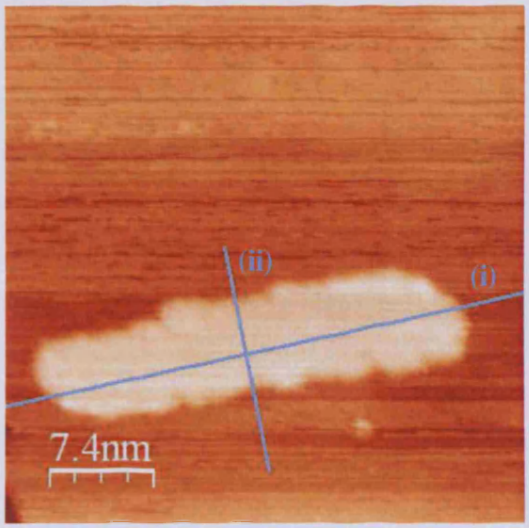

(d)

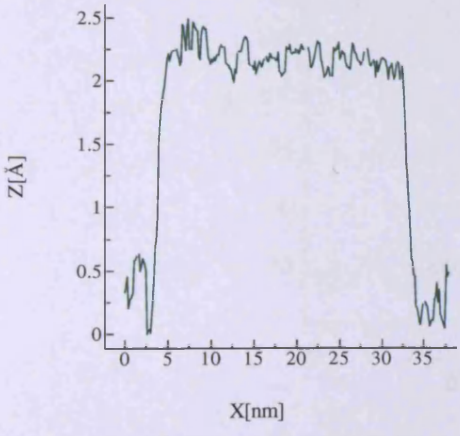

(d-i)

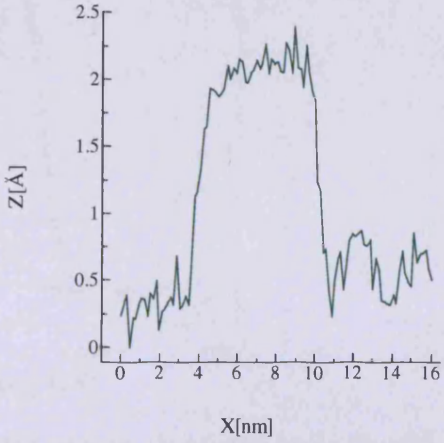

(d-ii)

Figure 4.40 – *a*) LEED image of Fe(110) after being dosed with 12 L of C_2H_4 at 473 K; E = 90 eV. *b*) *I*-image; *c*) 3D *I*-image and *d*) *Z*-image of the surface; sample bias = 1.1 V, feedback set = 0.91 nA. *d-i* & *d-ii*) line profiles of *d*; island length = 32 nm, width = 7.4 nm.

In a third experiment C_2H_4 was again dosed at ~473 K on a clean surface, but at a higher dose of 12 L (P = 1×10^{-7} mbar). Again the C 1s peak position was ~ 282.8 eV; the C coverage was ~ 0.31 $ML_{6\times6}$. The resulting LEED and STM images are shown in Figure 4.40. This time the LEED (Figure 4.40*a*) indicates order and is recognized as the carbon ring pattern. The STM images of the surface (Figure 4.40*b* – *d*) again show islands, but they now generally seem to be further apart. The sizes of the islands are in the same order of magnitude as before, but the size distribution between the features is smaller (*i.e.* they are generally of comparable size, compared to the larger size differences on the surface in Figure 4.39). The tops of the features are flatter than before (compare the uneven tops in Figure 4.39 *c-i* & *c-ii* against the smoother lines of Figure 4.40*d-i* & *d-ii*), but the height is again only about one atomic layer. The smoother structure might be due to the longer dosing time (at the elevated temperature) which gives the islands longer to form.

30 L of C_2H_4 dosed onto the clean surface under the same conditions (T ~ 473 K, P = 1×10^{-7} mbar) resulted in a higher C coverage, 0.65 $ML_{6\times6}$. The C 1s XPS peak, shown in Figure 4.41, is situated at ~282.8 eV, but a small component at ~284.2 eV is also visible. The higher energy component is in the region expected for graphite (CO is ruled out, since no O peak was present). Good quality STM images of the surface could not be obtained.

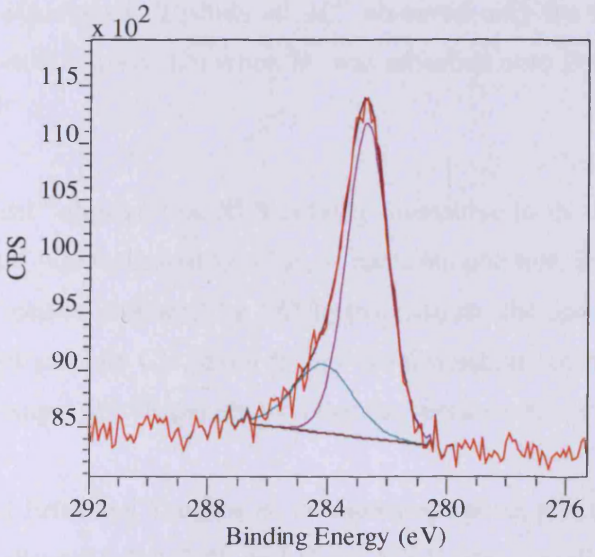

Figure 4.41 – XPS spectrum of Fe(110) dosed with 30 L of C_2H_4 (P = 1×10^{-7} mbar, T = 473 K).

On Fe(110) C_2H_4 first decomposes to C_2H_2 and H_2 before C-C bond scission occurs and eventually complete dehydrogenation is achieved.[31] This in contrast to the rapid decomposition of C_2H_4 on Fe(111) which already occurs at ~250 K without the formation of stable intermediates.[28] The dissociation energy of the C-C bond in C_2H_4 is ~724 kJ/mol, while the value for C_2H_2 is 962 kJ/mol.[85]

No shift in the binding energy of the Fe 2p peaks was observed in any of the experiments (Figure 4.39 – 4.42). This was also true in other studies, like that of Panzner,[13] who studied segregated C on Fe(100). Even when comparing the peaks of pure iron and Fe_3C the shift in BE is within experimental error ($\Delta BE_{Fe2p3/2} = +0.2$ eV).[86]

Erley[31] studied the adsorption and decomposition of C_2H_2 and C_2H_4 on Fe(110) by means of vibrational spectroscopy and found that decomposition of C_2H_4 to C_2H_2 and H_2 starts below 300 K and is completed by ~315 K. In that study a surface dosed with 6 L of C_2H_2 was annealed to 420 K, which led to the rupture of the C-C bond and the formation of CH species; it was suggested that CH_2 may also be present due to self-hydrogenation of the CH species. After heating to 550 K, vibrational loss peaks attributed to CH_x species were still observed; and complete decomposition to surface carbon (with a loss of all other peaks) was only accomplished above ~650 K. HREELS experiments were supplemented with TPD; H_2 desorption peaks were observed at 340 K, 440 K and 630 K due to the decomposition of C_2H_2. In a similar experiment, Yoshida *et. al.*[27] observed only the lower temperature H_2 desorption peaks (at 400 and 470 K); when H_2 was adsorbed onto Fe(110), desorption was complete by 400 K.[27]

Experiments by Bonzel[18] showed that XPS is fairly insensitive to the type of C-H bond. A BE value of ~283.2 eV was measured for C_2H_2 at room temperature, but the same value was obtained for a CH_x species produced by CO hydrogenation (the species was identified as partially hydrogenated carbidic C). Even though no distinction could be made with XPS, comparison of the C Auger line shapes showed that the species were clearly different.

Considering results of Erley and Yoshida *et. al.* discussed above, it is expected that C_2H_4 on Fe(110) would have dissociated to C_2H_2 and H_2 by 423 K (the annealing temperature of the surface shown in Figure 4.38). H_2 desorption and C-C bond rupture in C_2H_2 also occurs below this temperature, but complete decomposition is expected to occur only at a higher temperature, suggesting that the surface shown in Figure 4.38 is covered in CH_x species.

STM images of the surfaces dosed at 473 K (Figure 4.39 & 4.41) are clearly different than the one annealed at 423 K (Figure 4.38). Yoshida *et. al.* reported a weak (1×1) pattern for Fe(110) after higher exposures of C_2H_2 or C_2H_4 at ~400 K. After flashing to 500 K (adsorption was done at 273 K) a new LEED pattern started to develop, but the carbon ring pattern was only obtained after flashing to 700 K. The dosing temperature applied for the surfaces shown in Figure 4.39 and Figure 4.40 is close to the first change over temperature reported by Yoshida *et. al.* (~473 ± 10 K *vs.* ~500 K) and in addition the surface in Figure 4.40 was effectively annealed for a longer period than the one in Figure 4.39, which might explain the different LEED patterns obtained for the two surfaces.

Island formation at 473 K is not consistent with the predominance of hydrogenated species, especially not CH_2, since steric interaction is expected to lead to a wider and more random distribution across the surface. The C 1s BE of ~282.8 eV is similar to that observed for segregated C (*e.g.* Figure 4.25), which suggests that atomic carbon is present (as also evidenced by the LEED in Figure 4.40*a*). C species, however, tend to repel each other and will not form islands.[22] Graphite island formation, on the other hand, is common on Fe at higher C coverages[13] below the dissolution temperature (which is ~620 K for Fe(110)[17]). From the height measurement (~ one atomic layer), the islands are tentatively assigned to graphene. In agreement with this, a graphite component is detected in the XPS at higher C coverage (Figure 4.41).

Similar STM results could not be found in literature. LEED and STM images of Fujii (shown in Figure 4.2) illustrated a very different Fe-C interaction. C (segregated from the bulk after annealing between 573 – 823 K) caused reconstruction of the Fe(100) surface into a metastable $c(3\sqrt{2}\times\sqrt{2})$ phase by forming self-avoiding zigzag chains.[22, 23] The distance between the nearest neighbour atoms was ~0.29 nm and therefore equal to the lattice spacing of Fe(100) itself. Strong Fe-C bonds existed, but the chain formation was attributed to C-C repulsion which leads to short and long range order as a function of the relative C/Fe concentration in the surface.

4.6.3 Summary

Fe(111) forms a mixture of surface oxides when exposed to O_2 at 473 K; with FeO being the dominant oxide species. Sputtering and annealing the oxidized surface causes the overall oxygen concentration to decrease and the FeO : Fe_xO_y ratio to increase further. Dosing the

clean Fe(111) surface with O_2 followed by annealing results in simple LEED patterns, *e.g.* (4×4) or (6×6), in contrast to the complicated patterns brought about by the co-adsorption of oxygen and other contaminants originating from the bulk.

Exposing Fe(110) to C_2H_4 at 423 K results in a disordered surface, as evidenced by STM images and a bright background in the LEED. Dosing at 473 K leads to complete dissociation of C_2H_4, resulting in C surface species and the formation of single layer islands which are tentatively assigned to graphene.

4.7. References

1. R. Brady and R. Pettit, *J. Am. Chem. Soc.*, 1981, **103**, 1287.
2. W. Van Barneveld and V. Ponec, *J. Cat.*, 1984, **88**, 382.
3. N. D. Spencer, R. C. Schoonmaker and G. A. Somorjai, *J. Cat.*, 1982, **74**, 129-135.
4. J. Benziger and R. J. Madix, *Surf. Sci.*, 1980, **94**, 119-153.
5. U. Seip, M. C. Tsai, K. Christmann, J. Kuppers and G. Ertl, *Surf. Sci.*, 1984, **39**, 29-42.
6. G. Brodén, G. Gafner and H. Bonzel, *Appl. Phys. A*, 1977, **13**, 333-342.
7. S. Titmuss, A. Wander and D. A. King, *Chem. Rev.*, 1996, **96**, 1291-1306.
8. H. D. Shih, F. Jona, D. W. Jepsen and P. M. Marcus, *Physical Review Letters*, 1981, **46**, 731.
9. M. Kiskinova, *Chem. Rev.*, 1996, **96**, 1431-1448.
10. J. C. Dunphy, C. Knight, P. Sautet, D. F. Ogletree, G. A. Somorjai and M. B. Salmeron, *Surf. Sci.*, 1993, **280**, 313-324.
11. J. S. Lin, H. Cabibil and J. A. Kelber, *Surf. Sci.*, 1998, **395**, 30-42.
12. D. R. Strongin and G. A. Somorjai, *J. Catal.* , 1989, **118** 99.
13. G. Panzner and W. Diekmann, *Surf. Sci.*, 1985, **160**, 253-270.
14. W. Arabczyk, F. Storbeck and H. J. Mussig, *Appl. Surf. Sci.*, 1993, **65-66**, 94-98.
15. S. R. Kelemen and A. Kaldor, *J. Chem. Phys.*, 1981, **75**, 1530-1537.
16. A. Wiltner and C. Linsmeier, *Phys. Stat. Sol. A*, 2004, **201**, 881-887.
17. A. Wiltner, C. Linsmeier and T. Jacob, *J. Chem. Phys.*, 2008, **129**, 084704-084710.
18. H. P. Bonzel and H. J. Krebs, *Surf. Sci.*, 1980, **91**, 499-513.
19. F. R. McFeely, S. P. Kowalczyk, L. Ley, R. G. Cavell, R. A. Pollak and D. A. Shirley, *Phys. Rev. B*, 1974, **9**, 5268.
20. W. Arabczyk and U. Narkiewicz, *Vacuum*, 1997, **48**, 347-350.
21. W. Arabczyk, F. Storbeck and H. J. Mussig, *Appl. Surf. Sci.*, 1993, **65-66**, 94-98.
22. J. Fujii, M. Galaktionov, L. Giovanelli, G. Panaccione, F. Bondino, I. Vobornik and G. Rossi, *Thin Solid Films*, 2003, **428**, 30-33.
23. G. Panaccione, J. Fujii, I. Vobornik, G. Trimarchi, N. Binggeli, A. Goldoni, R. Larciprete and G. Rossi, *Phys. Rev. B (Condensed Matter and Materials Physics)*, 2006, **73**, 035431-035439.
24. H. J. Grabke, W. Paulitschke, G. Tauber and H. Viefhaus, *Surf. Sci.*, 1977, **63**, 377-389.
25. D. H. Buckley, *Wear*, 1972, **20**, 89.
26. G. Gafner and R. Feder, *Surf. Sci.*, 1976, **57**, 37-44.
27. K. Yoshida and G. A. Somorjai, *Surf. Sci.*, 1978, **75**, 46-60.
28. U. Seip, M. C. Tsai, J. Kuppers and G. Ertl, *Surf. Sci.*, 1984, **147**, 65-88.

29. J. B. Benziger and R. J. Madix, *J. Electron. Spectrosc. Relat. Phenom.*, 1980, **20**, 281-287.
30. C. Brucker and T. Rhodin, *J. Catal.*, 1977, **47**, 214-231.
31. W. Erley, A. M. Baro and H. Ibach, *Surf. Sci.*, 1982, **120**, 273-290.
32. M. Textor, I. D. Gay and R. Mason, *Proc. R. Soc. Lond. A*, 1977, **356**, 37.
33. http://www.answers.com/topic/iron-oxide.
34. V. S. Smentkowski and J. T. Yates Jr, *Surf. Sci.*, 1990, **232**, 113-128.
35. C. Leygraf and S. Ekelund, *Surf. Sci.*, 1973, **40**, 609-635.
36. H. J. Muessig and W. Arabczyk, *Cryst. Res. Technol.*, 1980, **15**, 1091-1099.
37. W. Arabczyk, U. Narkiewicz, K. Kalucki and E. Freidenberg, *Appl. Surf. Sci.*, 1993, **72**, 45-48.
38. F. Qin, N. P. Magtoto, M. Garza and J. A. Kelber, *Thin Solid Films*, 2003, **444**, 179-188.
39. A. Wight, N. G. Condon, F. M. Leibsle, G. Worthy and A. Hodgson, *Surf. Sci.*, 1995, **331-333**, 133-137.
40. G. Pirug, G. Brodén and H. P. Bonzel, *Surf. Sci.*, 1980, **94**, 323-338.
41. A. J. Pignocco and G. E. Pellissier, *Surf. Sci.*, 1967, **7**, 261-278.
42. W. Erley and H. Ibach, *Solid State Commun.*, 1981, **37**, 937-942.
43. A. Hodgson, A. Wight and G. Worthy, *Surf. Sci.*, 1994, **319**, 119-130.
44. W. Arabczyk, D. Moszynski, U. Narkiewicz, R. Pelka and M. Podsiadly, *Catal. Today*, 2007, **124**, 43-48.
45. A. Kotarba, J. Dmytrzyk, U. Narkiewicz and A. Barański, *React. Kinet. Catal. Lett.*, 2001, **74**, 143-149.
46. A. Steynberg and M. Dry, *Fischer-Tropsch Technology*, 2004, **Elsevier Science**.
47. S. L. Bernasek, *Annu. Rev. Phys. Chem.*, 1993, **44**, 265.
48. G. Ertl, S. B. Lee and M. Weiss, *Surf. Sci.*, 1982, **114**, 515-526.
49. G. Ertl, S. B. Lee and M. Weiss, *Surface Science*, 1982, **114**, 527-545.
50. M. Grunze, M. Golze, W. Hirschwald, H. J. Freund, H. Pulm, U. Seip, M. C. Tsai, G. Ertl and J. Küppers, *Physical Review Letters*, 1984, **53**, 850.
51. M. C. Tsai, U. Ship, I. C. Bassignana, J. Kuppers and G. Ertl, *Surface Science*, 1985, **155**, 387-399.
52. U. Seip, I. C. Bassignana, J. Kuppers and G. Ertl, *Surface Science*, 1985, **160**, 400-418.
53. F. Bozso, G. Ertl, M. Grunze and M. Weiss, *Applications of Surface Science*, 1977, **1**, 103-119.
54. F. Bozso, G. Ertl, M. Grunze and M. Weiss, *Journal of Catalysis*, 1977, **49**, 18-41.
55. F. Bozso, G. Ertl and M. Weiss, *Journal of Catalysis*, 1977, **50**, 519-529.
56. D. R. Strongin, J. Carrazza, S. R. Bare and G. A. Somorjai, *J. Cat.*, 1987, **103**, 213-215.
57. D. J. Dwyer and G. A. Somorjai, *J. Catal.*, 1979, **56**, 249-257.
58. S. R. Bare, D. R. Strongin and G. A. Somorjai, *J. Phys. Chem.*, 1986, **90**, 4726-4729.
59. D. R. Strongin and G. A. Somorjai, *J. Catal.*, 1988, **109**, Pages: 51-60.
60. S. Westerberg, C. Wang, K. Chou and G. A. Somorjai, *J. Phys. Chem. B*, 2004, **108**, 6374-6380.
61. W. Arabczyk and U. Narkiewicz, *Appl. Surf. Sci.*, 2005, **252**, 98-103.
62. W. Arabczyk and U. Narkiewicz, *Surf. Sci.*, 2000, **454-456**, 227-233.
63. W. Arabczyk, D. Moszynski and U. Narkiewicz, *Vacuum*, 1999, **54**, 3-7.
64. W. Arabczyk, T. Baumann, H. J. Mussig, F. Storbeck and A. Meisel, *Vacuum*, 1990, **41**, 79-81.
65. W. Arabczyk, M. Militzer, H. J. Mussig and J. Wieting, *Scr. Metall.*, 1986, **20**, 1549-1554.
66. H. Cabibil, J. S. Lin and J. A. Kelber, *Surf. Sci.*, 1997, **382**, L645-L651.
67. J. S. Lin, B. Ekstrom, S. G. Addepalli, H. Cabibil and J. A. Kelber, *Langmuir*, 1998, **14**, 4843-4852.

68. http://en.wikipedia.org/wiki/Ferrite.
69. http://www.answers.com/single+crystal?cat=technology.
70. *CasaXPS Version 2.3.15, Copyright (C) 1999 - 2009 Casa Software Ltd.*
71. *Omicron Scala Pro 5.0* ©, 2003.
72. I. Horcas, R. Fernandez, J. M. Gomez-Rodriguez, J. Colchero, J. Gomez-Herrero and A. M. Baro, *Rev. Sci. Instrum.*, 2007, **78** 013705
73. *Omicron Spectraview, 3.0* ©.
74. K. Hermann and M. A. Van Hove, *LEEDpat version 2.2*, 2009.
75. K. W. Kolasinski, *Surface Science: Foundations of Catalysis and Nanoscience, Wiley & Sons, Ltd*, 2002.
76. W. Arabczyk and U. Narkiewicz, *Surf. Sci.*, 1998, **402-404**, 502-507.
77. http://sharp.bu.edu/~slehar/fourier/fourier.html.
78. J. M. MacLauren, J. B. Pendry, P. J. Rous, K. K. Saldin, G. A. Somorjai, M. A. Van Hove and D. D. Vvedensky, *Surface Crystallographic Information Service, D. Reidel Publishing Company: Dordrecht, The Netherlands*, 1988, 86.
79. W. Arabczyk, H. J. Mussig and F. Storbeck, *Phys. Stat. Sol. (a)*, 1979, **55**.
80. D. P. Woodruff and T. A. Delchar, *Modern Techniques of Surface Science, Cambridge University Press*, 1986.
81. P. Weightman and J. R. Power, *Phys. Rev. B.*, 1998, **58**, 10532.
82. *WSxM program help*, Copyright 1990 - 2000 Microsoft Corp.
83. P. C. J. Graat and M. A. J. Somers, *Appl. Surf. Sci.*, 1996, **100/101**, 36.
84. C. S. Kuivila, J. B. Butt and P. C. Stair, *Appl. Surf. Sci.*, 1988, **32**, 99.
85. R. A. Van Santen and J. W. Niemantsverdriet, *Chemical Kinetics and Catalysis*, Plenum Publishing Corporation, New York, 1995.
86. I. N. Shabanova and V. A. Trapeznikov, *J. Electron Spectr. Rel. Phenom.*, 1975, **6**, 297.

CHAPTER 5

The Adsorption of C_2H_4 on Fe(111)

5.1. Introduction

5.1.1. General

Understanding the interaction of transition metal surfaces with unsaturated molecules, such as alkenes and alkynes, is important in elucidating the role that the metal plays in catalytic processes.

This chapter deals with the adsorption of C_2H_4 on Fe(111). Adsorption of a gas phase molecule on the surface is the first step in a heterogeneous catalytic reaction, without which the reaction cannot proceed. Sticking probability measurements are invaluable in learning about the nature of the adsorption, since it elucidates the kinetics of the process; in this study the molecular beam reactor was employed for this purpose. The reactor provides the advantage of being able to monitor adsorption in transient or steady state mode at temperatures above that accessible in TPD experiments. For more detail on the design and application of the reactor see references 1 & 2.

5.1.2. Adsorption Kinetics[1,3,4,5]

According to the Langmuir model of adsorption, a gas phase molecule is always transferred directly into the chemisorbed state upon adsorption on the surface, *i.e.* a strong chemical bond is formed. In practice adsorption frequently does not follow this type of behaviour, as will be illustrated in this chapter. This basic adsorption model for Langmuir associative adsorption was discussed in section 1.3 and in this section the general principles of Langmuir dissociative adsorption and precursor mediated adsorption will be reviewed, given its relevance to the results to follow.

Langmuir Dissociative Adsorption[6]

If a molecule undergoes Langmuir type dissociative adsorption, the rate of the process is not influenced appreciatively by the physisorbed layer; instead every gas phase molecule incident on the surface is chemisorbed if it finds two adjacent empty surface sites. If o represents an empty site and × represents a site filled with adsorbate, the molecule will only adsorb upon finding a landing position oo (two unoccupied nearest neighbour sites). In contrast, the molecule will be reflected upon landing on o× or ××. The probability of two

vacant sites occurring adjacent to one another is proportional to the square of the concentration of vacant sites. Keeping this additional condition in mind, the equation for dissociative adsorption can be derived in a similar fashion than for associative adsorption (see section 1.3.3). For a gas phase molecule (M) in dynamic equilibrium with the surface (S representing one surface site)

$$M_{2(g)} + 2S \underset{k'_d}{\overset{k'_a}{\rightleftharpoons}} 2(M\text{-}S) \qquad [5.1]$$

k_a and k_d are the rate constants for adsorption and desorption respectively. Then the

$$Rate\ of\ adsorption = k'_a P\,(1\text{-}\theta)^2 \qquad [5.2]$$

With P the gas pressure and $(1\text{-}\theta)$ the fractional monolayer coverage of sites on the surface not occupied by adsorbate molecules. Similarly the

$$Rate\ of\ desorption = k'_d\,\theta^2 \qquad [5.3]$$

At equilibrium

$$Rate\ of\ adsorption = Rate\ of\ desorption$$

$$\therefore\ k'_a P\,(1\text{-}\theta)^2 = k'_d\theta^2 \qquad [5.4]$$

$$\therefore\ \frac{\theta}{(1-\theta)^2} = \frac{k'_a P}{k'_d} = K'P \quad \left(K' = \frac{k'_a}{k'_d}\right) \qquad [5.5]$$

$$\therefore\ \frac{\theta}{(1-\theta)} = \sqrt{K'P} \qquad [5.6]$$

$$\theta = \frac{\sqrt{K'P}}{1+\sqrt{K'P}} \qquad [5.7]$$

Equation 1.12, which is applicable for associative adsorption, is modified to obtain an expression for the sticking probability in the case of dissociative adsorption

$$S = S_0(1-\theta)^2 \qquad [5.8]$$

Figure 1.3*b* shows the sticking curve shape expected for dissociative adsorption following Langmuir type kinetics.

Precursor Mediated Adsorption

One of the most serious deficiencies of the Langmuir adsorption model is its failure to describe the initial virtual independence of the sticking coefficient on surface adsorbate coverage. The concept of precursor states was developed to account for this discrepancy. While the Langmuir model dictates that an impinging molecule will desorb upon failure to chemisorb on the surface (*e.g.* when hitting a filled adsorption site), the precursor model allows for a molecule to physisorb on the surface and diffuse around until it finally chemisorbs. By definition a precursor is a weakly held, short-lived state that is thermally accommodated to the surface temperature. Even if the result of a gas-solid collision is the formation of a stable chemisorbed species, weakly bound precursor states can play a major role in the kinetic process.

An important feature of a precursor state is its mobility, which allows it to diffuse across the surface from where it first physisorbs (over a filled or empty site) to the final open site where it transitions into the chemisorbed state. Diffusion is possible because the potential energy in this weak well is relatively insensitive to the local atomic arrangement of the adsorbate, and the activation energy barrier for surface diffusion (E_m) is expected to be low compared to the well depth (E_d); a one dimensional potential energy diagram showing the barriers was presented in Figure 1.5.

A precursor state needs to be distinguished from an intermediate state, I_a, (also called a transient state) which is a chemisorbed species; a transient state can be the final adsorbed state or can proceed to form products. A molecule will become trapped into a precursor state at the surface if it can lose its excess kinetic energy to the lattice so that it no longer has enough energy to leave the surface, *i.e.* the rate of the trapping process is determined by the rate of energy transfer. Trapping at first collision is not necessarily efficient and values lower than unity may be anticipated for the trapping coefficient, α (defined in equation 1.14). Values of the trapping coefficient will be close to 1 for molecules with a large heat of adsorption. Such molecules stay long enough at the surface for energy exchange to occur so that accommodation can be achieved. The values of α are difficult to estimate for reactive gases, but has been estimated for unreactive gases. It has been shown that both the trapping

probability, α, and the thermal accommodation coefficient, γ (defined in equation 1.15), rise monotonically with increasing heat of physisorption: ~0.2 for Ar, ~0.4 for Kr and ~0.7 for Xe.[7] By inference the same range is expected for reactive gases.

Sticking refers to the chemisorption of a molecule on the surface. In sticking the incident molecule not only has to lose energy (as in trapping), it also has to form a strong bond with the surface. Hence, sticking rates are determined by both the rate of energy transfer and the ability of the surface to form bonds with the molecule. Adsorption of a gas phase molecule may proceed through a sequence of steps: trapping of the molecule into a precursor state, desorption of the precursor state or transitioning from the precursor to the chemisorbed state. In addition an intrinsic precursor (*i.e.* a precursor adsorbed over an empty surface site) can adsorb directly onto that site or diffuse to another empty site and chemisorb there; while an extrinsic precursor (which is chemisorbed over a filled surface site) will diffuse until it finds an empty surface site and chemisorb. These various possibilities are depicted in Figure 5.1.[3] The measured *sticking coefficient, S,* is the sum total of all these processes. A low sticking probability can result from a low absolute sticking rate *or* a high sticking rate that is counter balanced by a high rate of desorption, which means that all of these processes should be considered when deriving an expression for the sticking probability, *S*.

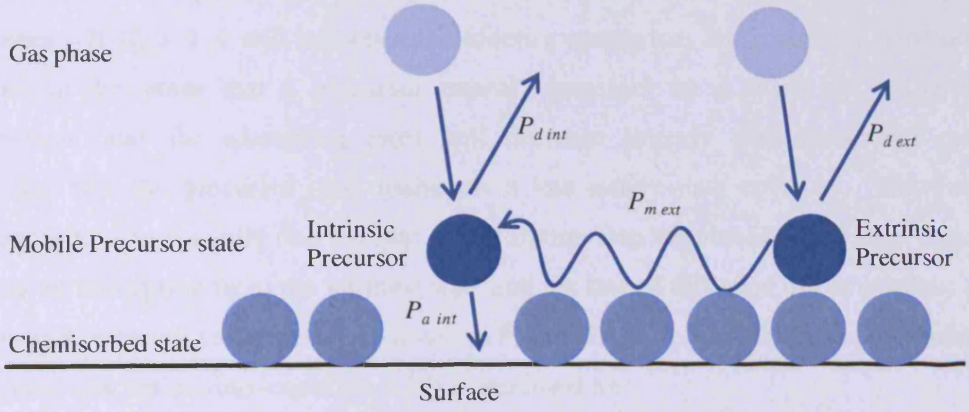

Figure 5.1 – Adsorption of a gas phase molecule into an intrinsic or extrinsic precursor state and the probability of each to desorb (P_d), migrate (P_m) or adsorb into the chemisorbed state (P_a). Migration of the intrinsic state is also possible, but not shown.[3]

Reaction 5.9 represents the adsorption of a molecule into the precursor state which then proceeds to a chemisorbed intermediate and the final products. Pre-equilibrium is established between the first and the second step:

$$A \overset{K}{\leftrightarrow} P + S \overset{k2}{\rightarrow} I_a \overset{k3}{\rightarrow} B + C \quad [5.9]$$

A is the reactant, P is the physisorbed precursor, S is the surface site, I_a is the chemisorbed intermediate and B & C are the products. The rate of formation of the chemisorbed intermediate state is

$$\frac{d[I_a]}{dt} = k_2 \theta_P (1 - \theta_I) \quad [5.10]$$

Since by definition the population of the precursor is negligibly small, the steady state approximation apply and

$$\frac{d[I_a]}{dt} = \frac{k_2 K_P P_A}{(1 + K_P P_A)} \quad [5.11]$$

Where K_P is the equilibrium constant for the first step and a measure of the precursor influence. If $K_p > 1$ it will influence the kinetics somewhat, but Langmuir conditions still applies in the sense that a precursor cannot chemisorb on a filled site. The sticking coefficient (and the adsorption rate) will decrease linearly with increasing coverage, assuming that the precursor state maintains a low steady-state coverage. However, it is important to also consider that the rate of adsorption into the chemisorbed state depends on the rate of adsorption from the intrinsic state and the rate of diffusion of the extrinsic state to empty sites where it can adsorb (as shown in Figure 5.1). To include these probabilities, the Langmuir adsorption rate (equation 1.12) is modified to:

$$S = \frac{S_0}{1 + K_P \theta / (1 - \theta)} \quad [5.12]$$

The equation reduces to the simple Langmuir form when $K_P = 1$; *i.e.* if no precursor effect is involved in the adsorption process. If K_P is very small, the precursor effect is large (*i.e.* diffusivity is high) and a high sticking coefficient is maintained even at high coverage. Figure 5.2 illustrates the effect of the precursor parameter on associative adsorption. In

terms of the relevant probability factors (illustrated in Figure 5.1), the precursor parameter is given by

$$K_p = S_0 P_{d\,ext} / P_{a\,int} \qquad [5.13]$$

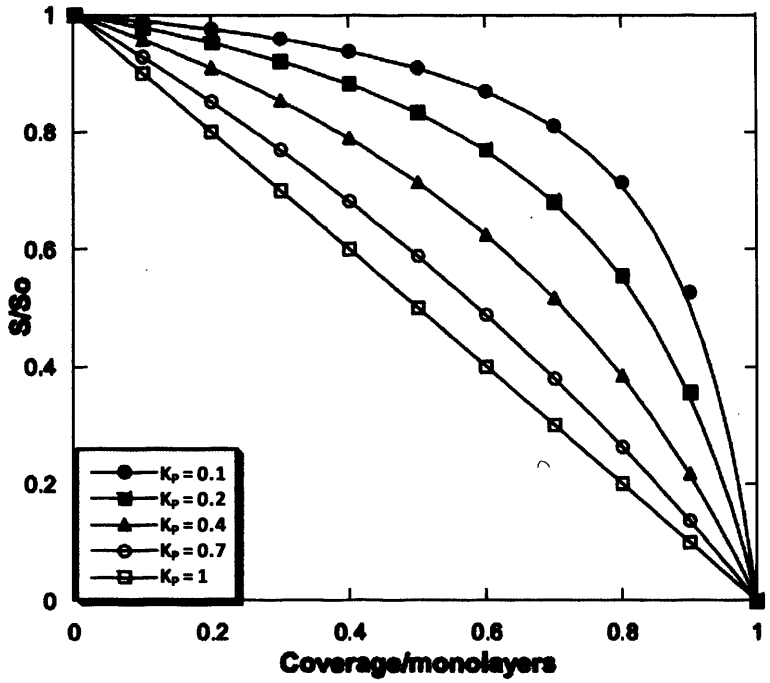

Figure 5.2 – The effect of the precursor parameter, K_P, on adsorption.[3]

Equation 5.13 implies that the lower the desorption probability from the extrinsic precursor, the more chance it has to diffuse to an adjacent empty site where it can chemisorb. In such cases K_p is small. The value of K_p strongly relates to the nature of the adsorption potential and the relative barriers for adsorption and desorption from the precursor state; that is the relative sizes of the desorption barrier from the precursor state (E_d, which is equal to the heat of adsorption, ΔH_{phys}; see Figure 1.4 & 1.5) and the barrier from the physisorbed to the chemisorbed state (E_a) dictates the adsorption rate and the temperature dependence (E_a and E_d are defined in Figure 1.5). The substrate temperature dependence of the initial sticking probability is related to the difference between these two factors, according to

$$\frac{\alpha}{S_0} - 1 = \frac{A_d}{A_a} e^{-(\Delta E_d - E_a)/RT_s} \qquad [5.14]$$

Where α is the trapping coefficient into the precursor state (defined in 1.14) and A_d & A_a are the prefactors for desorption and chemisorptions from the precursor state. In general, if the apparent activation energy (E_d – E_a) is positive (*i.e.* if the crossover point of the physisorption and chemisorption curves is below the zero potential as in Figure 1.5) the initial sticking probability decreases with increasing substrate temperature. If the reverse is true (if the cross over point is above the zero potential, as in Figure 1.4) the initial sticking increases with increasing substrate temperature. For example, if the apparent activation energy is 20 kJ/mol, the crossover point between the physisorption and chemisorption wells is at -20 kJ/mol and the initial sticking probability will decrease with increasing substrate temperature.

5.1.3. Adsorption and Decomposition of C_2H_4 on Fe Single Crystals

Alkenes are much more reactive than alkanes. Their adsorption generally does not require activation and they easily establish chemisorption bonds with a surface under vacuum conditions and at low temperatures. Alkenes show a variety of surface bonding depending on the surface. On a Pt surface, C_2H_4 generally forms a di-σ bond with two adjacent metal atoms with a single intra-molecular C-C bond, while on metals like Cu, Pd and Ni it usually establishes a π-interaction via the double C=C bond to a single metal atom. However, the type of bonding may vary between different facets of the same substrate.

Different C_2H_4 derived species, such as vinyl (CH_2CH) or acetylene (C_2H_2) have been observed on Fe surfaces. On Fe(100) C_2H_4 is initially di-σ bound and dehydrogenates to C_2H_2 around 123 K.[8] At 400 K the triple C≡C bond breaks to yield CH and CH_2 fragments which eventually decompose completely to H_2 and carbidic or graphitic C at elevated temperatures. The same sequence of events is relevant for Fe(110), but at higher temperatures: C_2H_2 and H_2 are formed at ~300 K and CH_x fragments are formed around 340 K; complete decomposition occurs around 470 K.[9,10] At low temperatures (~120 K) C_2H_4 on Fe(111) is strongly rehybridized with the C atoms being multiple coordinated and some of the H atoms interacting strongly with Fe too.[11] Heating to >200 K results in partial desorption of the molecule, while the remaining surface species dissociate to C_{ads} and H_2 gas. C_2H_4 decomposition on Fe(111) is unusually rapid and unlike the other two low Miller indices, no CH_x intermediates are observed. Decomposition starts at temperatures as low as 250 K and is complete by 370 K, indicating that C-H dissociation precedes or parallels C-C

bond scission. C_2H_2 decomposition, on the other hand, produce stable CH and CH_2 intermediates.

TPD results of C_2H_4 on Fe(111) are in agreement with results of HREELS. H_2 evolution due to the decomposition of C_2H_4 starts at ~250 K and is complete by ~450 K; and apart from C_2H_4 only H_2 desorption is observed. In fact, for C_2H_4 exposures below 1 L, H_2 desorption profiles resemble those of H/Fe(111) at corresponding coverages, also implying that C_2H_4 decomposition has occurred well below 300 K. Above C_2H_4 exposures of 1 L, however, rapid H_2 evolution is observed above 250 K and the TDS profile is quite different from that of H/Fe(111) at corresponding coverages. This indicates that H_2 desorption becomes reaction limited at higher C_2H_4 surface concentrations. The reaction schemes of C_2H_4 and C_2H_2 decomposition on Fe(111) is shown in Scheme 5.1.

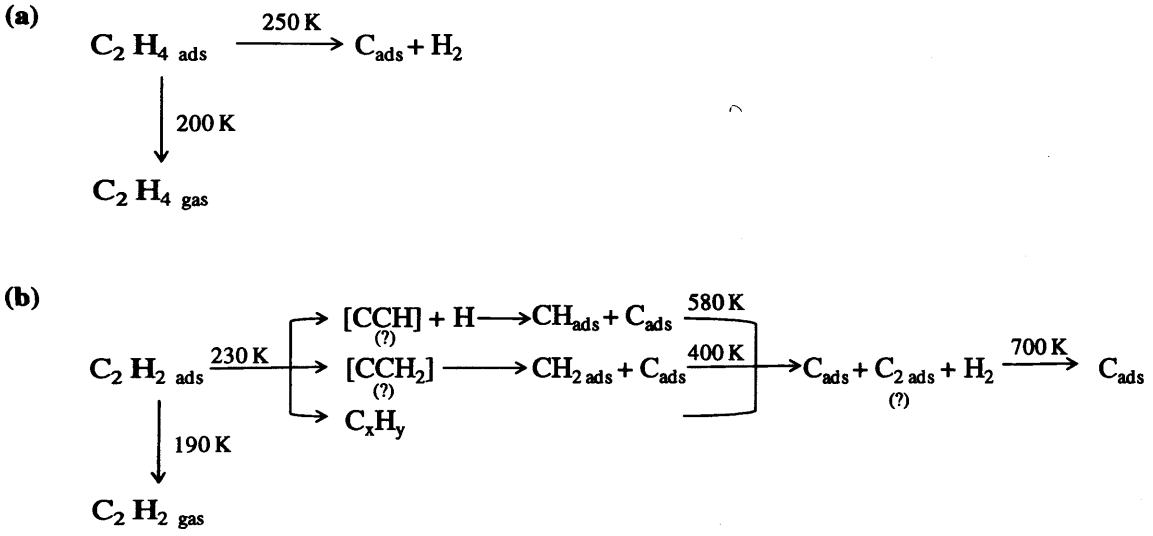

Scheme 5.1 – The decomposition of *a*) C_2H_4 and *b*) C_2H_2 on Fe (111).[12]

Comparing the temperatures at which these processes occur on the different surfaces, Fe(111) is considered to be more reactive than Fe(110), but considerably less reactive than Fe(100). This order does not follow the relative "roughness" of the surfaces. It is thought that the Fe-Fe distances on Fe(110) is too small and on Fe(111) too large to effectively pull the C atoms apart. Comparing Fe(110) with Fe(111), the latter is more reactive since all three top layers are available for adsorption and so provide a stepped (110) plane (made up out of 1 Fe1, 2 Fe2 & 1 Fe3). Bonding in this site should increase the interaction with a H atom of the molecule and thus lower the activation energy for dissociation.

5.1.4. Carbon Diffusion and Dissolution in Fe

Jiang & Carter studied C diffusion in bcc iron[13] as well as the adsorption and diffusion of C into Fe(110) and Fe(100) from first principles.[14] C has a covalent radius of 0.77 Å which is larger than the interstitial sites of α-Fe. The octahedral sites in the bulk have a radius of 0.19 Å, while the tetrahedral sites have a radius of 0.36 Å; the respective positions are shown in Figure 5.3. Even though the tetrahedral sites are larger, the preferred site for C in α-Fe is the octahedral. Since these are too small to accommodate C, the metal lattice has to rearrange to incorporate them. The calculated solution enthalpy of C in the octahedral site is +0.74 eV, which is consistent with the small solubility of C in this Fe phase. Diffusion proceeds through a tetrahedral site TS with a calculated barrier of 0.86 eV (the experimental value is 0.87 eV[15]). An attractive interaction exists between C and α-Fe, in keeping with the existence of Fe_3C.

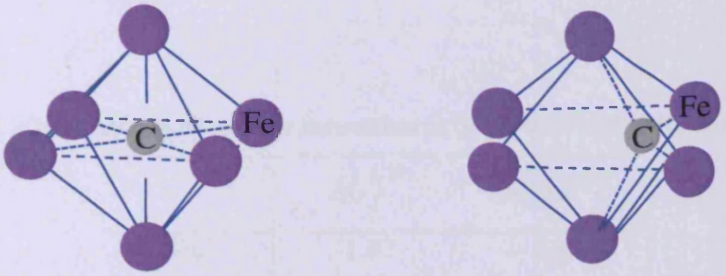

(a) (b)

Figure 5.3 – *a*) C in the octahedral site of bcc Fe, which is the preferred position in the bulk. *b*) C in the tetrahedral site, which is the TS for bulk diffusion.[13]

It was found that C adsorbs strongly on the Fe surfaces and prefer high coordination sites; specifically the long-bridge site on Fe(110) and the four fold hollow site on Fe(100).[14] C binds more strongly on Fe(100) due to the short distance between C and the subsurface Fe atom (which essentially makes it fivefold coordinated). In the subsurface region C prefers the octahedral site as in bulk iron. C is more stable in the subsurface octahedral site of Fe(110) than in Fe(100). In the former the strain caused by C is released by pushing one Fe atom towards the vacuum by 0.5 Å to create a hole for C to pass through to the subsurface octahedral site,[14,16] but in the latter distortion is propagated far into the lattice. Barriers for C diffusion into the subsurface regions are 1.18 eV and 1.47 eV for Fe(110) and Fe(100) respectively (Wiltner[16] calculated a barrier of 1.44 eV for Fe(110) and also determined it

experimentally as 1.3 ± 0.2 eV); and the overall reaction energy is endothermic by 0.62 eV. The larger barrier for Fe(100) is mainly due to the stronger C-Fe surface bond. It was predicted that the rate limiting step for C incorporation into bulk Fe is the initial diffusion into the subsurface sites, while the rate limiting step for C segregation to the surface is bulk diffusion with no difference between the surfaces. It was concluded that C prefers to stay on the surface compared to residing in the bulk, which provides a driving force for bulk C to segregate to the surface. It was also predicted that graphite formation will be more favourable on C-covered Fe(110) than on C-covered Fe(100).

At least two factors determine the mobility of species (in this case C) in solid state reactions: *i*) the reactivity between the metal and C; *ii*) the metal and carbide structures. The free energy of Fe_3C formation is positive and the reaction is therefore endothermic.[17] This is also true for Ni_3C, whereas the formation various other metal carbides are exothermic (see Table 5.1). The onset of C diffusion is related to the bulk diffusion barrier (also given in Table 5.1) as well as the surface structure; with more open structures generally having lower onset temperatures for diffusion into the bulk.[16]

Table 5.1 – Free energy of carbide formation at 300 K and bulk diffusion barriers.

	$\Delta G_f^{0\ a}$	$E_{D\,bulk}{}^{b}$
TiC	-1.87	1.3
Be_2C	-1.19	---
SiC	-0.73	---
WC	-0.40	1.8
W_2C	-0.23	1.8
Fe_3C	+0.21	0.87
Ni_3C	+0.66	1.5

Notes: *a)* Values presented in eV; taken from ref. 17.
b) Bulk diffusion barriers for C in the pure metal (in eV) from ref. 18.

5.2. Experimental

All sticking probability measurements were performed in a thermal molecular beam reactor (System B) shown in Figure 2.24 with the schematic diagram in Figure 2.25. The pressure in the main UHV chamber was ~2×10^{-10} mbar and the pressure in molecular beam chamber filled with reactant gas was typically 5×10^{-8} mbar.

In each sticking probability measurement experiment C_2H_4 gas (at ambient temperature) was beamed onto the clean, pre-heated Fe(111) crystal over a period of ~300 s. The first experiment was performed at 373 K, after which the surface temperature was increased in steps of 50 – 100 K for each new experiment up to 873 K, to establish the effect of the substrate temperature on the sticking probability. Over the duration of the experiment the change in concentration of C_2H_4 (mass 27) and H_2 (mass 2) were monitored with a mass spectrometer to follow the adsorption of C_2H_4 on the surface and the evolution of H_2, which results from the dissociation process. The principle peak of C_2H_4 is actually mass 28, but CO, which is expected to be present in the background, is of the same mass and will contribute to the mass 28 peak. Conversely, the mass 27 fragment is unique to C_2H_4 (in the current system) which makes it a better choice for identifying C_2H_4. The sticking probability was determined as described in section 2.12.4; reported values have an error of ~0.02.

Directly after each C_2H_4 sticking experiment, a carbon clean off experiment was performed with an equivalent dose of O_2 at the same surface temperature; *i.e.* if C_2H_4 was adsorbed for 300 s at a sample temperature of 473 K, O_2 was dosed onto the surface for 300 s (covered in C) at a sample temperature of 473 K. In preparation for this the molecular beam chamber was flushed to remove all traces of C_2H_4 gas and then filled with O_2 gas. The O_2 (at ambient temperature) was then dosed onto the surface while monitoring oxygen adsorption (mass 32) along with CO & CO_2 evolution (mass 28 & 44) with the mass spectrometer.

In background dosing experiments 60 L of C_2H_4 at ambient temperature was dosed at a pressure of 5×10^{-8} mbar onto a pre-heated surface. XPS was used to evaluate the surface composition before and after dosing. Binding energies were calibrated relative to the Fe $2p_{3/2}$ peak, positioned at 706.7 eV and coverages were calculated with the *Carley and Roberts* equation, as discussed in section 2.8.5. Uptake values (which in some cases are equivalent to coverage values) were calculated from sticking data by using equation 2.24; the

flux on the surface is ~1.5×10^{17} $m^{-2}.s^{-1}$. These values are presented in monolayer equivalents relative to the number of atoms in the top layer of Fe(111), 7.04×10^{18} atoms/m^2.

Gases were supplied by *Argo Int.* and purity levels were 99.7% for C_2H_4 and 99.999% for Ar and O_2. Molecular beam experiments were performed in collaboration with Lee Gilbert.

5.3. Results

5.3.1. C_2H_4 Sticking Measurements

Ethene sticking on Fe(111) was measured over a range of surface temperatures, 373 – 873 K. Figure 5.4 shows the mass spectrometer signals obtained during the adsorption of C_2H_4 at the lowest temperature.

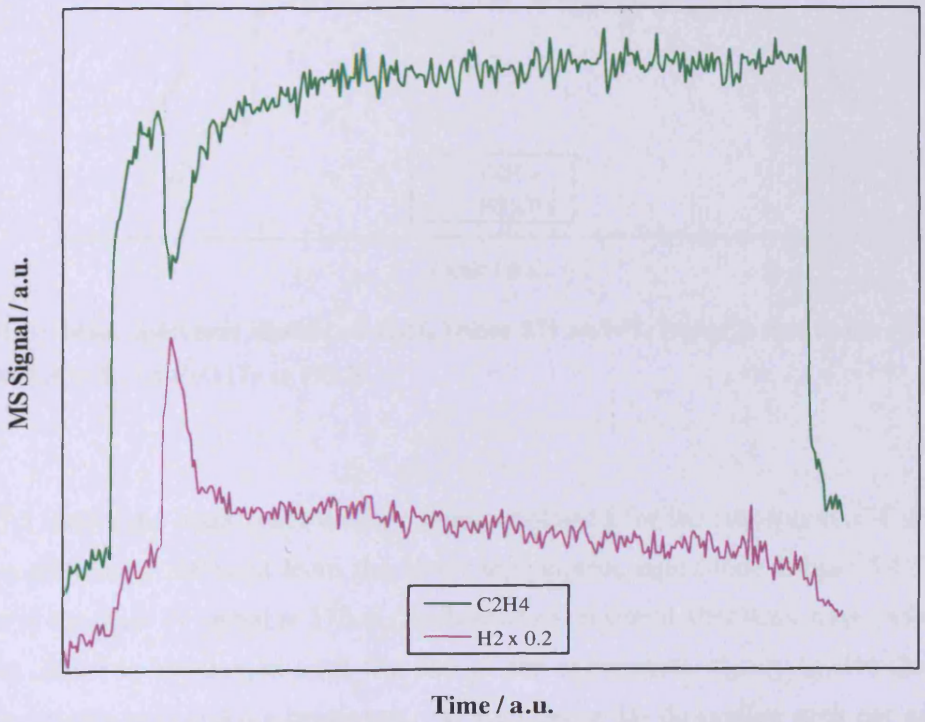

Figure 5.4 – Mass spectrum signals of C_2H_4 (mass 27) and H_2 (mass 2) due to the transient adsorption of C_2H_4 on Fe(111) at 373 K.

The sequence of events responsible for the change in signal is described in section 2.12.4. At $t = 0$ the C_2H_4 gas hits the crystal surface and is adsorbed as observed by the rapid drop in the concentration of mass 27 in the gas phase. Over the next minute or so the signal

gradually increases again until the base line is recovered. This behaviour was observed in experiments performed at lower temperatures (373 – 573 K). The start of C_2H_4 adsorption on the surface coincides with start of H_2 evolution (as observed by the rapid increase in mass 2 signal), which is rapid at all substrate temperatures employed.

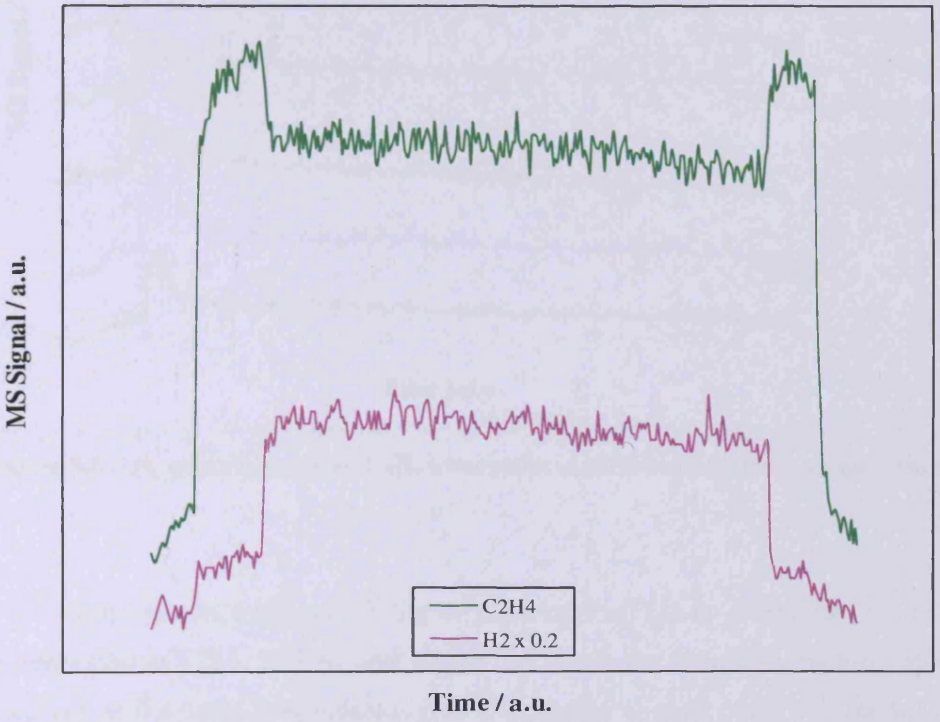

Figure 5.5 – Mass spectrum signals of C_2H_4 (mass 27) and H_2 (mass 2) due to the steady state adsorption of C_2H_4 on Fe(111) at 773 K.

Figure 5.5 shows the mass spectrometer signals obtained for the adsorption of C_2H_4 at 773 K, which are clearly different from the lower temperature equivalents (Figure 5.4). After a decrease in the mass 27 signal at 373 K, the baseline is restored after some time, but at 773 K the lower signal is maintained until the end of the experiment, signifying that the surface does not saturate and sticking continues. In accordance H_2 desorption does not cease, but also continues until the end of the experiment. This trend was obtained for C_2H_4 adsorption at higher temperatures (673 – 873 K). Figure 5.6 shows the desorption of H_2 with increasing temperature that resulted from C_2H_4 decomposition on the surface; the figure is discussed with the sticking curves below.

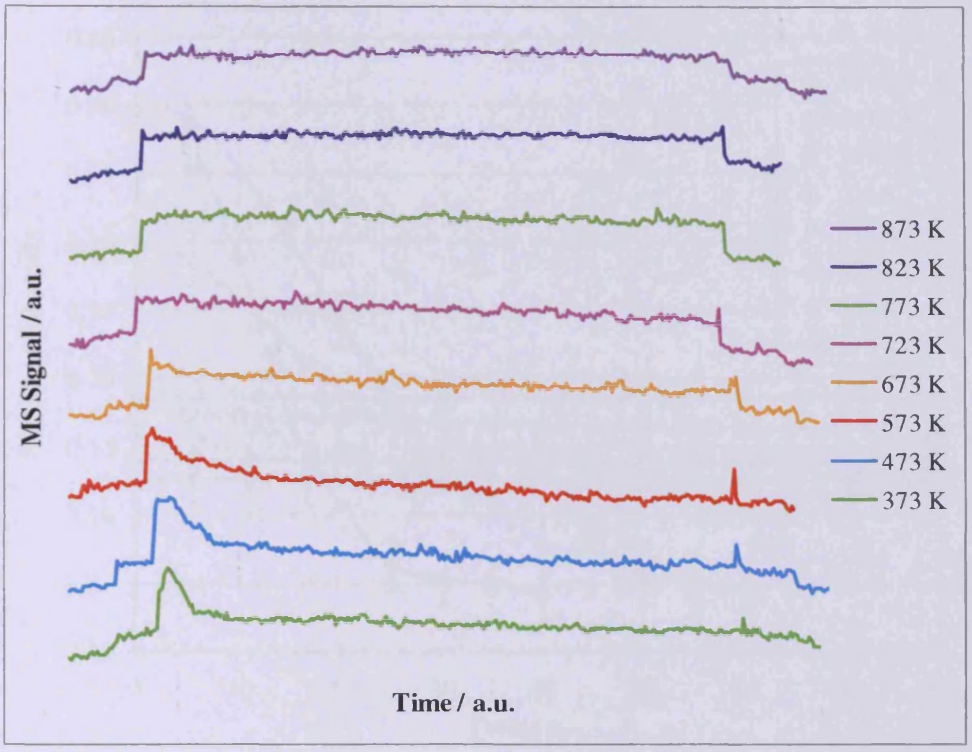

Figure 5.6 – H_2 evolution due to C_2H_4 adsorption at different substrate temperatures.

Figure 5.7 shows the sticking probability of C_2H_4 on Fe(111) as a function of time at the surface temperatures 373 – 873 K; and Figure 5.8 shows the change in sticking probability with coverage at the same temperatures (the C coverage at each point was calculated with equation 2.24; see experimental section). The curve shapes between 373 K – 573 K are similar in that sticking stays high for some time (over a broad coverage range), but approaches zero at higher coverages. At 673 K the sticking initially drops off somewhat, but unlike at lower temperatures, the value then stabilizes and is maintained until the end of the experiment. For each experiment above 673 K, the sticking is constant over time.

The corresponding H_2 evolution over time (Figure 5.6) agree well with the sticking *vs.* time plots (Figure 5.7). At 373 K H_2 initially evolves, but diminishes almost completely after ~25 s. A broader H_2 peak is observed at 473 K (*i.e.* H_2 was given off for a longer period), in agreement with the increased peak area in the C_2H_4 $S - t$ plot at the same temperature. Less H_2 is initially given off at 573 K and the decrease is more gradual than at 473 K, in correspondence with the lower S_0 value and the more moderate slope over time. At $T \geq 673$ K continuous H_2 evolution is observed, but overall the signal generally decreases slightly with increasing temperature. The precursor parameter (defined in equation 5.12) was estimated to be $K_P = 0.4$ at 373 K.

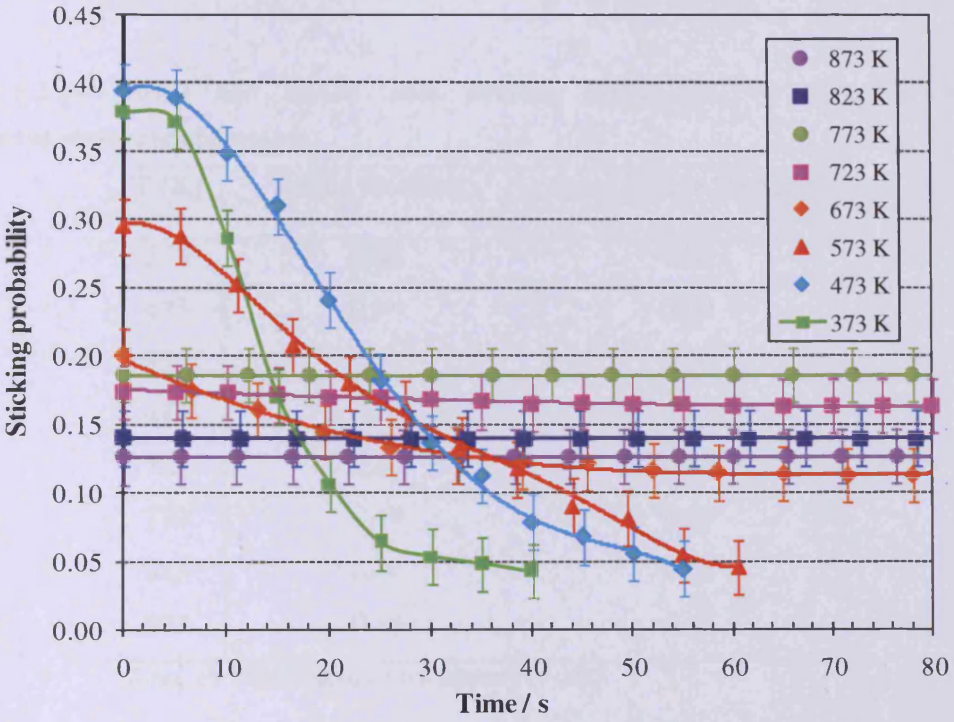

Figure 5.7 - Sticking probability of C_2H_4 on Fe(111) as a function of time at various substrate temperatures. The dosing time was 300 s; see Table 5.5 for total uptake values.

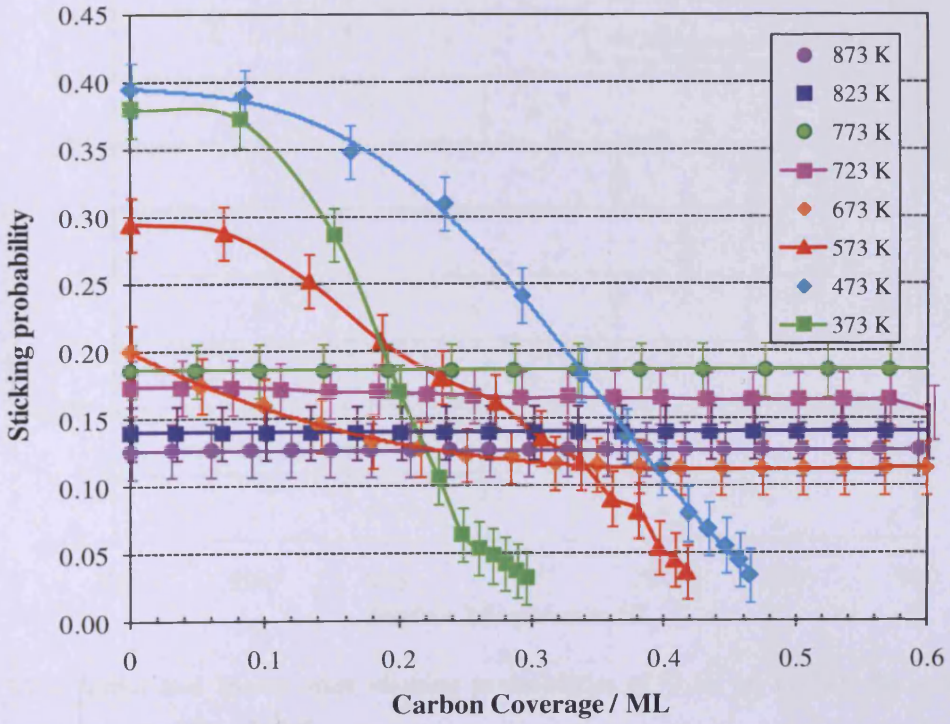

Figure 5.8 – Sticking probability of C_2H_4 on Fe(111) as a function of surface coverage at various sample temperatures.

Table 5.2 – Initial and steady state sticking probabilities of C_2H_4 on Fe(111) at different surface temperatures.

T (K)	Initial Sticking[a]	Steady State Sticking[a]
373	0.38	0.00
473	0.39	0.00
573	0.30	0.00
673	0.20	0.11
723	0.17	0.16
773	0.19	0.19
823	0.14	0.14
873	0.13	0.13

Notes: *a*) Values have an uncertainty of 0.02.

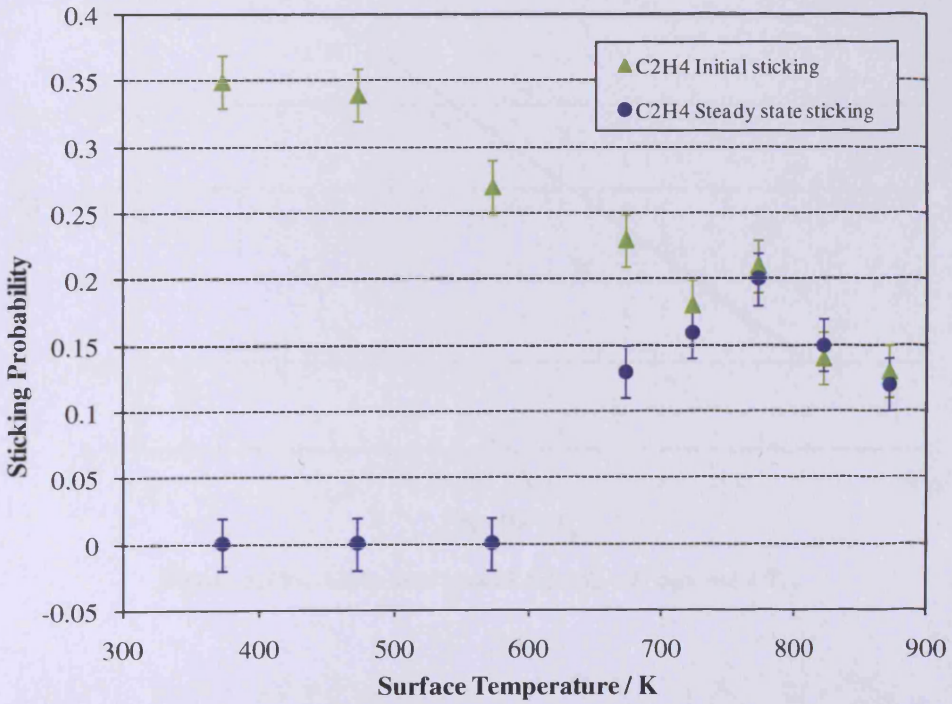

Figure 5.9 – Initial and steady state sticking probabilities of C_2H_4 on Fe(111) for substrate temperatures between 373 – 873 K.

The sticking probability values at $\theta = 0$ on the S – θ plots corresponds to the initial sticking probability, S_0. These values are summarized in Table 5.2 & Figure 5.9 and steady state sticking values are also shown where applicable. The highest initial sticking is observed at 373 K & 473 K (the lowest temperatures in the range); a value of ~0.39 was measured. S_0 then decreases with increasing substrate temperature; at 673 K it is approximately half of maximum value and at 873 K a value of 0.13 is reached. Between 373 – 573 K the surface saturates and the sticking ceases at high coverages, *i.e.* no steady state sticking occurs. At 673 K the sticking probability initially decreases from 0.20 to 0.11, but the surface does not saturate and sticking continues until the end of the experiment. Between 723 – 873 K the sticking is constant over the duration of the whole experiment and the initial sticking probability matches the steady state sticking value in each case.

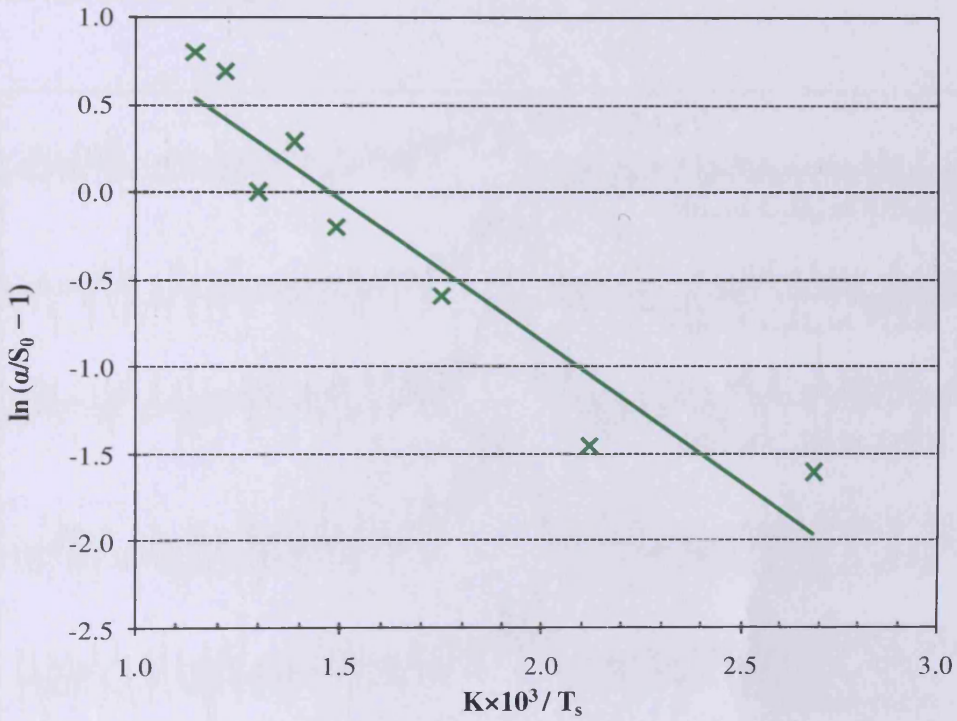

Figure 5.10 – Arrhenius plot of $ln(\alpha/S_0 - 1)$ against $1/T_s$.

In order to evaluate the relationship between the adsorption and desorption barriers from the precursor state, E_a & E_d (as defined in Figure 1.5), the data in Table 5.2 was used to plot $ln(\alpha/S_0 - 1)$ against $1/T_s$ according to equation 5.14; the plot is shown in Figure 5.10. α, the low temperature limit of S_0, was not determined experimentally, but estimated by considering the trend of the measured values of S_0. If it is assumed that $\alpha = 0.42$, it follows

that $E_d - E_a$ is ~13.5 kJ/mol (from the gradient) and the ratio of the rate constants ν_d / ν_a ~ 11 (from the intercept). Varying the value of α from 0.40 to 0.60 caused $E_d - E_a$ to change from 15 to 9 kJ/mol; and ν_d / ν_a to change from 13 to 9.

5.3.2. Background Dosing of C_2H_4

Although the sticking measurements can show whether or not the reactant gas is adsorbed on the surface, it cannot be used to conclusively determine whether the deposited carbon builds up on the surface or is absorbed into the bulk. To accomplish this and to establish the identity of the surface C species, sticking probability measurements were supplemented with XPS analysis. The preheated surface was dosed with C_2H_4 from the background and then analyzed with XPS. Dosing was done at those temperatures at which steady state sticking was observed, 673 – 873 K.

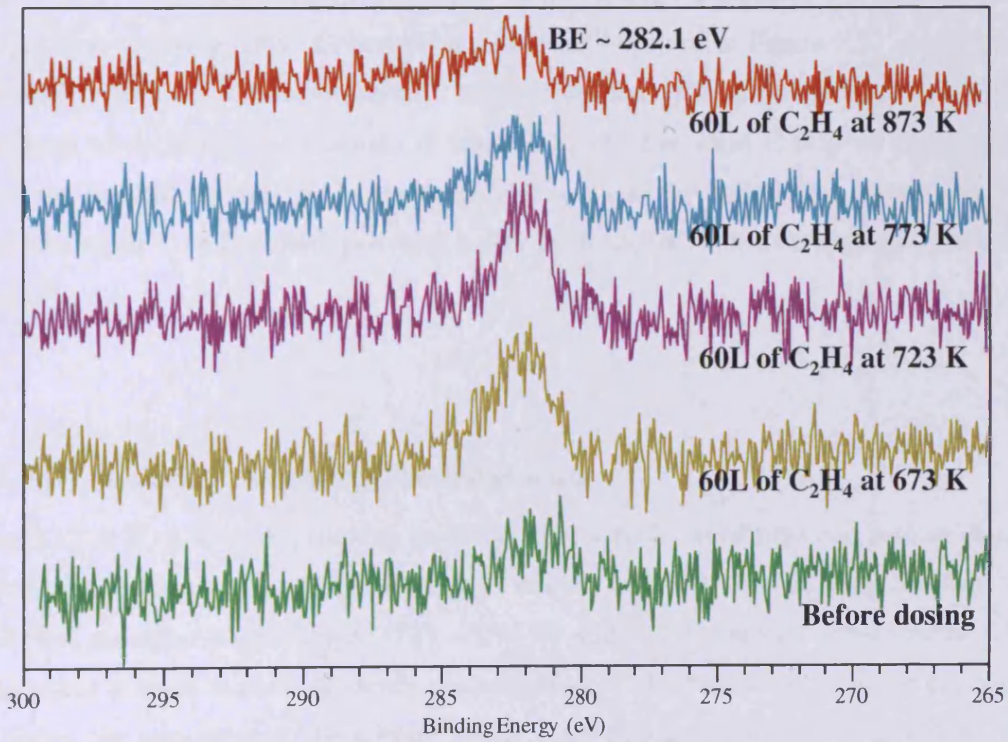

Figure 5.11 – XPS spectra of the C 1s region before and after dosing C_2H_4 at different surface temperatures; 60 L of C_2H_4 was dosed at a background pressure of 5×10^{-8} mbar in each case; see Table 5.3 for uptake and coverage values.

Figure 5.11 shows the XPS C 1s peak area before and after dosing C_2H_4; the resulting surface coverages are presented in Table 5.3 along with a comparison of the total C uptake values that were estimated from sticking experiments.

Table 5.3 – C surface coverages after dosing 60 L of C_2H_4 on Fe(111) at substrate temperatures between 673 – 873 K compared to the total C uptake.[a]

T (K)	C Coverage	C Uptake
673	0.92	5.79
723	0.89	7.50
773	0.43	9.51
873	0.18	6.48

Notes: *a*) Coverage values were calculated from XPS data and C uptake values from sticking data; both presented in ML.

The C 1s peak is situated ~282 eV regardless of the dosing temperature and no shift in Fe 2p peak position was observed. Comparison of the XPS spectra in Figure 5.11 shows that the amount of surface carbon decreases with temperature from 673 K onwards, so that at 873 K the amount of surface C is minimal. A small amount of residual C may be expected to be present on the surface, even if C completely diffused into the bulk during dosing, due to the low solubility of C in Fe which provides a driving force for bulk C to segregate back to the surface.[16]

5.3.3. O_2 Sticking Probability Measurements

Figure 5.12 & 5.13 show O_2 sticking on Fe(111) as a function of time and surface coverage respectively. The substrate temperature does not seem to influence sticking between 400 – 573 K; but at higher temperatures (723 – 773 K) sticking diminishes considerably. At all temperatures a small amount of steady state sticking is observed later on in the experiment. The higher the temperature, the sooner steady state sticking commences; at 773 K only a small, unchanging steady state sticking value is measured.

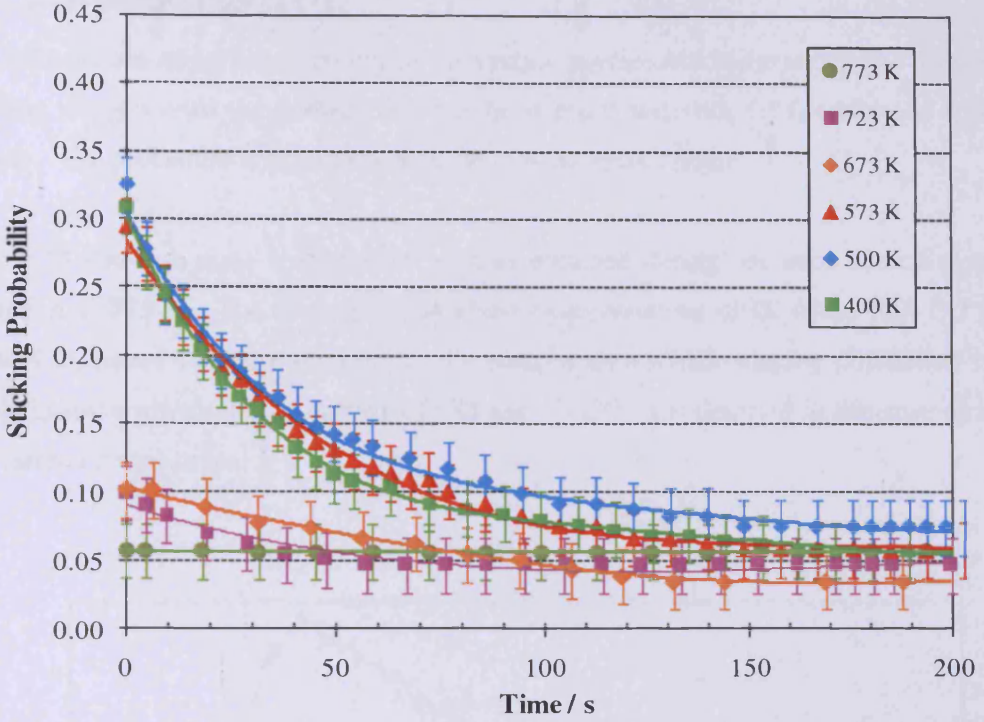

Figure 5.12 – Sticking probability of O_2 on Fe(111) as a function of time at various substrate temperatures. The dosing time was 300 s; see Table 5.5 for uptake and coverage values.

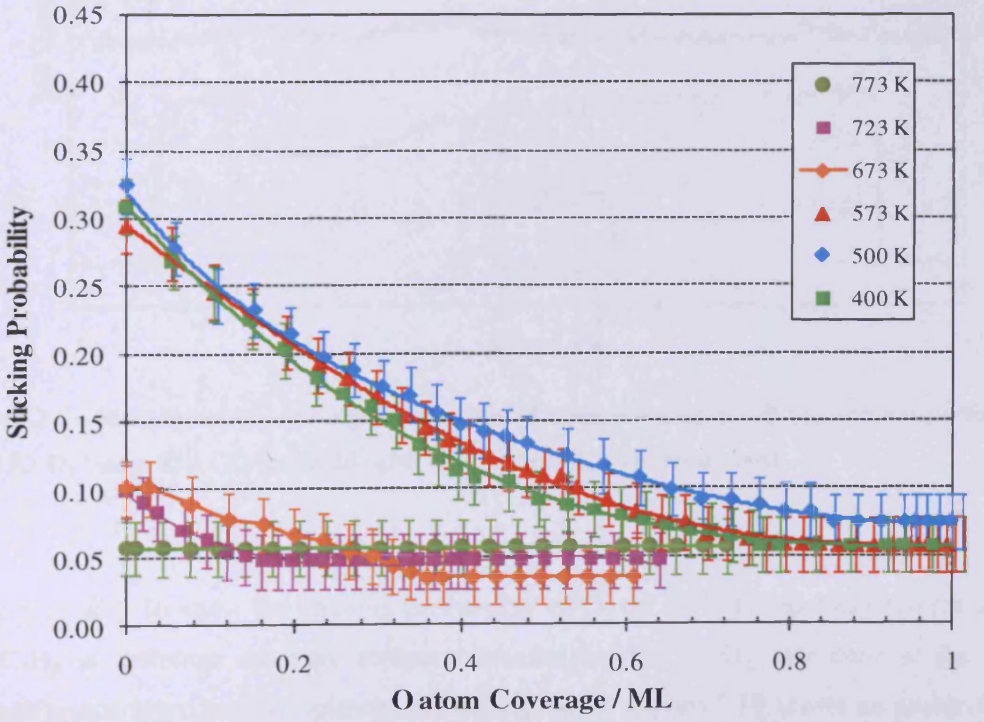

Figure 5.13 – Sticking probability of O_2 on Fe(111) as a function of surface coverage at various substrate temperatures.

5.3.4. Post-adsorption of O_2

More information about the reactivity of the surface species and substrate can be deduced by adsorbing oxygen onto the surface that has been pre-dosed with C_2H_4 and monitoring the products. The procedure was described in the experimental section.

Figure 5.14 shows a mass spectrometer signals obtained during one such carbon clean off experiment at 773 K. The change in gas phase concentrations of O_2 (mass 32), CO (mass 28) and CO_2 (mass 44) were monitored. O_2 adsorbs with a high sticking probability on the C/Fe(111) surface with the desorption of CO gas; no CO_2 was detected in this case or at any other surface temperature.

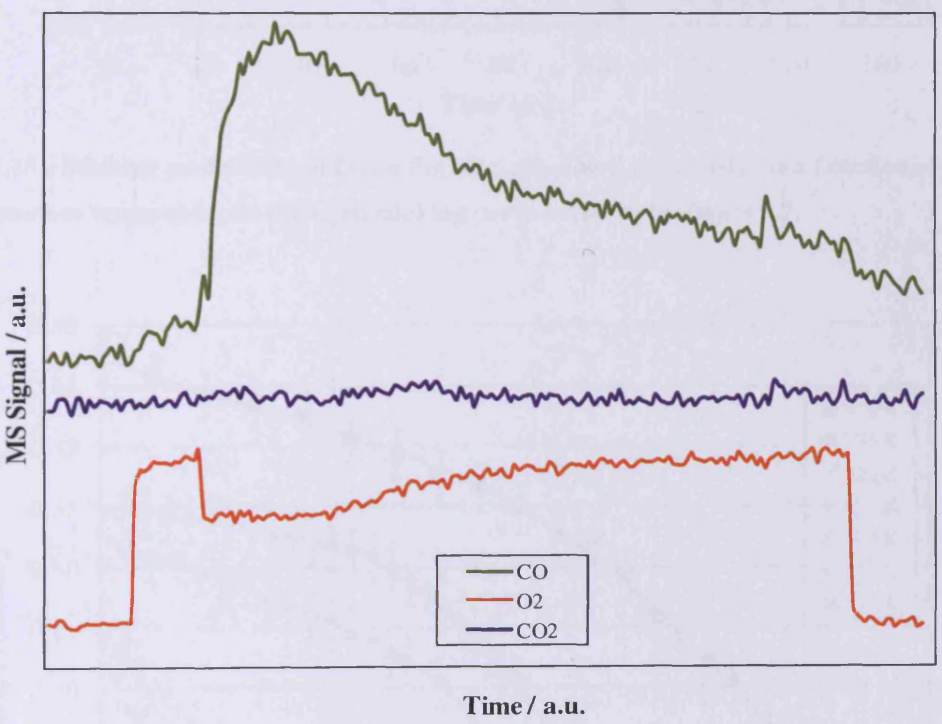

Figure 5.14 – Mass spectrometer signals obtained during the C clean off experiment performed at 773 K; O_2 (mass 32), CO (mass 28) and CO_2 (mass 44) were monitored.

Figure 5.15 & 5.16 show the sticking probability of O_2 on Fe(111) that has been pre-dosed with C_2H_4 at different substrate temperatures (adsorption of O_2 was done at the same substrate temperature as C_2H_4 adsorption in each case). Figure 5.17 shows an expansion of the O_2 $S - \theta$ curves at 373 – 673 K along with the clean surface equivalents and Table 5.4 compares the initial sticking values on the clean and C_2H_4 precovered surfaces.

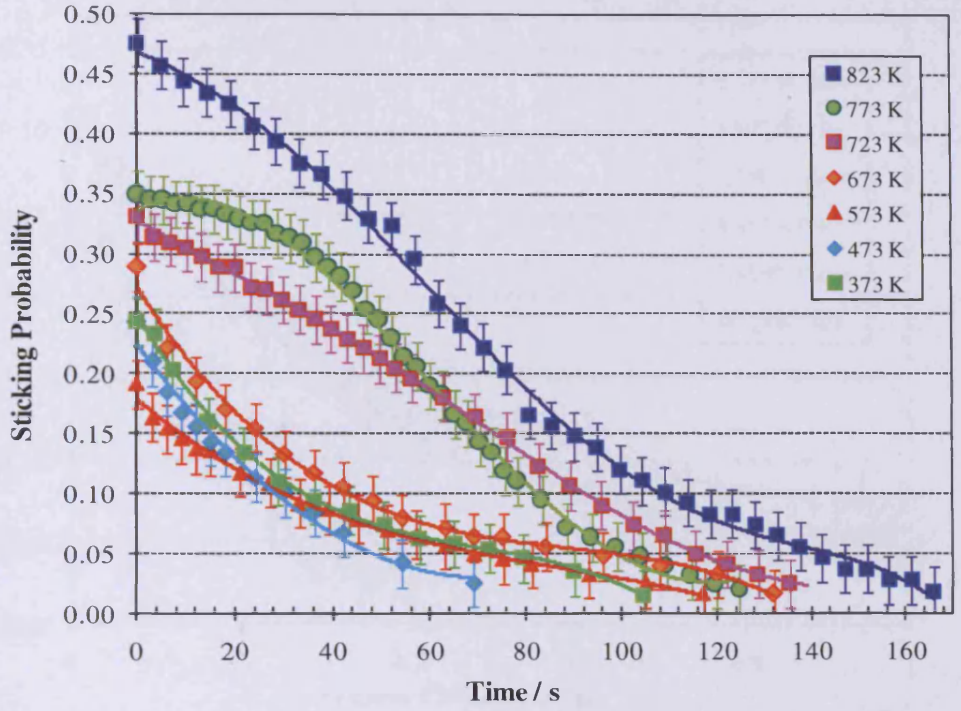

Figure 5.15 - Sticking probability of O_2 on Fe(111), pre-dosed with C_2H_4, as a function of time at various surface temperatures; the C_2H_4 sticking curve is shown in Figure 5.7.

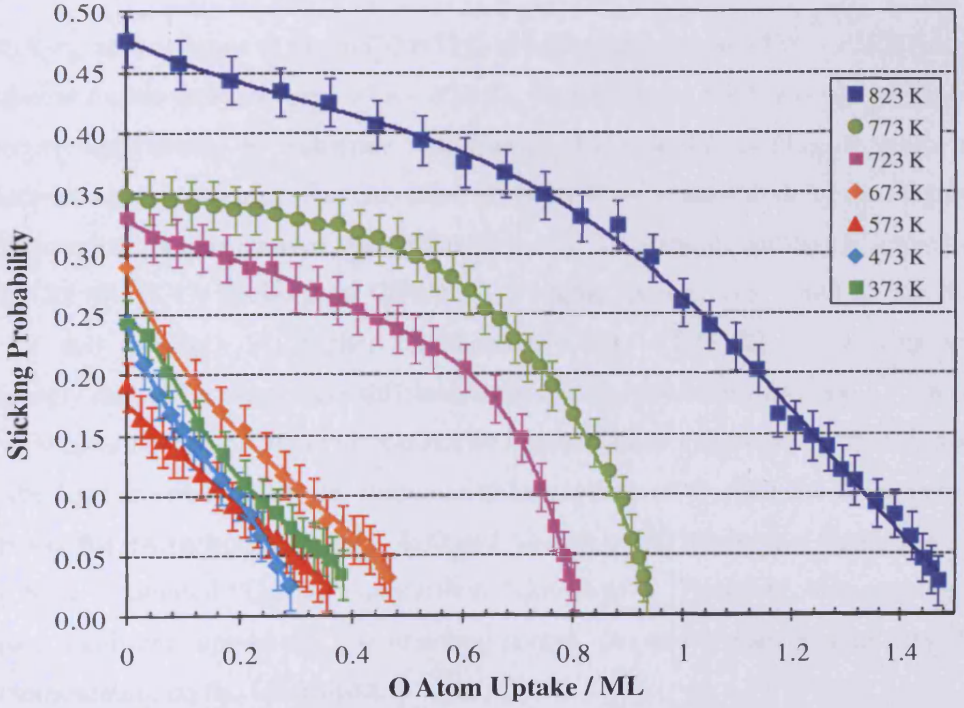

Figure 5.16 - Sticking probability of O_2 on Fe(111), pre-dosed with C_2H_4, as function of coverage at various sample temperatures; the C_2H_4 sticking curve is shown in Figure 5.8.

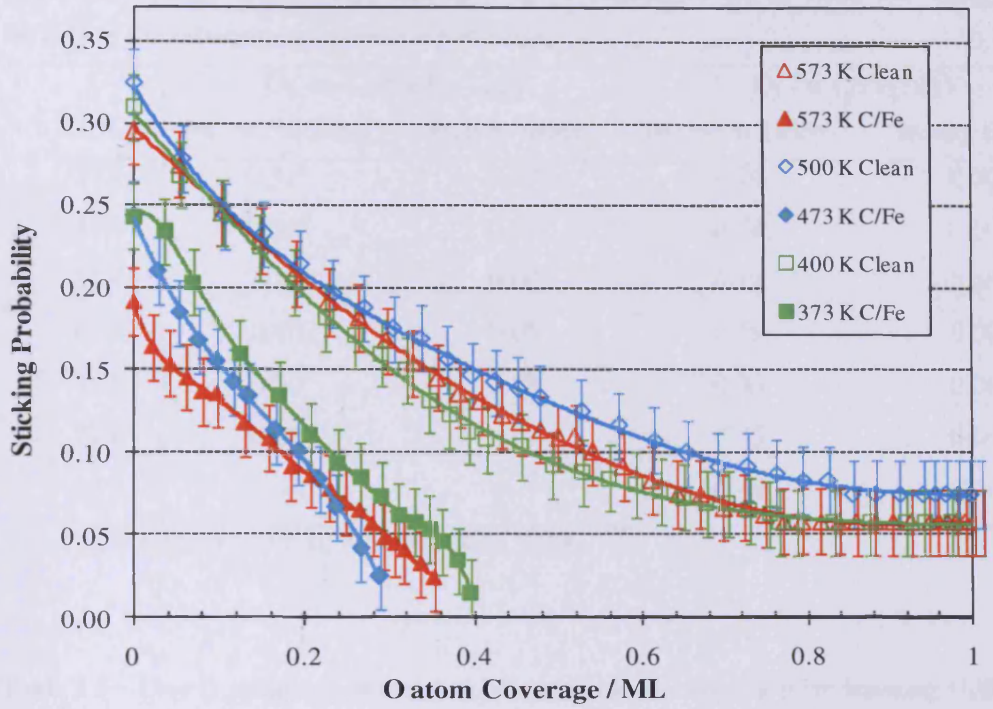

Figure 5.17 – Comparison of O_2 sticking on clean and C_2H_4 pre-dosed Fe(111) at similar substrate temperatures.

The sticking curve shapes of O_2 on C/Fe(111) at lower temperature (373 – 573 K) are distinct from that at higher temperatures, 723 – 823 K. O_2 sticking at the lower temperatures is not influenced significantly by substrate temperature although the sticking decreases slightly with increasing temperature. The curvature of the lines are similar than for the clean surface, *i.e.* characteristic of dissociative adsorption, however, the absolute sticking is lower by ~0.07 – 0.11. At 673 K O_2 sticking on C/Fe(111) is higher than at 373 – 573 K, but the curve shape is still similar. At higher temperatures (723 – 823 K) O_2 sticking increases significantly and curve shapes are different from those at lower temperature. $S - \theta$ (and $S - t$) curve shapes of O_2 on C/Fe(111) cannot be interpreted as simply as on the clean surface, since the former entails only the dissociative adsorption of O_2 and the latter involves O_2 adsorption, the interaction between C & O and ultimately CO production (hence the x-axis of Figure 5.16 is labelled "Uptake" rather than "Coverage"). However, the curve shapes do indicate a significant uptake of O_2 over a long period. No steady state sticking was observed at any temperature on the C/Fe surface.

Table 5.4 – Initial and steady state sticking probability of O_2 on clean and C_2H_4 pre-dosed Fe(111) at the substrate temperature indicated.

	O_2 on Clean Fe(111)		O_2 on C/Fe(111)	
T (K)	Initial Sticking	Steady State	Initial Sticking	Steady State
373	0.31[a]	0.07[a]	0.24	0.00
473	0.33[b]	0.07[b]	0.24	0.00
573	0.30	0.06	0.19	0.00
673	0.10	0.05	0.29	0.00
723	0.10	0.05	0.33	0.00
773	0.06	0.06	0.35	0.00
823	---	---	0.48	0.00

Notes: *a*) Measured at 400 K; *b*) Measured at 500 K

Table 5.5 – C or O uptake (presented in ML equivalent) resulting from beaming C_2H_4 or O_2 for 300 s at the substrate temperatures shown.[a]

T (K)	C on clean Fe(111)	O on clean Fe(111)	O on C/Fe(111)
373	0.31	1.10[b]	0.40
473	0.47	1.33[c]	0.30
573	0.44	1.14	0.37
673	1.50	0.60	0.48
723	1.94	0.64	0.80
773	2.38	0.72	0.93
823	1.79	---	1.48
873	1.63	---	---

Notes: *a*) Uptake values were calculated from sticking data as described in the experimental section.
b) Measured at 400 K; *c*) Measured at 500 K.

Table 5.5 shows the uptake of C atoms that resulted from dosing C_2H_4 on the clean Fe(111) surface and the uptake of O atoms that resulted from dosing O_2 on the clean or C_2H_4 predosed surface.

Figure 5.18 shows the comparison between the initial sticking values of O_2 on the clean and C_2H_4 predosed surface. The initial sticking probability between 373 – 573 K is less in the presence of C, but only by ~0.07 – 0.11. Figure 5.17 shows that these $S - \theta$ curve shapes are

different than that of the clean surface. The first change is observed at 673 K, where O_2 sticking on the C/Fe surface is higher than on the clean surface; this is the first temperature at which C_2H_4 steady state sticking was observed. The main difference between the initial sticking trends (Figure 5.9) is that sticking diminishes quickly at higher temperatures on the clean surface, while sticking on the C/Fe(111) surface increases significantly. Another difference is that a small amount of steady state sticking is observed on the clean surface at all temperatures, where as this was not the case in the presence of C (at any temperature).

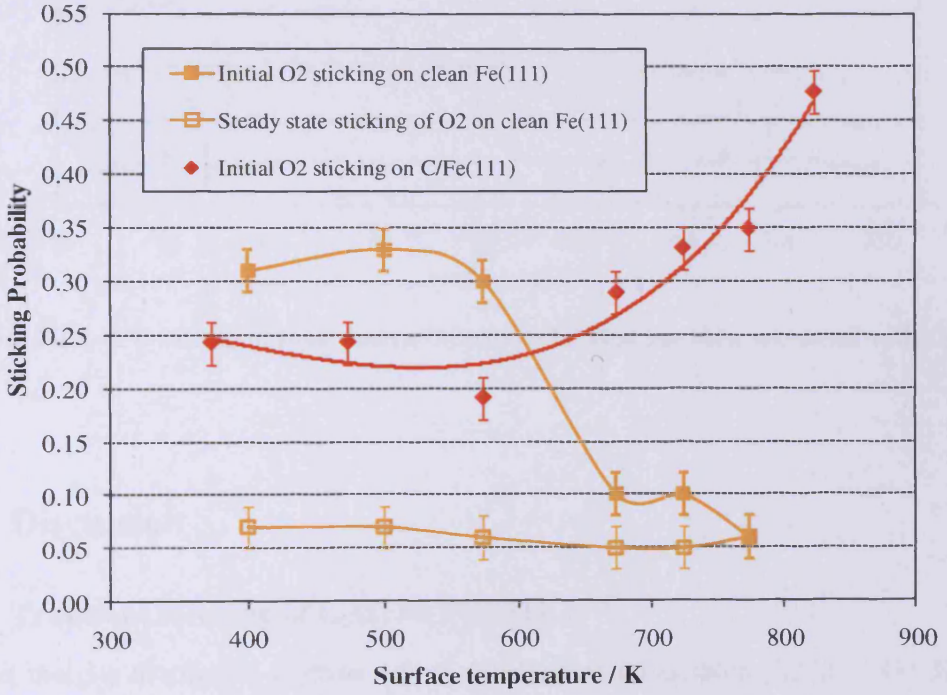

Figure 5.18 – O_2 sticking on clean Fe(111) and Fe(111) pre-dosed with C_2H_4; steady state sticking is observed on the clean surface, but not on the C/Fe surface.

Figure 5.19 shows the CO evolution curves obtained during O_2 adsorption on the C/Fe(111) surface. CO gas is not detected at 373 – 573 K, but starts to desorb from the surface from 673 K. At 673 K only a small amount of CO is given off, but the amount increases with increasing substrate temperature. At 673 & 723 K a time lag of ~2.5 s is observed between O_2 sticking and the start of CO evolution. At 773 & 823 K O_2 sticking and CO desorption starts simultaneously, as shown in Figure 5.14 (for the 773 K experiment). CO desorption at 723 & 773 K increases, peak and then diminishes; and at 823 K CO evolution also peak early on, but decreases more gradually.

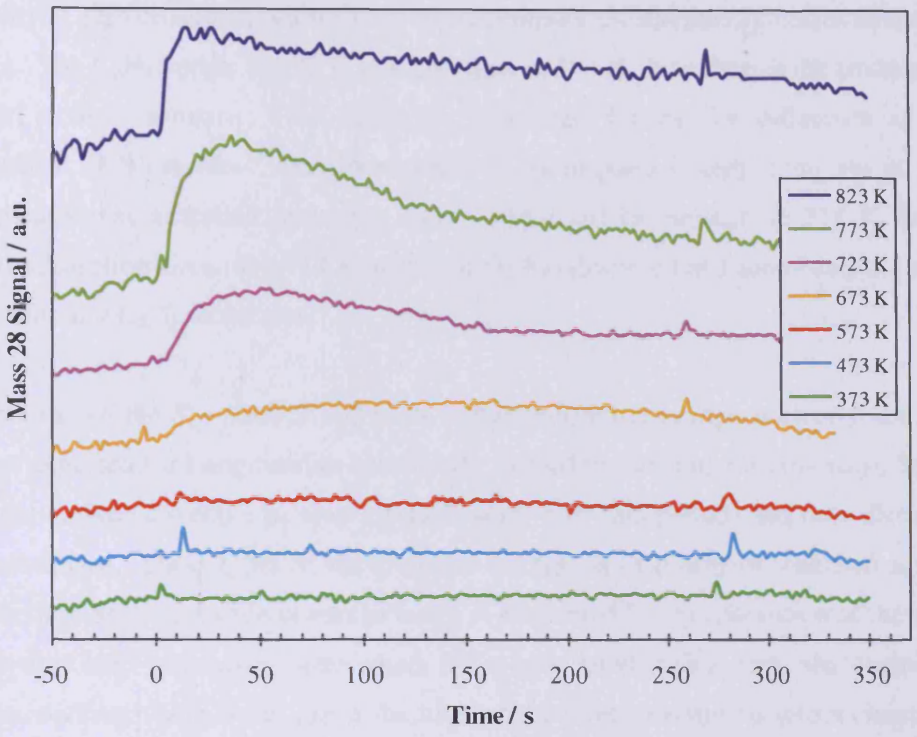

Figure 5.19 – CO evolution from dosing O_2 on Fe(111) that has been pre-dosed with C_2H_4.

5.4. Discussion

5.4.1. Transient Sticking of C_2H_4 on Fe(111)

The fact that H_2 desorption is observed at all substrate temperatures (373 – 873 K) is in agreement with adsorption studies of C_2H_4 on Fe(111)[12] which show that decomposition to surface C and H_2 gas commences already below room temperature and is complete by ~370 K, implying that no molecular species are present in the temperature range of this study. Unlike other surfaces of Fe, the (111) plane does not accommodate long lived CH_x species, hence the high degree of H_2 desorption observed in the MS. The immediate release of H_2 with C_2H_4 adsorption indicates that C_2H_4 decomposition and H_2 desorption occur instantaneously, *i.e.* desorption is fast and H_2 evolution is reaction limited. Under these conditions the hydrogen surface coverage is expected to be low.

In general the rate of adsorption is expected to decrease as the surface fills with adsorbate, because fewer sites become available. The mass spectrum signals at 373 K (Figure 5.4) as well as the $S - t$ and $S - \theta$ plots at 373 – 573 K (Figure 5.7 & Figure 5.8) indicate that

sticking is transient at these temperatures; the gas at first adsorbs with a high sticking probability at zero coverage, but sticking then decreases and eventually ceases as the surface saturates. The C_2H_4 uptake at 473 K is higher than at 373 K, even though the sticking at zero coverage is very similar. This might be accounted for by the difference in surface composition: TPD studies[12] have shown that H_2 desorption is only complete at ~450 K, which means that adsorbed hydrogen species will still be present at 373 K and block potential adsorption sites. By 473 K all of the H_2 has desorbed and more sites are available for the incoming C_2H_4 molecules.

The curvature of the $S - t$ and $S - \theta$ plots in this temperature range is clearly not linear as would be expected for Langmuirian behaviour. Instead the sticking initially stays high (even though the surface coverage increases significantly over this period) and only diminishes at higher coverages. These types of curve shapes are typical of precursor mediated adsorption. The high sticking over a wide coverage range is accounted for by adsorption of the molecule into a weakly held (precursor) state which is not associated with a particular chemisorption site. The sticking value is not just a function of the direct adsorption into a chemisorption site (as predicted by the Langmuir model), but also depends on the desorption and migration from the extrinsic precursor state and adsorption and desorption into/from the intrinsic precursor state. The curve is thus described by equation 5.12, which includes an equilibrium constant for the inter-conversion between the reactants and the precursor state. The precursor effect is quantified by the equilibrium constant, the *precursor state parameter* (K_p), given by equation 5.13. The precursor parameter at 373 K was estimated to be 0.4 (with the default value for Langmuir type adsorption being $K = 1$). The smaller this value, the greater the precursor effect, signifying that the relative rate of desorption from the extrinsic precursor state is small compared to the rate of chemisorption from the intrinsic precursor state. The precursor effect on adsorption is illustrated in Figure 5.2. The value of 0.4 confirms that adsorption is indeed precursor mediated, but the value is relatively high compared to *e.g.* N_2 adsorption on W, for which the value is ~0.1 is obtained at a similar temperature.[1] This indicates that migration does occur in the physisorbed state during C_2H_4 adsorption, but mobility is limited to some extent.

Seip[12] showed that the C coverage on Fe(111) obtained from the decomposition of 0.5 L of C_2H_4 is enough to inhibit subsequent C_2H_4 dissociation at low temperatures. Adsorption of C_2H_4 still proceeds on the C/Fe surface, but no dissociation occurs under these conditions. In addition to the "normal" C_2H_4 features in the HREELS, vibrational losses at lower frequencies were now also present. Two C_2H_4 desorption maxima, at 150 K & 210 K, were

observed in TPD, while C_2H_4 desorption on the clean surface is characterized by a single peak at ~200 K. These results suggest the presence of two differently bound states which were explained by the lowering of the molecular desorption energy and the increase in activation energy for decomposition; the weakly held state corresponds to molecules π-bonded to Fe1 atoms. This behaviour is attributed to the electronic modification of the surface due to the presence of C. Flashing the surface to 190 K removes the weakly held states from the surface and leaves the strongly bound molecules, which desorbs at 250 K as on the clean surface. These findings are in agreement with our results which show that C_2H_4 sticking decreases with increasing C coverage (at 373 K $\leq$ T $\leq$ 573 K), because C_2H_4 decomposition is prevented and molecular species will desorb at these temperatures.

5.4.2. Steady State Sticking of C_2H_4 on Fe(111)

As mentioned earlier, C_2H_4 decomposes completely to surface C and H_2 gas on Fe(111) without the formation of intermediates. α-Fe and C can co-exist in one of two states depending on the C concentration and temperature of the system: a stable equilibrium state between α-Fe and graphite or a metastable equilibrium state between α-Fe and Fe_3C. On clean iron surfaces (and UHV conditions) C is present as atomic (chemisorbed) carbon or graphite.[19,20,21] Graphite generally forms on the surface at particularly high C coverages and below the dissolution temperature.

Figure 5.7 & 5.8 show that steady state sticking of C_2H_4 commences between 573 – 673 K. The XPS binding energy of the C 1s peak after C_2H_4 adsorption at this temperature is ~282 eV and the value is the same for higher surface temperatures (673 – 873 K). The low BE value of ~282 eV is characteristic of atomic C on iron (see Table 4.1). The presence of C does not affect the Fe binding energy values, in agreement with other studies.[12,22] Carbidic carbon, *e.g.* C in Fe_3C, is typically found at ~283.5 eV[19] and graphitic carbon on Fe is expected at a higher BE still, > 284 eV, due to the stronger C-C interaction which results in a weaker C-Fe bonding. The relatively low binding energy of especially chemisorbed carbon (compared to solid graphite, ~284.7 eV[23]) suggests electron transfer from Fe to C.

The C coverages that resulted from these doses are not particularly high (Figure 5.11 & Table 5.3) and the C 1s peak diminishes gradually so that at 873 K the C surface coverage is minimal. In this temperature range (673 – 873 K) the amount of surface C is estimated to be less than 16 % than the total C uptake in each case. The large amount of C adsorbed during

the sticking experiment (under steady state conditions) compared to the small C coverage measured with XPS suggests that C diffusion into the subsurface region (or bulk) already starts at or below 673 K (see Table 5.5). This notion is in agreement with literature findings, as discussed below.

Kelemen[21] facilitated graphite formation on the Fe(110) surface by dosing 200 L of C_2H_2 at ~500 K. A large Auger C signal characteristic of graphite was observed (shown in Figure 2.13; and AES C/Fe = 2.6. LEED showed weak substrate spots with two concentric rings characteristic of graphite on metal surfaces. The peak did not change at higher exposure or temperature up to 673 K. Heating the surface above this temperature for a few minutes caused the graphite Auger line shape to be replaced with the carbidic line shape (Figure 2.13) and the LEED to convert to the C-ring pattern, characteristic of chemisorbed carbon on Fe(110) (Figure 4.7); the AES C/Fe ratio at the time was 0.6. Our results are in good agreement with these findings, even though different Fe surfaces were studied. The decrease in AES C/Fe ratio observed by Kelemen is attributed to the dissolution of C into the Fe bulk, since our XPS measurements show that the surface C coverage decreases $\geq$ 673 K despite the fact that steady state sticking occurs at these temperatures. The XPS C 1s BE obtained in this study (673 K $\leq$ T $\leq$ 873 K) supports the notion that the surface species is atomic C.

Wiltner[16] estimated the onset temperature for C diffusion into the bulk of Fe(110) to be 620 K. The onset temperature for diffusion was shown to be related to the activation barrier for C diffusion in the bulk of the metal as well as the surface atom density. One example is Fe and Ni: the onset temperature for C diffusion into the Fe(110) crystal is 620 K, correlating to the lower activation barrier for bulk diffusion (E_D = 0.86 eV) compared to Ni(111) (E_D = 1.5 eV) for which C diffusion into the bulk starts at 770 K. Comparing different surfaces of Ni, the onset temperature is lower for the more open Ni(100) compared to the close packed Ni(111); 670 K *vs.* 770 K. In agreement with this substrate and surface structure dependency, the activation energies for diffusion in these three crystals were experimentally determined as 1.3 eV, 1.4 eV & 1.9 eV respectively for Fe(110) < Ni(100) < Ni(111). The same trend was found for other metals.[24] It was shown that the thermal behaviour of the substrates is independent of the initial C film thickness, which was up to several nanometers thick (C films were deposited at room temperature through vapour deposition from a graphite rod).

In contrast C diffusion into Fe(100) was calculated to have a higher barrier than Fe(110), which is more densely packed. This is because C have higher coordination, and is therefore more strongly bound to Fe(100).

Our results suggest that C diffusion into the bulk of the Fe(111) crystal starts between 573 K and 673 K (Figure 5.7 & 5.8). Since C diffusion into Fe(110) starts at 620 K, a lower value is expected for the more open Fe(111), *i.e.* between 573 and 620 K. Seip[10] reported that dissolution of C into Fe(111) commences at ~610 K, which fits well with findings of this and other Fe studies.

5.4.3. Barrier for Chemisorption and Desorption from the Precursor State

Figure 5.9 shows that the initial sticking probability of C_2H_4 on Fe(111) decreases with increasing substrate temperature. The measured sticking probability is the net sum of the absolute sticking and desorption back into the gas phase, implying that the relative probability of desorption from the physisorbed state increases with respect to adsorption into the chemisorption state (from the physisorbed state) as the substrate temperature increases, causing the net sticking value to decrease. The fact that S_0 decreases with increasing substrate temperature indicates that the apparent activation energy, E_d - E_a, is positive, according to the relation in equation 5.14, *i.e.* adsorption is non-activated. Indeed, according to the plot of $ln(\alpha/S_0 - 1)$ against $1/T_s$ in Figure 5.10 (assuming α = 0.42) E_d is ~11 kJ/mol larger than E_a and the rate constant of desorption, ν_d, is ~11 times bigger than ν_a, the rate constant of adsorption.

5.4.4. O_2 Adsorption on Clean Fe(111)

As expected for Langmuir type adsorption the plots of O_2 sticking on the clean surface display a monotonic drop in sticking with coverage (or time); however the lines are not linear, but curved and the sticking values are consistently lower than expected for associative adsorption. This curve shape is typical of Langmuir dissociative adsorption, decreasing as $(1-\theta)^2$ (see equation 5.8), because one gas phase molecule needs two neighbouring surface sites to adsorb. The sticking curves at 400 – 573 K are the same within experimental error, suggesting that in this regime the substrate temperature does not affect adsorption with respect to the amount of sticking that occurs or the mechanism by which it occurs. At higher

temperatures, however, the net chemisorption is minimal as the relative rate of desorption increases relative to the rate of adsorption. At all temperatures, a small degree of steady state sticking is observed at the highest coverages. This is attributed to formation of oxide islands or O incorporation into the subsurface region.[25] Adsorption on the metal surface itself is site specific and therefore limited by the structure of the substrate, the availability of pairs of open sites and often also repulsive interaction between adsorbates. In islands, however, these limitations are not (or less) detrimental; O atoms are packed closer together and can even stack in layers, which translates into a continuous uptake in gas phase molecules. In practice both island formation and O incorporation into the bulk are probably applicable.

Oxidation studies of Fe(111),[26] Fe(100)[27] and Fe films[28] have been performed, although indirect methods were usually employed to derive the sticking probability and results are rather difficult to compare with ours. In the study of Fe(111) AES was used to follow the adsorption of O_2 at different exposures and especially the influence that K or S has on this. An inflection in the Coverage *vs.* O_2 Exposure curve was observed, which indicates an increase in the sticking probability (this was explained in terms of the formation of oxide islands). Our O_2 sticking results seems to be similar to the findings for Fe films at 300 K of which the sticking curve is shown in Figure 5.20.

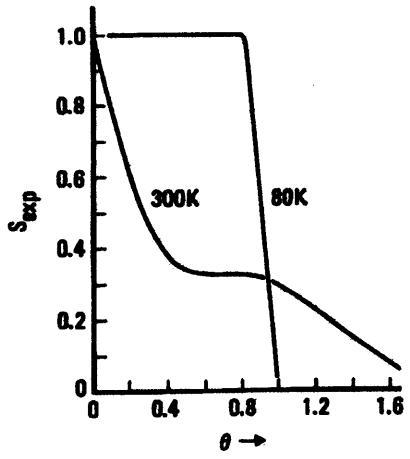

Figure 5.20 – O_2 Sticking with coverage on a Fe film at 80 & 300 K.[28]

In that study O_2 uptake was monitored with XPS during adsorption, and the data was used to derive the S *vs.* θ plot. The S_0 and coverage values shown in Figure 5.20 were calibrated to previous results of Horgan,[29] who measured the sticking of O_2 on Fe films directly. In the

graph S is unity at zero coverage, but then drops off between $\theta = 0 - 0.5$, after which it is constant up to ~1 ML (the constant uptake in this coverage range was said to be due to the growth of oxide islands). At higher coverages the sticking drops further to < 0.1, but a small sticking probability is measured up to the end of the experiment, which implies diffusion into the bulk. The adsorption kinetics could only be explained in terms of a mobile precursor state, which is thought to be active at both 80 K and 300 K; and the difference in kinetics at the two temperatures were attributed to the higher degree of order at 300 K.

5.4.5. O_2 Adsorption on C_2H_4 Predosed Fe(111)

O_2 sticking on the surface pre-dosed with C_2H_4 is lower than on the clean surface for substrate temperatures of between ~375 – 573 K (Figure 5.17). This suggests that the presence of C hinders O_2 adsorption somewhat at these temperatures, but surprisingly O_2 still sticks with a relatively high probability even though C_2H_4 uptake ceased early on in these experiments (the only reaction product from C_2H_4 adsorption expected on the surface is C and potentially H [12]). No gases are produced at these temperatures, which means that the surface now accommodates both C and O. From DFT calculations it is known that C prefers highly coordinated sites (see section 3.3.3). In the case of Fe(111) these are the fourfold sites: the quasi fourfold site (QFF), consisting of 2 Fe1, 1 Fe2 & 1 Fe3 or the quasi plane site (QP), consisting of 1 Fe1, 2 Fe2 & 1 Fe3 respectively (where Fe1, Fe2 & Fe3 refers to Fe atoms in the first, second and third layer of Fe(111); see Figure 3.1). On the other hand, the site preference of atomic O is not as specific and adsorption in the QFF site, the top-shallow bridge site (TSB, bonded to 1 Fe1 & 1 Fe2) or the shallow hollow site (SH, terminally bonded to 1 Fe2 atom) occurs with comparable stability (see Table 5.3 for adsorption energies and Figure 5.1 for a diagram of the surface sites). In the current situation, it is thus probable that C fills the fourfold sites and O adsorbs on the remaining available QFF / SH / TSB sites; although the close proximity of the C / O atoms could distort the most favourable adsorption positions to some degree (*e.g.* Figure 3.19).

On the clean Fe(111) surface O_2 sticking decreases drastically at higher temperatures, 673 – 823 K (see Figure 5.13). In contrast O_2 sticking increases significantly with increasing substrate temperatures on the C/Fe(111) surface – the net S values are higher and sticking continues for longer causing the total uptake of O_2 to be significantly more than on the clean surface. Curve shapes at these temperatures indicate that adsorption is not hindered by limited surface sites like on the clean surface (where S decreases as $(1-\theta)^2$). Figure 5.19

shows that CO desorption commences at $T \geq 673$ K and the amount of O_2 adsorbed is related to the amount of CO desorption (compare Figure 5.18 & 5.19). The reaction that results in the evolution of CO (Figure 5.19) consists of the following steps:

C_2H_4 (gas) → C_2H_4 (ads) (i)

C_2H_4 (ads) → 2C (ads) + $2H_2$ (gas) (ii)

O_2 (gas) → O_2 (ads) (iii)

O_2 (ads) → 2 O (ads) (iv)

C (ads) + O (ads) → CO (ads) (v)

CO (ads) → CO (gas) (vi)

Scheme 5.2 – CO production from surface C and O

Incoming O_2 molecules (producing O atoms) react rapidly with surface C atoms and leave the surface as CO, which frees up surface sites for incoming O_2 molecules. In this sense the process is the reverse of O_2 adsorption on the clean surface, in which case the surface fills up with O atoms over time. The fact that CO desorption occurs suggests that the atoms are mobile enough at these temperatures to form CO and that the desorption barrier is surmounted. The kinetic parameters for the recombinative desorption of C + O on Fe(111) at low coverages are available from literature.[30] This reaction occurs at ~760 K (peak maximum) at the lowest C/O coverages, however, at higher CO exposures recombinative desorption already commences at ~680 K (see Figure 5.21).

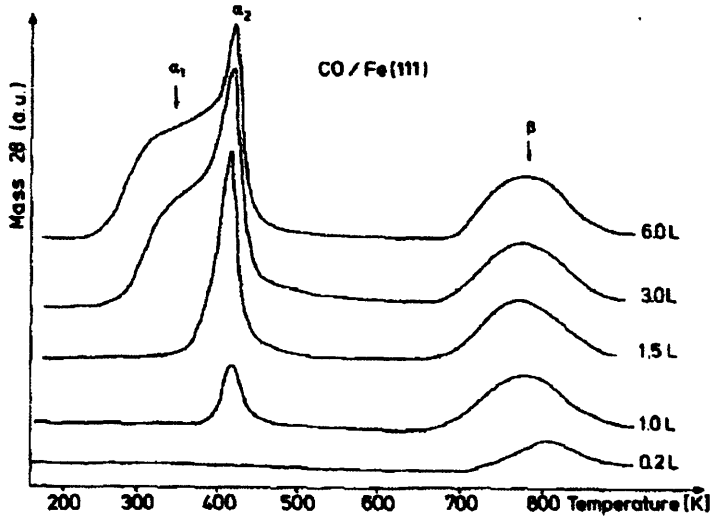

Figure 5.21 – Thermal desorption spectra for CO after varying exposures at 220 K.[31]

The activation energy was estimated to be $E \sim 2.08$ eV and the second order pre-exponential $\nu_2 \sim 0.1$ cm^2.s^{-1} (the prefactor is $\theta_o \nu_2 \sim 10^{13}$ s^{-1}, where θ_o is the initial coverage of C or O in cm^2). Desorption of molecular CO at higher coverages occurs around 400 K – 450 K; $E \sim$ 1.39 eV and $\nu_1 \sim 10^{17}$ s^{-1} (however, some atomic species from dissociated CO is also present on the surface). In the current experiments, with high coverages of C / O, CO desorption is observed at 673 K. This might be because the high coverage of C & O reduces the bond strength between the atoms and the surface (*i.e.* C essentially acts as a poison for O adsorption and vice versa).

Sticking experiments have shown that *steps i – iv* are facile and it is known that molecular CO desorption from Fe(111) (*step vi*) occurs already at ~450 K.[31] This suggests that *step v* above is most likely the rate determining step. The temperature at which CO desorption is evident, is also the first temperature at which C_2H_4 steady state sticking is observed. The steady state sticking has been related to C diffusion away from the surface which indicates that C becomes mobile at this temperature. This suggests that mobility of the atoms (perhaps especially C) is an important determining factor in CO production; C adsorption on Fe(111) is ~1.30 – 1.60 eV stronger than O adsorption (see Table 5.3).

No gas phase CO_2 is detected, even in the later stages of the clean off process when less surface C is available. This is another indication that CO desorption is rapid – the molecule is not bound to the surface long enough to have another O atom added, but desorbs as soon as it is formed.

The sticking of O_2 on C/Fe(111) at 673 K – 823 K is directly related to the amount of CO given off and both increase with increasing temperature. Figure 5.19 shows that the rate of CO desorption changes over time. This change is related to the varying concentrations of the surface species as the reaction proceeds. In a given experiment only C is initially present on the surface. As more O is adsorbed, CO production increases and the amount of C on the surface decreases. A maximum production rate is reached followed by a decrease as the availability of surface C becomes the limiting factor. A time lag between O_2 sticking and the onset of CO desorption exists at 673 K & 723 K, while CO desorbs instantaneous at 773 & 823 K; this suggests that the process speeds up with temperature. This is also noticeable when comparing the curve shapes. At 673 K the rate of CO desorption does not vary very much over time, but at higher temperatures a peak in CO desorption is observed. At 723 K the gradient is gradual compared to 773 K, but at 823 K CO production increases to a maximum almost as soon as O_2 is adsorbed.

Note that CO evolution continues to increase between 673 and 823 K, despite the fact that the amount of surface carbon decreases (see XPS spectra in Figure 5.11). This shows that the presence of O on the surface provides a driving force for C in the subsurface / shallow bulk region to segregate to the surface and be reacted away as CO. At 823 K the amount of CO desorption per second is less than at 773 K, but desorption continues at a steady rate, whereas CO desorption reaches a maximum and then diminishes at 773 K. This suggests that C may initially be located deeper in the bulk, and the reaction becomes dependent on the bulk diffusion rate. Nevertheless, the diffusion rate of C in Fe is high enough for C to reach the surface quickly and a significant amount of C is therefore reacted away. However, when one compares the O / C coverages from the respective $S - \theta$ plots, it becomes clear that the C uptake is significantly higher compared to O (see Table 5.5). This indicates that not all of the C is removed during the clean off experiment, which in turn suggests that a large portion of the deposited C resides in the bulk. Since segregation from the bulk is a function of the bulk C concentration, it will become less favourable at a lower bulk concentration (later on in the clean off experiment) and C will prefer to stay in the bulk instead of segregating to the surface.

Unlike on the clean surface, O_2 sticking on the C/Fe(111) surface seems to cease after some time. The continued sticking on the clean surface was attributed to the formation of oxide islands, which apparently do not form on the C/Fe(111) surface. It is possible that some of the C atoms on the surface might not be cleaned off, because C interacts very strongly with Fe and the heat of adsorption is expected to be even stronger at low coverages (later on in the

experiment), which would make C very unreactive. The fact that the O_2 sticking diminishes completely suggests that the presence of C prevents the Fe oxide phase from nucleating due to electronic or steric effects (or both).

Seip[12] dosed O_2 and C_2H_4 in the reverse order at ~127 K (*i.e.* Fe(111) was pre-dosed with O_2, after which C_2H_4 was adsorbed) and studied the surface species with HREELS and the decomposition products with TPD. O acts similarly to C (discussed above). 0.2 L of O_2 did not affect C_2H_4 adsorption, but 0.4 L of O_2 led to new features in the HREEL spectrum, indicating the formation of different bonding configurations. Vibration losses of the clean surface were still visible, but in addition higher frequency losses were also present. It was suggested that the partially oxidized surface still allows some strong Fe-C_2H_4 interaction (possibly di-σ bonded species with some strong Fe-H-C interactions), but that the remaining molecules consisted of weakly held species which are π-bonded due to the structural or electronic effect of O. 1L of O_2 resulted in only weak π-bonded C_2H_4 surface species which desorbed completely upon heating to 170 K.

5.4.6. C_2H_4 Sticking on Fe(111) Compared to Pd(110)

Results of C_2H_4 adsorption on Fe(111) is compared to a similar study on Pd(110).[32] Pd(110) presents an interesting comparison for Fe(111), since the metal is a late transition element in the second row of Group X in the periodic table, while Fe is a Group VIII element in the first row of transition metals. In addition the (110) plane is the most open of the low Miller index fcc surfaces, whereas the (111) plane is the most open of the low Miller-index bcc surfaces.

C_2H_4 sticking on Pd(110) is higher compared to Fe(111), ~0.65 – 0.34, *vs.* ~0.40 – 0.14, for substrate temperatures between 373 – 873 K. For both metals the sticking probability decreases with increasing substrate temperature (*i.e.* the apparent activation energy ($E_d - E_a$) is positive). Dehydrogenation occurs at a lower temperature on Fe(111); ~250 K compared to ~350 K on Pd(110); but interestingly Pd(110) absorbs C at a lower temperature than Fe(111), ~450 K *vs.* ~610 K. This is in contrast to the lower dissolution temperature of Fe(110) compared to Ni(100) or Ni(111) (which is positioned directly above Pd on the periodic table), showing that the dissolution temperature is not merely a function of the element's position in the periodic table and that the exact surface structure can have a pronounced influence.

In the Pd study it was found that other hydrocarbons behave similarly and can also be used as a source of carbon; including alcohols, acetaldehyde and acetic acid. C clean-off experiments were also performed. CO evolution starts at 573 K and in addition CO_2 is also produced as shown below.

$$C\ (ads) + O\ (ads) \rightarrow CO\ (ads)$$

$$CO\ (ads) \rightarrow CO\ (gas)$$

$$CO\ (ads) + O\ (ads) \rightarrow CO_2\ (ads)$$

$$CO_2\ (ads) \rightarrow CO_2\ (gas)$$

Scheme 5.3 – The production of CO and CO_2 gas during C clean off on Pd(110)

CO_2 desorption starts later in the reaction as the CO level starts to diminish; this was ascribed to the changing balance of carbon and oxygen atoms on the surface as more and more carbon atoms are reacted away over time. CO_2 was not produced on Fe(111), which suggests that CO is held more strongly on Pd(110), which allows time for CO to oxidize further.

XPS measurements done after dosing C_2H_4 show that the nature of the C on Pd(110) is different from C on Fe(111). On Pd(110) the C 1s peak is positioned at ~284.1 – 284.5 eV, depending on the dosing temperature (473 – 323 K). The corresponding value on Fe(111) is lower by about 2 eV (~282 eV, for dosing temperatures between 673 – 823 K), indicating that the C-Fe bond is stronger than C-Pd. The chemical nature of C on Pd(110) could not be determined unambiguously.

To summarise, C_2H_4 decomposition on Fe(111) and Pd(110) is similar in that the same sequence of events occur; however Fe is the more active metal and dehydrogenation occurs at a lower temperature. On the other hand C dissolution into the bulk of Pd occurs at a lower temperature compared to Fe, indicating that the Pd-C interaction is weaker than the Fe-C bond.

5.5. Summary

The initial sticking probability of C_2H_4 on Fe(111) decreases with temperature from 0.35 at 373 K to 0.13 at 873 K. Steady state sticking commences above 573 K and only steady state sticking is observed above 723 K. Between 373 and 673 K the carbon deposits resulting from C_2H_4 dosing decreases O_2 sticking compared to the clean surface (~0.24 on C/Fe(111) *vs.* ~0.30 on the clean surface), since the surface now accommodates both species. Above this temperature O_2 sticking increases significantly compared to the clean surface as it reacts with surface C to form CO gas: 0.06 *vs.* 0.34 at 773 K. CO production continues to increase with increasing surface temperature even though the XPS C 1s signal decreases above 673 K (apparently due to C diffusing into the subsurface region). This implies O on the surface provides a driving force for C in the subsurface / bulk to segregate to the surface. However, a large portion of the C resides in the bulk and can therefore not be cleaned off in this way.

5.6. Acknowledgements

I am grateful to Lee Gilbert for his assistance in the sticking probability measurements.

5.7. References

1. D. A. King and M. G. Wells, *Proceedings of the Royal Society of London. Series A, Mathematical and Physical Sciences (1934-1990)*, 1974, **339**, 245-269.
2. M. Bowker, *Appl. Cat. A*, 1997, **160**, 89-98.
3. M. Bowker, *J. Phys.: Condens. Matter*, 2010, **22**, 263002.
4. A. Cassuto and D. A. King, *Surf. Sci.*, 1981, **102**, 388.
5. R. I. Masel, *Principles of adsorption and reaction on solid surfaces*, John Wiley & Sons Inc., 1996.
6. G. Attard and C. Barnes, *Surfaces*, 1998, Oxford Univesity Press.
7. D. A. King, *CRC Critical Rev. Solid State Mater. Sci.*, 1978, **7**, 167.
8. C. Brucker and T. Rhodin, *J. Cat.*, 1977, **47**, 214-231.
9. W. Erley, A. M. Baro and H. Ibach, *Surface Science*, 1982, **120**, 273-290.
10. K. Yoshida and G. A. Somorjai, *Surf. Sci.*, 1978, **75**, 46-60.
11. M. Grunze, M. Golze, W. Hirschwald, H. J. Freund, H. Pulm, U. Seip, M. C. Tsai, G. Ertl and J. Küppers, *Physical Review Letters*, 1984, **53**, 850.
12. U. Seip, M. C. Tsai, J. Kuppers and G. Ertl, *Surf. Sci.*, 1984, **147**, 65-88.
13. D. E. Jiang and E. A. Carter, *Physical Review B*, 2003, **67**, 214103.
14. D. E. Jiang and E. A. Carter, *Phys. Rev. B.*, 2005, **71**, 045402.
15. C. A. Wert, *Phys. Rev.*, 1950, **79**, 601.
16. A. Wiltner, C. Linsmeier and T. Jacob, *J. Chem. Phys.*, 2008, **129**, 084704-084710.
17. I. Barin, *Thermochemical Data of Pure Substances*, VCH, Weinheim, 1995.
18. H. Bakker, H. P. Bonzel, C. M. Bruff, M. A. Dayananda, W. Gust, J. Horváth, I. Kaur, G. V. Kidson, A. D. Le Claire, H. Mehrer, G. G. E. Murch, Neumann, N. Stolica and N. A. Stolwijk, *in Diffusion in Solid Metals and Alloys*, Springer-Verlag, Berlin, 1990.
19. W. Arabczyk, F. Storbeck and H. J. Mussig, *Appl. Surf. Sci.*, 1993, **65-66**, 94-98.
20. G. Panzner and W. Diekmann, *Surf. Sci.*, 1985, **160**, 253-270.
21. S. R. Kelemen and A. Kaldor, *J. Chem. Phys.*, 1981, **75**, 1530-1537.
22. I. N. Shabanova and V. A. Trapeznikov, *J. Electron Spectr. Rel. Phenom.*, 1975, **6**, 297.
23. F. R. McFeely, S. P. Kowalczyk, L. Ley, R. G. Cavell, R. A. Pollak and D. A. Shirley, *Phys. Rev. B*, 1974, **9**, 5268.
24. J. Luthin and C. Linsmeier, *Phys. Scr.*, 2001, **T91**, T134.
25. C. Daitzchman, C. Aharoni and M. Ungarish, *Surf. Sci.*, 1991, **244**, 362.
26. W. Arabczyk, U. Narkiewicz, K. Kalucki and E. Freidenberg, *Applied Surface Science*, 1993, **72**, 45-48.
27. G. W. Simmons and D. J. Dwyer, *Surf. Sci.*, 1975, **48**, 373.
28. C. R. Brundle, *Surf. Sci.*, 1977, **66**, 581.
29. A. M. Horgan and D. A. King, *Surface Science*, **23**, 259-282.
30. L. J. Whitman, L. J. Richter, B. A. Gurney, J. S. Villarrubia and W. Ho, *J. Chem. Phys.*, 1989, **90**, 2050-2062.
31. U. Seip, M. C. Tsai, K. Christmann, J. Kuppers and G. Ertl, *Surface Science*, 1984, **39**, 29-42.
32. M. Bowker, C. Morgan, N. Perkins, R. Holroyd, E. Fourre, F. Grillo and A. MacDowall, *J. Phys. Chem. B*, 2005, **109**, 2377-2386.

CHAPTER 6

Conclusions & Outlook

6.1. Introduction

In accordance with the aims stipulated in *Chapter 1*, the structure and reactivity of the open Fe(111) and more densely packed Fe(110) surface was explored in the results section, *Chapter 2 – 5*. More specifically the interaction of small molecules with Fe was investigated, given its relevance to the Fischer-Tropsch reaction. The current chapter presents a summary of important results and conclusions from previous chapters as well as an outlook of potential future work.

6.2. Summary

6.2.1 The Interaction of CO with Fe(111) and the Influence of C

In *Chapter 3* the adsorption, diffusion and dissociation of CO on Fe(111) was explored to better understand the interaction of this FT reactant with the unpromoted catalytic surface. The effect of surface carbon at low coverage (¼ ML) was also evaluated, since it is an important influence under reaction conditions.

We found that CO can adsorb onto Fe(111) in a number of configurations with varying stability. We identified five minima at ¼ ML coverage, namely (in order of stability): SH, TSH, BL, DB and OT; at 1 ML coverage the DB converts to the BL state. The SH is the most favourable site, but diffusion from one site to another is very facile and it is expected that site occupation will only be dependent on the relative adsorption energies of the states. The barrier for CO dissociation is not greatly dependent on the molecular adsorption mode, but is considerably lower if O occupies a bridged position in the transition state. This is the case for (*1*) pathways (starting from any molecular state) that end with C in a fourfold coordinated quasi-plane position and oxygen bridged between an Fe1 and Fe2 atom (QFF-C & TSB-O) and (*2*) pathways starting from the DB molecular state and ending in any of the dissociated states that were considered. Neither of these groups of pathways have not been considered in previous studies.

¼ ML of additional C was shown to stabilize the CO molecule if close interaction is avoided, which in practice is possible at low C converges, since increased C coverages will inevitably lead to crowding. In agreement with this notion TPD experiments on Fe(100) have shown

that surface C reduces the binding energy of CO.[1] C has a destabilizing effect on the dissociated species, since it frequently blocks the most favourable site for O adsorption, which forces both atoms into less favourable configurations. However, results from our molecular beam study (*Chapter 5*) have shown that pre-adsorbed C will not block the adsorption of O_2 completely, and the molecule will continue to stick until a saturation coverage of ~0.4 ML of O is reached. This uptake is in addition to the 0.3 – 0.5 ML of C that is already present on the surface from pre-dosing C_2H_4 to saturation. This finding is in agreement with DFT calculations that showed that C adsorption on Fe(111) is rather site specific, while O can adsorb unto various sites with similar stability.

Barriers for dissociation pathways with / without C are generally similar, but since the DB state (which gives the lowest barrier on the clean surface) converts to the BL on C/Fe(111), these pathways are not available on the C/Fe(111) surface. On the other hand, dissociation from the DH (which is a hsp on the clean surface, but a formal minimum on the C/Fe surface) is now possible and the barrier for the DH to QFF-C & TSHμ^3 pathway is only 0.63 eV, which is ~0.4 eV lower than any other pathway on the clean or carbided surface. This is due to the short, highly coordinated route that the atoms follow to reach the end state. The reaction energies of all CO dissociation pathways on C/Fe(111) are endothermic and significantly higher compared to the clean surface due to the unfavourable end states, which should make CO dissociation on this surface rather improbable.

Finding the SH as the most favourable adsorption site is in agreement with previous experimental[2-4] and DFT studies.[5-7] CO stretch frequencies calculated here (but not in previous DFT studies) agree excellently with experimental values.[2-4] In addition we find that the energy and stretch frequency of the TSH minima is very close to that of the SH, which suggests that in practice the molecule is undergoing a rocking motion and that both states contribute to the frequency band. We calculate unusually low stretch frequencies for the tilted BL and DB states (1471 & 1422 cm^{-1}) which interact with Fe through both C and O. Two low frequency states in the same region (1325 – 1420 cm^{-1} & 1530 – 1573 cm^{-1}) were observed in experiment, but relative stabilities were said to be different than BL and DB. This might be so because the experimental states do not correspond to BL and DB (which means that the states observed in the experiment were not optimized in DFT) or because of the difference in the systems under consideration, brought about by the presence of dissociated surface species which are expected to be present in practice. Bartosch[3] tentatively assigned these low frequencies to variations of the DH which interconvert with change in coverage. We find that the two calculated states are indeed very similar, with the

main difference being the tilting angles. However, the DFT study shows that interaction with Fe3 is not a requirement for obtaining frequencies in this region, and this can be achieved through the additional Fe...O interaction of the tilted states instead. We find that the DH is not a formal minima, but a hsp, and is therefore not expected to be detected experimentally. The DH is stabilized to become a formal minima in the presence of C, but the C-O frequency we calculate is even lower, ~1000 cm^{-1} and therefore out of range of the experimental frequency band. In agreement with the small (or zero) barriers we calculate for CO diffusion, Whitman[4] assessed that CO is mobile even at 83 K and that the surface composition should only be a function of the relative stability of the states.

We found that the newly optimized DB follows lower energy dissociation pathways compared to other states due to the fact that the O atom is bridged (and therefore more stable) in the TS, in contrast to higher energy TS structures where O is terminally bonded. The lowest activation barrier calculated is 1.0 eV for DB to QP-C + TSB-O, which is in excellent agreement with the activation barrier for dissociation reported by Whitman.[3] The DB is higher in energy than the SH, but given the lack of significant diffusion barriers, it is likely that the SH converts to the DB before dissociating. In agreement with our finding DFT studies on other Fe single crystal surfaces, Fe(100),[8, 19] Fe(211),[10] Fe(310) & Fe(710)[7], have shown that CO dissociation is likely to proceed from a tilted configuration.

Table 6.1 and Figure 6.1 shows a comparison of the lowest calculated adsorption states of CO and activation barriers for dissociation on different Fe surfaces. CO adsorption is the strongest on Fe(100) and Fe(111). The smallest barriers for CO dissociation on Fe(111), calculated in this study and by Sorescu, are in line with that obtained for Fe(211) and Fe(100). These barriers are lower compared to Fe(110), but higher compared to the stepped surfaces Fe(310) and Fe(710); which correlates well with the relative roughness of the surfaces.

Table 6.1 – Minimum CO adsorption energies and activation energies for dissociation on various Fe surfaces.

	E_{ads_CO} (eV)	$E_{act\_CO\ diss}$ (eV)	Functional	Ref.
Fe(110)	-1.92	1.54	PBE	7
	-1.88	1.52	PBE	11
Fe(111)	-2.16[a]	1.00[b]	PBE	This work
	-2.09	1.05[c]	PBE	7
Fe(100)	-2.12	1.07	PBE	7
	-2.56	1.11	PW91	11
Fe(211)	-1.92	0.93	RPBE	10
	-1.96	1.02	PBE	7
Fe(310)	-1.76	0.73	PBE	7
Fe(710)	-1.80	0.67	PBE	7

a) Value for the SH state, ZPE not included
b) From DB, E_{ads} = -1.73 eV.
c) From BL, E_{ads} = -1.94 eV.

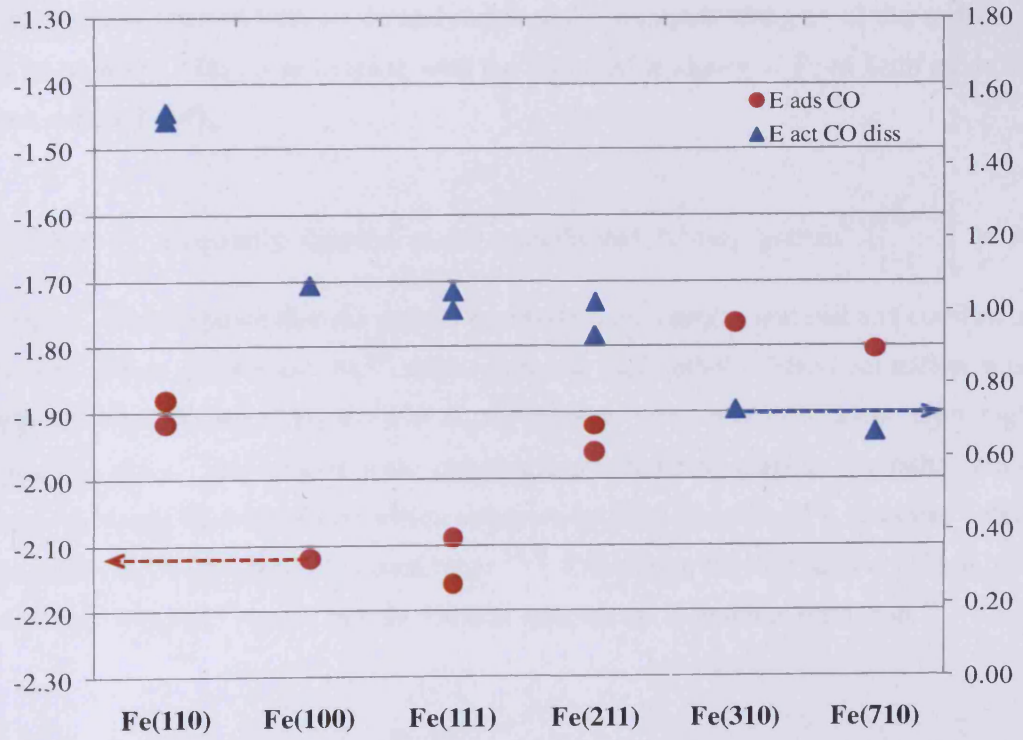

Figure 6.1 – CO adsorption energies ($E_{ads\ CO}$) of the most stable minima and activation energies for CO dissociation ($E_{act\ CO\ diss}$) on various Fe surfaces; see Table 6.1 for specific values (PW91 values excluded from the graph). E_{ads} values (red dots) are plotted on the primary vertical axis and E_{act} (blue triangles) on the secondary axis.

6.2.2 The Structure of Fe(111) & Fe(110) and the Influence of Adsorbates

In *Chapter 4* the structure of clean and adsorbate covered Fe(111) and Fe(110) surfaces were studied and limited adsorption studies of C_2H_4 on Fe(110) and O_2 on Fe(111) were carried out.

Fe(111) was shown to be very prone to adsorbate induced restructuring, even at low coverages. The surface seems to restructure to lower energy surfaces like Fe(100) and Fe(110) or forms highly symmetric triangular facets. LEED patterns of Fe(111) frequently exhibited split spots with threefold symmetry, in agreement with faceting observed with STM.

Oxidation of Fe(111) at 473 K results in a mixture of oxides, with FeO being the dominant species. Submonolayer coverages of O on Fe(111) leads to simple LEED structures, *e.g.* (4×4) and (6×6), whereas O in combination with other surface contaminants lead to complicated patterns arising from more than one unique overlayer structure. XPS spectra of some surfaces showed both oxide and metal peaks, implying that part of the surface might not be oxidized. This is in keeping with the observed tendency of Fe to form oxide islands when exposed to O_2.[13]

C on Fe(110) frequently resulted in the complicated "C-ring pattern" ($\begin{vmatrix} 4 & 0 \\ -1 & 3 \end{vmatrix}$ in matrix notation). It was shown that the pattern possesses a rectangular unit cell and consists of two domains which are rotated 70.5° with respect to each other. Island formation was also observed when dosing C_2H_4 at ~473 K; the features were only one atomic layer high and aligned in rows. The islands were tentatively attributed to graphite (or rather graphene, given the height measurements) which is known to form islands on Fe surfaces;[14] atomic C species, on the other hand, repel each other.[14-16] Comparing Fe(100) and Fe(110), it has been concluded from DFT studies that the latter is more prone to graphite formation.[17]

6.2.3 The Adsorption of C_2H_4 on Fe(111)

In *Chapter 5* the adsorption of C_2H_4 on Fe(111) was studied with a molecular beam reactor. The sticking probability of C_2H_4 was estimated at surface temperatures between 373 – 873 K

and the reactivity of the resulting surface species were explored in oxygen clean off experiments. Molecular beam adsorption studies on Fe are lacking in literature and the study provided valuable fundamental information.

Sticking is transient between 373 K – 573 K and the surface saturates at ~0.3 – 0.5 ML. Sticking in this temperature range is precursor mediated and the precursor parameter was calculated to be 0.4. Above this temperature steady state sticking commences and only steady state sticking is observed by 723 K; at this stage the surface does not saturate and the C uptake in 300 s exceeds 1.5 ML. The initial sticking probability decreases with increasing substrate temperature: ~0.35 at 373 K to ~0.13 at 673 K. The apparent activation energy, E_d - E_a is ~11 kJ/mole. O_2 sticking on the clean surface exhibits associative Langmuir type adsorption behaviour. The initial sticking probability at 400 K is ~0.30 and the value does not change with increasing surface temperature up to 573 K. At higher temperatures (673 – 773 K) sticking drops significantly as desorption is favoured over adsorption. O_2 sticking did not cease at high surface coverages at any of the substrate temperatures considered, but continues at a low rate up to the end of the experiment. Between 400 – 573 K coverages greater than 1 ML are reached within 300 s; at higher temperatures this value is lower (~0.6 ML) due to the lower rate of sticking. Between 400 – 573 K O_2 sticking on the C_2H_4 pre-dosed surface is somewhat lower compared to the clean surface value (~0.30 *vs.* 0.25). Nevertheless, a significant amount of O_2 is adsorbed and sticking only ceases at an O coverage of ~0.40 ML; the total surface coverage (C + O) at saturation is ~0.7 – 0.8 ML. DFT results from this study showed that C prefers fourfold sites on the Fe(111) surface, which is almost 1 eV lower in energy than the bridged or terminally bonded states. O adsorption, on the other hand, is less specific and the difference in energy between the QFF, TSB and SH sites is only ~0.3 eV. This implies that C from C_2H_4 will occupy the QFF and QP sites, while O will subsequently adsorb into TSB, SH or any remaining QFF sites. Above 723 K O_2 sticking on the C/Fe(111) surface increases significantly as O reacts with surface C to produce CO gas. However, a large portion of the C that was originally adsorbed is not cleaned off (between ~20 – 70%). In contrast to the clean surface, O_2 sticking on the C/Fe(111) surface eventually ceases at all temperatures.

Unlike Fe(100) and Fe(110), C_2H_4 decomposes completely on Fe(111) to adsorbed C and H below room temperature. H_2 evolution starts immediately, but this is not complete until ~470 K, which means that some of the hydrogen fills up surface sites below this temperature. In agreement with these results, we find that the uptake of C_2H_4 at 473 K is greater than at 373 K (0.5 ML *vs.* ~0.3 ML) even though the initial sticking probabilities are comparable.

Steady state sticking does not occur at 573 K, but is observed by 673 K (measurements at intermediate temperatures were not performed), in agreement with observations of Seip who reported that C diffusion into the bulk commences at ~610 K. The same sequence of events (as a function of temperature) was also observed for C_2H_4 adsorption on Pd, although the relative temperatures differ. C_2H_4 dehydrogenation on Pd(110) only occurs at 350 K, 100 K higher than on Fe(111). On the other hand, C is adsorbed into the bulk at a lower temperature on Pd(110); 450 K *vs.* 610 K. In a separate study it has been shown that C starts to dissolve into Fe(110) at a lower temperature than in Ni(100) or Ni(111) (which lies directly above Pd in Group X); indicating that both the type of substrate and surface structure are important variables in governing dissolution into the bulk.

Continuous sticking of O_2 on Fe is common, even at ambient temperature, and has been attributed to island formation and/or diffusion into the subsurface region. In contrast O_2 sticking ceases at 0.25 ML at a surface temperature of 318 K on Pd(110), while continuous sticking only commences at higher temperatures. Interestingly O_2 sticking ceases on the C/Fe(111) surface, implying that island formation or diffusion into the bulk is prevented.

CO was the only reaction product observed in the gas phase when O_2 was dosed onto the C/Fe(111) surface. This indicates that desorption is fast, in contrast to Pd(110) where CO_2 gas was also observed at a later stage in the experiment when the C coverage has decreased.

6.3. Relevance of This Work to Fischer-Tropsch Catalysis

Although the studies that were performed are very fundamental and involved metallic Fe and UHV conditions as opposed to real FT catalysts and reaction conditions, some correlations can be drawn between the model and the real system. Before the introduction of reactant gases, the High Temperature Fischer Tropsch Fe catalyst exists in the metallic phase.[18] With the introduction of CO and H_2 the catalyst undergoes a phase transition from metallic iron to iron carbide, although other phases (various oxides and carbides) co-exist.

Results from *Chapter 4* illustrated that adatoms (like sulphur and oxygen), even when present in small quantities, can severely influence the structure of (especially) the Fe(111) surface. This restructuring will most likely impact the adsorption/reaction of FT reactants and intermediates, as was shown in studies of Strongin & Somorjai.[12] Their experiments showed that ammonia induced reconstruction of Fe single crystal surfaces causes a change in

the relative reactivity towards Ammonia Synthesis. The restructured Fe(111) surface was less active compared to the original surface, while the modified Fe(100) and Fe(110) surfaces were more active than before. It is known that sulphur is a severe poison for FT catalysts and can lead to a significant loss in activity and a shift in product spectrum towards lighter/more hydrogenated products; in light of the results discussed above it is suggested that these changes may (at least in part) be due to structural effects.

It was shown in *Chapter 4* that the oxidation of Fe(111) is very facile and can lead to a mixture of oxides, which can be difficult to remove. In general, the strength of chemisorption increases with decreasing d-band filling, which would make the Fe-O bond stronger than the bonds between O and other FT active metals (Fe > Co > Ni > Ru) which possess more electrons. Under reaction conditions surface oxygen may form from the unassisted dissociation of chemisorbed CO (CO → C + O), which can react with adsorbed hydrogen to yield a surface hydroxyl group; react with adsorbed CO to yield CO_2 or diffuse into the bulk to generate an oxide phase. Our (and other) results from XPS and sticking probability measurements suggest that O will continue to adsorb and penetrate the bulk, even at low temperatures. The formation of magnetite from α-Fe under FT conditions is well documented. Under reaction conditions the removal of oxygen is assumed to be fast, since the catalytic surface is mainly covered with carbon. The results from the C clean off experiments in *Chapter 5* supports this assumption, since it show that the incoming O_2 molecules readily convert to and desorb as CO gas molecules in the presence of surface C. In each case an excess amount of C atoms that could not be removed was left on the surface (or in sub-surface region). In our experiments gas phase CO_2 was not observed, even though it is postulated to form from the removal of surface O from the catalytic surface. The main route for CO_2 formation under reaction conditions, however, is the Water Gas Shift reaction, which is thought to be catalysed by the magnetite phase.

Adsorption of CO followed by its dissociation is the first step in the FT reaction. The unassisted decomposition of CO to C and O (in contrast to hydrogen assisted dissociation), as presented in *Chapter 3*, is still considered to be an active reaction pathway, especially on the Fe surface on which CO dissociates more easily than on other FT metals. This agrees with the relative barriers calculated here for unassisted dissociation and hydrogen assisted dissociation as calculated by Huo (E_{act} ~ 1.0 eV for DB to C + O and E_{act} ~ 1.4 eV for CO to QP-C & TSB-O pathways as calculated in RPBE *vs.* ~1.2 eV for the most favourable hydrogen assisted pathways calculated in PBE).

The difficulty of cleaning C off from the Fe surface in experimental work as well as DFT calculated adsorption energies have shown that the interaction between Fe and C is very strong, which in part may explain the high percentage of Fe carbides that are present under reaction conditions. O_2 clean off experiments have shown that C can be removed from the surface (and even the subsurface region) at higher coverages and temperatures (> 573 K), but a percentage of residual C always remain, presumably due to the stronger heat of adsorption at lower coverages and/or the fact that the C is situated too deep into the bulk to be accessible to O. DFT calculations showed that (the most favourable state of) C adsorbs more strongly onto Fe(111) than (the most favourable state of) O by > 1 eV.

Although the HTFT catalyst is a carbide, DFT calculations have shown that CO adsorption onto Fe rich surface areas (of cementite) are favourable.[20] Our studies showed that C adsorbed in the vicinity of CO will stabilize the molecule if it is not situated too close to it. Other studies have shown that subsurface C can stabilize species like CO, CH_x and C/H/O atoms.[21] In fact, results from *Chapter 3* show that having a small amount of C on the surface can open up dissociation pathways that are not accessible on the clean surface (*ex.* DH to QFF-C & TSHμ^3-O), which might play an important part in the early stages of Fe carbide formation. Our results show that C diffusion into the bulk occurs between 573 – 673 K. This is in line with other studies that suggest that C starts to diffuse into the bulk of Fe(111) (or Fe(110)) at ~610 – 620 K and also falls within the typical temperature regime of the commercial HTFT process.

Chapter 5 dealt with the adsorption of C_2H_4 on Fe(111); and more specifically the sticking probability of the molecule and the influence of substrate temperature. α-olefins are primary products of the FT reaction, with C_2H_4 being the simplest olefin produced. In the early days of FT research it has been noticed that the desorption of olefins is reversible and that they can readsorb unto the surface to undergo secondary reactions such as hydrogenation to the corresponding paraffin; incorporation into growing chains; the formation of olefins with internal double bonds via a double bond shift and to a minor extent hydroformylation to produce alcohols and aldehydes or hydrogenolysis. These secondary reactions will clearly affect the composition and distribution of the entire product spectrum; which makes knowledge of the olefin adsorption process important. For specific results obtained in this study, see section 6.2.3.

6.4. Outlook

A limited number of studies involving C_2H_4 and Fe are available in literature despite its importance in industrial processes and fundamental research. To supplement the work reported here, the following is proposed:

Study the adsorption of C_2H_4 on other Fe surfaces, *eg.* Fe(100) and Fe(110) or polycrystalline Fe, to compare with results from this study. It has already been illustrated that the dehydrogenation of C_2H_4 on Fe(111) in the low temperature regime is very different compared to other low Miller index planes;[22-25] and sticking measurements would help to elucidate these difference further. Adsorption studies at higher temperatures are lacking at this stage.

The interaction between C and O needs further exploration. It has been shown that the clean Fe(111) surface continues to adsorb (/absorb) O_2 at high coverages, but that surface C prevents this from happening. STM studies combined with XPS and ISS will be useful in elucidating the composition and structure of the surface as well as the relative amounts of adsorbate accommodated on the surface compared to the subsurface/bulk. Furthermore it will be useful to establish whether conditions can be optimized to clean off a higher percentage of surface C with O_2 while minimizing the amount of surface oxidation.

In relation to the C_2H_4 studies, the diffusion and dissolution of C in Fe(111) needs to be explored further. Some work on Fe(100) and Fe(110) have been performed, notably the DFT study of Jiang & Carter[17] on Fe(100) and Fe(110) and the experimental study of Wiltner[26] on Fe(110), but similar studies on Fe(111) and documented Arrhenius parameters are still lacking.

The STM study of surface C on Fe(110) (and the proposed adsorption study of C_2H_4 on Fe(110)) can be supplemented with additional STM/LEED imaging at higher temperatures and coverages to compare with results from this work, but also with that of Fujii[15] who carried out C segregation on Fe(100) at temperatures between 650 – 850 K.

Ideally DFT results should be supplemented with TPD and/or molecular beam work of CO on Fe(111) with and without C. Further DFT calculations to elucidate the effect of C situated in the immediate subsurface region on the reactivity of CO will be insightful.

6.5. References

1. J. Benziger and R. J. Madix, *Surf. Sci.*, 1980, **94**, 119-153.
2. U. Seip, M. C. Tsai, K. Christmann, J. Kuppers and G. Ertl, *Surface Science*, 1984, **39**, 29-42.
3. C. E. Bartosch, L. J. Whitman and W. Ho, *J. Chem. Phys.*, 1986, **85**, 1052.
4. L. J. Whitman, L. J. Richter, B. A. Gurney, J. S. Villarrubia and W. Ho, *J. Chem. Phys.*, 1989, **90**, 2050-2062.
5. Y.-H. Chen, D.-B. Cao, Y. Jun, Y.-W. Li, J. Wang and H. Jiao, *Chem. Phys. Lett.*, 2004, **400**, 35-41.
6. C.-F. Huo, J. Ren, Y.-W. Li, J. Wang and H. Jiao, *J. Cat.*, 2007, **249**, 174-184.
7. D. C. Sorescu, *J. Phys. Chem. C*, 2008, **112**, 10472-10489.
8. D. C. Sorescu, D. L. Thompson, M. M. Hurley and C. F. Chabalowski, *Phys. Rev. B*, 2002, **66**, 035416.
9. D. W. Moon, S. Cameron, F. Zaera, W. Eberhardt, R. Carr, S. L. Bernasek, J. L. Gland and D. J. Dwyer, *Surf. Sci. Lett.*, 1987, **180**, L123-L128.
10. D. Borthwick, V. Fiorin, S. J. Jenkins and D. A. King, *Surf. Sci.*, 2008, **602**, 2325-2332.
11. D. E. Jiang and E. A. Carter, *Surface Science*, 2004, **570**, 167-177.
12. D. R. Strongin and G. A. Somorjai, *J. Catal.*, 1989, **118**, 99.
13. A. Wight, N. G. Condon, F. M. Leibsle, G. Worthy and A. Hodgson, *Surface Science*, 1995, **331-333**, 133-137.
14. G. Panzner and W. Diekmann, *Surf. Sci.*, 1985, **160**, 253-270.
15. J. Fujii, M. Galaktionov, L. Giovanelli, G. Panaccione, F. Bondino, I. Vobornik and G. Rossi, *Thin Solid Films*, 2003, **428**, 30-33.
16. G. Panaccione, J. Fujii, I. Vobornik, G. Trimarchi, N. Binggeli, A. Goldoni, R. Larciprete and G. Rossi, *Phys. Rev. B (Condensed Matter and Materials Physics)*, 2006, **73**, 035431-035439.
17. D. E. Jiang and E. A. Carter, *Phys. Rev. B.*, 2005, **71**, 045402.
18. A. Steynberg and M. Dry, *Fischer-Tropsch Technology*, 2004, **Elsevier**.
19. T. C. Bromfield, D. Curulla Ferré and J. W. Niemantsverdriet, *ChemPhysChem*, 2005, **6**, 254-260.
20. X.-Y. Liao, D.-B. Cao, S.-G. Wang, Z.-Y. Ma, Y.-W. Li, J. Wang and H. Jiao, *Journal of Molecular Catalysis A: Chemical*, 2007, **269**, 169-178.
21. D. C. Sorescu, *Phys. Rev. B*, 2006, **73**, 155420.
22. U. Seip, M. C. Tsai, J. Kuppers and G. Ertl, *Surf. Sci.*, 1984, **147**, 65-88.
23. C. Brucker and T. Rhodin, *J. Cat.*, 1977, **47**, 214-231.
24. W. Erley, A. M. Baro and H. Ibach, *Surface Science*, 1982, **120**, 273-290.
25. K. Yoshida and G. A. Somorjai, *Surf. Sci.*, 1978, **75**, 46-60.
26. A. Wiltner, C. Linsmeier and T. Jacob, *J. Chem. Phys.*, 2008, **129**, 084704-084710.